Aus dem Bereich medizinische Biochemie

Theoretische Medizin und Biowissenschaften

Der Medizinischen Fakultät

Der Universität des Saarlandes, Homburg/Saar

Multidisciplinary analyses reveal distinct intramembrane positioning of UBXD8 in endoplasmic reticulum and lipid droplet membranes

Dissertation zur Erlangung des Grades eines

Doktors der Naturwissenschaften

Der Medizinischen Fakultät

Der Universität des Saarlandes

2024

vorgelegt von: Ravi Dhiman

Tag der Promotion:	18.07.2024
Dekan:	Univ.-Prof. Dr. med. Michael D. Menger
Berichterstatterin:	Prof. Dr. Bianca Schrul
	Prof. Dr. Gabriela Krasteva-Christ

Zusammenfassung

Lipidtropfen (LDs) sind allgegenwärtige zytoplasmatische Organellen, die für die Speicherung von Fett in Form von neutralen Lipiden, insbesondere Triacylglycerolen (TAGs), verantwortlich sind. Aufgrund ihrer integralen Rolle im Fettstoffwechsel wird den LDs eine entscheidende Rolle bei einer Vielzahl menschlicher Krankheiten zugeschrieben. In der Vergangenheit haben Studien gezeigt, dass eine Reihe von Proteinen durch hydrophobe Haarnadel-Domänen und amphipathische Helices spezifisch mit der Phospholipid-Monolage assoziiert sind. Dieses dynamische LD-Proteom spielt eine entscheidende Rolle bei der Regulierung der Funktionen dieser Organelle im zellulären Stoffwechsel. Die LD-Proteine, die auf das endoplasmatische Retikulum (ER) ausgerichtet sind, assoziieren nachweislich mit der ER-Doppelschicht, indem sie eine monotopische Haarnadel-Topologie annehmen. Es wurde vermutet, dass diese einzigartige topologische Assoziation mit dem zytosolischen Blatt des ER die laterale Diffusion von LD-Haarnadelproteinen aus dem ER in die LDs fördert.

In dieser Studie habe ich UBXD8 als Modell-Haarnadelprotein verwendet, das sich sowohl in der ER-Doppelschicht als auch in der LD-Monolayer-Membran befindet. Eine Kombination aus multidisziplinären Ansätzen wie biochemischen Cystein-Lösungsmitteltests, Intramembran-Vernetzung und atomistischen MD-Simulationen wurde verwendet, um die Intramembran-Positionierung der in die Membran eingebetteten Region von UBXD8 sowohl in der ER-Doppelschicht als auch in den LD-Monolayer-Membranen zu bestimmen. Die Ergebnisse dieser Studie zeigten, dass die in die Membran eingebettete Region von UBXD8 in zwei verschiedenen physikalisch-chemischen Membranumgebungen unterschiedliche Konformationen annimmt. In der ER-Doppelschicht wurde festgestellt, dass UBXD8 tief integriert ist und eine V-förmige Topologie mit zwei antiparallelen α-Helices annimmt, die einander gegenüberliegen, während in LD-Monoschichten die in die Membran eingebettete Region von UBXD8 eine offenere und flachere Konformation annimmt. Die Berechnungen der freien Energie am Rand der LD in Kontinuität mit der planaren Doppelschicht unterstützten eine stabile Deep-V-Konformation für UBXD8 in der ER-Doppelschicht. Damit sich UBXD8 vom ER auf die LDs aufteilen kann, ist daher eine strukturelle Umlagerung von der Deep-V- zur Flat-Konformation unvermeidlich. Die zusätzlichen Faktoren, die diesen Übergang regulieren, wie z. B. akzessorische Proteine, müssen jedoch noch identifiziert werden. Diese Studie stellt ein neues

Paradigma vor, das darauf hindeutet, dass die Abtrennung von Haarnadelproteinen aus dem ER in die LDs möglicherweise nicht nur von passiver Diffusion abhängt, sondern dass einige Proteine eine strukturelle Umstrukturierung durchlaufen müssen. In Zukunft könnten weitere Studien, die biochemische Experimente mit MD-Simulationen kombinieren, dazu beitragen, die molekularen Mechanismen zu entschlüsseln, die die Verteilung von Haarnadelproteinen vom ER zu den LDs steuern.

Abstract

Lipid droplets (LDs) are ubiquitous cytoplasmic organelles, responsible for storing fat in the form of neutral lipids, specifically triacylglycerols (TAGs). Given their integral role in lipid metabolism, LDs have been implicated in playing a crucial role in a plethora of human diseases. In the past, studies have revealed that a diverse set of proteins specifically target and associate with the phospholipid monolayer through hydrophobic hairpin domains and amphipathic helices. This dynamic LD proteome plays a crucial role in regulating the functions of this organelle in cellular metabolism. The LD proteins targeted to the endoplasmic reticulum (ER) have been shown to associate with the ER bilayer adopting a monotopic hairpin topology. It has been suggested that this unique topological association with the cytosolic leaflet of ER drives the lateral diffusion of LD hairpin proteins from the ER-to-LDs.

In this study, I employed UBXD8 as a model hairpin protein which resides in both the ER bilayer and LD monolayer membranes. A combination of multidisciplinary approaches such as biochemical cysteine solvent-accessibility assay, intramembrane crosslinking, and atomistic MD simulations were used to determine the intramembrane positioning of UBXD8 membrane-embedded region in both the ER bilayer and LD monolayer membranes. The findings from this study revealed that the UBXD8 membrane-embedded region adopts distinct conformations in two different physicochemical membrane environments. In the ER bilayer, UBXD8 was found to be deeply integrated adopting a V-shaped topology with two antiparallel α-helices facing each other, whereas in LD monolayers the UBXD8 membrane-embedded region adopted an open and shallow conformation. The free energy calculations at rim of LD in continuity with planar bilayer further supported a stable deep-V conformation for UBXD8 in the ER bilayer. Therefore, in order for UBXD8 to partition from the ER-to-LDs, a structural rearrangement from deep-V to shallow conformation is inevitable. The additional factors regulating this transition such as accessory proteins, however, need to be identified. This study introduces a novel paradigm, suggesting that the partitioning of hairpin proteins from the ER-to-LDs may not be solely reliant on passive diffusion, and may necessitate some proteins to undergo a structural rearrangement. In the future, more studies combining biochemical experiments with MD simulations could help us in unravelling the molecular mechanisms that govern the partitioning of hairpin proteins from the ER-to-LDs.

Publications

1. Dhiman, R., Caesar, S., Thiam, A. R., & Schrul, B. (2020). Mechanisms of protein targeting to lipid droplets: A unified cell biological and biophysical perspective. **Seminars in Cell & Developmental Biology, 108, 4-13.**

2. Hairpin protein partitioning from the endoplasmic reticulum to lipid droplets involves major structural rearrangements. **(In preparation)**

Authors

Ravi Dhiman[1], Rehani Shinuka Perera[1], Chetan Poojari[2], Haakon Tassilo Adam Wiedemann[3], Reinhard Kappl[4], Christopher William Michael Kay[3,5], Jochen Sebastian Hub[2], Bianca Schrul[1].

Affiliations

[1] Medical Biochemistry and Molecular Biology, Center for Molecular Signaling (PZMS), Faculty of Medicine, Saarland University, 66421 Homburg/Saar, Germany

[2] Theoretical Physics and Center for Biophysics, Saarland University, 66123 Saarbrücken, Germany.

[3] Physical Chemistry and Chemistry Education, Saarland University, 66123 Saarbrücken, Germany.

[4] Department of Biophysics, Center for Integrative Physiology and Molecular Medicine (CIPMM), Saarland University, 66421 Homburg/Saar, Germany

[5] London Centre of Nanotechnology, University College London, London, WC1H 0AH, United Kingdom

Abstract

Lipid droplet (LD) function relies on proteins that partition between the ER phospholipid bilayer and the LD monolayer membrane to control cellular adaptation to metabolic changes. Although experimental evidence was lacking, it has been proposed that these hairpin proteins integrate into both membranes in a monotopic topology, enabling their passive lateral diffusion during LD emergence at the ER. Here, we combine biochemical solvent-accessibility assays, cwEPR spectroscopy and intra-molecular crosslinking experiments with MD simulations, and determine the intramembrane positioning of the ER/LD protein UBXD8 in both ER bilayer and LD monolayer membranes. We find that the hydrophobic domain of UBXD8 adopts distinct and stable conformations in these membranes. While UBXD8 is deeply inserted into the ER bilayer with a V-shaped topology, it adopts an open-shallow conformation in the LD monolayer. Thus, major structural rearrangements are required to enable ER-to-LD partitioning. Free energy calculations suggest that additional proteins are required to assist in this structural transition, indicating that ER-to-LD protein partitioning relies on more complex mechanisms than anticipated and providing regulatory means for this trans-organelle protein trafficking.

Posters

1. Establishing a fine-resolution topology map of the monolayer-integrated hairpin protein UBXD8.

Ravi Dhiman[1], Martin Leibrock[1], and Bianca Schrul[1]

[1] Center for Molecular Signaling (PZMS), Medical Biochemistry & Molecular Biology, Saarland University, Homburg (Germany)

Poster presented at Cell Physics Conference 2019, Saarbrücken, Germany. (awarded 2nd prize)

2. Insight into the topology of the monotopic hairpin protein UBXD8 in endoplasmic reticulum bilayer and lipid droplet monolayer membranes.

Ravi Dhiman[1], Chetan Poojari[2], Jochen S. Hub[2] and Bianca Schrul[1]

[1] Center for Molecular Signaling (PZMS), Medical Biochemistry & Molecular Biology, Saarland University, Homburg, Germany

[2] Theoretical Biophysics, Saarland University, Saarbrücken, Germany

Poster presented at Cell Physics Conference 2021, Saarbrücken, Germany. (awarded 2nd prize)

Table of Contents

1. Introduction

1.1 Lipid droplets- An historical perspective

A cell is packed with multiple membrane-bound organelles, each of which has a distinct membrane organization and composition. Organelles such as the nucleus, endoplasmic reticulum (ER), and mitochondria, for example, are surrounded by a phospholipid bilayer that separates the two aqueous environments. The wide range of proteins and enzymes that target these organelles have been well-characterized from both a structural and functional standpoint, and has been demonstrated to play a critical role in regulating the functions of these organelles, which are enclosed by a phospholipid bilayer (Palade, 1956; Porter et al., 1945; Porter & Palade, 1957). However, the lipid droplet (LD) is the only organelle in the cell that is enclosed by a phospholipid monolayer, which delineates a highly hydrophobic core from the surrounding aqueous environment (Walther & Farese, 2009). Currently, we know relatively little about LD biogenesis and function. This knowledge gap is mostly due to a lack of understanding of the proteins and enzymes that target these organelles and how they interact with the monolayer membrane environment to regulate their functions (Walther & Farese, 2012).

Richard Altmann and Edmund Wilson were the first to observe lipid droplets (LDs) within cells as “oil drops” using light microscopy (Altmann, 1894; Wilson, 1896). At that time, LDs were considered to be inert globules of fat with no specific functions in the cells. This led to the LDs being ignored and understudied in comparison to other organelles such as the ER and mitochondria (Palade, 1956; Porter et al., 1945; Porter & Palade, 1957).

The elucidation of the biochemical pathways and enzymes associated with the synthesis of phospholipids and triacylglycerols (TAGs) within the ER by Eugene Kennedy and coworkers (Kennedy, 1957; Weiss et al., 1956), and the critical observation of LDs being in close proximity to the ER, and the ER to be the main site for the esterification of the fatty acids into TAGs pointed towards the potential transfer of neutral lipids from the ER into cytoplasmic LDs (Angel & Angel, 1970; Lutas et al., 1977; Stein & Stein, 1968). Despite these important clues, the paucity of available research tools and technological hurdles made it difficult to study the functional relationship of LDs to other organelles and how they are formed in the cell. While other

organelles have been the central focus of research, LDs received comparatively little attention or were mostly ignored (Coleman, 2020; Henne, 2020).

In the early 1990s, perilipin 1 (PLIN1) and perilipin 2 (PLIN2) were identified to be associated with the LDs isolated from adipocytes by subcellular fractionation (Brasaemle et al., 1997; Greenberg et al., 1991). The discovery of perilipins as LD-associated proteins not only brought this organelle back into light, but also invoked interest in the identification and characterization of new LD-associated proteins. In 1999, Athenstaedt and coworkers identified a total of 16 proteins on LDs isolated from *Saccharomyces cerevisiae* using systematic mass spectrometric analysis (Athenstaedt et al., 1999). The identified proteins were attributed to be mainly involved in lipid metabolism. This study also speculated on the possible mechanisms by which proteins associate or target the yeast LDs. For instance, proteins might target the LDs surface by intrinsic targeting signals or by using vesicular machinery. In addition, the proteins with no transmembrane domains (TMDs) might remain associated with the phospholipid monolayer of LDs as they bud from the ER (Athenstaedt et al., 1999). Prior to the observations made in yeast, the ideas were already put forth that the plant LDs, termed oil bodies, and their associated proteins such as oleosin bud together from the ER (Huang, 1992; Hunag, 1996) .

In an effort to identify novel genes that are important for LD function and biogenesis, two microscopy-based genome-wide screens were carried out in *Saccharomyces cerevisiae* to generate a library of around ~4936 single-gene deletion mutants (Fei et al., 2008; Szymanski et al., 2007). These screens identified many genes whose deletion resulted in yeast strains with abnormalities in LDs number and morphology. One of the main highlights of these two screens is the identification of yeast seipin (Fld1p/Sei1). The *fld1Δ* (few lipid droplets) yeast cells could still generate a few LDs, but these LDs were either unexpectedly bigger in size or tended to form clusters of small-sized LDs (Fei et al., 2008; Szymanski et al., 2007). In human patients, a near or complete loss of adipose tissue (lipodystrophy) was linked to the ablation of Berardinelli-Seip congenital lipodystrophy-2 or congenital generalized lipodystrophy (*BSCL2/CGL2)* gene, which encodes the protein seipin, of which yeast and *Drosophila* seipin is a homolog (Berardinelli, 1954; Magré et al., 2001; Seip, 1959). As of today, seipin is the most studied protein in the field of LD biology. Another genome-wide RNA interference (RNAi) screen performed by Farese and Walther group in *Drosophila* S2 cells identified 227 genes (~1.5% of the total *Drosophila*

genome), which they conclude to be involved in LD biogenesis and regulation (Guo et al., 2008). Despite the identification of LD-associated proteins and genes implicated in LD abundance, there remains a significant gap in our understanding of the precise molecular mechanisms governing the function and regulation of LDs in cellular metabolism.

1.2 Lipid droplets in heath and disease

In the last decades, LDs have acquired the status of an authentic organelle with a multitude of functions in the cell (Fujimoto & Parton, 2011). Most organelles in the cell are enclosed by a phospholipid bilayer; however, LDs have a unique architecture. This ubiquitous dynamic cytoplasmic organelle is comprised of a highly hydrophobic core packaged with neutral lipids (mainly TAGs and sterol esters (SEs)) and encapsulated by a monolayer of phospholipids (Walther et al., 2017a; Walther & Farese, 2012). Furthermore, the hydrophobic core of LDs may also contain other lipid species such as retinol esters, waxes, and ether lipids depending on the cell type and organism (Alvarez, 2016; Lundquist, 2020; Molenaar et al., 2021). For instance, LDs in foam cells contain primarily sterol esters, yeast LDs are made up of ~50% TAGs and ~50% sterol esters, and LDs in adipocytes are mainly composed of TAGs (Bartz et al., 2007; Czabany et al., 2008; Tauchi-Sato et al., 2002; Walther & Farese, 2009). Despite their well-known function of serving as a metabolic hub for energy storage, LDs play a crucial role in fatty-acid trafficking, membrane homeostasis, protein degradation, and regulation of lipophagy (Ogasawara, 2020; Petan et al., 2018; Welte, 2015). Due to these diverse functions, malfunctioned LDs are linked to metabolic disorders such as obesity, lipodystrophy, hepatic steatosis, and cardiovascular diseases such as atherosclerosis (Krahmer et al., 2013; Onal et al., 2017). The question of whether these hallmark metabolic diseases are caused by direct LD aberrations or by other cell malfunctions that cause LD aberrations leading to such pathologies remains unanswered. This knowledge gap is mostly attributed to a lack of understanding of the molecular mechanisms governing LD biogenesis, regulation, and turnover in cells. Recently, LDs have been implicated to complex with anti-bacterial proteins in mammalian cells to provide immunity against invading bacterial species (Bosch et al., 2020; Bosch & Pol, 2022). Moreover, some viruses, such as hepatitis C virus (HCV) (Herker & Ott, 2011), SARS-COV-2 (Dias et al., 2020), and parasites (*Toxoplasma gondii*) (Nolan et al., 2017), hijack LDs for their growth and survival. In a recent study,

the partitioning of small lipophilic drug molecules (bedaquilne) into the hydrophobic core of macrophage LDs enhanced its efficacy in targeting *Mycobacterium tuberculosis* (Greenwood et al., 2019). Another study showed the accumulation of a potential hydrophobic cancer drug lasonolide A (Las A) inside the core of LDs, where it is cleaved into a cytotoxic metabolite LasF by a serine hydrolase (LDAH) (Dubey et al., 2020). In the future, LD-based action of hydrophobic drugs can be exploited to combat infectious pathogens and devise new therapeutic strategies for certain cancer types with elevated LD numbers (Dubey et al., 2020; Walther & Farese, 2019).

1.3 Biogenesis of lipid droplets

The biogenesis of LDs is driven by the metabolic state of the cell (Henne et al., 2018). In the past, different models have been proposed on how LDs are formed in the cell (Farese & Walther, 2009). The model which is widely accepted in the field posits that LDs are derived from specific ER-subdomains as shown in Figure 1 (Jackson, 2019; Olzmann & Carvalho, 2019; Pol et al., 2014; Walther et al., 2017). Experimental evidence that the ER membrane is often in close contact with LDs and the fact that most enzymes involved in neutral lipid synthesis reside in the ER membrane, strongly supports this model (Blanchette-Mackie et al., 1995; Buhman et al., 2001; Farese & Walther, 2009; Harris et al., 2011; Kassan et al., 2013; Novikoff et al., 1980; Robenek et al., 2006; Valm et al., 2017). In eukaryotes, *de novo* LD biogenesis is a well-orchestrated process that takes place in the ER membrane. The process of LD biogenesis is divided into three distinct steps: (i) neutral lipids synthesis (nucleation), (ii) LD growth, and (iii) LD budding. However, the exact underlying molecular mechanisms governing each step are still not fully understood. In recent years, technical advancements in electron and super-resolution microscopy (Salo & Ikonen, 2019), the use of a combination of biophysical approaches (*in vitro* reconstitution of artificial LDs), and molecular dynamics (MD) simulations have greatly enhanced our understanding of LD biogenesis (Thiam et al., 2013; Zoni et al., 2019).

LD biogenesis begins with the synthesis of neutral lipids between the two phospholipid leaflets of ER. When the neutral lipid concentration reaches a certain threshold within the ER, they undergo phase separation to give rise to lens-shaped oil blisters. This early step of LD biogenesis is called nucleation (Choudhary et al., 2015; Kassan et al., 2013; Khandelia et al., 2010; Kim et al., 2022; Thiam & Ikonen, 2020; Zoni, Khaddaj, Campomanes, et al., 2021). In the growth phase, the nascent LDs

(lens-shaped oil blisters) grow into larger droplets *via* Ostwald ripening, a process which allows the diffusion of neutral lipids from the small LDs due to their high internal pressure into larger LDs (Salo et al., 2019; Thiam et al., 2013; Thiam & Forêt, 2016). Following the growth phase, the LDs bud off into the cytosol taking phospholipids from the cytoplasmic ER leaflet. In yeast, the mature LDs have been found to remain attached to the ER *via* membrane tethers (Bohnert, 2020; Jacquier et al., 2011). Whether this is true for all LDs and especially for LDs in mammalian cells remains unknown. After budding into the cytosol, the LDs can still grow by merging with other LDs *via* a process called coalescence (Gong et al., 2011; Lyu et al., 2021). In addition, relocalization of TAGs synthesizing enzymes such as GPAT4 from the ER-to-LDs may promote the local synthesis of TAGs on their surface and promote LD growth (Wilfling et al., 2013, 2014).

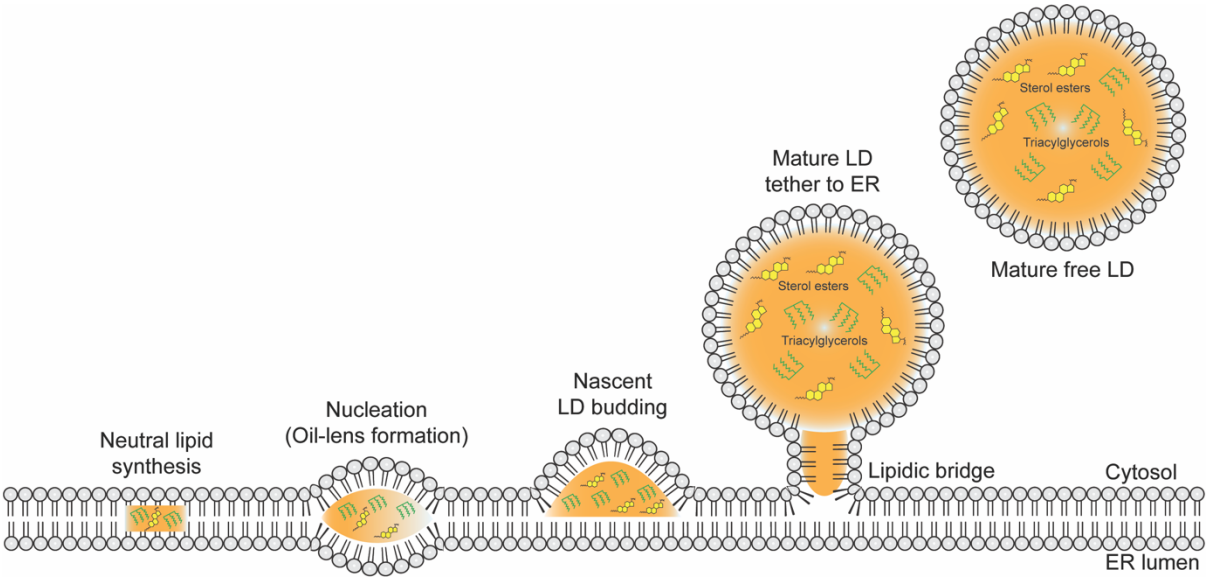

Figure 1: Model of LD biogenesis depicting individual steps from its formation in the ER to budding into the cytosol.

The LD biogenesis starts with the synthesis of neutral lipids within the ER. After reaching a critical concentration, neutral lipids undergo phase separation to generate lens-shaped oil blisters, a process termed as nucleation. The nascent LDs then grow in size by acquiring more neutral lipids and bud off into the cytosol. The channeling of neutral lipids into the growing LDs is tightly regulated by a network of proteins and a physical phenomenon called Oswald ripening.

1.4 Proteins involved in LD biogenesis

1.4.1 Neutral lipid synthesis enzymes

In mammals, neutral lipid synthesis is mediated by a network of enzymes and proteins involved in lipid metabolism. This intricate process of neutral lipid synthesis (mainly TAGs and SEs) is mediated by a cascade of enzymes residing in the ER membrane as outlined in Figure 2. These enzymes are conserved across kingdoms and localize permanently or transiently to the ER and LDs (Oelkers & Sturley, 2004). The synthesis of neutral lipids initiates with the activation of inert fatty acids (FAs). In mammals, long-chain free FAs are esterified with coenzyme A (CoA) by acyl-CoA synthetase (ASCL) to form fatty acyl-CoA. These fatty acyl-CoAs are channeled into different metabolic pathways depending on the metabolic state of the cell (Ellis et al., 2010).

In eukaryotic cells, *de novo* TAG synthesis occurs *via* either glycerol-3-phosphate (G3P) or monoacylglycerol (MAG) pathway. In the G3P pathway, glycerol-3-phosphate is catalyzed to TAGs by a set of four enzymes: glycerol-3-phosphate acyltransferase (GPAT), 1-acyl glycerol-3-phosphate acyltransferase (AGPAT), phosphatidic acid phosphohydrolase (PAP or lipin), and acyl-CoA: diacylglycerol acyltransferase (DGAT1 and DGAT2) enzymes. In the MAG pathway, monoacylglycerol is catalyzed to TAGs by monoacylglycerol acyltransferase (MGAT), DGAT1 and DGAT2 enzymes (Coleman & Lee, 2004; Kennedy, 1957; Weiss et al., 1956; Yen et al., 2008).

Not all cells store neutral lipids as TAGs. Some cells, such as macrophages, store them mainly as SEs. The synthesis of SEs is catalyzed by acyl-CoA: cholesterol acyltransferase (ACAT1 and ACAT2) enzymes (Chang et al., 2009; Khelef et al., 1998).

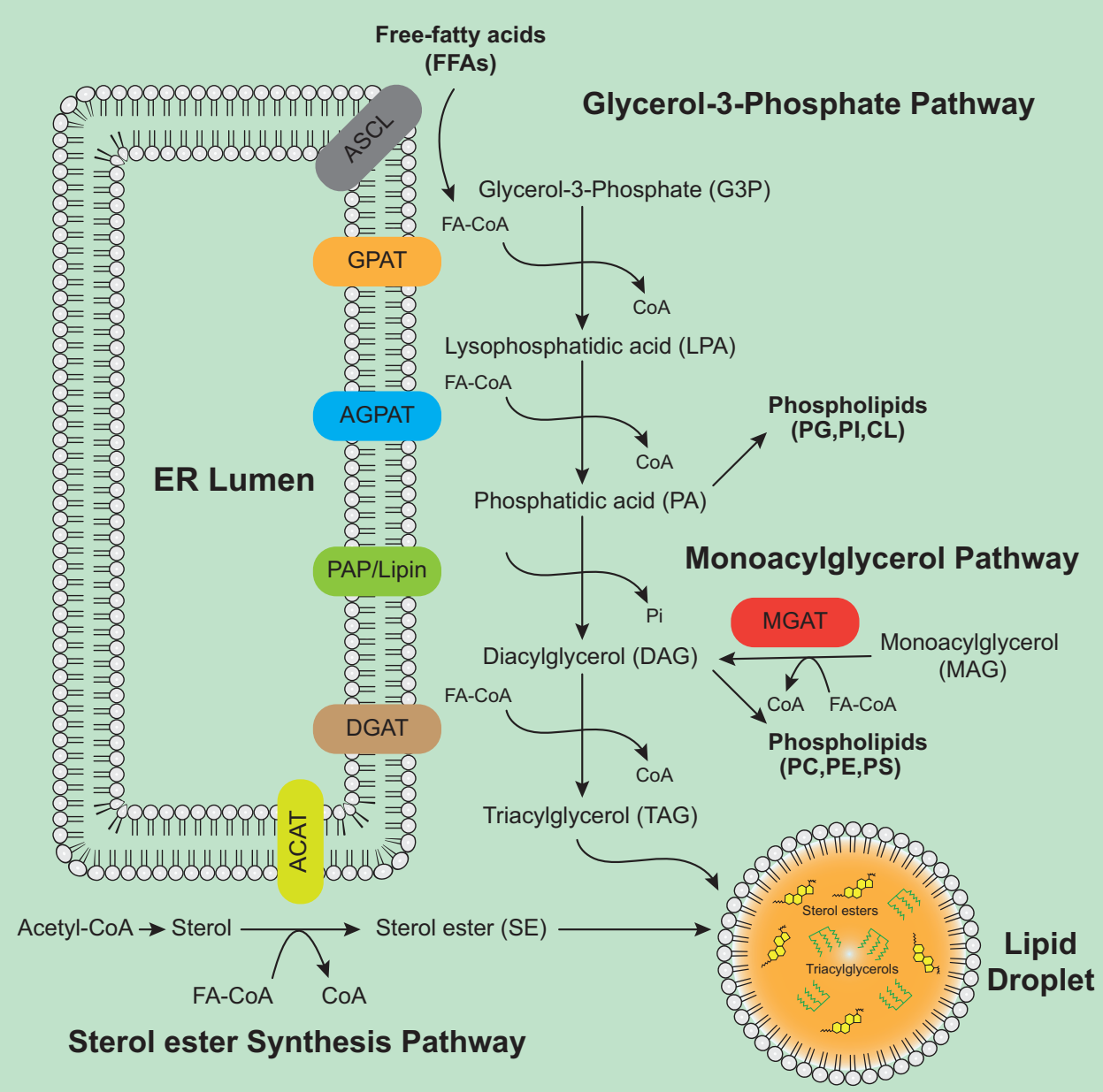

Figure 2: Schematic representation of the major pathways and proteins involved in the synthesis of TAGs and SEs.

For the synthesis of neutral lipids, the FFAs activation is carried out by ACSL before they enter into downstream metabolic pathways. In the G3P pathway, G3P is acylated to LPA by GPAT. Subsequently, LPA is acylated to PA by AGPAT. PA is then either hydrolyzed to DAG or channeled to the synthesis of phospholipids such as phosphatidylglycerol (PG), phosphatidylinositol (PI), and cardiolipin (CL). Finally, the DGAT acylate DAG to TAG by catalyzing the formation of an ester linkage between the free hydroxyl group of DAGs and a fatty acyl CoA. Depending on the metabolic need of the cell, DAG can also be channeled to the synthesis of phospholipids such as phosphatidylcholine (PC), phosphatidylethanolamine (PE), and phosphatidylserine (PS). In MAG pathway, MAG is acylated to DAG by MGAT. In sterol ester synthesis pathway, the ACAT catalyze the formation of sterol esters by

acylation of the substrates, such as sterols. The end products (TAGs and SEs) are then stored in the LD core.

1.4.2 Fat storage-inducing (FIT) transmembrane proteins

FIT proteins are evolutionarily conserved and, in humans, the FIT protein family is comprised of two members (FIT1 and FIT2). FIT proteins reside in the ER membrane, and topology mapping studies revealed that they have six transmembrane domains with N-and C-termini oriented toward the cytoplasm (Gross et al., 2010, 2011; Kadereit et al., 2008). In mammalian cells, overexpression of either FIT1 and FIT2 results in the accumulation of LDs. *In vitro*, purified FIT1 and FIT2 bind to neutral lipids such as TAGs and DAGs (diacylglycerols) although with different affinities. This observation pointed in the direction of FIT proteins being involved in LD biogenesis (Gross et al., 2011). In mammalian fibroblasts and *C. elegans*, the depletion of FIT2 resulted in LDs being trapped and wrapped with ER membranes inside the ER lumen (Choudhary et al., 2015, 2016, 2018). Recently, FIT2 was identified to function as a fatty acyl-coenzyme A diphosphatase to maintain phospholipid metabolism and ER homeostasis. *In vitro*, phosphatidic acid and lysophosphatidic acid were identified as FIT2 substrates. The enzymatic activity of FIT2 was predicted to take place on the lumenal side of the ER bilayer. The absence of FIT2 resulted in increased phosphatidic acid cellular levels. Based on these findings, it was speculated that FIT2 may be involved in maintaining phospholipid asymmetry between the ER leaflets to ensure unidirectional LD budding (Becuwe et al., 2020; Yap et al., 2020). In biophysical studies, by reconstitution of artificial LDs into giant unilamellar vesicles (GUVs) to create droplet-embedded vesicles (DEVs), it was shown that differences in surface tension between monolayer leaflets control the direction of LD budding. A reduction in cytosolic phospholipid leaflet surface tension promotes LD budding towards the cytoplasm (Chorlay & Thiam, 2018). A change in surface tension could be achieved by increased phospholipid coverage and by insertion of proteins (Chorlay et al., 2019). Thus, it could be that FIT2 acts on PA on the lumenal side of the ER and dephosphorylates it to DAG, thereby increasing surface tension on the lumenal leaflet which ultimately promotes LD budding towards the cytoplasm (Chorlay et al., 2019; M'Barek et al., 2017). A recent study in mammalian cells have revealed that the formation of nascent LDs requires the interaction of FIT2 with the ER-tubule forming

proteins (such as Rtn4 and REEP5) through its transmembrane domain, as well as with the cytoskeletal protein septin 7 *via* cytosolic loops (Chen et al., 2021).

1.4.3 Seipin

In 2001, mutations in seipin were found to cause Berardinelli-Seip congenital lipodystrophy-2 or congenital generalized lipodystrophy. This rare genetic condition is characterized by loss of adipose mass in human patients (Dollet et al., 2014; Magré et al., 2001). In recent years, the majority of the work on seipin was aimed at understanding its function in LD formation. Seipin is an evolutionarily conserved homo-oligomeric integral ER membrane protein and is comprised of two TMDs with N-and C-termini oriented toward the cytoplasm. The two TMDs are connected *via* a highly conserved long lumenal loop (Binns et al., 2010; Lundin et al., 2006).

Recently, cryo-electron microscopy (cryo-EM) structure of the lumenal domain of seipin, which consists of 11 homo-oligomeric subunits in human (Yan et al., 2018), 12 in *Drosophila* (Sui et al., 2018), and 10 in yeast (Klug et al., 2021) have been reported to form a ring-shaped complex with a cavity in the center. The lumenal domain of both human and *Drosophila* seipin consists of a hydrophobic helix, which is positioned against or inside the lumenal ER leaflet and is appended to a β-sandwich domain made up of eight β strands (Sui et al., 2018; Yan et al., 2018). The β-sandwich domain is predicted to bind anionic phospholipids such as phosphatidic acid (PA) and was found to be structurally related to known lipid-binding proteins such Niemann-Pick type C2 (NPC2) (Yan et al., 2018). The TMDs which were not part of the resolved lumenal domain structure were predicted to anchor it to the ER membrane (Sui et al., 2018; Yan et al., 2018). Using MD simulations, the polar amino acid residues such as serine located in the hydrophobic helix of seipin is suggested to be necessary for the entrapment and transfer of TAGs to the growing LDs (Prasanna et al., 2021; Zoni et al., 2021). In yeast, the identification of Ldb16, which possesses critical hydroxyl-containing residues, together with the seipin transmembrane segments compensate the loss of hydrophobic helix and is sufficient for recruitment of TAG molecules necessary for LD assembly (Arlt et al., 2022; Klug et al., 2021). Recently, by combining MD simulations with cell-based experiments, the positively charged amino acid residues (arginines) located at the end of seipin TMDs are suggested to be crucial for neutral lipids nucleation and LD budding from the ER (Kim et al., 2022).

In yeast, the homolog of human seipin Fld1/Sei1 is necessary for maintaining a normal LD phenotype (Fei et al., 2008; Szymanski et al., 2007). In addition, the ER membrane protein Ldb16 was identified as a binding partner of Fld1 (Grippa et al., 2015). The yeast seipin Fld1 is required for maintaining the stability of Ldb16, and depletion of Ldb16 results in yeast cells with aberrant LDs, similar to *fld1*Δ mutants. Together, it was proposed that Fld1and Ldb16 form a stable complex that stabilizes the ER-LD contact sites and establishes a diffusion barrier for neutral lipids to ensure normal LD morphology (Grippa et al., 2015; Wang et al., 2014). In human and *Drosophila* S2 cells, endogenously-tagged seipin forms mobile foci in the ER (Wang et al., 2016). These foci immobilize upon localization to ER-LD contact sites to facilitate the growth of nascent LDs by diffusion of neutral lipids and proteins to the growing LDs (Salo et al., 2016; Wang et al., 2016). In seipin knockout cells, the nascent LDs are dispersed throughout the ER and often fail to grow into mature LDs (Salo et al., 2016; Wang et al., 2016). Eventually, some of these tiny LDs turn into “supersized” abnormal LDs (Salo et al., 2016; Wang et al., 2016), a phenotype similar to Fld1/Ldb16 yeast deletion mutants (Grippa et al., 2015; Wang et al., 2014). A recent observation made in yeast showed that nuclear envelope morphology protein (Nem1) in complex with Fld1 recruit additional known LD biogenesis factors (such as Yft2 and Pex30) to initiate LD biogenesis at discrete ER subdomains (Choudhary et al., 2020; Choudhary & Schneiter, 2020).

Two model peptides, LiveDrop (hydrophobic hairpin-motif of GPAT4) (Wang et al., 2016) and HPos (a chimera generated by fusion of the associated with lipid droplet protein 1 (ALDI) hydrophobic domain with last 20 amino acid residues of caveloin-1) (Kassan et al., 2013) accumulate into puncta-like structures within ER subdomains under starvation. Upon lipid loading, these puncta grow into mature LDs, which suggests that these puncta are early nascent LDs (pre-LDs). Both of these model peptides were able to mark the early nascent LD sites before their detection by lipophilic LD-staining dyes such as BODIPY (Kassan et al., 2013; Wang et al., 2016). In mammalian cells, the mobility of seipin foci was found to be ceased prior to accumulation of LiveDrop and ASCL3, which indicates that seipin localizes and stabilizes the early LD-forming sites prior to other known players (Salo et al., 2019, 2020).

In yeast, the lipid droplet organization (LDO) family consisting of Ldo16 and its splicing isoform Ldo45 was found to play a role in LD biogenesis by interacting with

yeast seipin complex (Fld1/Lbd16) (Eisenberg-Bord et al., 2018; Teixeira et al., 2018). Recently, lipid droplet assembly factor 1 (LDAF1/Promethin) with remote structural homology to yeast Ldo45 was copurified with seipin from mammalian cells (Chung et al., 2019). This oligomeric (LDAF1-seipin) complex within the ER marks the sites of nascent LDs formation by promoting neutral lipids nucleation. As the nascent LDs grow in size, LDAF1 dissociates from the seipin and localizes to the surface of the growing LDs as depicted in Figure 3 (Chung et al., 2019). In summary, these studies proposed that seipin in complex with other accessory proteins such as LDAF1 regulates LD biogenesis within the ER (Castro et al., 2019; Chung et al., 2019).

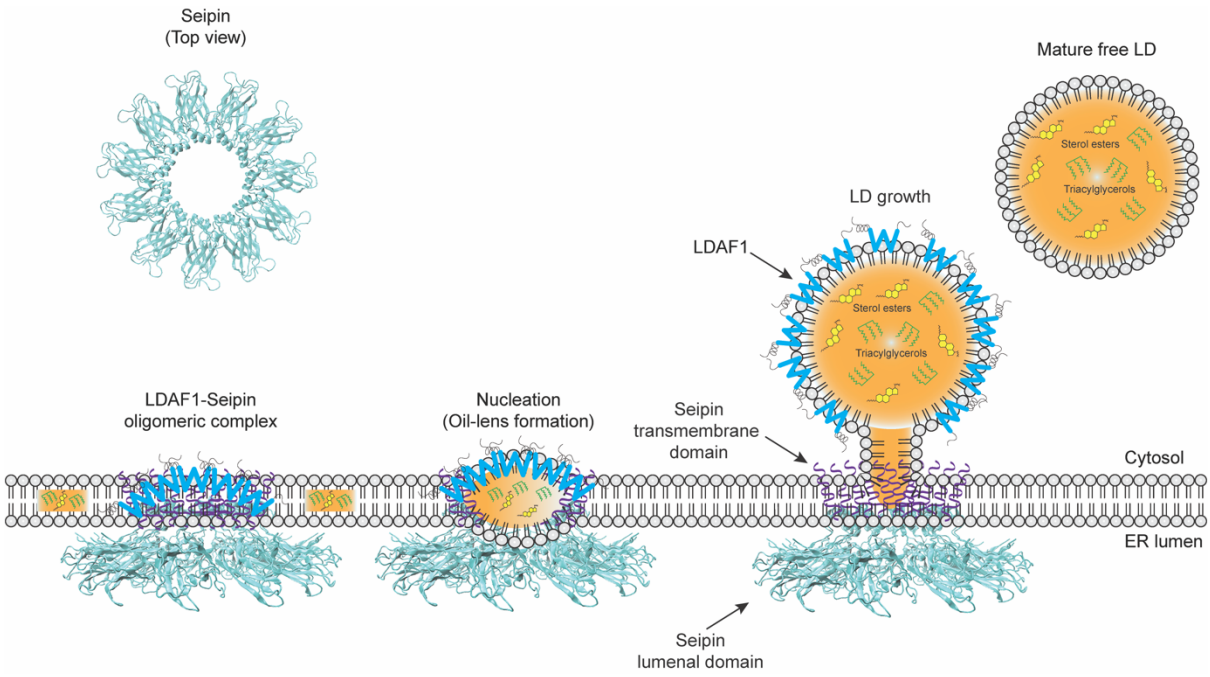

Figure 3: The LDAF1-seipin complex governs the LD formation sites.
LDAF1 and seipin scans the ER and together form foci at the early LD-forming sites. The LDAF1-seipin complex facilitates oil-lens formation (nucleation) by channeling neutral lipids *via* their hydrophobic helices at the ER-LD contact sites. As the LDs grow by accumulating more neutral lipids, the LDAF1 dissociates from the seipin and translocates to the phospholipid monolayer of the growing LD (figure adapted from Chung et al., 2019).

1.4.4 Pex30/MCTP

The ER is not only the site for *de novo* LD biogenesis but also serves as a platform for the biogenesis of preperoxisomal vesicles (PPVs). Later, these PPV develop into mature functional peroxisomes (Farré et al., 2019; Joshi & Cohen, 2019). ER-shaping

proteins such a reticulons and reticulon-like proteins are known to stabilize tubular ER shape and membrane curvature (Shibata et al., 2009; Voeltz et al., 2006). A unique feature of reticulons is the presence of a highly conserved reticulon homology domain (RHD). In yeast, a structurally similar protein named Pex30 with an N-terminal RHD (Vizeacoumar et al., 2006) and a C-terminal Dysferlin domain have been identified (Yan et al., 2008). The Dysferlin domain of Pex30 has been suggested to have lipid binding capacity (Therrien et al., 2009; Wang et al., 2018). Pex30 localizes in punctate discrete ER subdomains and PPVs were found to originate from these ER subdomains marked by Pex30 (Joshi et al., 2016). The overexpression and deletion of Pex30 resulted in aberrant PPVs biogenesis in yeast cells (Joshi et al., 2016). In addition, Pex30-marked ER subdomains also act as nascent LD biogenesis sites. A lack of Pex30 resulted in defective LD biogenesis in yeast cells (Joshi et al., 2018; Wang et al., 2018). This phenotype became more pronounced in cells lacking both Pex30 and seipin leading to accumulation of neutral lipids and changes in ER morphology. Additionally, in Pex30/seipin double deletion mutants, PPV biogenesis was also found to be negatively affected. Therefore, these observations suggest that a cooperation between Pex30 and seipin is necessary for organization of ER subdomains to regulate the biogenesis of both LDs and peroxisomes (Joshi et al., 2018; Wang et al., 2018).

In mammals, the multiple C2 domain containing transmembrane protein (MCTP) family is comprised of two members: MCTP1 and MCTP2 (Joshi & Cohen, 2019; Shin et al., 2005). MCTP2 was suggested as a functional homolog of Pex30 and knockdown of MCTP2 resulted in aberrant LD biogenesis in mammalian cells. Recently, functional characterization of RHD and C2 domains of MCTPs revealed that the RHD domain promotes LD biogenesis by inducing membrane curvature, which facilitates TAG accumulation. On the other hand, C2 domains regulate LD size by mediating interaction with phospholipids on the LD surface (Joshi et al., 2021). Santinho et al. showed that membrane curvature promotes LD formation *in vitro* by reducing the critical TAGs concentration and energy barrier required for LD nucleation event. In cells, seipin acts as a gatekeeper in ER tubules to control the condensation process of TAGs to prevent uncontrolled LD nucleation events (Santinho et al., 2020).

1.4.5 Sorting-Nexin family proteins

The Sorting-nexins (SNXs) are a large evolutionarily conserved family of proteins. One of the sub-families of this group, called SNX-RGS proteins, are characterized by their regulator of G-protein signaling domain (RGS) (Amatya et al., 2021). In mammals, the family is comprised of four members (Snx13, Snx14, Snx19, and Snx25), whereas yeast and fly each have one member, named mitochondrial distribution and morphology 1 (Mdm1) and Snazarus (Snz), respectively (Henne et al., 2015; Paul et al., 2022). All the SNX-RGS protein family members have the same domain architecture consisting of an N-terminal integral membrane domain (IMD), followed by phox homology associated (PXA), a regulator of G-protein signaling (RGS), phox homology (PX), and C-terminal nexin (CN) domains (Bohnert, 2020).

In yeast, Mdm1 was identified as an ER-vacuole tether protein that localizes at the rim of the nucleus-vacuole junction (NVJ). Mdm1 resides in the nuclear ER (nER) and interacts with the phosphatidylinositol 3-phosphate on the vacuolar membrane *via* its phox domain (Henne et al., 2015). Under nutrient-limiting conditions, NVJ acts as a site for LD biogenesis (Hariri et al., 2018). Mdm1 associates with LDs induced at the edge of the NVJ *via* its IMD and PXA domain. Further, the ability of the PXA domain to bind free FAs and its interaction with the fatty acyl-coenzyme A ligase (FAA) point toward its role in the sequestration of free FAs into neutral lipids to promote LD biogenesis at the NVJ. Interestingly, the deletion of Mdm1 resulted in the elevation of free FAs levels that perturbed ER morphology and delayed LD biogenesis (Hariri et al., 2019). In mammalian cells, Snx14 (human homolog of Mdm1) tethers the ER-to-LDs *via* an amphipathic helix present in the CN domain. Upon oleate feeding, it localizes to the ER-LD contact sites and promotes LDs maturation. In Snx14 KO cells, the ER-LD contacts were drastically reduced leading to the formation of aberrant LDs. This phenotype was rescued upon overexpression of Snx14, thus supporting a potential role in LD biogenesis (Datta et al., 2019). In *Drosophila*, an ortholog of Snx14/Mdm1 named Snazarus (Snz) tethers ER to peripheral LDs (pLDs) *via* its CN domain and plasma membrane through its PX domain to create a tri-organelle contact. Loss of *Snz* perturbed the population of pLDs and its overexpression promoted the pLDs expansion by regulating the neutral lipids storage (Ugrankar et al., 2019). Despite the importance of SNX-RGS family members in the spatial regulation of lipid metabolism, their exact role in LD biogenesis is still not fully understood.

1.5 LD proteome

The repertoire of proteins that associates with the phospholipid monolayer of LDs through amphipathic helices, hydrophobic hairpin-motifs, or lipid anchors plays a crucial rule in defining the functions of this unique organelle. The LD proteome is highly dynamic and varies depending on the metabolic state, cell type, tissue, and the organism (Bersuker & Olzmann, 2017; Zhang & Liu, 2019). The phospholipid composition of the monolayer has also been suggested to be crucial in defining the LD proteome. For instance, studies reveal that in mammalian cells, the LD monolayer is primarily composed of PC, followed by PE, and PI (Bartz et al., 2007; Tauchi-Sato et al., 2002). On the contrary, in *Drosophila* S2 cells, the LD monolayer was enriched in PE and the PC content was found to be lower (Guan et al., 2013; Jones et al., 1992; Krahmer et al., 2011). In addition to the type of phospholipid, the neutral lipid core composition of the LDs also influences the recruitment of proteins to the phospholipid monolayer of LDs (Chorlay & Thiam, 2020; Rogers et al., 2021; Swanson, 2022).

In the last two decades, a number of proteomic studies were carried out to catalogue the LD proteome across different species and cell types (Beller et al., 2006; Brasaemle et al., 2004; Yang et al., 2012; Zhang & Liu, 2019). Biochemical and microscopy studies have revealed that LDs are tightly associated with other organelles in the cell. Therefore, purifying LDs to homogeneity is always challenging and raises the question whether these studies represent the *bona fide* LD proteome. To overcome this limitation of potential cross-organelle contamination, a methodology based on high-resolution mass spectrometry and protein correlation profiling (PCP) strategy curated a list of 111 proteins that were specifically enriched in the isolated LD fractions from *Drosophila* S2 cells and 35 in yeast cells with high confidence (Krahmer et al., 2013). The identified proteins were further validated by verifying their localization to LDs by microscopy (Currie et al., 2014; Krahmer et al., 2013). Recent work from Bersuker et al. employed the APEX2 proximity labeling approach to revisit the LD proteome and identified new proteins with high confidence along with the *bona fide* LD marker proteins (Bersuker et al., 2018; Nguyen et al., 2020).

Apart from the well-known LD resident proteins such as the members of the perilipin (PLIN1-5) family (Brasaemle et al., 2004; Kimmel & Sztalryd, 2016), a large proportion of the proteins identified in these studies are the enzymes involved in neutral lipid synthesis such as ACSL3, GPAT4, DGAT1, and DGAT2 (Athenstaedt & Daum, 2006; Buhman et al., 2001; Gimeno & Cao, 2008), lipolysis such as adipose

triglyceride lipase (ATGL) (Grabner et al., 2021), and regulators of lipolysis such as comparative gene identification (CG1-58) (Radner et al., 2010; Yang & Mottillo, 2020), G0/G1 switch gene 2 (G0S2) (Cerk et al., 2014; Yang et al., 2010). Although there is variation in the results among different studies, surprisingly, some protein groups were consistently identified (Bersuker et al., 2018; Krahmer & Mann, 2019; Yang et al., 2012). These groups include: (i) Proteins involved in membrane trafficking and signaling such as SNAREs, Arfs, and GTPases. For instance, Rab18 was shown to mediate tethering of LDs to the ER (Dejgaard & Presley, 2019). (ii) Proteins involved in ER-associated protein degradation (ERAD) such as ancient ubiquitous protein 1 (AUP1) (Klemm et al., 2011; Smith et al., 2021; Spandl et al., 2011) and ubiquitin regulatory X domain-containing protein 8 (UBXD8) (Suzuki et al., 2012; Ye et al., 2017; Zehmer et al., 2009). (iii) Proteins involved in phospholipid synthesis such as phosphocholine cytidyltransferase (CCT), the rate-limiting enzyme in PC synthesis. CCT binds to growing LD surface under PC deficiency and meets the requirement by catalyzing PC synthesis on the LD surface (Krahmer et al., 2011). The lipid transfer proteins (LTPs) such as oxysterol binding protein (ORP5) acts at ER-LD contact sites to mediate transfer of phosphatidylinositol-4-phopshate from LDs to the ER and phosphatidylserine (PS) from LDs to the ER (Du et al., 2020). (iv) Cell death-inducing DNA fragmentation factor 45-like effector (CIDE) protein family members such as fat-specific protein 27 (FSP27) which mediates LD fusion. Surprisingly, some transcription factors such as MLX-family members (Mejhert et al., 2020) and histones (Li et al., 2012, 2014) were also identified as LD proteins.

Currently, a big question in the LD field is how this diverse set of proteins are specifically targeted to the LDs. This question is intriguing because LD proteins do not possess any characterized LD targeting or sorting signal. This is in contrast to all other organelle-resident or secretory proteins.

1.5.1 Protein targeting to LDs

The cytoplasm of eukaryotic cells is packed with organelles (such as the ER, mitochondria, or peroxisomes), which are surrounded by a phospholipid bilayer separating two aqueous environments. Unique proteins are found in each of the cell's subcellular compartments, and a multitude of studies over the years unraveled different protein targeting pathways that govern the targeting of proteins to different

organelles, such as signal recognition particle (SRP) pathway (Hegde & Keenan, 2022), guided-entry of tail-anchored proteins (GET) pathway (Chio et al., 2017), SRP-independent (SND) pathway (Aviram et al., 2016), and TIM/TOM complexes (Pfanner et al., 2019). These pathways govern the targeting and insertion of hydrophobic transmembrane membrane proteins with bitopic and polytopic topology to phospholipid-bilayer-encapsulated organelles and are conserved across species. A common feature of these distinct organelle targeting pathways is the recognition of cargo-intrinsic signal sequences by cytosolic recognition factors that are often the hydrophobic membrane-spanning domains of the cargo. The docking of the cytosolic recognition factors with specific receptor proteins at the destination organelle together with insertases or protein-translocation channels facilitate the insertion of the cargo into the destination membrane (Hegde & Keenan, 2022).

However, from a structural point of view, LDs are unique and are encircled by a phospholipid monolayer that acts as a surfactant and delineates the highly hydrophobic neutral lipid core from the aqueous cytosol (Olzmann & Carvalho, 2019; Thiam et al., 2013; Walther et al., 2017). Although we have in-depth knowledge on the molecular mechanisms that govern the targeting and insertion of integral membrane proteins (bitopic and polytopic) into the bilayer environment, there is no dedicated protein targeting machinery and specific lipids that assist the targeting and insertion of proteins to the LD surface have been discovered yet. The LD hydrophobic core is devoid of any proteins and only monotopic proteins with their hydrophilic domains oriented toward the cytosol associate with the phospholipid monolayer of LDs (Bersuker & Olzmann, 2017; Dhiman et al., 2020; Khaddaj et al., 2021).

According to the prevailing model on LD biogenesis, LDs are derived from the ER and, to some extent, have a similar phospholipid composition to the ER (Bartz et al., 2007; Tauchi-Sato et al., 2002). However, when it comes to the targeting and partitioning of proteins associated with the LDs, the principles that govern the targeting of bilayer-spanning proteins does not apply to monotopic proteins. One of the reasons for that is the unique biophysical characteristics of LDs. In addition, the metabolic state of the cell governs the LD size and surface properties by regulating the cycle of lipogenesis and lipolysis. During the state of expansion, the LD surface area increases, and more surface-triacylglycerol (SURF-TAG) molecules intercalate between the monolayer phospholipids to reduce surface tension and, in turn, modulate LD surface features which facilitates binding of some proteins to the LD surface (Kim et al., 2021).

When LDs undergo lipolysis, the phospholipid monolayer surface area reduces, and non-specifically or weakly bound proteins get displaced due to protein crowding (Kory et al., 2015).

Some of the monotopic proteins play crucial roles in local synthesis of neutral lipids (Wilfling et al., 2013, 2014) and lipolysis (Olzmann et al., 2013) to control LDs growth and turnover. Thus, in order to get insight into the molecular mechanisms underpinning LDs biogenesis, first we need to understand how monotopic proteins are inserted and targeted to the LDs. To achieve that, it is important to discern the topology of monotopic proteins at atomistic scale to define the key sequence determinants and the length of the membrane-embedded motifs in both the bilayer and monolayer membrane environments.

1.5.2 Classification of LD-targeted proteins

Proteins targeting the LDs are divided into two general classes: class I LD proteins, and class II LD proteins:

Class II LD proteins target the LD surface *via* the CYTOLD (cytosol-to-LD) pathway as illustrated in Figure 4 (Olarte et al., 2022). After translation in the cytosol, they can directly associate with the LD phospholipid monolayer. A well-known example of class II proteins is the PLIN family. The PLIN family includes five (PLIN1-5) members, and a common feature among them is the presence of an 11-mer helical repeat region of varying length (Itabe et al., 2017; Kimmel & Sztalryd, 2016). These highly conserved N-terminal 11-mer repeat regions mediate the binding of PLIN proteins to LDs by folding into an amphipathic helix on the LD surface (Ajjaji et al., 2019; Čopič et al., 2018; Giménez-Andrés et al., 2021; Rowe et al., 2016). In case of PLIN4, the 11-mer repeat region forms a giant amphipathic helix and, *in vitro*, directly interacts with neutral lipids forming a coat on the LD surface. This direct interaction with the neutral lipids stabilizes the LDs under conditions when the monolayer phospholipids are limiting (Čopič et al., 2018). In addition to 11-mer amphipathic repeat regions, PLIN1-3 have an additional C-terminal four-helix bundle which stabilizes and regulates the hierarchical binding of PLINs to the surface of LDs (Ajjaji et al., 2019).

The presence of amphipathic helices is a common feature shared by proteins to target different subcellular compartments. How class II proteins explicitly target the

LD phospholipid monolayer, as opposed to other bilayer-bound organelles, is an active area of research (Olarte et al., 2022; Prevost et al., 2018; Roberts & Olzmann, 2020). Recently, MD simulations and biophysical studies have revealed the presence of large and persistent phospholipid packing defects on the LD surface (Bacle et al., 2017; Chorlay & Thiam, 2020). The packing defects expose neutral lipids and phospholipid acyl chains to the cytosol. The amphipathic helices with large hydrophobic aromatic amino acids (e.g., tryptophan, phenylalanine) sense these packing defects and mediate selective binding to the LD surface depending on their affinity for the exposed neutral lipids (Chorlay & Thiam, 2020; Prevost et al., 2018). In MD simulations, the interaction of tryptophan with the glycerol moiety of exposed SURF-TAG molecules was shown to be crucial for the initial association with LDs (Kim et al., 2021). The binding of CGI-58 to the LD surface also requires tryptophan as revealed by its solution-state nuclear magnetic resonance (NMR) structure (Boeszoermenyi et al., 2015). However, the amphipathic helix of PLIN4 lacks bulky hydrophobic residues, and its stable association with the LD surface depends on the nature and distribution of polar amino acids (Giménez-Andrés et al., 2021).

The association of a few class II proteins with the LDs occurs through fatty acid modifications such as palmitoylation (e.g., SNAP23 and ELMOD2) (Boström et al., 2007; Suzuki et al., 2015), myristoylation (e.g., FSP1 and ANKRD22) (Doll et al., 2019; Utsumi et al., 2021), and prenylation (e.g., ALDH3B2) (Kitamura et al., 2015). These fatty acid modifications act as a hydrophobic anchor that facilitates the binding of these proteins to the LD phospholipid monolayer. Finally, some proteins indirectly associate with the LDs *via* their interaction with either class I or class II proteins. For instance, the UBX domain of UBXD8 recruits VCP/p97 to the LDs (Olzmann et al., 2013; Suzuki et al., 2012), and UBE2G2 recruitment to the LDs occurs *via* its interaction with the AUP1 G2-binding region (Klemm et al., 2011; Smith et al., 2021; Spandl et al., 2011).

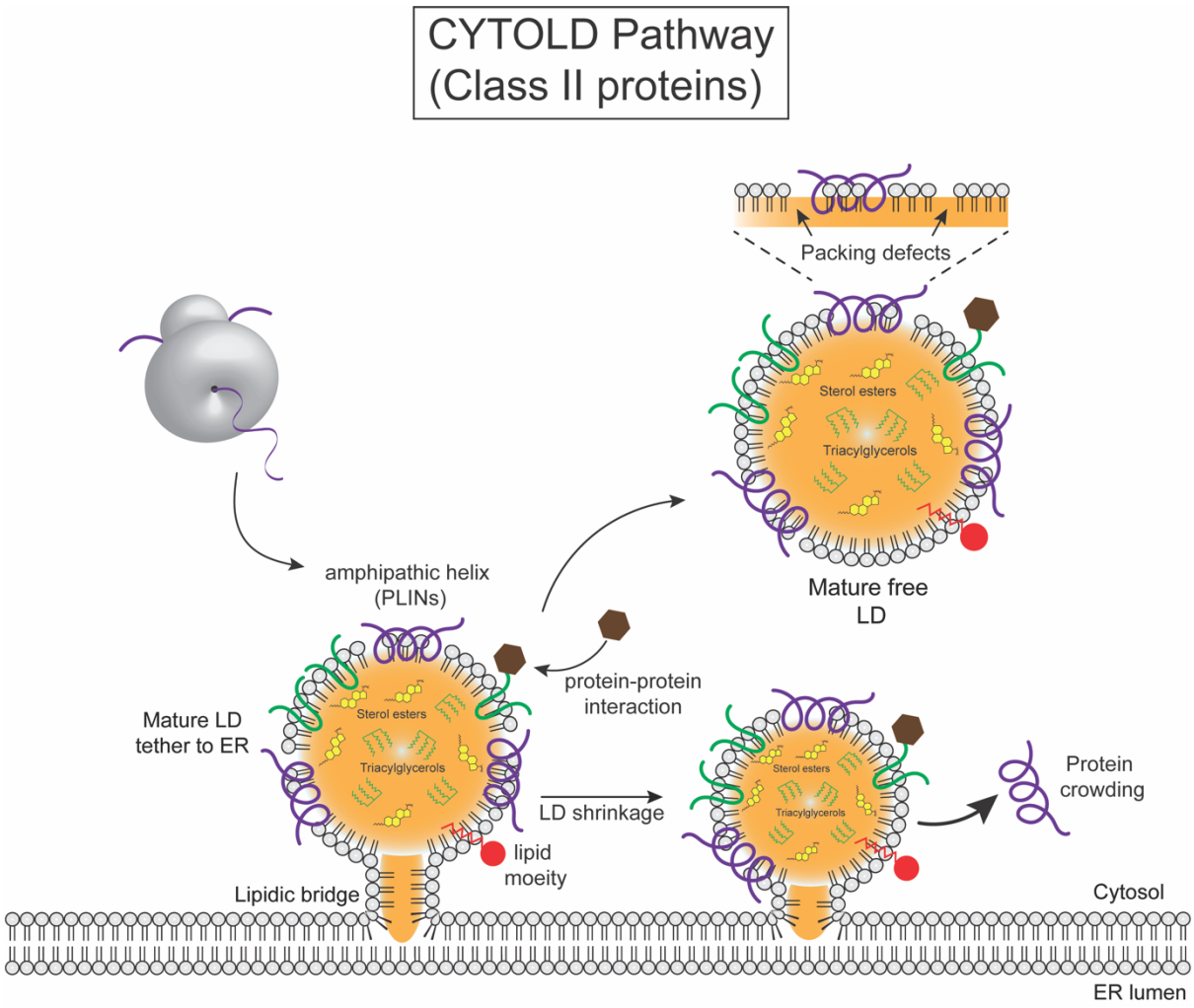

Figure 4: CYTOLD pathway for class II proteins targeting to LDs.
Class II proteins are soluble proteins that target the LDs *via* amphipathic helices. The bulky hydrophobic amino acids in the amphipathic helices sense the packing defects on the phospholipid monolayer. This interaction mediates the folding and stable association with the LD surface. Depending on the metabolic state of the cell, the LDs undergo lipolysis to mobilize neutral lipids. This reduces the LD surface area and leads to an increase in protein density. The increase in protein density displaces the weakly bound proteins from the LD surface due to protein crowding. The other class II proteins associate indirectly with the LDs *via* protein-protein interactions or lipid moieties (figure adapted from Olarte et al., 2022).

Class I LD proteins target the LD surface *via* the ERTOLD (ER-to-LD) pathway (Olarte et al., 2022; Song et al., 2022). After translation in the cytoplasm, the proteins that use this pathway are either co-or post-translationally inserted into the ER bilayer. The co-translation insertion of class I proteins such as AUP1, HSD17B11, METTL7A/AAM-B, METTL7B, and HIG2 into the ER bilayer is shown to be mediated by ER membrane complex (EMC) along with Sec61 *via* the SRP pathway (Leznicki et al., 2022). Co-translationally inserted proteins first expose their N-terminus to the ER

lumen before reconfiguring to take on a hairpin topology for trafficking to LDs (Leznicki et al., 2022). On the other hand, class I proteins such as UBXD8 (Schrul & Kopito, 2016) and HSD17B7 (Leznicki et al., 2022) are post-translationally inserted into the ER, while for UBXD8 it was shown to be mediated by the PEX3-PEX19 protein targeting machinery. PEX3 and PEX19 are peroxisomes biogenesis factors that were originally identified to mediate the post-translational insertion of peroxisomal membrane proteins directly to the peroxisomes (Jansen & Klei, 2019). In cells, soluble PEX19 binds to the hydrophobic hairpin motif of the UBXD8 and delivers it to specific ER subdomains containing the integral ER membrane protein PEX3. In addition, PEX19 farnesylation was shown to be a critical factor that controls the targeting of UBXD8 to the ER and LDs (Schrul & Kopito, 2016).

After insertion into the ER, class I proteins can partition to the LD surface. The underlying molecular mechanisms governing the partitioning of class I proteins from the ER-to-LDs remain elusive. A few examples of experimentally verified class I proteins that target LDs from the ER include: AAM-B (Zehmer et al., 2008, 2009), AUP1 (Klemm et al., 2011; Stevanovic & Thiele, 2013), ALDI (Turró et al., 2006), DHRS3 (Pataki et al., 2018), LDAH (Kory et al., 2017), NSDHL (Caldas, 2003; Ohashi et al., 2003), RDH10 (Jiang & Napoli, 2013), UBXD8 (Schrul & Kopito, 2016), GPAT4 and ALG14 (Olarte et al., 2020). The proteins targeting the LD surface *via* the ERTOLD pathway are characterized by containing a hydrophobic domain that adopts a hairpin configuration in the ER bilayer and LD monolayer membranes. Class I LD proteins were initially categorized as hairpin proteins, but later it became apparent that this is not an ultimate definition. For example, DHRS3, which lacks a hairpin structure, but still partition from the ER-to-LDs (Pataki et al., 2018). Consequently, the terminology in the LD field has recently changed, focusing on the partitioning route rather than relying on assumed structural characteristics.

Although there are no crystal structures available for class I proteins, topology models based on biochemical approaches such as protease protection assays provided evidence that class I proteins adopt monotopic topology with N- and C-termini oriented toward the cytosol, both within the ER bilayer and the LD monolayer (Leznicki et al., 2022; Schrul & Kopito, 2016). The other characteristic feature of many class I proteins is the presence of the amino acid proline in the center of hydrophobic domain. Proline alone or in combination with other amino-acids introduces a kink in the

secondary structure, which further suggests that these proteins adopt a monotopic hairpin topology (Abell et al., 1997; Huang, 1996). Based on the monotopic hairpin topology and the positioning of the class I LD proteins within the cytoplasmic leaflet of the ER, it was proposed that class I LD proteins diffuse passively in lateral fashion from the ER-to-LDs *via* lipidic bridges physically connecting them or actively recruited through interactions with gatekeeper proteins such as seipin, as illustrated in Figure 5 (Dhiman et al., 2020; Song et al., 2022).

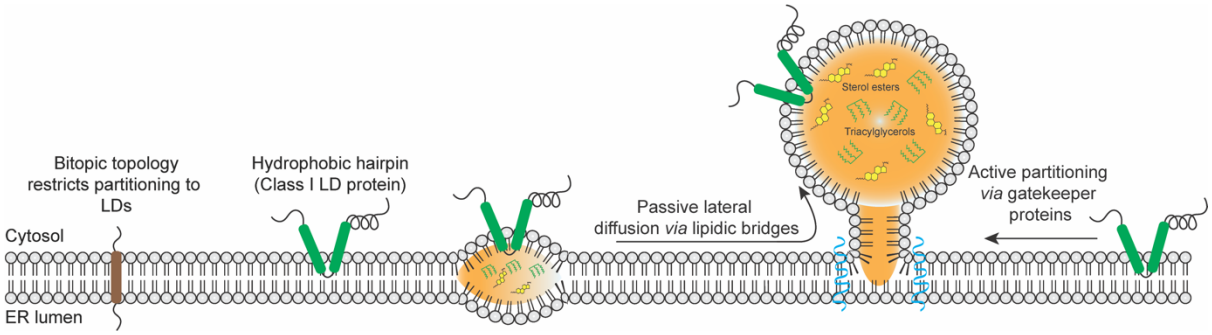

Figure 5: Regulation of class I LD proteins ER-to-LD partitioning.
Class I LD proteins with hairpin topology partition to LDs from the ER *via* passive lateral diffusion or get actively recruited *via* interactions with gatekeeper proteins. The bitopic proteins with transmembrane domains restrict their partitioning to LDs from the ER (figure adapted from Dhiman et al., 2020).

Furthermore, it was also suggested that sequestering of class I LD proteins such as UBXD8 to ER-tether proteins restrict the population of UBXD8 that is free to partition from the ER-to-LDs (Dhiman et al., 2020; Olzmann et al., 2013). Currently, there is a lack of experimental evidence available on the underlying molecular mechanisms that govern the partitioning of class I LD proteins from the ER-to-LDs and whether they adopt similar conformations in both the ER bilayer and LD monolayer membrane environment.

1.6 Monolayer-integrated membrane proteins

Biological membranes are highly dynamic structures made up of varying amounts of lipids, carbohydrates, and proteins. This ~50Å protective barrier harbors a diverse set of membrane proteins (Nicolson & Nicolson, 2014; Singer et al., 1972). Membrane proteins are an appealing target for the development of new therapeutics because they make up nearly a third of our genome (~30%) and are the root cause of many

human disorders (Elofsson & von Heijne, 2007). Additionally, membrane proteins are also involved in several critical physiological activities such as signaling, vesicular trafficking, metabolism, molecular transport, and immunological response (Arinaminpathy et al., 2009; Nugent & Jones, 2012; Wallin et al., 1998).

Membrane proteins are classified into two major groups (integral and peripheral) based on their topology. Topology is defined as the relative orientation or the number of times protein segments (α-helices or β-sheets) span the phospholipid membrane. Integral membrane proteins are characterized by their hydrophobic TMDs and soluble domains that are exposed to the aqueous environment on both sides of the membrane. They associate with the phospholipid bilayer in an irreversible fashion through strong hydrophobic interactions with the fatty acyl chains of phospholipids. A well-known example is the G protein-coupled receptors (GPCRs) (Ott & Lingappa, 2002; von Heijne, 2006).

On the other hand, peripheral proteins associate with the phospholipid membranes in a reversible fashion *via* interactions with other proteins or phospholipid headgroups. For example, the peripheral protein p97/VCP binds to the stably membrane-integrated UBX domain containing proteins such as UBXD8 *via* hydrophobic interactions (Olzmann et al., 2013; Schuberth & Buchberger, 2008). Integral membrane proteins on the basis of their relative orientation to the phospholipid bilayer are further classified into polytopic, bitopic, and monotopic as shown in Figure 6. Polytopic membrane proteins span the bilayer multiple times and are usually connected by hydrophilic loops. Bitopic proteins span the membrane once with hydrophilic soluble domains on both sides of the transmembrane segment. These proteins can have different orientations in the phospholipid bilayer membrane depending on the location of their termini relative to the membrane plane. Type I bitopic proteins have their N-terminus oriented toward the lumenal side and C-terminus on the cytoplasmic side, and are identified by the presence of a cleavable N-terminus sequence. In contrast, type II bitopic proteins exhibit an opposite orientation with their N-terminus oriented towards the cytoplasmic side and C-terminus on the lumenal side. Unlike the cleavable N-terminus sequence found in type I proteins, the type II proteins utilize a signal-anchor sequence to facilitate their membrane insertion. Both type I and type II bitopic proteins employ the SRP pathway for their co-translational insertion into the ER membrane (Hegde & Keenan, 2022). On the other hand, tail-anchored proteins are characterized by having an N-terminus cytosolic

region followed by a transmembrane domain near or at the C-terminus, which is embedded in the phospholipid bilayer membrane. These proteins are post-translationally inserted into the membrane and their targeting is facilitated by specific chaperone proteins that recognize the hydrophobic transmembrane domain at the C-terminus, directing the protein to its designated membrane location (Borgese & Fasana, 2011; Chio et al., 2017)

To date, over 1600 crystal structures of TMD-containing proteins have been submitted in the PDB (https://blanco.biomol.uci.edu/mpstruc/). As TMD-containing proteins can be reconstituted into artificial membrane-mimetics particularly phospholipid bilayer membranes, we can anticipate a continual increase in the number of experimentally determined membrane protein structures in the future. Furthermore, advancements in techniques like nuclear magnetic resonance (NMR) and cryo-electron microscopy (cryo-EM) will continue to play a pivotal role in unraveling the complex structures of membrane proteins.

Unlike the polytopic and bitopic proteins, which have soluble domains on either side of the membrane, monotopic proteins enter and exit the bilayer from the same side with N- and C-termini exposed to the cytosol (Allen et al., 2019; Blobel et al., 1980), and are found to be resistant to chaotropic treatments (Pataki et al., 2018). On the basis of structural information, monotopic proteins associate with biological membranes through amphipathic helices, hydrophobic loops, lipid anchors, or hydrophobic hairpins (Allen et al., 2019; Entova et al., 2018; Ray et al., 2018). Monotopic proteins are assumed to be easy to express, solubilize, and purify due to the nature of their membrane association (Eriksson et al., 2009). In comparison to TMD-containing proteins, however, only a few monotopic protein structures are available. The dearth of structural information on monotopic proteins could be attributed to the understudy of this class of proteins by researchers worldwide. Furthermore, as monotopic proteins can reside in both phospholipid bilayer and LD monolayer membrane environments, it may be difficult to express them in high concentrations for structural determination (Allen et al., 2019; Eriksson et al., 2009). Another important question is how such proteins stably integrate into phospholipid bilayer and LD monolayer membranes. The application of coarse-grained MD simulations to 11 monotopic proteins that reside in a phospholipid bilayer membrane environment and have high-resolution 3-D X-ray structures available in the protein data bank (PDB), separated them into two groups based on their membrane

association (Balali-Mood et al., 2009). One group was comprised of proteins that adopted shallow conformation in the bilayer mediated *via* basic residues interaction with the negatively charged phosphate headgroups. The other group was found to be deeply inserted into the hydrophobic plane of the bilayer resulting in local perturbations in bilayer properties such as membrane thickness (Balali-Mood et al., 2009; Fowler et al., 2007). In the future, MD simulations and experimental studies must be combined in order to better comprehend the interaction of monotopic proteins with bilayer and LD monolayer membrane environments.

Topology of proteins in phospholipid bilayer vs monolayer membrane environment

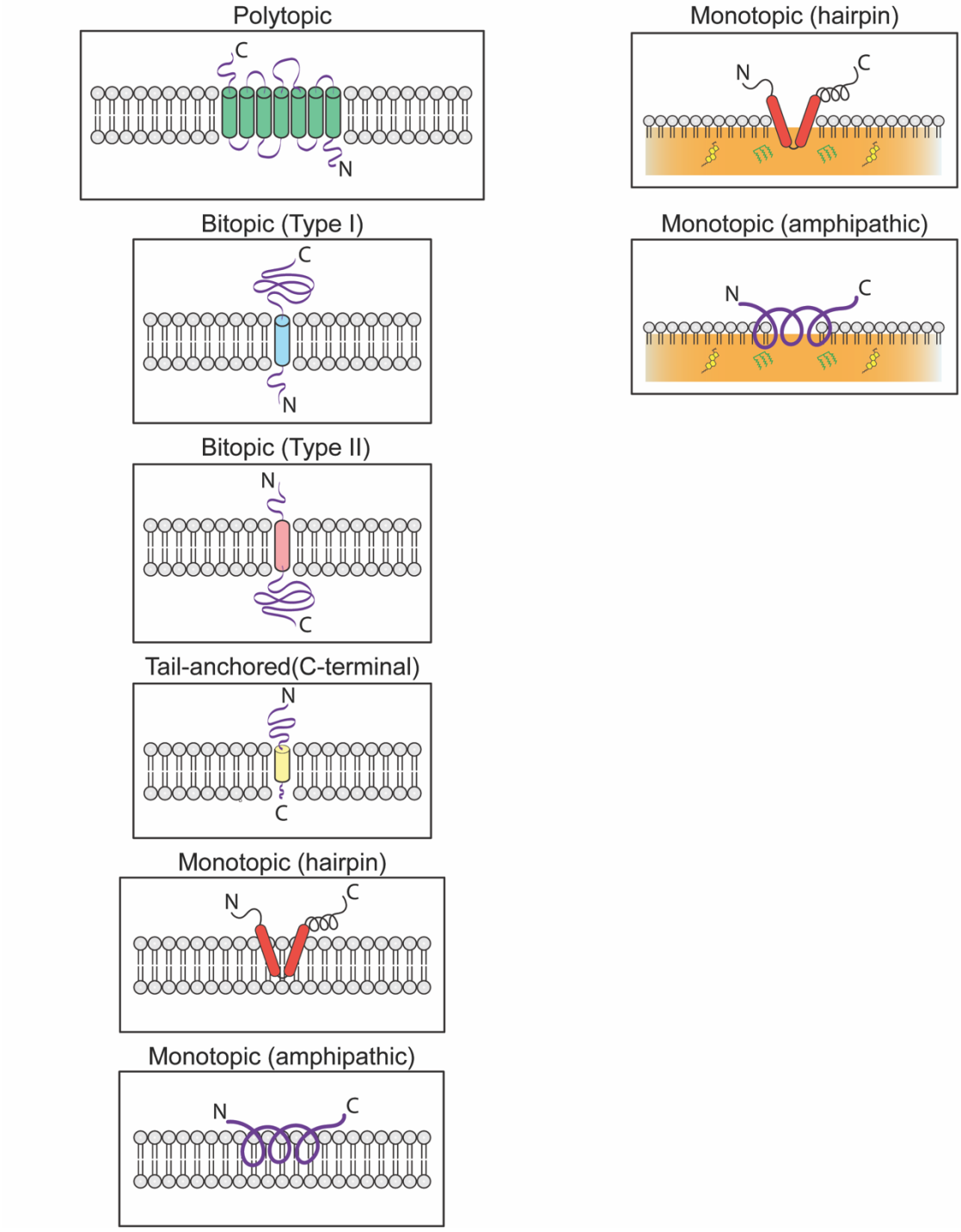

Figure 6: Topological representation of membrane proteins.

The above schematic represents the various topologies that membrane proteins can adopt within a specific membrane environment. Integral membrane proteins are classified as polytopic, bitopic (type I and type II), tail-anchored (C-terminal), and monotopic based on their relative orientation to the lipid bilayer or monolayer membranes. Peripheral proteins (not depicted in the schematic above) associate with the membrane indirectly *via* interaction with the phospholipids or stably integrated membrane proteins.

1.7 Membrane topology prediction algorithms are designed for bilayer-spanning proteins

Currently, membrane proteins constitute only 2% of the total deposited structures in the PDB (Doerr, 2009; Elofsson & von Heijne, 2007). This is primarily due to technical bottlenecks associated with purifying membrane proteins and obtaining high-resolution structures. As a consequence, prediction algorithms were developed to obtain insight into the topology of membrane proteins and to better understand their function. These algorithms use primary amino acid sequences as input to distinguish between integral and peripheral membrane proteins. The initial programs based on the hydropathy scale took into account the hydrophobicity and hydrophilicity of each amino acid. The Kyte-Doollitle scale, depending on the amino acid window size, can distinguish between the transmembrane and surface-exposed regions based on their average hydrophobicity value (Engelman et al., 1986; Kyte & Doolittle, 1982).

Later, the positive-inside rule was put forth, which states that the cytosolic flanking regions of the hydrophobic transmembrane helices are enriched in positively charged amino acid residues such as lysine and arginine. The inclusion of the positive-inside rule improved the topology prediction of prokaryotic proteins but was less applicable to eukaryotic proteins (von Heijne, 1992). The use of artificial neural networks and machine-learning algorithms called hidden Markov models (HMM), trained to account for the distribution of all amino acids and not just hydrophobic or charged amino acids, were much more reliable in predicting membrane proteins topology than their predecessors (Krogh et al., 2001; Tsirigos et al., 2015; Weill et al., 2019). The availability of a large number of validated TMD structures in the PDB database as training sets for prediction algorithms assist them in reliably predicting the topology of polytopic and bitopic proteins. However, these existing algorithms are limited in their ability to distinguish between monotopic and bitopic proteins. These limitations arise due to the poor understanding of the key sequence determinants that distinguish the monotopic hairpin domain from a transmembrane helix on a structural level (Nørholm et al., 2011). The study of monotopic hairpin proteins, which co-exist in phospholipid bilayer and LD monolayer membranes, is made more difficult by the lack of structural information on these proteins and the constraints associated with the available protein topology prediction algorithms like TOPCONS (Tsirigos et al., 2015), which misclassify membrane-embedded hydrophobic regions of monotopic hairpin proteins as TMDs and presume the biological membrane to be a phospholipid bilayer.

The topology prediction by such algorithms often contradicts with the experimental findings for monotopic hairpin proteins that reside in both phospholipid bilayer and LD monolayer membranes.

1.8 UBXD8-Class I LD protein

From a functional perspective, UBXD8, also known as Fas-associated factor family member 2 (FAF2), is a well-studied protein that plays a crucial role in ERAD and cellular metabolism (Lee et al., 2010; Loregger et al., 2017; Olzmann et al., 2013; Suzuki et al., 2012). The domain structure of UBXD8 is illustrated in Figure 7A. As an integral component of the ERAD machinery, UBXD8 acts as an anchor for the recruitment of p97/VCP *via* its UBX domain to mediate the degradation of ERAD substrates (Xu et al., 2013). For e.g., UBXD8 interaction with Derlin-1 mediates the dislocation of lipidated apolipoprotein B-100 (ApoB) from the ER lumen to the LD surface for ubiquitin-mediated proteasomal degradation (Suzuki et al., 2012). Recently, in a genetic screen, UBXD8 has been identified as a key determinant to mediate proteasomal degradation of ubiquitinated 3-hydroxy-3-methylglutaryl coenzyme A reductase (HMGCR) under sterol stimulation (Loregger et al., 2017). In fatty acid depleted cells, UBXD8, together with p97/VCP, subjects ubiquitinated Insig-1 to proteasomal degradation by dislocating it from the ER and thereby regulates the synthesis of fatty acids by promoting the proteolytic activation of sterol-regulatory binding protein SREBP-1 (Lee et al., 2008; Ye, 2012). In the ER, UBXD8 has also been proposed to play a crucial role in TAG metabolism by acting as a sensor for long-chain unsaturated fatty acids. In mammalian cells, long-chain unsaturated fatty acids interaction with the UAS domain of UBXD8 promotes its oligomerization, which in turn stimulates the channeling of excess fatty acids into TAGs and inhibits the synthesis of endogenous FAs. However, in cells depleted of fatty acids, UBXD8 promotes fatty acids synthesis but inhibits their conversion into TAGs (Kim et al., 2013; Lee et al., 2010). A rise in fatty acid levels promotes UBXD8 trafficking from the ER-to-LDs where it recruits p97/VCP *via* its UBX domain on the LD surface. On LDs, UBXD8 in conjunction with p97/VCP promotes dissociation of ATGL (the rate-limiting enzyme in lipolysis) from its coactivator CGI-58. This results in inhibition of ATGL-mediated lipolysis activity leading to an increase in LDs size in cells (Olzmann et al., 2013; Stevenson et al., 2016).

Previous studies have shown that UBXD8 is an integral membrane protein, as after alkaline carbonate and chaotrope treatments, UBXD8 remains elusively in the ER and LD monolayer membranes (Pataki et al., 2018; Schrul & Kopito, 2016). Currently, there is no crystal structure available for UBXD8; however, there is experimental evidence that UBXD8 is first inserted into the ER, and the deletion of the region encompassing amino acids (91-111) inhibits the integration of UBXD8 into the ER membrane (Schrul & Kopito, 2016; Suzuki et al., 2012). From the ER, UBXD8 can partition to the LDs depending on the metabolic state of the cell (Lee et al., 2010; Schrul & Kopito, 2016; Suzuki et al., 2012; Zehmer et al., 2009). UBAC2, a polytopic ER-resident rhomboid pseudoprotease was identified in a large proteomic screen designed to map the ERAD interaction network as a UBXD8 interaction partner (Christianson et al., 2012). UBAC2 acts as an ER tether for UBXD8, and restricts a specific pool of UBXD8 in the ER from being trafficked to the LDs under fatty acid induced conditions (Olzmann et al., 2013; Stevenson et al., 2016). Indeed, the knockdown of endogenous UBAC2 leads to an enrichment of UBXD8 on LDs. However, overexpression of UBAC2 completely abolished the trafficking of UBXD8 to LDs.

Currently, our knowledge of the underlying molecular mechanisms that govern the partitioning of hairpin proteins from the ER-to-LDs is still limited. This is mainly due to lack of experimental data available on the structural arrangements and the exact positioning of the membrane-embedded domain of LD-destined hairpin proteins that enable them to partition from the phospholipid bilayer to the LD monolayer. In order to unravel how hairpin proteins partition between the ER and LDs, first, we need to understand how a monotopic hairpin structure is defined on a molecular scale. This knowledge gap is mainly due to the lack of structural information and the constraints associated with the available protein topology prediction algorithms such as TOPCONS (Tsirigos et al., 2015), which are designed on the premise that a biological membrane is a phospholipid bilayer. As a consequence, topology prediction by such algorithms often contradicts the experimental findings on monotopic hairpin proteins that reside in both phospholipid bilayer and LD monolayer membranes, and misclassifies the hydrophobic regions of monotopic hairpin proteins as transmembrane helices. For example, when primary sequence of UBXD8 was subjected to TOPCONS analysis (Tsirigos et al., 2015), which combines topology prediction outcomes from five different algorithms (OCTOPUS, Philius, PolyPhobius,

SCAMPI, and SPOCTOPUS). Four out of five algorithms predicted a bitopic, transmembrane-spanning topology for UBXD8 as shown in Figure 7B. However, the experimental results on UBXD8 topology derived from the protease protection assay have revealed that both N- and C-termini of UBXD8 are oriented toward the cytosol (Schrul & Kopito, 2016).

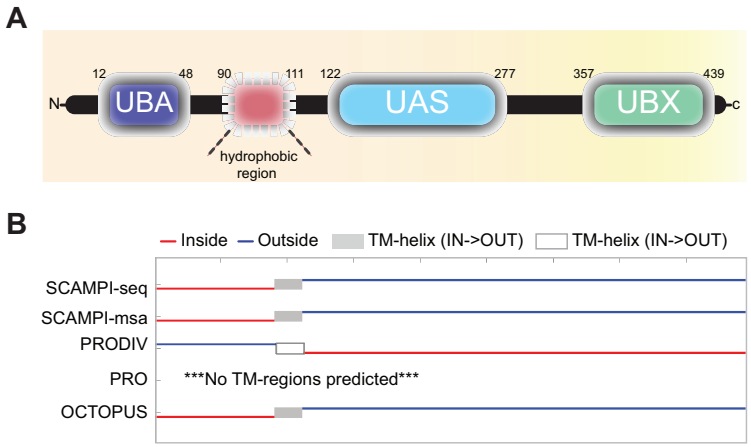

Figure 7: *In silico* topological prediction of UBXD8.

(A) Schematic representation of UBXD8 domain architecture: The full-length UBXD8 is 445 amino acids long, and is comprised of a UBA domain (amino acids, 12-48) located at the N-terminus, followed by a UAS domain (amino acids,122-277), and the conserved UBX domain (amino acids, 357-439) located at the C-terminus. The hydrophobic region (amino acids, 90-111) is positioned between the UBX and UBA domains. UBA domain binds ubiquitin and ubiquitylated proteins. UAS domain mediates interaction with long-chain unsaturated FAs and UBXD8 oligomerization. UBX domain recruits p97/VCP for proteasomal-mediated degradation. The hydrophobic region (amino acids, 91-111) is required for UBXD8 targeting to the ER and LDs.

(B) Comparison of the UBXD8 topology predicted by TOPCONS (accessed in February, 2019), which combines the output from five different topology prediction algorithms. The predicted TM-regions are indicated as white and gray colored bars, and solid lines indicate the soluble domains orientation.

1.9 Aims of this thesis

The 3-D structure of membrane proteins can unravel a lot of information about their functionality in living systems. Currently, sophisticated techniques such as cryo-EM, solid-state NMR, and X-ray crystallography are employed to determine the structure of membrane proteins. Most of these methods require the membrane proteins to be purified and reconstituted into a lipid environment. The complexities and technical hurdles associated with the expression, solubilization, and purification of integral

membrane proteins have made their structural determination more cumbersome in relation to the soluble proteins (Allen et al., 2019; Doerr, 2009). Membrane topology reveals information about a protein's structure in relation to the plane of the membrane, including whether a particular amino acid is positioned inside or outside the lipid bilayer membrane (Lee & Kim, 2014). The final topology of a membrane protein in a given membrane environment is influenced by many key determinants such as positive inside rule, membrane lipids, hydrophobicity of TMD domain, the flanking charged residues positioned at the N-and C-termini, and the protein targeting machinery (von Heijne, 1992). As a starting point, topology prediction algorithms are often used to obtain topological information from the primary sequence of a given protein. The topological information from the prediction algorithms in combination with the experimental approaches such as protease protection and substituted cysteine accessibility assays could provide a more concrete insight into the structure of membrane proteins (Lee & Kim, 2014; von Heijne, 1992).

As described above (in section 1.5.2), proteins targeting the LDs are divided into two categories based on their targeting route to LDs: class I LD proteins target LDs *via* the ERTOLD pathway, and class II LD proteins target LDs *via* the CYTOLD pathway (Olarte et al., 2022). The proteins belonging to class II have been well-characterized in terms of their structural aspects and targeting to LDs (Bersuker & Olzmann, 2017; Kory et al., 2016). However, we still have limited understanding of the underpinning molecular mechanisms that govern how class I LD proteins are targeted to the ER and LDs, as well as their structural characteristics (Dhiman et al., 2020; Olarte et al., 2022). Class I LD proteins associate with the ER and LDs adopting a monotopic topology (Bersuker & Olzmann, 2017; Kory et al., 2016; Olarte et al., 2022). Due to the co-existence of class I LD proteins in two distinct physicochemical membrane environments and the fact that there are not many hairpin proteins that have been identified and experimentally verified, class I LD proteins are generally assumed to partially inserts into one leaflet of a phospholipid bilayer, and this configuration facilitates their lateral partitioning to the LD monolayer during their biogenesis (Dhiman et al., 2020). Although, there is no structural data available for these proteins in bilayer and monolayer membranes, and despite the fact that these proteins are monotopic in both types of membranes, it is still conceivable that structural rearrangements occur during partitioning and that such rearrangements may be crucial to regulate partitioning dynamics of different proteins. A well-characterized

example of class I LD protein is DHRS3, which is shown to be chaotrope-resistant and associates with the ER bilayer and LD monolayer membranes by adopting an interfacial amphipathic helix (Pataki et al., 2018). This study also suggested that most class I LD proteins that target LDs *via* the ERTOLD pathway, including UBXD8, adopt an interfacial amphipathic helix to anchor both the ER and LD membranes (Pataki et al., 2018). However, the primary sequence analysis of the membrane-embedded region of UBXD8 does not show any indication of possessing an amphipathic character. Therefore, it is worthwhile studying the membrane-embedded region of UBXD8 in detail.

Additionally, not all proteins with a monotopic topology partition to LDs. Similar to LD-targeted hairpin proteins, the ER-shaping proteins reticulons with a RHD adopt a hairpin-like or wedge-shaped topology with N and C-termini oriented toward the cytosol, but do not necessarily localize to LDs (Shibata et al., 2009; Voeltz et al., 2006; Yang & Strittmatter, 2007). To better understand how proteins partition between the ER bilayer and LD monolayer membranes of distinct physicochemical properties, we first need to know how a monotopic hairpin structure is defined on a molecular scale and which parameters determine such structures. To date, the intramembrane positioning of the membrane-embedded region of UBXD8 has not been conclusively discerned in both the ER phospholipid bilayer and monolayer LD membranes. Therefore, a precise determination of the positioning of amino acids located within the membrane-embedded region of UBXD8 could help us to identify key sequence determinants that govern the partitioning of UBXD8 from the ER-to-LDs. The aim of this study is to bridge this knowledge gap by performing topology mapping with single amino acid resolution using UBXD8 as a model protein.

The specific objectives of this thesis are:

Aim 1: Determining the solvent-accessibility of UBXD8 membrane-embedded region in both the ER bilayer and LD monolayer membranes.

In order to accomplish this, a solvent-accessibility assay will be established, in which a library of 48 individual cysteine mutants covering the UBXD8 membrane-embedded hydrophobic region and the flanking regions will be probed in order to construct a fine-resolution topological map of the UBXD8 membrane-embedded region in both the ER phospholipid bilayer and LD monolayer membranes.

Aim 2: Determining the intramembrane configuration of UBXD8 membrane-embedded region in both the ER bilayer and LD monolayer membranes by intramolecular crosslinking.

To ascertain the presence of distinct structural conformations, such as changes in the angle opening between UBXD8 helices within the ER bilayer and LD monolayer membranes, an intramolecular crosslinking assay will be implemented.

Aim 3: Comparison of experimental data with the MD simulation data of UBXD8 membrane-embedded region modeled within ER bilayer and monolayer membranes.

To achieve this, MD simulations will be employed to model the membrane-embedded region of UBXD8 in both the ER bilayer and LD monolayer membrane environment. (All MD simulations are performed by Dr. Chetan Poojari in the laboratory of Prof. Jochen Hub, Theoretical Physics, Saarland University, Saarbrücken).

2. Materials

2.1 Chemicals

Unless stated otherwise, all standard chemicals and reagents used in this work were procured from Sigma-Aldrich, Merck, and Roth.

Chemical	**Manufacturer**
Acrylamide/bisacrylamide 30 (37,5:1)	Roth
Acetone (analytical grade)	Fisher Scientific
Agarose NEEO ultra	Roth
Ampicillin sodium salt	Roth
Ammonium persulphate (APS)	Roth
1,6-Bismaleimidohexane (BMH)	Thermo Scientific **(REF: 22330, LOT: WA308702)**
Bovine serum albumin, fatty acid-free (BSA)	Sigma-Aldrich
Bromophenol blue	Roth
Complete®, Mini, EDTA-free protease inhibitor-Cocktail	Roche
Dithiothreitol (DTT)	Roth
Dimethyl sulfoxide (DMSO)	Roth
Dry fat-free milk powder	Sucofin
Ethidium bromide (EtBr)	Roth
Ethylenediaminetetraacetic acid disodium salt dihydrate (EDTA)	Roth
Ethanol (analytical grade)	Fisher Scientific
Glacial acetic acid (analytical scale)	Fisher Scientific
Glycine	Roth
Glycerol (analytical grade)	Fisher Scientific
4-(2-Hydroxyethyl) piperazine-1-ethanesulfonic acid (HEPES)	Roth
Maltose	Roth
Magnesium acetate $Mg(OAC)_2$	Roth
Methoxypolyethylene glycol maleimide (mPEG, 5 kDa)	Sigma-Aldrich **(REF: 63187-1G, LOT: BCBW3293)**
Methanol (analytical grade)	Fisher Scientific
Oleic acid	Sigma-Aldrich **(REF: O1383-1G, LOT: SLCB8616)**
Phenylmethylsulfonyl fluoride (PMSF)	Roth
Potassium acetate (KOAc)	Roth
Sodium Chloride (NaCl)	Roth

Sodium dodecyl sulphate (SDS)	Roth
Sucrose	Roth
N,N,N',N'-Tetramethylethylenediamine (TEMED)	Roth
Tween®-20	Roth
Tris(2-carboxyethyl)phosphine Hydrochloride (TCEP)	Roth
Tris-base (Tris(hydroxymethyl)aminomethane)	Roth
Triton X-100 (TX-100)	Fisher Scientific

2.2 Materials and reagents for cell culture

Material/Reagent	**Manufacturer**
Cell culture dishes	Greiner Bio-one
Dubecco's Modified Eagle Medium (DMEM)	GIBCO **(REF: 41966-029, LOT: 2406727)**
Dimethyl sulfoxide (DMSO, analytical grade)	Fisher Scientific
Fetal bovine serum (FBS)	Biochrom AG **(REF: S0115, LOT: 133EE)**
Polyethylenimine (PEI, 25 kDa)	Polysciences, Inc **(Catalog: 23966-2)**
1x Phosphate buffered saline (PBS, pH- 7.2) without calcium and magnesium	GIBCO **(REF: 20012019, LOT: 2293647)**
Serological pipettes	Greiner Bio-one
Trypsin-EDTA (0.05%)	GIBCO **(REF: 25300-054, LOT: 2193204)**
35-mm Glass-bottom dishes with 14 mm micro-well, #1.5 cover glass	Cellvis
UltraPure™ DNase/RNase-free distilled water	Invitrogen

2.3 Standard reagents and assay kits

Reagent/Kit	**Manufacturer**
Amino-acid mixture, complete	Promega **(REF: L446A, LOT: 0000012471)**
Deoxynucleotide (dNTP) solution mix	N.E. Biolabs
GE Illustra Microspin G-25 column	GE Healthcare
PureLink™ HiPure Plasmid Midiprep Kit	Invitrogen
QIAprep Spin Miniprep kit	Qiagen
QIAquick PCR purification kit	Qiagen
Rabbit reticulocyte lysate	Promega **(REF: L4960, LOT: 0000380122)**
Ribonucleotide Triphosphates (rNTPs) mix	Promega
T7 RiboMAXTM Large Scale RNA Production System	Promega **(REF: P1300, LOT: 000037655)**

2.4 Enzymes

Enzyme	Manufacturer
DpnI	N.E. Biolabs
EcoRI-HF	N.E. Biolabs
KpnI-HF	N.E. Biolabs
XbaI	N.E. Biolabs
Phusion High-Fidelity DNA Polymerase	N.E. Biolabs

2.5 Markers and dyes

Marker/dye	Manufacturer
6x DNA loading dye	N.E. Biolabs
2x RNA loading dye	N.E. Biolabs
GeneRuler™ 1 kb plus DNA ladder	Thermo Scientific
Precision plus protein all Blue standards	BioRad

2.6 Antibodies

2.6.1 Primary antibodies

1° Antibody	Manufacturer
anti-Calnexin (Rabbit polyclonal, 1:2000)	Enzo Life Sciences **(Catalog: ADI-SPA-865-F)**
anti-mCherry (Rabbit polyclonal, 1:5000)	Invitrogen **(Catalog: PA534974)**
anti-Tubulin (Mouse monoclonal,1:10,000)	Sigma-Aldrich **(Catalog: T6199-100UL)**

2.6.2 Secondary antibodies

2° Antibody	Manufacturer
anti-rabbit immunoglobulins, IRDye® 680LT, conjugated (Goat polyclonal,1:20,000)	Li-Cor Biosciences **(REF: 926-68021, LOT: C71114-15)**
anti-mouse immunoglobulins, IRDye® 800CW, conjugated (Goat polyclonal, 1:15,000)	Li-Cor Biosciences **(REF: 926-32210, LOT: D00812-08)**

2.7 Equipment

Equipment	Manufacturer
Agarose gel electrophoresis chamber	Thermo Scientific
AxioObserver.Z1/7 inverted fluorescence microscope	Zeiss
Centrifuge (Table-top)	Eppendorf
Class II laminar flow hood	Heraeus

Digital gel imaging system	BioRad
Trans-blot turbo transfer system	BioRad
Gradient PCR thermocycler	Biometra TAdvanced
Incubators	Binder
NanoDrop (ND-1000)	Thermo Scientific
Microfuge	Biozym
Inverted light microscope (Eclipse Ts2)	Nikon
SDS-PAGE electrophoresis chamber	BioRad
Thermomixer	Eppendorf
Ultracentrifuge (Table-top)	Beckman Coulter
Water bath	VWR

2.8 Cell lines and bacterial strains

2.8.1 Cell line

The original human cervical carcinoma HeLa cell line variant named HeLa Kyoto cell line was used in this study (Landry et al., 2013; Liu et al., 2019).

2.8.2 Bacterial strains

Escherichia coli (DH5α).

2.9 Vectors

In this study, pcDNA3.1(-) mammalian expression vector was used.

Promoter- CMV

Size- 5428 bp

Cloning method- Restriction based

Bacterial resistance- Ampicillin

Selectable marker- Neomycin/Kanamycin

3. Methods

3.1 Cell culture

All cell culture procedures were carried out in a biosafety level 1 (BSL-1) lab equipped with a class II laminar flow hood, temperature-controlled humidified incubator, water bath, and an inverted light microscope.

3.2 Cell line maintenance and transfection

HeLa Kyoto cell line (Schrul & Kopito, 2016) was used in this work. This cell line was cultured in Dulbecco's Modified Eagle Medium (DMEM) containing glucose (4.5 g/l) and glutamine, to which 10% (v/v) fetal bovine serum (FBS) was added freshly. The cells were seeded in p100 tissue culture plates and cultured at 37°C in a 5% CO_2 temperature-controlled humidified incubator. To detect any aberrant growth pattern, the growth and morphology of the cells were monitored daily using an inverted light microscope. Cells were passaged after every two days when they reached 85-90% confluency. To passage cells, first, the spent medium was aspirated and then the cells were rinsed once with 10 ml 1x phosphate-buffered saline (PBS) without calcium and magnesium. Following that, the cells were rinsed with 1 ml Trypsin-EDTA (0.05%) and excess trypsin was aspirated leaving a thin layer on top of the cells. To ensure cells were fully trypsinized, the plates were incubated for 5 min at 37°C in a 5% CO_2 temperature-controlled humidified incubator. After trypsinization, the cells were resuspended in a fresh medium and were seeded onto new p100 tissue culture plates. The size of the culture plate was decided as per the planned experiment. In addition, the cells were screened for mycoplasma contamination once every month or when a new cell vial was thawed by standard polymerase chain reaction (PCR).

3.3 Transient mammalian cell transfection

For transient transfection, HeLa Kyoto cells were seeded onto p100 tissue culture plates at a seeding density of 800,000 cells/plate in 10 ml DMEM the day before transfection was performed. The next day, cells at approximately 50% confluency were transfected using Polyethylenimine (PEI, 25kDa) to DNA ratio of 4:1, as stated below in Table 1**.** Each plate was transfected with 2.5 µg of pcDNA3.1(-) encoding the UBXD8 (op-UBXD8$_{53\text{-}153}$-mCherry) harboring the introduced cysteine and an empty vector (2.5 µg) to maintain a constant PEI:DNA ratio for all plates. The transfection

mixture (PEI-DNA) after incubation for 20 min at room temperature was gently added dropwise to the cells, and the plates were incubated at 37°C in a 5% CO_2 temperature-controlled humidified incubator for 24 h.

Table 1: Pipetting scheme for PEI-mediated transfection

Reagents	Final concentration	Volume
Ultrapure water (nuclease-free)		To reach final volume of 500 µl
NaCl (1.5 M)	150 mM	50 µl
Mix by pipetting		
Plasmid DNA (pDNA)	2.5 µg	as per pDNA concentration
Empty vector	2.5 µg	as per empty vector concentration
Mix by flicking the tubes		
Polyethylenimine (PEI, 1 mg/ml)		20 µl
Final Volume		**500 µl**

3.4 Cell counting

For manual counting using Neubauer hemocytometer, cells were harvested in DMEM medium and an aliquot of the cell suspension was loaded onto the hemocytometer chamber. Cells were counted in the four main large corner squares of the hemocytometer. The average of the cells was multiplied by 10^4 to obtain the cell number per 1 ml.

3.5 Cryopreservation and thawing of cells

For long term storage, cells were first rinsed with 1x PBS without calcium and magnesium, trypsinized and harvested in DMEM medium supplemented with 10% FBS and 10% dimethyl sulfoxide (DMSO). After resuspension, cells were transferred into cryogenic storage vials. Following that, the vials were promptly stored at -80°C before being used again. To initiate a new culture, the vial was briefly warmed at room temperature to defrost the cells and the cell suspension was transferred to a falcon tube containing 9 ml pre-warmed DMEM medium. The cells were resuspended and seeded onto the same size plate as before they were frozen.

3.6 Molecular cloning

Human UBXD8 (op-UBXD8-s) expressing vector pcDNA3.1(-) as previously described in the study from Schrul & Kopito,2016, was used as a template to generate C-terminal mCherry-tagged UBXD8 (op-UBXD8$_{53-153}$-mCherry), and C-terminal mCherry and opsin-tagged UBXD8 (UBXD8$_{53-153}$-mCherry-op) by restriction-based cloning as illustrated in Figure 8.

To generate C-terminal mCherry-tagged UBXD8 (op-UBXD8$_{53-153}$-mCherry), mCherry cDNA was PCR amplified with primers containing *EcoRI* and *KpnI* restriction sites and ligated into linearized pcDNA3.1(-). Subsequently, the amino-acid sequence (53-153) of UBXD8 was PCR amplified from the parental template plasmid (op-UBXD8-S) with a forward primer bearing *XbaI* restriction site and an N-terminal opsin-tag (MGPNFYVPFSNKTG) and a reverse primer with an *EcoRI* restriction site. After digesting the amplified PCR product (UBXD8$_{53-153}$) with the indicated enzymes, the digested product was ligated into mCherry pcDNA3.1(-) digested with the corresponding enzymes.

To generate C-terminal mCherry and opsin-tagged UBXD8 (UBXD8$_{53-153}$-mCherry-op), mCherry cDNA was PCR amplified with a forward primer containing an *EcoRI* restriction site and a reverse primer with an opsin-tag and *KpnI* restriction site and ligated into linearized pcDNA3.1(-). Thereafter, UBXD8$_{53-153}$ was PCR amplified from the parental template plasmid (op-UBXD8-s) with primers bearing *XbaI* and an *EcoRI* restriction sites. The amplified PCR product (UBXD8$_{53-153}$) after digestion with the indicated enzymes was ligated into mCherry-op pcDNA3.1(-) digested with the same enzymes. All constructs were verified by Sanger DNA sequencing prior to usage.

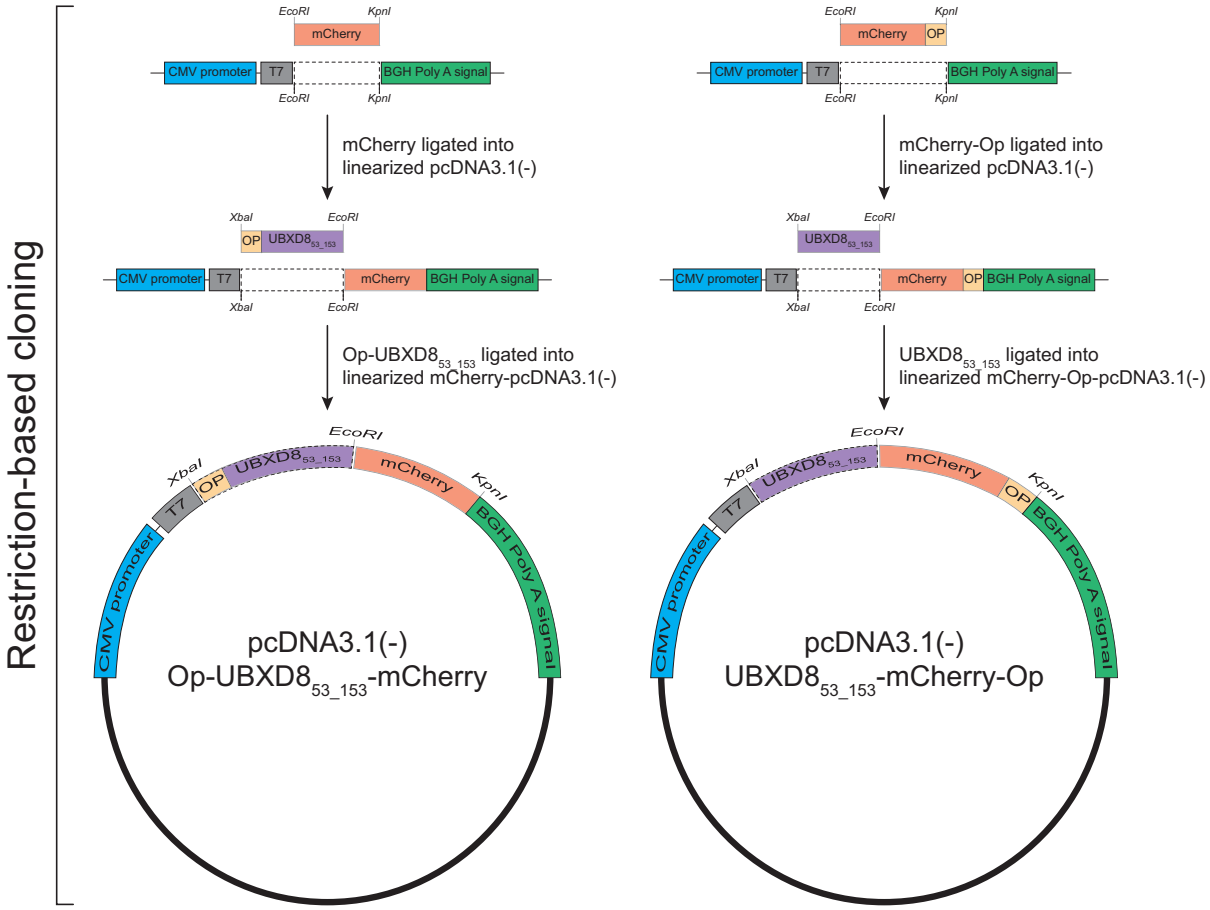

Figure 8: Schematic illustrating the restriction-based cloning of op-UBXD8$_{53_153}$-mCherry and UBXD8$_{53_153}$-mCherry-op (for details refer to main text, section 3.6).

3.7 Site-directed mutagenesis

Plasmid pcDNA3.1(-), encoding cysteine-less derivative of the UBXD8 (op-UBXD8$_{53-153}$-mCherry) covering the membrane-embedded region with an opsin-tag on N-terminus and mCherry on C-terminus, was used as a DNA template for site-directed mutagenesis (Figure 9) to generate single cysteine mutant library as listed in Table 2. The forward and reverse primer pairs used to introduce single cysteine in the parental cysteine-less UBXD8 DNA template (op-UBXD8$_{53-153}$-mCherry) are listed in Table 3. For introducing single cysteine via overlap extension PCR, the reaction components were pipetted in a thin-walled PCR tube on ice as stated below in Table 4. Overlap extension PCR was performed using a thermal cycler with lid pre-heated to 98°C, using cycling parameters as stated below in Table 5**.** Annealing temperature was calculated as per primer's melting temperature (Tm). The PCR products were digested with 1µl of the restriction enzyme *Diplococcus pneumoniae* (*DpnI*) at 37°C for 1h in a

thermocycler to degrade any residual parental plasmid DNA. The *DpnI* digested PCR products were checked by agarose gel electrophoresis as described in Section (3.8). Next, 5 µl of the *DpnI* digested PCR products were transformed into chemically competent *E. coli* (DH5α) cells as described in Section (3.9).

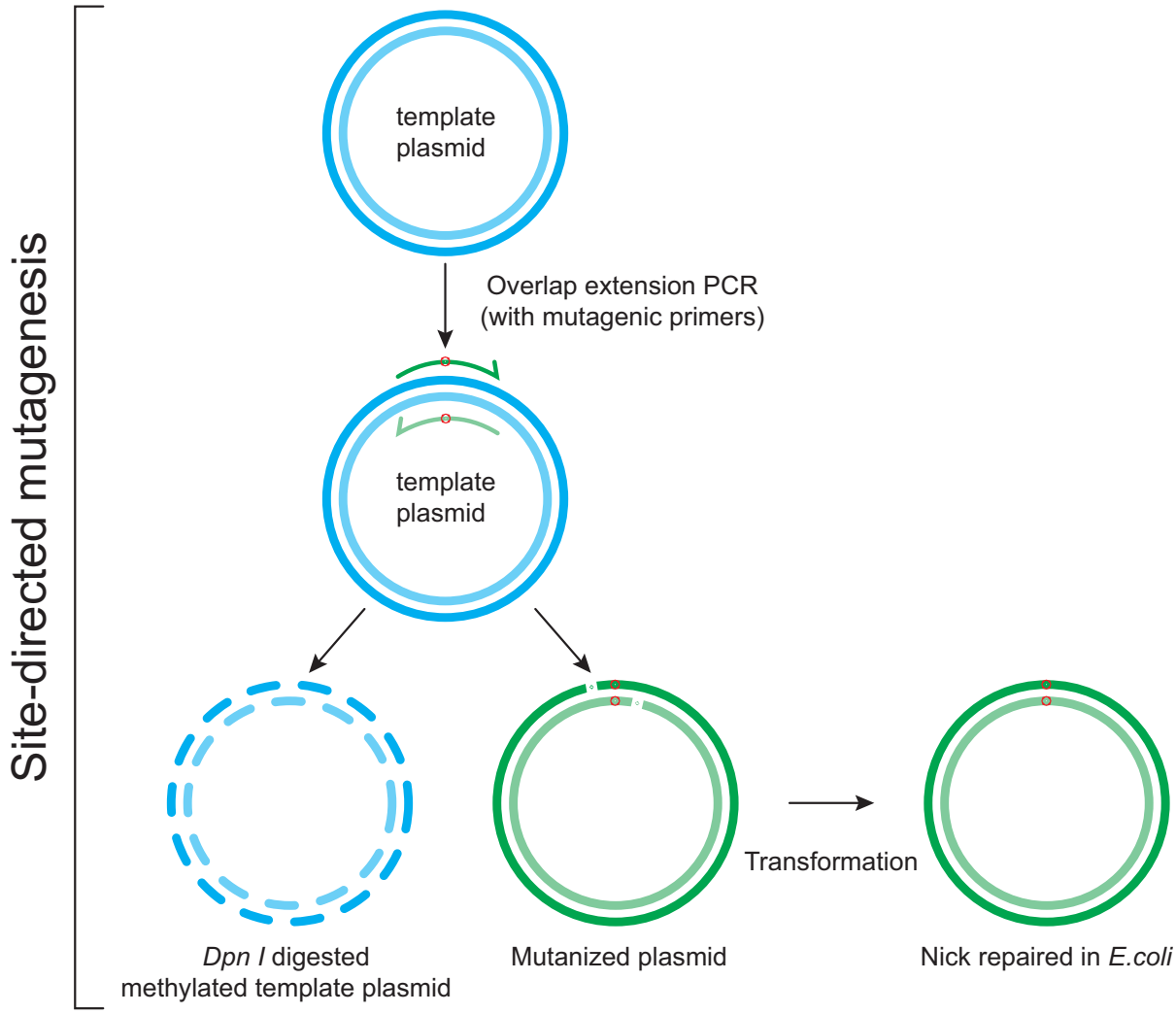

Figure 9: Outline of site-directed mutagenesis to introduce point mutations (for details refer to main text, section 3.7).

Table 4: Reagents and final concentration used for overlap extension PCR

Reagents	Final concentration	Volume
UltraPure™ DNase/RNase-free distilled water		29.5 µl
5x Phusion HF reaction buffer	1x	10 µl
Forward primer (10 µM)	0.5 µM	2.5 µl
Reverse primer (10 µM)	0.5 µM	2.5 µl
Dimethyl Sulfoxide (DMSO)	6%	3 µl
Deoxynucleotide (dNTP) solution mix (10 mM)	200 µM	1 µl
Template plasmid DNA (10 ng/µl)	10 ng	1 µl
Phusion high-fidelity DNA polymerase (2U/µl)	1U/50 µl	0.5 µl
Final volume		**50 µl**

Table 5: Cycling parameters used for overlap extension PCR

Step	Temperature	Time	
Initial denaturation	98°C	3 min	
Denaturation	98°C	10 sec	17 cycles
Annealing	70°C	30 sec	
Extension	72°C	2 min 30 sec	
Final extension	72°C	10 min	
Hold	4°C	∞	

3.8 Agarose gel electrophoresis

The *DpnI* digested PCR products (5µl), after mixing with 6x Purple DNA loading dye, were separated by agarose gel electrophoresis on 1% (w/v) agarose gel prepared in 1x TAE buffer (composition listed in Table 6).

The PCR products were loaded onto the gel alongside with a 1kb plus DNA ladder to monitor the size of the PCR products. The run was carried out at 80 V in 1x TAE buffer till the purple dye reaches the bottom front of the gel. The gel was stained for 10 min in ethidium bromide (EtBr) solution prepared by mixing five drops of EtBr in 500 ml 1x TAE buffer. After staining, bands were visualized by exposing the gel to ultra-violet light and imaged using a Gel Doc imaging system.

Table 6: Composition of 50x Tris-acetate-EDTA (TAE) buffer

Reagents	Concentration	50x stock
Tris-base (MW-121.14 g/mol)	2 M	242 g
EDTA disodium salt dihydrate (MW- 372.24 g/mol)	50 mM	18.61 g
Glacial Acetic acid	1 M	57.1 ml
Milli-Q H_2O		**Raise the volume to 1 liter**

3.9 Transformation of chemically competent *E. coli* (DH5α) cells

First, chemically competent *Escherichia coli* (*E. coli*, DH5α) cells were thawed on ice and 5 µl of the *DpnI* digested PCR product was mixed with 50 µl of the thawed cells by gently tapping the tube. The cells were left on ice for 30 min before heat-shock at 42°C for exactly 45 sec in a thermomixer and placed on ice for 2 min. Then, 100 µl of pre-warmed 1x Luria-Bertani (LB) medium was added to each tube and the cells were incubated at 37°C for 30 min in a thermomixer with continuous shaking at 850 rpm. Out of 150 µl cell suspension, 50 µl was spread onto LB agar-plates supplemented with ampicillin (100 µg/ml). The plates were incubated at 37°C overnight with the lid facing down. The next day, two colonies were picked from each plate and inoculated into 5 mL 1x LB medium containing tubes supplemented with ampicillin (100 µg/ml), followed by incubation at 37°C overnight in a shaker at 200 rpm.

3.10 Plasmid DNA isolation (Miniprep) and DNA sequencing

The next day, using QIAprep Spin Miniprep kit, plasmid DNA was isolated from the 5 mL overnight grown bacterial culture following the manufacturer's recommended protocol. Finally, the plasmid DNA was eluted in 50 µl of ultrapure water, and concentration was measured using a Nanodrop spectrophotometer. The correct introduced mutations were confirmed by Sanger sequencing using the primers listed in Table 7. The DNA sequencing was performed by the company Eurofins Genomics, Germany. Samples for sequencing were prepared as per company recommended guidelines.

Table 7: Primers used for sequencing

Primer	Sequence (5'-3')
CMV_for	CGCAAATGGGCGGTAGGCGTG
pRD_0021_seq_for	GCAAGGGCGAGGAGGATAAC

3.11 Plasmid DNA isolation (Midiprep)

After the correct transformants (clones) were confirmed by sequencing, a mini-culture was set by inoculating 5 ml of 1x LB medium supplemented with ampicillin (100 µg/ml) with a single bacterial colony and incubated at 37°C for 5 h at 220 rpm. This mini-culture was then inoculated into 50 ml 1x LB medium supplemented with ampicillin (100 µg/ml) and incubated at 37°C overnight at 220 rpm. The next day, using PureLink™ HiPure Plasmid-Filter-Midiprep kit, plasmid DNA was isolated from the 50 mL overnight grown bacterial culture following the manufacturer's recommended protocol. Finally, the plasmid DNA was eluted in 100 µl of ultrapure water and concentration was measured using a Nanodrop spectrophotometer.

3.12 Standard PCR for construct amplification

Plasmid pcDNA3.1(-), encoding the UBXD8 (op-UBXD8$_{53-153}$-mCherry) harboring the introduced mutations were PCR amplified using the primers binding within the T7 promoter sequence and the bovine growth hormone polyadenylation signal (listed in Table 8). The reaction components were pipetted in a thin-walled PCR tube on ice as stated below in Table 9. The PCR was performed using a thermal cycler with lid pre-heated to 98°C, using cycling parameters as stated below in Table 10.

The size of the amplified PCR products was verified by agarose gel electrophoresis as described above in Section (3.8). Next, amplified PCR products were purified using QIAquick PCR purification kit following the manufacturer's recommended protocol. The purified PCR products were eluted in 30 µl of ultrapure water and concentration was measured using a Nanodrop spectrophotometer.

Table 8: Primers used for construct amplification

Primer	Sequence (5'-3')
pBS_008_for	TAATACGACTCACTATAGG
pBS_009_rev	TAGAAGGCACAGTCGAGG

Table 9: Pipetting scheme for standard PCR

Reagents	Final concentration	Volume
UltraPure™ DNase/RNase-free distilled water		32.5 µl
5x Phusion HF reaction buffer	1x	10 µl
Forward primer (10 µM)	0.5 µM	2.5 µl
Reverse primer (10 µM)	0.5 µM	2.5 µl
Deoxynucleotide (dNTP) solution mix (10 mM)	200 µM	1 µl
Template plasmid DNA (10 ng/µl)	10 ng	1 µl
Phusion high-fidelity DNA polymerase (2U/µl)	1U/50 µl	0.5 µl
Final volume		**50 µl**

Table 10: Cycling parameters used for standard PCR

Step	Temperature	Time	
Initial denaturation	98°C	3 min	
Denaturation	98°C	10 sec	34 cycles
Annealing	63°C	30 sec	
Extension	72°C	2 min 30 sec	
Final extension	72°C	10 min	
Hold	4°C	∞	

3.13 *In vitro* transcription

Capped mRNAs were synthesized *in vitro* from amplified purified PCR products using the T7 RiboMax express large scale RNA production system supplemented with m7G cap analogue. The *in vitro* transcription reaction was pipetted as stated below in Table 11 and the tubes were incubated at 37°C for 4 h in a thermomixer. Thereafter, the transcribed product (mRNAs) was treated with 1µl of RQ1 RNase-free DNase (1U/µl) at 37°C for 30 min to degrade the residual DNA template. Next, the DNase treated transcribed product volume was raised to 50 µl by adding 25 µl of nuclease-free water and subjected to column purification using microspin G-25 columns following the manufacturer's instructions. During the *in vitro* transcription, for quality control, an aliquot was collected immediately after transcription (1µl), DNase treatment (1µl), and

column purification (2µl). Each aliquot was mixed with 2x RNA loading dye and ultrapure water to reach a final volume of 6µl. The quality of each sample was assessed by agarose gel electrophoresis described above in Section (3.8). The run was carried out in 1x TAE buffer at 25 V for 3 h. Before loading onto the gel, the samples were heated at 65°C for 10 min and immediately chilled on ice for 2 min to get rid of the secondary structures. The purified transcribed mRNAs were quantified using a Nanodrop spectrophotometer and stored in aliquots at -80°C after snap-freezing in liquid nitrogen.

Table 11: Pipetting scheme for *in vitro* transcription

Reagents	**Final concentration**	**Volume**
5x Transcription buffer	1x	5 µl
rNTPs (25 mM (ATP, CTP, UTP); 2 mM GTP) *	7.5 mM (ATP, CTP, UTP); 0.6 mM GTP	7.5 µl
DNA template (purified PCR product)	1-2 µg	9.25 µl
m7G Cap analogue (40 mM)	1.2 mM	0.75 µl
T7 enzyme-mix (10x)	1x	2.5 µl
Final volume		**25 µl**

***Composition of Ribonucleotide Triphosphates (rNTPs) mix**

Reagents	**Final concentration**	**Volume**
rATP (100 mM)	25 mM	50 µl
rCTP (100 mM)	25 mM	50 µl
rUTP (100 mM)	25 mM	50 µl
rGTP (100 mM)	2 mM	4 µl
Raise volume to 200 µl with milli-Q H_2O		

3.14 *In vitro* translation

For *in vitro* translation, we used rabbit reticulocyte lysate (RRL), which is a cell-free eukaryotic translational system derived from immature red blood cells and contains all the necessary components of translation machinery required for exogenously supplied mRNA translation. RRL are treated with micrococcal nuclease to degrade the endogenously present mRNAs to reduce the background translation to a minimum and achieve efficient translation of exogenous mRNAs (Pelham and Jackson, 1976). The purified transcribed mRNA (300 ng), after heat denaturation at 65°C for 3 min in a thermal cycler, was used as a template for *in vitro* translation in the presence of RRL.

The translation reaction was supplemented with complete amino-acid mix and canine pancreatic rough microsomes (2 eq/µl) prepared in rough microsome (RM) buffer (composition listed in Table 12) to allow co-translational insertion of UBXD8 (op-UBXD8$_{53-153}$-mCherry) into the membranes. The *in vitro* translation reaction was pipetted on ice as stated below in Table 13 and the tubes were incubated at 30°C for 45 min in a thermomixer with continuous shaking at 450 rpm. The mRNA translation was terminated by incubating the tubes for 5 min at 30°C in a thermomixer shaking at 450 rpm, after adding 2.5 mM puromycin. Next, the translation product (30µl) was loaded on a 150 µl sucrose cushion (composition listed in Table 14) and centrifuged in a TLA-100 rotor (Beckman Coulter) at 100,000 x g for 5 min at 4°C. After first centrifugation, 50 µl of the supernatant containing soluble proteins were collected and subjected to ammonium sulfate precipitation as described in Section (3.15). The membrane-integrated fraction of UBXD8 after solubilization in PEG buffer was again loaded on a 150 µl sucrose cushion and centrifuged at 100,000 x g for 10 min at 4°C. The final pellet (UBXD8 membrane fraction) was resuspended in 30 µl of PEG buffer (composition listed in Table 15) and subjected to PEGylation as described in Section (3.16).

Table 12: Pipetting scheme for *in vitro* translation

Reagents	**Final concentration**	**Volume**		
		IVT #1	**IVT#2**	**IVT #3**
Rabbit reticulocyte lysate (100%, Nuclease-treated)	70%	21 µl	21 µl	21 µl
Complete amino-acid mix (400 µM)	20 µM	1.5 µl	1.5 µl	1.5 µl
Rough microsomes (2 eq/µl)	10 eq	5 µl	5 µl	5 µl
mRNA	300 ng	as per mRNA stock conc.	as per mRNA stock conc.	as per mRNA stock conc.
UltraPure™ DNase/RNase-free distilled water		Raise the volume to 30 µl with DNase/RNase-free H_2O		
Final volume		**30 µl**	**30 µl**	**30 µl**

Table 13: Composition of rough microsome (RM) buffer

Reagents	Stock concentration	Final concentration	Volume
Sucrose (MW-342.4 g/mol)	2 M	250 mM	1.25 ml
Hepes-KOH, pH 7.6 (MW-238.30 g/mol)	1 M	50 mM	0.5 ml
Potassium acetate (KOAc, MW-98.15 g/mol)	4 M	50 mM	125 µl
Magnesium acetate ($Mg(OAc)_2$, 142.39 g/mol)	1 M	2 mM	20 µl
Dithiothreitol (DTT)	1 M	1 mM	10 µl
Raise volume to 10 ml with milli-Q H_2O			

Table 14: Composition of sucrose cushion

Reagents	Stock concentration	Final concentration	Volume
Sucrose (MW-342.4 g/mol)	2 M	500 mM	2.5 ml
Hepes-KOH, pH 7.6 (MW-238.30 g/mol)	1 M	50 mM	0.5 ml
Potassium acetate (KOAc, MW-98.15 g/mol)	4 M	150 mM	375 µl
Magnesium acetate ($Mg(OAc)_2$, 142.39 g/mol)	1 M	2 mM	20 µl
Tris(2-carboxyethyl)phosphine Hydrochloride (TCEP)	0.5 M	1 mM	20 µl
Raise volume to 10 ml with milli-Q H_2O			

Table 15: Composition of PEGylation (PEG) buffer

Reagents	Stock concentration	Final concentration	Volume
Hepes-KOH, pH 7.6 (MW-238.30 g/mol)	1 M	50 mM	2.5 ml
Sodium chloride (NaCl, MW-58.44 g/mol)	5 M	150 mM	1.5 ml
EDTA disodium salt dihydrate (MW-372.24 g/mol)	0.5 M	1 mM	100 µl
Maltose (MW-342.3 g/mol)	0.5 M	10 mM	1 ml
Tris(2-carboxyethyl)phosphine Hydrochloride (TCEP)	0.5 M	1 mM	100 µl
Raise volume to 50 ml with milli-Q H_2O			

3.15 Ammonium sulfate precipitation

Ammonium sulfate precipitation is based on the principle of salting-in and salting-out. The solubility of globin proteins, which make up the major fraction of proteins in RRL, increases upon the addition of saturated ammonium sulfate, an effect termed as

salting-in. Protein solubility decreases at higher salt concentrations, leading to precipitation referred to as salting-out (Wingfield, 2001). To carry out ammonium sulphate precipitation, 100 µl (2 volumes) of the saturated ammonium sulfate was added to the 50 µl of the supernatant containing soluble proteins and mixed by vortexing. The samples were incubated on ice for 30 min and centrifuged at 13,000 rpm for 10 min at 4°C. After the supernatant was discarded, the protein pellets were resuspended in 30 µl ultrapure nuclease-free water and immediately 60 µl (2 volumes) of ice-cold 96% ethanol was added. After vortexing, the samples were incubated on ice for 15 min and centrifuged at 13,000 rpm for 5 min at 4°C. After the supernatant was discarded, the protein pellets were dried at 37°C for 1-2 min and resuspended in 2x Laemmli buffer supplemented with fresh 100 mM DTT. Finally, the precipitated protein samples were heated at 95°C for 5 min in a thermomixer and separated by sodium dodecyl sulfate-polyacrylamide gel electrophoresis (SDS-PAGE) on 10% acrylamide gels followed by western blotting.

3.16 PEGylation assay on ER-derived RMs

PEGylation assay exploits the unique side-chain chemistry of the amino-acid cysteine (Bogdanov et al., 2005). The assay employs methoxypolyethylene glycol maleimide (mPEG, 5 kDa), a probe that is membrane-impermeable. The mPEG reacts covalently and in an irreversible fashion to the thiol (-SH) groups of exposed free cysteines i.e., cysteine residues not involved in disulfide bonds, therefore, adding an extra molecular weight (5 kDa) to the protein. After PEGylation, the number of higher molecular weight bands represents the number of free cysteines that reacted with the mPEG.

For sulfhydryl labeling with mPEG, membrane-integrated fraction of UBXD8 (op-UBXD8$_{53\text{-}153}$-mCherry) suspended in PEG buffer was divided into three 10 µl aliquots. Each aliquot with or without Triton X-100 treatment as shown below in Figure 10 was incubated with 2 mM mPEG for 30 min on ice. A positive control was set-up by subjecting one aliquot to mPEG in the presence of Triton X-100 to solubilize the UBXD8 (op-UBXD8$_{53\text{-}153}$-mCherry) from the membrane to achieve maximal PEGylation possible for an introduced cysteine residue, and a negative control was carried out without the addition of mPEG. The reactions were quenched with 10 mM dithiothreitol (DTT) for 10 min on ice and, thereafter, mixed with 4x Laemmli buffer supplemented with fresh 100 mM DTT (composition listed in Table 16). PEGylated protein samples after heating at 95°C for 5 min in a thermomixer were separated by

SDS-PAGE on 10% acrylamide gels followed by western blotting. The PEGylation reactions were pipetted on ice as stated below in Table 17. For each cysteine mutant, relative PEGylation (side-chain accessibility) percentage was calculated in relation to the densitometry intensity of the PEGylated band in the Triton X-100 treated condition, set to 100%.

Table 16: Pipetting scheme for PEGylation assay on ER-derived RMs

Reagents	Final concentration	Negative control (DMSO)	mPEG-treated sample	Positive control (mPEG and Triton X-100)
Membrane fraction		10 µl	10 µl	10 µl
Triton X-100 (20%)	1%	-	-	0.53 µl
Ultrapure water		0.53 µl	0.53 µl	-
Mix and incubate on ice for 5 min				
mPEG (20 mM)	2 mM	-	1.17 µl	1.17 µl
DMSO		1.17 µl	-	-
Mix and incubate on ice for 30 min				
DTT (100 mM)	10 mM	1.3 µl	1.3 µl	1.3 µl
Mix and incubate on ice for 10 min				
Laemmli buffer (4x, with 100 mM, DTT)	1x	4.33 µl	4.33 µl	4.33 µl
Final volume		**17.33 µl**	**17.33 µl**	**17.33 µl**

Table 17: Composition of 4x Laemmli buffer

Reagents	Final concentration	10 ml of 4x stock
1 M Tris-HCl, pH 6.8	200 mM	2 ml
SDS (MW- 288.38 g/mol)	8% (w/v)	0.8 g
Glycerol (100%)	40% (v/v)	4 ml
Bromophenol blue	0.04% (w/v)	4 mg
Raise volume to 10 ml with milli-Q H_2O and before use add 100 mM DTT		

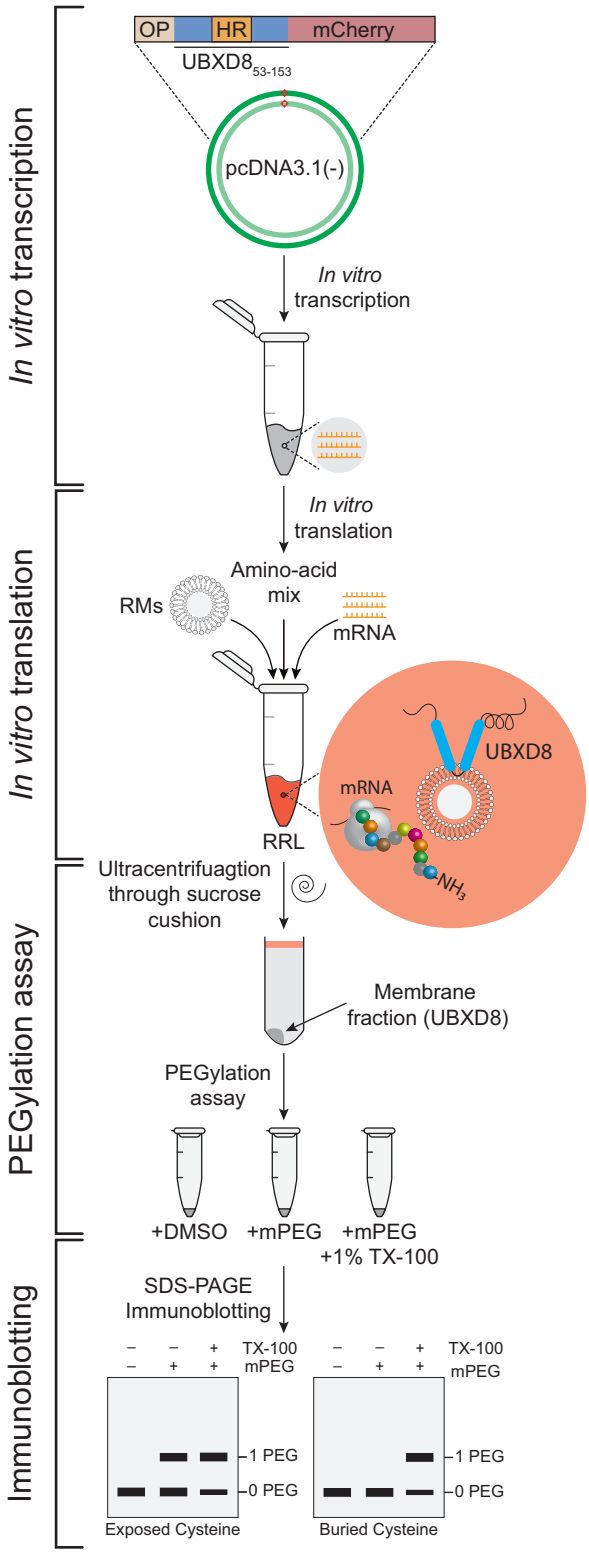

Figure 10: Workflow for PEGylation assay on ER-derived RMs (for details refer to main text, section 3.16).

3.17 Cellular fractionation of LDs

HeLa Kyoto cells harvested from three p100 tissue culture plates were used to isolate the lipid droplets (LDs) by biochemical fractionation. LDs were typically induced by treating the cells with 200 µM oleic acid (18:1) complexed with 0.2% fatty acid-free bovine serum albumin (BSA) in DMEM medium, 24 h after transfection. After 16 h of oleate treatment, cells were washed once with 1x ice-cold PBS and harvested by scraping using a cell-scraper in ice-cold 1x PBS. Thereafter, cells were pelleted down by centrifugation at 500 x g for 5 min at 4°C. Cell pellets were resuspended in ice-cold hypotonic lysis medium (HLM) buffer supplemented with 250 mM sucrose, 1 mM phenylmethylsulfonyl fluoride (PMSF) and Complete EDTA-free protease inhibitors (composition listed in Table 18) and incubated on ice for 20 min. The volume of HLM buffer used was five times the cell pellet size. The cells were disrupted by 26 passages through a 27 G $1^{1/2'}$ syringe needle. Cellular debris and nuclei were removed by centrifugation at 3,000 x g for 10 min at 4°C. The post-nuclear supernatant (PNS) was transferred to a new tube and adjusted to a final concentration of 20% sucrose by adding ice-cold HLM buffer containing 60% sucrose (composition listed in Table 19). The suspension was then transferred to the bottom of a 2 ml ultracentrifuge tube and overlaid with ice-cold HLM buffer. After centrifugation at 172,000 x g for 1 h in a TLS-55 rotor at 4°C, the buoyant LD-fraction was collected using a tube slicer, the cytosolic fraction and membrane-containing pellet by pipetting. The collected cellular fractions were resolved by SDS-PAGE on 10% acrylamide gels followed by western blotting.

Table 18: Composition of HLM buffer containing 250 mM sucrose

Reagents	Stock concentration	Final concentration
Tris/HCl, pH 7.5 (MW-121.14 g/mol)	1 M	20 mM
EDTA disodium salt dihydrate (MW-372.24 g/mol)	0.5 M	1 mM
Sucrose (MW- 342.2 g/mol)	2 M	250 mM

**Complete EDTA-free protease inhibitor (1x) and 1 mM phenylmethylsulfonyl fluoride (PMSF) were added immediately before use.*

Table 19: Composition of HLM buffer containing 60% sucrose

Reagents	Stock concentration	Final concentration
Tris/HCl, pH 7.5(MW-121.14 g/mol)	1 M	20 mM
EDTA disodium salt dihydrate (MW-372.24 g/mol)	0.5 M	1 mM
Sucrose (MW- 342.2 g/mol)	60% (w/v)	60 g in 100 ml water

3.18 PEGylation assay on isolated LDs

To carry put PEGylation (sulfhydryl labeling) on LDs isolated from UBXD8 (op-UBXD8$_{53-153}$-mCherry) transfected cells, 300 µl of isolated LDs suspended in HLM buffer was divided into three 100 µl aliquots. Each 100 µl aliquot was first treated with 1 mM TCEP and incubated on ice for 10 min. Each aliquot with or without Triton X-100 treatment as shown below in Figure 11 was incubated with 2 mM mPEG for 1 h on ice. A positive control was set-up by subjecting one aliquot to mPEG in the presence of Triton X-100 to solubilize the UBXD8 (op-UBXD8$_{53-153}$-mCherry) from the membrane to achieve maximal PEGylation possible for an introduced cysteine residue, and a negative control was carried out without the addition of mPEG. The reactions were quenched with 10 mM DTT for 10 min on ice. After PEGylation, proteins were solubilized in 2% Triton X-100 and subjected to trichloroacetic acid (TCA) precipitation as described in Section (3.19). The PEGylation reactions were pipetted on ice as stated below in Table 20.

Table 20: Pipetting scheme for PEGylation assay on isolated LDs

Reagents	Final concentration	Negative control (DMSO)	mPEG-treated sample	Positive control (mPEG and Triton X-100)
LD fraction		100 µl	100 µl	100 µl
TCEP (20 mM)	1 mM	5.26 µl	5.26 µl	5.26 µl
Mix and incubate on ice for 5 min				
Triton X-100 (20%)	2%	-	-	11.7 µl
Ultrapure water		11.7 µl	11.7 µl	-
Mix and incubate on ice for 5 min				
mPEG (20 mM)	2 mM	-	13 µl	13 µl
DMSO		13 µl	-	-
Mix and incubate on ice for 1 h				
DTT (100 mM)	10 mM	14.44 µl	14.44 µl	14.44 µl
Mix and incubate on ice for 10 min				
Triton X-100 (2% in PBS)		-	-	305.56 µl
PBS		260.56 µl	260.56 µl	-
Triton X-100 (20% in PBS)		45 µl	45 µl	-
Final volume		**450 µl**	**450 µl**	**450 µl**
Subjected to TCA precipitation				

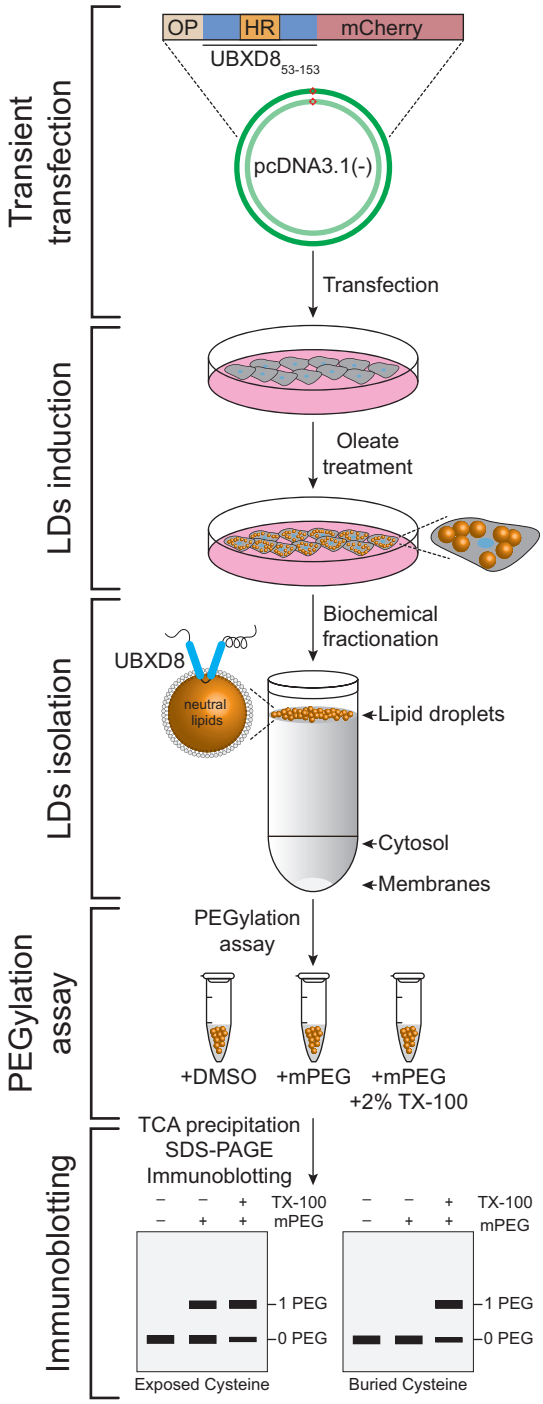

Figure 11: Workflow for PEGylation assay on LDs isolated from cells (for details refer to main text, section 3.18).

3.19 Trichloroacetic (TCA) precipitation

Following PEGylation and solubilization in Triton X-100, the PEGylated protein samples were precipitated by adding 1 volume of 100% TCA (i.e., add 50 µl of 100% TCA to 450 µl of the protein sample). After vortexing, samples were incubated on ice

for 30 min and centrifuged at 13,000 x g for 25 min at 4°C in a table-top centrifuge. After the supernatant was discarded, the pellets were washed twice with 1 ml ice-cold acetone by incubating on ice for 15 min, followed by two cycles of centrifugation at 13,000 x g for 20 min at 4°C to remove any residual TCA. The pellets were dried overnight under a hood and solubilized in 4x Laemmli buffer supplemented with fresh 100 mM DTT, and analyzed by SDS-PAGE and quantitative immunoblotting.

3.20 Fluorescence microscopy

For fluorescence microscopy, 100,000 HeLa Kyoto cells were seeded onto 35-mm glass-bottom dishes in 2 ml DMEM medium. To transiently transfect cells, PEI-mediated transfection method was used as described above in Section (3.3). Each plate was transfected with 500 ng of pcDNA3.1(-) encoding the UBXD8 (op-UBXD8$_{53-153}$-mCherry) and an empty vector (500 ng) to maintain a constant PEI to DNA (4:1) ratio as stated below in Table 21. The next day, LDs were induced by treating the cells with 200 µM oleic acid complexed with 0.2% bovine serum albumin (BSA), fatty acid-free in DMEM medium. After 16 h of oleate treatment, cells were washed twice with 1x PBS, and LDs were stained with HCS LipidTOX green (1:1000) as per manufacturer's recommended protocol. For imaging cells, Zeiss AxioObserver.Z1/7 inverted microscope equipped with a Plan-Apochromat oil objective (63x, NA 1.4) with appropriate filter sets was used. Using a Rolera EM-C^2 camera (QImaging), 15 individual z-sections per image with a step size of 0.25 µm were obtained. Images were pseudo-colored and set to maximum intensity z-projection in Fiji. The final images were cropped in Adobe Photoshop and assembled using Adobe Illustrator.

Table 21: Pipetting scheme for PEI-mediated transfection

Reagents	Final concentration	Volume
Ultrapure water (nuclease-free)		To reach final volume of 100 µl
NaCl (1.5 M)	150 mM	10 µl
Mix by pipetting		
Plasmid DNA (pDNA)	500 ng	as per pDNA concentration
Empty vector	500 µg	as per empty vector concentration
Mix by flicking the tubes		
Polyethylenimine (PEI, 1 mg/ml)		4 µl
Final Volume		**100 µl**

3.21 Intramolecular cysteine crosslinking on ER-derived RMs

The protocol used for intramolecular cysteine crosslinking on RMs was adapted from (Tu et al., 2014). First, amino-acids (L91 and L118) located in the membrane-embedded region of UBXD8 (op-UBXD8$_{53-153}$-mCherry) were substituted to a cysteine (L91C and L18C) using site-directed mutagenesis. This UBXD8 cysteine construct was first subjected to *in vitro* transcription and then translation in RRL in the absence of RMs. The mRNA translation was terminated by incubating the tubes for 5 min at 30°C in a thermomixer shaking at 450 rpm, after adding 2.5 mM puromycin. After translation, the tubes were centrifuged at 13,000 x g for 5 min to remove any aggregates. To allow post-translational insertion, RMs were added to the translated protein in RRL and the tubes were incubated at 30°C for 30 min in a thermomixer shaking at 450 rpm. Thereafter, the translation product was loaded onto a 150 µl sucrose cushion and subjected to two cycles of ultracentrifugation in a TLA-100 rotor at 100,000 x g for 10 min at 4°C. The membrane pellet, after resuspension in 20 µl PEG buffer (composition stated in Table 15), was divided into two 10 µl aliquots. For chemical crosslinking, one aliquot was used to set a negative control by adding DMSO only and the other was treated with 500 µM 1,6-Bismaleimidohexane (BMH) for 1 h on ice. The crosslinker was quenched with 10 mM DTT for 10 min on ice. To remove any residual DTT, samples were loaded onto a 150 µl sucrose cushion (without DTT and TCEP) and ultracentrifuged for 30 min at 48,000 rpm at 4°C. After ultracentrifugation, the membrane pellets were resuspended in 10 µl 1x PBS containing 1mM TCEP and solubilized by adding 1% Triton X-100 for 10 min on ice. The solubilized membrane fractions were PEGylated by treatment with 2 mM mPEG for 30 min on ice and

quenched with 10 mM DTT for 10 min on ice. After resuspension in 4x Laemmli buffer supplemented with 100 mM fresh DTT, BMH crosslinked and PEGylated protein samples were resolved by 10% SDS-PAGE and probed by quantitative immunoblotting. The crosslinking and PEGylation reactions were pipetted on ice as stated below in Table 22 and Table 23.

Table 22: Pipetting scheme for BMH crosslinking on ER-derived RMs

Reagents	Final concentration	Negative control	BMH-treated sample
Membrane fraction		10 µl	10 µl
BMH (10 mM)	500 µM	-	0.53 µl
DMSO		0.53 µl	-
Mix and incubate on ice for 1h			
DTT (100 mM)	10 mM	1.17 µl	1.17 µl
Mix and incubate on ice for 10 min			
Final volume		**11.7 µl**	**11.7 µl**

Table 23: Pipetting scheme for PEGylation on BMH crosslinked samples

Reagents	Final concentration	Negative control	mPEG-treated sample
BMH crosslinked membrane fraction		10 µl	10 µl
Triton X-100 (20%)	1%	0.53 µl	0.53 µl
Mix and incubate on ice for 10 min			
PEG-Mal (20 mM)	2 mM	1.17 µl	1.17 µl
Mix and incubate on ice for 30 min			
DTT (100 mM)	10 mM	1.3 µl	1.3 µl
Mix and incubate on ice for 10 min			
Laemmli buffer (4x, with 100 mM, DTT	1x	4.33 µl	4.33 µl
Final volume		**17.33 µl**	**17.33 µl**

3.22 Intramolecular cysteine crosslinking on LDs

For intramolecular cysteine crosslinking on LDs, first, three p100 tissue culture plates were transfected with UBXD8 (op-UBXD8$_{53\text{-}153}$-mCherry) in which leucine at position 91 and 118 were substituted to a cysteine, respectively. After transfection, the cells were treated with oleic acid complexed with BSA to induce the formation of LDs. The next day, LDs were isolated and resuspended in 300 µl ice-cold HLM buffer. For crosslinking, 300 µl of LDs suspended in ice-cold HLM buffer was divided into two 150

µl aliquots. After treatment with 1 mM TCEP for 10 min on ice, one aliquot was treated with DMSO (negative control) and the other was subjected to crosslinking by adding 500 µM BMH and incubated on ice for 1h. After quenching with 4 mM DTT for 10 min on ice, the samples were diluted with 2% Triton X-100 and subjected to PEGylation by treatment with 2 mM mPEG for 1 h on ice. The reactions were quenched with 10 mM DTT for 10 min on ice and subjected to TCA precipitation as described above in Section (3.19). BMH crosslinked and PEGylated protein samples were resolved by 10% SDS-PAGE and probed by quantitative immunoblotting. The crosslinking and PEGylation reactions were pipetted on ice as stated below in Table 24 and Table 25.

Table 24: Pipetting scheme for BMH crosslinking on isolated LDs

Reagents	Final Concentration	Negative control	BMH-treated sample
LD fraction		150 µl	150 µl
TCEP (20 mM)	1 mM	7.89 µl	7.89 µl
Mix and incubate on ice for 10 min			
BMH (20 mM)	500 µM	-	4.05 µl
DMSO		4.05 µl	-
Mix and incubate on ice for 1h			
DTT (100 mM)	4 mM	0.65 µl	0.65 µl
Bring 4 mM DTT to 0.5 mM by adding 1300.72 µl 2% Tx-100 in PBS and incubate on ice for 10 min			
Final volume		**1463.31 µl**	**1463.31 µl**

Table 25: Pipetting scheme for PEGylation on BMH crosslinked samples

Reagents	Final Concentration	Negative control	mPEG-treated sample
BMH crosslinked LD fraction		1463.31 µl	1463.31 µl
mPEG (20 mM)	2 mM	162.59 µl	162.59 µl
Mix and incubate on ice for 1 h			
DTT (1M)	10 mM	16.42 µl	16.42 µl
Mix and incubate on ice for 10 min			
Final volume		**1642.32 µl**	**1642.32 µl**
Subjected to TCA precipitation			

3.23 Sodium dodecyl sulphate polyacrylamide gel electrophoresis (SDS-PAGE)

SDS-PAGE employs sodium dodecyl sulphate (SDS) which is a strong anionic detergent. Each protein is made-up of a unique set of amino-acids and therefore, have different electrical charge. In SDS-PAGE, SDS denature proteins and effectively coat them in negative charge. As a result, the proteins can be sorted according to their molecular weight. Depending on the molecular weight of the protein to be resolved, separating gel (10%) overlaid with a stacking gel (4%) was prepared as per the standard laboratory protocol (composition listed in Table 26). Per lane, an equal volume of protein sample was loaded alongside with a pre-stained protein ladder as a molecular mass indicator. The run was carried out in 1x SDS running buffer (composition listed in Table 27) at 70 V until the bromophenol blue dye front ran through the stacking gel and then increased to 140 V till the dye reached the bottom front of the separating gel.

Table 26: Pipetting scheme for SDS-polyacrylamide gel

Reagents	**Separating gel (10%)**	**Stacking gel (10%)**
	Volume	**Volume**
Milli-Q H_2O	2.24 ml	1.2 ml
2 M Tris-HCl, pH 8.8	1 ml	-
0.5 M Tris-HCl, pH 6.8	-	0.5 ml
30% (w/v) Acrylamide/bis-acrylamide (37.5:1)	1.66 ml	0.27 ml
SDS (10%)	50 µl	20 µl
TEMED (Roth)	4 µl	2 µl
10% Ammonium persulphate (APS)	40 µl	20 µl

** Volume is sufficient for making one gel*

Table 27: Composition of 10x SDS-running buffer

Reagents	**Concentration**	**10x Stock**
Tris-base (MW- 121.14 g/mol)	250 mM	30.3 g
Glycine (MW- 75.07 g/mol)	1.92 M	144.4 g
SDS (MW- 288.38 g/mol)	1% (w/v)	10 g
Milli-Q H_2O		**Raise the volume to 1 liter**

3.24 Western blotting

After electrophoresis is complete, the separated proteins can be transferred from the gel onto a membrane using electroblotting. For electroblotting proteins- the resolving gel, nitrocellulose membrane, and the filter papers were soaked in 1x ice-cold transfer buffer (composition stated in Table 28). Next, the membrane and resolving gel were placed between filter papers (filter paper > membrane > gel > filter paper) to create a sandwich. The blotting was carried out at 25 V, 1.0 A for 30 min using a Trans-Blot Turbo semi-dry transfer system. After blotting, the membrane was blocked for 1 h in 5% milk in TBS-T (composition listed in Table 29) at room temperature with gentle shaking to block non-specific binding sites. Subsequently, the membrane was probed with a primary antibody diluted in 5% milk in TBS-T for 2 h at room temperature with gentle shaking. Thereafter, the membrane was washed 3 times, 10 min each in TBS-T at room temperature and probed with an infrared dye-labeled (IRDye) secondary antibody diluted in 5% milk in TBS-T for 1 h at room temperature with gentle shaking. Bands were visualized at a wavelength of 700 nm and 800 nm using Odyssey CLx imaging system (LiCor), after washing the membrane 3 times, 10 min each in TBS-T at room temperature. Band intensities were quantified by densitometry using Image Studio™ Lite software from LiCor.

Table 28: Composition of 10x transfer buffer

Reagents	**Concentration**	**10x Stock**
Tris-base (MW-121.14 g/mol)	250 mM	30.3 g
Glycine (MW-75.07 g/mol)	1.92 M	144.4 g
Milli-Q H_2O		**Raise the volume to 1 liter**

** To prepare 1x transfer buffer from 10x stock: Mix 100 ml of 10x transfer buffer, 200 ml of methanol (20%, (v/v) and raise the volume to 1 liter with milli-Q water.*

Table 29: Composition of 10x Tris-Buffered Saline with Tween 20 (TBS-T) buffer

Reagents	**Concentration**	**10x Stock**
Tris/HCl, pH 7.5 (MW-121.14 g/mol)	200 mM	24.23 g
Sodium Chloride (NaCl, MW-58.44 g/mol)	1.5 M	87.66 g
Tween-20	2% (v/v)	2 ml
Milli-Q H_2O		**Raise the volume to 1 liter**

3.25 $UBXD8_{80\text{-}128}$ structure prediction

The $UBXD_{80\text{-}128}$ structure was predicted using the *ab initio* structure prediction tool QUARK (Xu & Zhang, 2012, 2013). The predicted structure has a kink at position P102 (proline 102) with two anti-parallel α-helices facing each other resulting in a monotopic topology. In the past, UBXD8 has been shown to adopt a monotopic topology in bilayer membranes using protease protection assay (Schrul & Kopito, 2016), which corroborates the predicted $UBXD_{80\text{-}128}$ structure.

3.26 Atomistic MD simulations

All MD simulations were performed by Dr. Chetan Poojari in the laboratory of Prof. Jochen Hub (Theoretical Physics, Saarland University, Saarbrücken). For completeness the employed simulation methods are described in this thesis. The MD simulation method details were kindly provided by Dr. Chetan Poojari.

3.26.1 $UBXD8_{80\text{-}128}$ in bilayer

CHARMM-GUI server (Lee et al., 2016) and charmm36m (WYF) parameters (Huang et al., 2017; Khan et al., 2019) were used to process the $UBXD_{80\text{-}128}$ generated from QUARK (Xu & Zhang, 2012, 2013). The $UBXD_{80\text{-}128}$ N- and C-termini were capped with acetyl (ACE) and N-methyl amide (NME) neutral groups, respectively. The capped $UBXD_{80\text{-}128}$ structure was then inserted into a 1-palmitoyl-2-oleyl-sn-glycero-phosphocholine (POPC) bilayer (charmm36 lipids) at varying depths (Klauda et al., 2010). The bilayer system was solvated with TIP3 water and the system charge was neutralized by adding counter-ions. CHARMM-GUI generated mdp-files were used to subject the solvated system to energy minimization and several short position-restrained equilibrations. The temperature of 310 K was maintained using a Berendsen thermostat with a time constant (tau_t) of 1.0 ps during equilibration (Berendsen et al., 1984). The pressure was maintained using a Berendsen barostat coupled to a semi-isotropic coupling scheme with a time constant (tau_p) of 5.0 ps. In x-y and z directions, a reference pressure of 1.0 bar was maintained. For neighbor list search, verlet cutoff-scheme with a cut-off distance (rlist) of 1.2 nm was used. Using the particle-mesh Ewald and cutoff methods, non-bonded van der Waals interactions were computed with a cutoff distance of 1.2 nm (Darden et al., 1993; Essmann et al., 1995). Using the Lincs algorithm, H-bonds were constrained (Hess et al., 1997). For

the final production simulations, thermostat was switched to Nose-Hoover (Hoover, 1985; Nosé, 2002) and barostat to Parrinello-Rahman (Parrinello et al., 1981; Parrinello & Rahman, 1980), and all restraints were removed. The production simulations were carried out for 2 μs and integrated with a 2 fs timestep. GROMACS 2020.2 simulation package was used to carry out all-atom simulations (Abraham et al., 2015).

3.26.2 UBXD8$_{80\text{-}128}$ in monolayer

To simulate UBXD8$_{80\text{-}128}$ in monolayer membranes, a lipid trilayer system consisting of neutral lipids triolein (TRIO) and cholesteryl oleate (CLOL) molecules sandwiched between two POPC monolayers were assembled (Olarte et al., 2020). Using available PACKMOL (Martínez et al., 2009) program neutral lipid patches were built. The lipid trilayer system was subjected to energy minimization, followed by short equilibration to compress the simulation box in the z-direction. The temperature of 310 K was maintained using a Berendsen thermostat with a time constant (tau_t) of 1.0 ps during equilibration. The pressure was maintained using a Berendsen barostat (Berendsen et al., 1984) coupled to a semi-isotropic coupling scheme with a time constant (tau_p) of 20 ps. Using a reference pressure of 1.0 bar in x-y direction and 1000.0 bar in z-direction, the simulation box was compressed in the z-direction.

In order to prevent flipping during compression, terminal tail atoms of POPC and P-atom were position-restrained during equilibration. After compression, the trilayer system was solvated with TIP3 water and re-equilibrated for 1 μs without any restraints. For the final production simulations, thermostat was switched to Nose-Hoover (tau_t = 1.0 ps) (Hoover, 1985; Nosé, 2002), and barostat to Parrinello-Rahman (tau_p = 5.0 ps) (Parrinello et al., 1981; Parrinello & Rahman, 1980). A reference pressure of 1 bar was set in x, y and z direction. UBXD8$_{80\text{-}128}$ was inserted at varying depths to the equilibrated monolayer system (Javanainen & Martinez-Seara, 2016), and the system charge was neutralized by adding counter ions. The final production simulations were carried out for 2 μs. The final analysis was performed on the last 500 ns of the trajectories for both the bilayer and monolayer simulations employing Gromacs tools. Python matplotlib library package was used for plotting data and image rendering was done using visual molecular dynamics (VMD) program (Humphrey et al., 1996).

Table 30: The table list the systems simulated

Simulation type	Membrane system	Lipid Composition	Monolayer Thickness (nm)	No. of Repeats	Total Simulation Time (μs)
Atomistic MD simulations	Bilayer Partial Insertion (PI)	POPC	-	5	10
	Bilayer-Deep Insertion (DI)	POPC	-	5	10
	Monolayer-DI / PI	POPC:TRIO	4	5	10
	Monolayer-DI / PI	POPC:TRIO:CLOL	4	5	10
Umbrella Sampling	Bilayer-DI (Upward Pulling)	POPC	-	1	3.3
	Bilayer-DI (Downward Pulling)	POPC	-	1	3.3
	LD-DI (Upward Pulling)	POPC:TRIO	-	1	1.45
Bilayer-LD partition	Deep-V peptide conformation	POPC:TRIO	-	1	5
	Shallow-open peptide conformation	POPC:TRIO	-	1	5

Table 2: Single cysteine mutant library

Plasmid identifier	Cysteine mutants
RD_001	Op_UBXD8$_{53\text{-}153}$_**V83C**_mCherry in pcDNA 3.1(-)
RD_002	Op_UBXD8$_{53\text{-}153}$_**P86C**_mCherry in pcDNA 3.1(-)
RD_003	Op_UBXD8$_{53\text{-}153}$_**R89C**_mCherry in pcDNA 3.1(-)
RD_004	Op_UBXD8$_{53\text{-}153}$_**L92C**_mCherry in pcDNA 3.1(-)
RD_005	Op_UBXD8$_{53\text{-}153}$_**G95C**_mCherry in pcDNA 3.1(-)
RD_006	Op_UBXD8$_{53\text{-}153}$_**I110C**_mCherry in pcDNA 3.1(-)
RD_007	Op_UBXD8$_{53\text{-}153}$_**I113C**_mCherry in pcDNA 3.1(-)
RD_008	Op_UBXD8$_{53\text{-}153}$_**F116C**_mCherry in pcDNA 3.1(-)
RD_009	Op_UBXD8$_{53\text{-}153}$_**R119C**_mCherry in pcDNA 3.1(-)
RD_0010	Op_UBXD8$_{53\text{-}153}$_**R122C**_mCherry in pcDNA 3.1(-)
RD_0011	Op_UBXD8$_{53\text{-}153}$_**Y81C**_mCherry in pcDNA 3.1(-)
RD_0012	Op_UBXD8$_{53\text{-}153}$_**V82C**_mCherry in pcDNA 3.1(-)
RD_0013	Op_UBXD8$_{53\text{-}153}$_**S84C**_mCherry in pcDNA 3.1(-)
RD_0014	Op_UBXD8$_{53\text{-}153}$_**R85C**_mCherry in pcDNA 3.1(-)
RD_0015	Op_UBXD8$_{53\text{-}153}$_**Q87C**_mCherry in pcDNA 3.1(-)
RD_0016	Op_UBXD8$_{53\text{-}153}$_**P88C**_mCherry in pcDNA 3.1(-)
RD_0017	Op_UBXD8$_{53\text{-}153}$_**G90C**_mCherry in pcDNA 3.1(-)
RD_0018	Op_UBXD8$_{53\text{-}153}$_**L91C**_mCherry in pcDNA 3.1(-)
RD_0019	Op_UBXD8$_{53\text{-}153}$_**G93C**_mCherry in pcDNA 3.1(-)
RD_0020	Op_UBXD8$_{53\text{-}153}$_**W94C**_mCherry in pcDNA 3.1(-)
RD_0021	Op_UBXD8$_{53\text{-}153}$_**Y96C**_mCherry in pcDNA 3.1(-)
RD_0022	Op_UBXD8$_{53\text{-}153}$_**Y97C**_mCherry in pcDNA 3.1(-)
RD_0023	Op_UBXD8$_{53\text{-}153}$_**I99C**_mCherry in pcDNA 3.1(-)
RD_0024	Op_UBXD8$_{53\text{-}153}$_**M100C**_mCherry in pcDNA 3.1(-)
RD_0025	Op_UBXD8$_{53\text{-}153}$_**L101C**_mCherry in pcDNA 3.1(-)
RD_0026	Op_UBXD8$_{53\text{-}153}$_**P102C**_mCherry in pcDNA 3.1(-)
RD_0027	Op_UBXD8$_{53\text{-}153}$_**F103C**_mCherry in pcDNA 3.1(-)

RD_0028	Op_UBXD8$_{53\text{-}153}$_**R104C**_mCherry in pcDNA 3.1(-)
RD_0029	Op_UBXD8$_{53\text{-}153}$_**F105C**_mCherry in pcDNA 3.1(-)
RD_0030	Op_UBXD8$_{53\text{-}153}$_**Y107C**_mCherry in pcDNA 3.1(-)
RD_0031	Op_UBXD8$_{53\text{-}153}$_**Y108C**_mCherry in pcDNA 3.1(-)
RD_0032	Op_UBXD8$_{53\text{-}153}$_**T109C**_mCherry in pcDNA 3.1(-)
RD_0033	Op_UBXD8$_{53\text{-}153}$_**L111C**_mCherry in pcDNA 3.1(-)
RD_0034	Op_UBXD8$_{53\text{-}153}$_**D112C**_mCherry in pcDNA 3.1(-)
RD_0035	Op_UBXD8$_{53\text{-}153}$_**F114C**_mCherry in pcDNA 3.1(-)
RD_0036	Op_UBXD8$_{53\text{-}153}$_**R115C**_mCherry in pcDNA 3.1(-)
RD_0037	Op_UBXD8$_{53\text{-}153}$_**A117C**_mCherry in pcDNA 3.1(-)
RD_0038	Op_UBXD8$_{53\text{-}153}$_**L118C**_mCherry in pcDNA 3.1(-)
RD_0039	Op_UBXD8$_{53\text{-}153}$_**F120C**_mCherry in pcDNA 3.1(-)
RD_0040	Op_UBXD8$_{53\text{-}153}$_**I121C**_mCherry in pcDNA 3.1(-)
RD_0041	Op_UBXD8$_{53\text{-}153}$_**P123C**_mCherry in pcDNA 3.1(-)
RD_0042	Op_UBXD8$_{53\text{-}153}$_**D124C**_mCherry in pcDNA 3.1(-)
RD_0043	Op_UBXD8$_{53\text{-}153}$_**P125C**_mCherry in pcDNA 3.1(-)
RD_0045	Op_UBXD8$_{53\text{-}153}$_**S127C**_mCherry in pcDNA 3.1(-)
RD_0046	Op_UBXD8$_{53\text{-}153}$_**R128C**_mCherry in pcDNA 3.1(-)
RD_0083	Op_UBXD8$_{53\text{-}153}$_**L91C_L118C**_mCherry in pcDNA 3.1(-)

ML_003_cysteine less	Op_UBXD8$_{53\text{-}153}$_mCherry in pcDNA 3.1(-)
ML_004_cysteine less	UBXD8$_{53\text{-}153}$_mCherry_Op in pcDNA 3.1(-)
ML_009	Op_UBXD8$_{53\text{-}153}$_**S80C**_mCherry in pcDNA 3.1(-)
ML_005	Op_UBXD8$_{53\text{-}153}$_**L98C**_mCherry in pcDNA 3.1(-)
ML_006	Op_UBXD8$_{53\text{-}153}$_**T106C**_mCherry in pcDNA 3.1(-)
ML_008	Op_UBXD8$_{53\text{-}153}$_**S142C**_mCherry in pcDNA 3.1(-)

Table 3: Primers used for generating single cysteine mutants

Primer	Primer ID	Tm°	Sequence (5'-3')
S80C_F	pML_015	74.5°C	ctgaccacaggatctacTGCtatgttgtctcaagac
S80C_R	pML_016	74.5°C	gtcttgagacaacataGCAgtagatcctgtggtcag
Y81C_F	pRD_0021	78.7°C	ctacagcTGCgttgtctcaagacctcaaccaagg
Y81C_R	pRD_0022	76.4°C	acaacGCAgctgtagatcctgtggtcagc
V82C_F	pRD_0023	79.7°C	cagctatTGCgtctcaagacctcaaccaagggg
V82C_R	pRD_0024	75.8°C	gagacGCAatagctgtagatcctgtggtcagc
V83C_F	pRD_001	74.8°C	ctatgttTGCtcaagacctcaaccaagggg
V83C_R	pRD_002	71.4°C	cttgaGCAaacatagctgtagatcctgtgg
S84C_F	pRD_0025	80.6°C	tgttgtcTGCagacctcaaccaaggggc
S84C_R	pRD_0026	75.6°C	ggtctGCAgacaacatagctgtagatcctgtgg
R85C_F	pRD_0027	81.5°C	tgtctcaTGCcctcaaccaaggggctg
R85C_R	pRD_0028	75.9°C	tgaggGCAtgagacaacatagctgtagatcctg
P86C_F	pRD_003	81.0°C	ctcaagaTGCcaaccaaggggctgcttg
P86C_R	pRD_004	73.1°C	ggttgGCAtcttgagacaacatagctgtagatc
Q87C_F	pRD_0029	81.7°C	aagacctTGCccaaggggctgcttgga
Q87C_R	pRD_0030	74.7°C	cttggGCAaggtcttgagacaacatagctgt
P88C_F	pRD_0031	81.7°C	acctcaaTGCaggggctgcttggatgg
P88C_R	pRD_0032	76.4°C	cccctGCAttgaggtcttgagacaacatagc
R89C_F	pRD_005	84.2°C	tcaaccaTGCgggctgcttggatggggt
R89C_R	pRD_006	79.9°C	agcccGCAtggttgaggtcttgagacaaca
G90C_F	pRD_0033	78.8°C	accaaggTGCctgcttggatggggttattacttg
G90C_R	pRD_0034	78.4°C	agcagGCAccttggttgaggtcttgagacaac
L91C_F	pRD_0085	75.4°C	aaggggTGTcttggatggggttattacttgat
L91C_R	pRD_0086	75.0°C	ccaagACAccccttggttgaggtct
L92C_F	pRD_007	80.1°C	ggggctgTGCggatggggttattacttgataatgc
L92C_R	pRD_008	86.1°C	ccccatccGCAcagccccttggttgagg
G93C_F	pRD_0037	75.0°C	gctgcttTGCtggggttattacttgataatgcttc
G93C_R	pRD_0038	81.6°C	ccccaGCAaagcagccccttggttg
W94C_F	pRD_0039	74.0°C	gcttggaTGCggttattacttgataatgcttcc
W94C_R	pRD_0040	80.3°C	taaccGCAtccaagcagccccttgg
G95C_F	pRD_009	74.8°C	tggatggTGCtattacttgataatgcttccattcc
G95C_R	pRD_0010	75.0°C	agtaataGCAccatccaagcagcccct
Y96C_F	pRD_0041	78.6°C	atggggtTGCtacttgataatgcttccattccgg
Y96C_R	pRD_0042	76.0°C	aagtaGCAaccccatccaagcagccc
Y97C_F	pRD_0043	75.6°C	gggttatTGCttgataatgcttccattccgg
Y97C_R	pRD_0044	76.0°C	atcaaGCAataaccccatccaagcagcc
L98C_F	pML_007	81.2°C	gctgcttggatggggttattacTGCataatgcttccattcc

L98C_R	pML_008	81.2°C	ggaatggaagcattatGCAgtaataaccccatccaagcagc
I99C_F	pRD_0045	75.7°C	ttacttgTGCatgcttccattccggtttacc
I99C_R	pRD_0046	78.2°C	agcatGCAcaagtaataaccccatccaagcagc
M100C_F	pRD_0087	69.8°C	cttgataTGTcttccattccggtttacctattac
M100C_R	pRD_0088	72.2°C	ggaagACAtatcaagtaataaccccatccaagc
L101C_F	pRD_0049	75.6°C	gataatgTGCccattccggtttacctattacacga
L101C_R	pRD_0050	74.4°C	aatggGCAcattatcaagtaataaccccatcca
P102C_F	pRD_0051	73.5°C	aatgcttTGCttccggtttacctattacacga
P102C_R	pRD_0052	73.7°C	cggaaGCAaagcattatcaagtaataacccca
F103C_F	pRD_0053	75.4°C	gcttccaTGCcggtttacctattacacgatacttg
F103C_R	pRD_0054	74.7°C	aaccgGCAtggaagcattatcaagtaataaccc
R104C_F	pRD_0089	67.9°C	tccattcTGTtttacctattacacgatacttgat
R104C_R	pRD_0090	64.1°C	gtaaaACAgaatggaagcattatcaagt
F105C_F	pRD_0057	71.4°C	attccggTGCacctattacacgatacttgatat
F105C_R	pRD_0058	74.9°C	taggtGCAccggaatggaagcattatca
T106C_F	pML_009	76.8°C	gataatgcttccattccggtttTGCtattacacgatacttg
T106C_R	pML_010	76.8°C	caagtatcgtgtaataGCAaaaccggaatggaagcattatc
Y107C_F	pRD_0059	66.1°C	gtttaccTGCtacacgatacttgatatatttaggt
Y107C_R	pRD_0060	73.9°C	gtgtaGCAggtaaaccggaatggaagca
Y108C_F	pRD_0061	67.1°C	tacctatTGCacgatacttgatatatttaggtttg
Y108C_R	pRD_0062	73.2°C	atcgtGCAataggtaaaccggaatggaag
T109C_F	pRD_0063	65.1°C	ctattacTGCatacttgatatatttaggtttgctc
T109C_R	pRD_0064	67.8°C	agtatGCAgtaataggtaaaccggaatgg
I110C_F	pRD_0011	71.5°C	ttacacgTGCcttgatatatttaggtttgctcttc
I110C_R	pRD_0012	74.2°C	tcaagGCAcgtgtaataggtaaaccggaatg
L111C_F	pRD_0065	72.6°C	cacgataTGCgatatatttaggtttgctcttcgtt
L111C_R	pRD_0066	70.4°C	atatcGCAtatcgtgtaataggtaaaccggaa
D112C_F	pRD_0067	69.6°C	gatacttTGCatatttaggtttgctcttcgtttt
D112C_R	pRD_0068	69.3°C	aatatGCAaagtatcgtgtaataggtaaaccgg
I113C_F	pRD_0013	70.3°C	acttgatTGCtttaggtttgctcttcgttttatac
I113C_R	pRD_0014	65.1°C	ctaaaGCAatcaagtatcgtgtaataggtaaac
F114C_F	pRD _0069	68.4°C	tgatataTGCaggtttgctcttcgttttatac
F114C_R	pRD_0070	65.8°C	aacctGCAtatatcaagtatcgtgtaataggt
R115C_F	pRD_0071	63.2°C	tatatttTGCtttgctcttcgttttatac
R115C_R	pRD_0072	65.7°C	gcaaaGCAaaatatatcaagtatcgtgtaatag
F116C_F	pRD_0015	76.6°C	atttaggTGCgctcttcgttttatacggcctga
F116C_R	pRD _0016	68.7°C	agagcGCAcctaaatatatcaagtatcgtgtaa
A117C_F	pRD_0091	73.3°C	taggtttTGTcttcgttttatacggcctgacc
A117C_R	pRD_0092	67.2°C	cgaagACAaaacctaaatatatcaagtatcgtg

L118C_F	pRD_0075	76.4°C	gtttgctTGCcgttttatacggcctgacc
L118C_R	pRD_0076	68.8°C	aaacgGCAagcaaacctaaatatatcaagtatc
R119C_F	pRD_0017	75.3°C	tgctcttTGCtttatacggcctgaccctc
R119C_R	pRD_0018	64.9°C	ataaaGCAaagagcaaacctaaatatatcaag
F120C_F	pRD_0077	81.1°C	tcttcgtTGCatacggcctgaccctcgc
F120C_R	pRD_0078	71.0°C	cgtatGCAacgaagagcaaacctaaatatatca
I121C_F	pRD_0079	84.9°C	tcgttttTGCcggcctgaccctcgcagc
I121C_R	pRD_0080	77.2°C	ggccgGCAaaaacgaagagcaaacct
R122C_F	pRD_0019	79.3°C	ttttataTGCcctgaccctcgcagccgg
R122C_F	pRD_0020	71.3°C	tcaggGCAtataaaacgaagagcaaacc
P123C_F	pRD_0081	83.4°C	tatacggTGCgaccctcgcagccgggtc
P123C_R	pRD_0082	77.3°C	gggtcGCAccgtataaaacgaagagcaaacc
D124C_F	pRD_0083	88.1°C	acggcctTGCcctcgcagccgggtcactg
D124C_R	pRD_0084	79.1°C	cgaggGCAaggccgtataaaacgaagagcaaac
P125C_F	pRD_0085	85.4°C	gcctgacTGCcgcagccgggtcactgac
P125C_R	pRD_0086	80.1°C	ctgcgGCAgtcaggccgtataaaacgaagagc
R126C_F	pRD_0087	84.5°C	tgaccctTGCagccgggtcactgacccc
R126C_R	pRD_0088	79.9°C	cggctGCAagggtcaggccgtataaaacg
S127C_F	pRD_0089	86°C°	ccctcgcTGCcgggtcactgaccccgtt
S127C_R	pRD_0090	82.5°C	acccgGCAgcgagggtcaggccgtat
R128C_F	pRD_0091	87.5°C	tcgcagcTGCgtcactgaccccgttgggg
R128C_R	pRD_0092	84.7°C	gtgacGCAgctgcgagggtcaggccg

4. Results

4.1 Validation of UBXD8$_{53-153}$ localization to the ER and LDs in cells by fluorescence microscopy

To determine how class I LD proteins are embedded in two unique physicochemical membrane environments, namely the ER bilayer and the LD monolayer membranes (Figure 12A), I used UBXD8, a class I LD protein that has previously been demonstrated to reside in both the ER bilayer and LD monolayer membranes (Schrul & Kopito, 2016; Suzuki et al., 2012; Zehmer et al., 2009), as a model substrate. I, in particular, focused on the membrane-embedded region of UBXD8 and planned to precisely dissect the topological positioning of individual amino acids within this region both in ER bilayer and LD monolayer membranes by employing a cysteine solvent-accessibility assay, which relies on generating single cysteine variants of the protein. To this end, I designed a truncated version of UBXD8 that was naturally free of cysteine residues, therefore fulfils the cysteine solvent-accessibility assay criteria, and also lacks the well-characterized cytosol-exposed UBXD8 functional domains. This truncated UBXD8$_{53-153}$ version, which contains the membrane-embedded region, has previously been reported to be sufficient for targeting and insertion into the ER bilayer in a monotopic topology (Figure 12B) (Schrul & Kopito, 2016). The UBXD8$_{53-153}$ contains the hydrophobic region stretching from amino acids (91-111), which is suggested to be the membrane-embedded hairpin region of UBXD8, along with flanking regions, and is required for insertion into the ER bilayer membrane (Schrul & Kopito, 2016; Suzuki et al., 2012).

The prime goal is to assess the solvent-accessibility of individual amino acids positioned within the membrane-embedded region of UBXD8$_{53-153}$ both in ER bilayer and LD monolayer membranes. Beforehand, the truncated version of UBXD8 needs to fulfill certain criteria, one of which is that it must correctly insert into the ER adopting a monotopic topology. To verify that, an opsin-tag encoding a consensus N-glycosylation site was appended to the N-terminus of UBXD8$_{53-153}$, which upon translocation into the ER lumen undergoes glycosylation, resulting in a ~2 kDa shift in the molecular weight (Schrul & Kopito, 2016). Hence, the lack of glycosylation can be used as a readout that op-UBXD8$_{53-153}$-mCherry has been accurately inserted into the ER membrane in a monotopic orientation. To monitor the correct subcellular localization of UBXD8$_{53-153}$ to ER and LDs in cells by live microscopy, I fused mCherry

to the C-terminus of op-UBXD8$_{53-153}$. When transiently expressed in cells treated with oleate to induce LD biogenesis, the op-UBXD8$_{53-153}$-mCherry unveiled a distinctive reticular network-like pattern (pseudocolored in green) dispersed throughout the cytoplasm confirming its localization to the ER (Figure 12B). In addition, the localization of op-UBXD8$_{53-153}$-mCherry around LDs in the form of ring-like structures was confirmed by staining them with HCS LipidTOX green neutral lipid dye (Figure 12B). Taken together, these results suggest that op-UBXD8$_{53-153}$-mCherry localizes to the ER and LDs in cells.

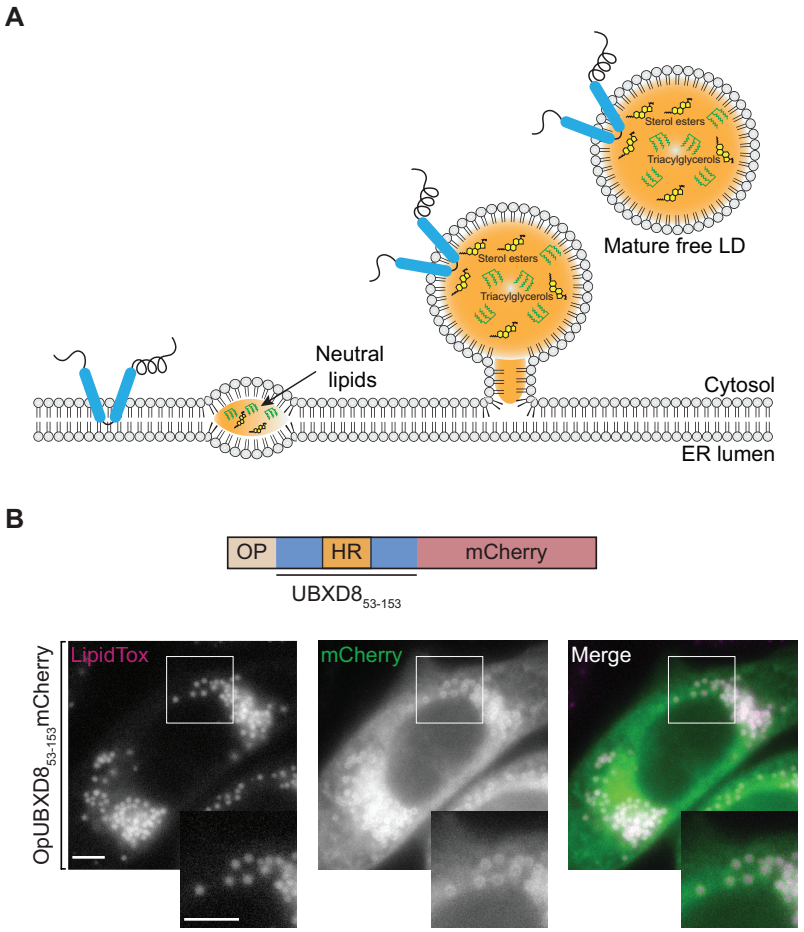

Figure 12: Validation of UBXD8$_{53-153}$ localization to the ER and LDs in cells by fluorescence microscopy.

(A) Schematic illustrating the LD biogenesis from the ER, and class I monotopic proteins residing in the ER and LDs adopting a hairpin topology.

(B) Top: Schematic representation of mammalian UBXD8$_{53-153}$ (amino acids, 53-153), including the hydrophobic region (indicated in orange) with an opsin-tag on the N-terminus and mCherry on C-terminus. Bottom: Live cell imaging of HeLa Kyoto cells expressing opsin- and mCherry-tagged

UBXD8$_{53-153}$ (pseudocolored in green) after overnight oleate treatment. LDs were stained with HCS LipidTOX green (pseudocolored in magenta). Scale bar: 10 µm.

4.2 Establishment of subcellular LD fractionation for assessment of membrane-embedded region of UBXD8$_{53-153}$ in LD monolayer membranes

In order to investigate the topological positioning of amino acids within the membrane-embedded region of op-UBXD8$_{53-153}$-mCherry by cysteine solvent-accessibility assay, I employed biochemical subcellular fractionation to isolate LDs containing op-UBXD8$_{53-153}$-mCherry from cells. To this end, op-UBXD8$_{53-153}$-mCherry was transiently expressed in cells and LD biogenesis was induced by oleate treatment. The oleate treated cells were mechanically disrupted and centrifuged to pellet down the cell debris and nuclei. The resulting post-nuclear supernatant (PNS) was subsequently fractionated using sucrose density gradient centrifugation into membranes, cytosol, and LD fractions. Because LDs are buoyant, they float as a fat layer on top of the gradient, whereas membranes will pellet down at the bottom (Figure 13A). Individual fractions were assessed by western blotting using antibodies against the marker proteins: α-calnexin for ER, α-tubulin for cytosol and α-mCherry for op-UBXD8$_{53-153}$-mCherry. Non-transfected cells (NT) were used as a control for the specificity of the anti-mCherry antibody. As expected, markers for ER (calnexin), cytosol (tubulin), and the transiently expressed op-UBXD8$_{53-153}$-mCherry were detected in the PNS (lane1, Figure 13B). Tubulin was exclusively detected in the cytosol fraction and calnexin was specifically detected in the membrane fraction (lane2 and lane3, Figure 13B) indicating that the LD fraction (lane 4, Figure 13B) was essentially devoid of contaminations from the cytosol and ER-resident proteins, since no tubulin and calnexin were detected in it. The presence of transiently expressed op-UBXD8$_{53-153}$-mCherry in the membrane and LD fraction was consistent with its expected dual localization to the ER and LDs (lane 2 and 4, Figure 13B). Additionally, a minor pool of op-UBXD8$_{53-153}$-mCherry was also detected in the cytosol fraction. This might be due to the overexpression of op-UBXD8$_{53-153}$-mCherry in cells, which could lead to oversaturation of the protein targeting machinery. Alternatively, this could be due to the disruption of LDs during their isolation, resulting in the release of op-UBXD8$_{53-153}$-mCherry into the cytosol. Overall, the absence of any cytosolic or ER-resident proteins in the LD fraction containing the op-UBXD8$_{53-153}$-mCherry suggests that the isolated LD fraction can be used to precisely evaluate the positioning of amino acids within the membrane-

embedded region of op-UBXD8$_{53-153}$-mCherry in a monolayer membrane environment.

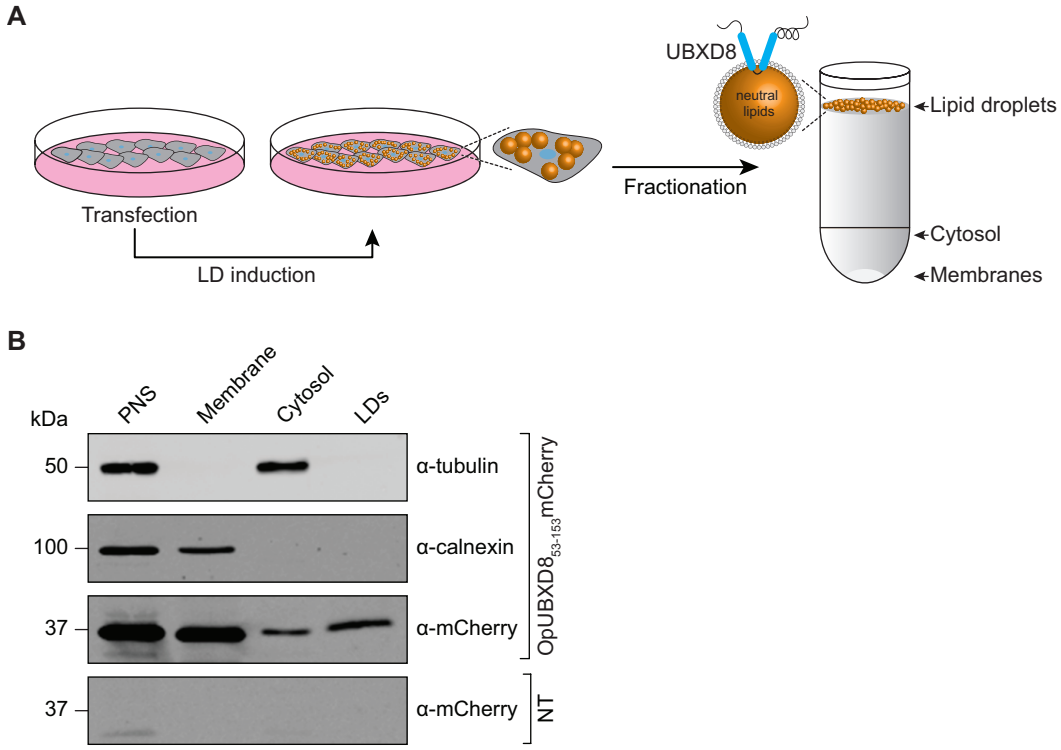

Figure 13: Establishment of subcellular LD fractionation for assessment of membrane-embedded region of UBXD8$_{53-153}$ in LD monolayer membranes.

(A) Schematic outline for isolation of membrane, cytosol, and LD fractions from oleate-treated cells transiently expressing op-UBXD8$_{53-153}$-mCherry. In transfected cells, LD biogenesis was induced by treatment with oleate and subcellular fractions were isolated from cells by sucrose density gradient centrifugation.

(B) Immunoblots of post-nuclear supernatant (PNS), membrane, cytosol, and LD fractions as indicated using anti-calnexin (ER-resident protein), anti-tubulin (cytosolic protein), and anti-mCherry antibodies recognizing overexpressed op-UBXD8$_{53-153}$-mCherry. Non-transfected cells (NT) serve as a specificity control for this antibody.

4.3 UBXD8$_{53-153}$ inserts into ER-derived RMs in a monotopic topology

Transient overexpression of op-UBXD8$_{53-153}$-mCherry in cells may result in its mislocalization to other organelles. In addition, the membrane fraction isolated from cells by density gradient centrifugation includes membranes from multiple organelles and not solely the ER. As a result, mistargeted op-UBXD8$_{53-153}$-mCherry to other organelles would be collected alongside the ER bilayer membranes. In order to exclusively discern the topology of correctly embedded op-UBXD8$_{53-153}$-mCherry into

the ER bilayer membranes, I employed an *in vitro* translation system in which newly *in vitro* translated op-UBXD8$_{53-153}$-mCherry in rabbit reticulocyte lysate (RRL) was inserted into ER-derived RMs. Previous studies have verified that *in vitro* translated full length UBXD8 is inserted into RMs in its correct hairpin topology (Schrul & Kopito, 2016). In order to ascertain whether mCherry-tagged UBXD8$_{53-153}$ is also correctly inserted into RMs, the opsin tag was either fused to the N- or the C-terminus of the protein. Glycosylation of the opsin-tag would indicate an incorrect topology of the protein, as this part would have been translocated across the ER membrane and exposed to the ER lumen. Hence, upon correct membrane integration, an absence of glycosylation is expected for both the N- and C-terminally tagged UBXD8$_{53-153}$-mCherry.

Following *in vitro* translation of these proteins and insertion into RMs, reactions were fractionated into soluble (S) and membrane fractions (M) by ultracentrifugation (Figure 14A). When translation was carried out in the presence of RMs without mRNA, no signal was detected in the soluble (S) and membrane fraction (M) confirming the specificity of the anti-mCherry antibody (Figure 14B). When no RMs were added during translation, both op-UBXD8$_{53-153}$-mCherry and UBXD8$_{53-153}$-mCherry-op remained in the soluble fraction (S). It is anticipated that UBXD8 should remain in the soluble fraction (S) in the absence of membranes, unless it aggregates (Figure 14B). When mRNA encoding either op-UBXD8$_{53-153}$-mCherry or UBXD8$_{53-153}$-mCherry-op were translated *in vitro* in the presence of RMs, the majority of the proteins were detected in the membrane fraction (M) indicating that UBXD8 is inserted into RMs (Figure 14B). Overall, the majority of either op-UBXD8$_{53-153}$-mCherry or UBXD8$_{53-153}$-mCherry-op proteins were not glycosylated, indicating their correct insertion into RMs in a monotopic topology, and only a minor fraction of the proteins were glycosylated (Figure 14B, indicated with arrows). After densitometric quantification, the glycosylated fraction was found to be ~2% of the correctly inserted UBXD8$_{53-153}$-mCherry fraction in a monotopic topology. Taken together, these results indicate that ER-derived RMs can be employed to determine the topological positioning of amino acids within the membrane-embedded region of UBXD8$_{53-153}$-mCherry in an ER bilayer environment.

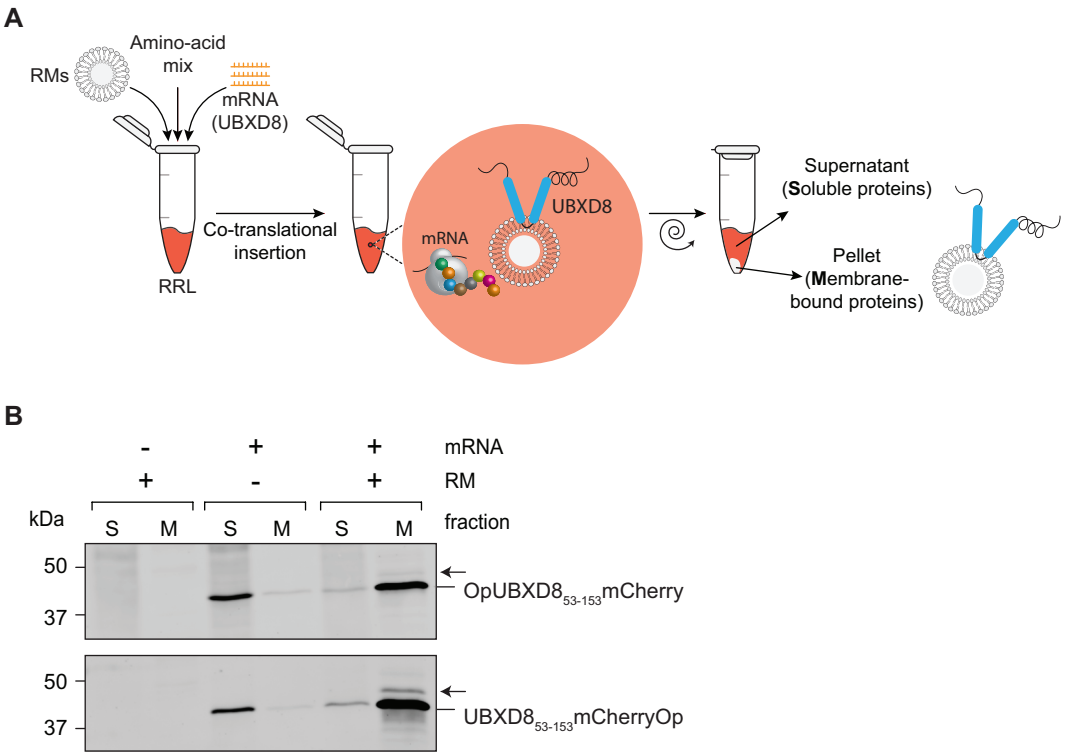

Figure 14: UBXD8$_{53-153}$ inserts into ER-derived RMs in a monotopic topology.

(A) Schematic outline of the *in vitro* translation/RM insertion assay: UBXD8$_{53-153}$ mRNA was translated in rabbit reticulocyte lysate (RRL) where ER-derived RMs were used as sources of ER membrane; following translation, soluble and membrane inserted UBXD8$_{53-153}$ was recovered by centrifugation.

(B) Immunoblots of soluble (S) and membrane inserted (M) fractions of N- or C-terminally opsin-tagged UBXD8$_{53-153}$-mCherry mRNAs translated *in vitro* in the absence and presence of RMs probed using an anti-mCherry antibody. The arrowhead indicates the glycosylated fraction of op-UBXD8$_{53-153}$-mCherry and UBXD8$_{53-153}$-mCherry-op, respectively.

4.4 Establishment of a solvent-accessibility assay to map the membrane-embedded region of the UBXD8$_{53-153}$ in ER-derived RMs by PEGylation

To assess the solvent-accessibility of the membrane-embedded region of op-UBXD8$_{53-153}$-mCherry in the ER phospholipid membrane, a PEGylation assay was established. The PEGylation assay takes advantage of the distinctive side-chain chemistry of the amino acid cysteine and has been widely utilized in the past to monitor the topology of membrane proteins (Bogdanov et al., 2005). The assay employs methoxypolyethylene glycol maleimide (mPEG), a membrane-impermeable probe. In a reducing environment, the maleimide moiety of mPEG reacts covalently with the thiol (-SH) group of exposed cysteine, imparting additional molecular weight to the protein, which can be detected as a shift in protein mobility on SDS-PAGE. The

PEGylation assay methodology relies on: (i) mock-treating the protein sample without mPEG, which will result in no apparent shift in protein's molecular weight after immunoblotting and will serve as a negative control, (ii) treating the protein sample with mPEG, which will only result in labeling of solvent-exposed cysteines and not the membrane-buried cysteines, and (iii) treating the protein sample with Triton-X 100 (TX-100) before subjecting it to mPEG, which will result in labeling of membrane-buried cysteines and indicates the maximal PEGylation possible for a given cysteine residue, therefore serves as a positive control for calculating the relative PEGylation efficiency of individual cysteine residues.

To establish a basis for comparison, I employed the naturally cysteine-free op-UBXD8$_{53\text{-}153}$-mCherry. Through site-directed mutagenesis, a single cysteine mutation (T109C) was introduced in the putatively solvent-exposed domain and one single cysteine (P88C) in the hydrophobic region (HR) of op-UBXD8$_{53\text{-}153}$-mCherry (Figure 15A). To probe the solvent-accessibility in the ER-derived RMs, cysteine-free and single cysteine mutant versions of op-UBXD8$_{53\text{-}153}$-mCherry were cotranslationally inserted into RMs *in vitro* (Figure 15B). In case of a cysteine-free op-UBXD8$_{53\text{-}153}$-mCherry, no labeling by mPEG, and consequently no discernible change in the protein's molecular weight after immunoblotting was observed. For the cysteine-free version an identical band pattern was detected under all three conditions, which was expected since it does not contain a free thiol group that can be modified by mPEG (0 PEG) (Figure 15C). However, cysteine (P88C) was labeled by mPEG, resulting in an apparent shift in the molecular weight of the modified protein (1 PEG), which indicates that cysteine (P88C) is solvent-exposed (Figure 15C). In case of cysteine (T109C), no labelling was observed after mPEG treatment, and it only become accessible after the membranes were solubilized using a detergent like TX-100 (Figure 15C), which indicates that this amino acid residue is buried inside the hydrophobic core of the membrane. These proof-of-concept results indicate that the PEGylation assay is suitable to probe the solvent accessibility of individual amino acid positions of op-UBXD8$_{53\text{-}153}$-mCherry in ER-derived RMs.

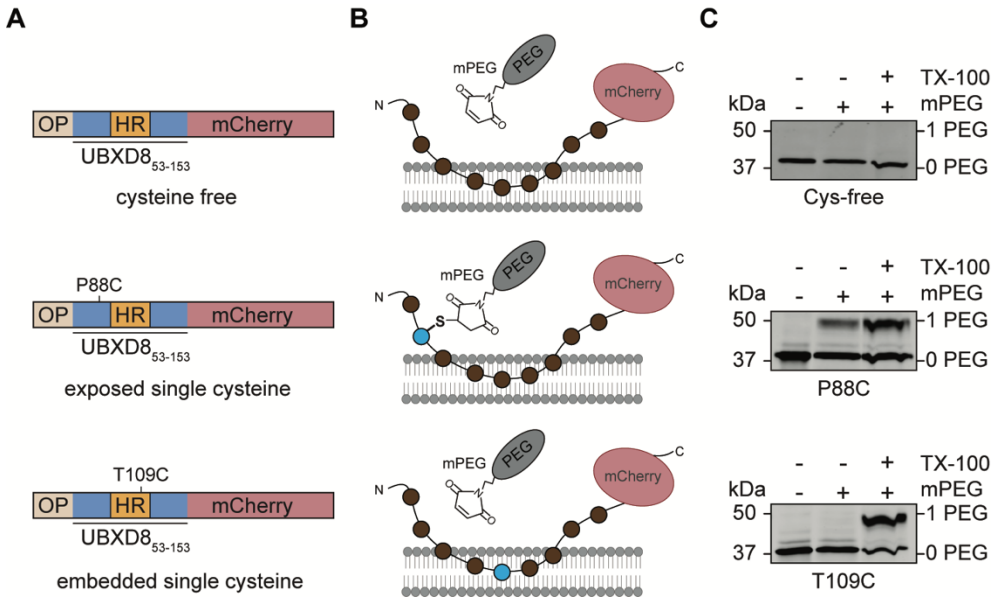

Figure 15: Establishment of a solvent-accessibility assay to map the UBXD8$_{53-153}$ membrane-embedded region in ER-derived RMs by PEGylation.

(A) Schematic illustration of op-UBXD8$_{53-153}$-mCherry fusion constructs without cysteine, with presumably solvent-exposed single cysteine (P88C), and presumably membrane-embedded single cysteine (T109C) as indicated.

(B) Schematic illustration depicting the solvent-accessibility of cysteine-free wild type and individual single-cysteine mutant versions of op-UBXD8$_{53-153}$-mCherry as shown in (A) in ER-derived RMs.

(C) Immunoblots probed with anti-mCherry antibody after PEGylation reaction on RMs-inserted op-UBXD8$_{53-153}$-mCherry variants as depicted in (A). Non-PEGylated protein is indicated by (0 PEG) and singly PEGylated protein by (1 PEG). A positive control was set up by solubilizing RMs containing op-UBXD8$_{53-153}$-mCherry with TX-100 before subjecting them to PEGylation to achieve maximal PEGylation possible for a cysteine residue, and a negative control was carried out without the addition of mPEG. mPEG: methoxypolyethylene glycol maleimide, TX-100: Triton X-100.

4.5 Establishment of a solvent-accessibility assay to map the membrane-embedded region of the UBXD8$_{53-153}$ in LD monolayer membranes by PEGylation

To assess the solvent-accessibility of the op-UBXD8$_{53-153}$-mCherry membrane-embedded domain in LD monolayer membranes, a PEGylation assay was employed. To this end, LDs were isolated by biochemical subcellular fractionation from oleate-treated cells transfected with cysteine-free and the single-cysteine mutants P88C and T109C of op-UBXD8$_{53-53}$-mCherry (Figure 16A and 16B). On LDs, cysteine-free op-UBXD8$_{53-153}$-mCherry displayed no apparent shift in molecular weight following immunoblotting under all three conditions: (i) when no mPEG was added, (ii) when

mPEG was added, and (iii) when LDs were first solubilized with TX-100 before mPEG treatment (Figure 16C). This indicates that the protein does not contain any free thiol group to be labeled by mPEG (0PEG). On LDs, the single cysteine mutant P88C was found to be labeled after mPEG treatment resulting in a mobility shift in protein's molecular weight (1PEG), which indicates that cysteine at position 88 is solvent-exposed (Figure 16C). The single cysteine mutant T109C become accessible for labeling to mPEG only after solubilizing the LDs with TX-100, indicating that T109C is buried inside the hydrophobic core of LDs (Figure 16C). Overall, the PEGylation assay on LDs yielded identical results to the single-cysteine mutants (P88C and T109C) inserted into ER-derived RMs. Taken together, these results indicate that the PEGylation assay can be used effectively to probe the solvent-accessibility of op-UBXD8$_{53-153}$-mCherry in LD monolayer membranes with single amino acid resolution.

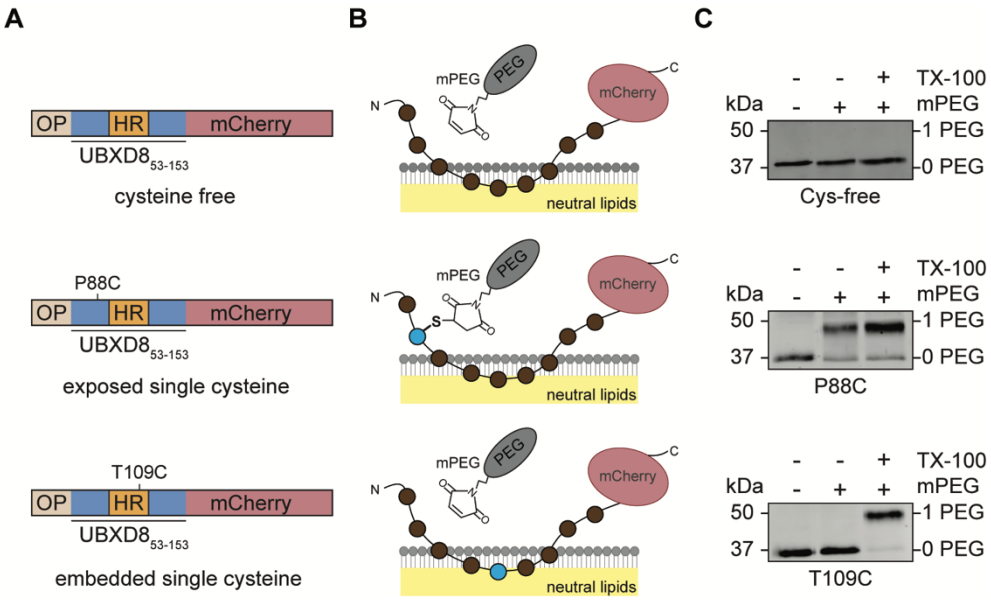

Figure 16: Establishment of a solvent-accessibility assay to map the membrane-embedded region of the UBXD8$_{53-153}$ in LD monolayer membranes by PEGylation.

(A) Schematic illustration of op-UBXD8$_{53-153}$-mCherry fusion constructs with no cysteine, solvent-exposed single cysteine (P88C), and membrane-embedded single cysteine (T109C) as indicated.

(B) Schematic illustration depicting the solvent-accessibility of cysteine-free wild type and individual single-cysteine mutant versions of op-UBXD8$_{53-153}$-mCherry in LD monolayer membranes.

(C) Immunoblots probed with anti-mCherry antibody after PEGylation reaction on LD-inserted op-UBXD8$_{53-153}$-mCherry. Non-PEGylated protein is indicated by (0 PEG) and singly PEGylated protein by (1 PEG). mPEG: methoxypolyethylene glycol maleimide, TX-100: Triton X-100.

4.6 The membrane-embedded region of UBXD8$_{53-153}$ is more solvent-exposed in LD monolayer membranes than in ER bilayer membranes

To obtain a fine-resolution topology map of op-UBXD8$_{53-153}$-mCherry in both the ER bilayer and LD monolayer membranes, I systematically substituted each native amino acid to a cysteine between position 80 and 128 (S_{80}-R_{128}) by site-directed mutagenesis. This library of 48 individual single cysteine mutants were then probed for solvent-accessibility by PEGylation (Figure 17A and Figure 17B).

To probe the topology of op-UBXD8$_{53-153}$-mCherry in ER bilayer membranes by PEGylation assay, the individual single cysteine mutants were *in vitro* translated and inserted into ER-derived RMs (Figure 17B). The topology map of op-UBXD8$_{53-153}$-mCherry in the ER bilayer suggested a monotopic hairpin topology. Specifically, amino acids (S_{80}-R_{89}) at the N-terminus and amino acids (D_{124}-R_{128}) at the C-terminus were found to be fully solvent-exposed, with a membrane-embedded region located between N- and C-termini. Furthermore, this was indicated by a relatively high PEGylation efficiency and low hydrophobicity values obtained from the helical wheel projections of these segments, whereas for the membrane-embedded region a high hydrophobicity value of 1.102 was obtained (Figure 17C and 17D). The membrane-embedded region was found to be consisted of amino acids (W_{94}-R_{122}), as they exhibited minimal reactivity with mPEG. Amino acids (G_{90}-G_{93}) located upstream of membrane-embedded region (W_{94}-R_{122}) exhibited partial exposure to the solvent, as indicated by their varying reactivity with mPEG. Additionally, arginines at positions R115, R119, and R122 were observed to be partially solvent-exposed, as they showed minimal PEGylation upon reaction with mPEG. The periodical pattern of every third to fourth amino acid in this region being more solvent-exposed indicates an amphipathic segment at the membrane-solvent interface in the hinge region followed by a fully solvent-exposed C-terminus (Figure 17C). Additionally, the helical wheel projection of the sequence stretching from amino acid residue I110 to S127 including the polar arginines (R115, R119, R122) showed a clear enrichment of polar and non-polar amino acid residues on either side of the helix with a hydrophobic moment (an indicator of α-helix amphiphilicity) of 0.483 *μH*, further supporting the amphipathic nature of this C-terminally located segment of op-UBXD8$_{53-153}$-mCherry (Figure 17D). The positioning of an amino acid within the hydrophobic membrane core determines whether it could be efficiently labeled by mPEG after detergent solubilization (Bogdanov et al., 2010; Ruan et al., 2018). We noted that the proline at position 102

substituted to a cysteine (P102C) and amino acid residues (G90C, I113C, and F114C) could not be labeled with mPEG after solubilizing the membranes with TX-100 (Figure 17B). I also carried out PEGylation on cysteine at position 102 (P102C) after solubilizing the membranes with different concentrations of SDS, which is an anionic detergent with stronger denaturing and solubilizing properties than TX-100. However, even after solubilizing the membranes with SDS, no modification by mPEG could be detected (Figure 17E). The absence of labeling in the presence of either TX-100 or SDS suggests that the cysteine at position 102 is located in a region where op-UBXD8$_{53-153}$-mCherry secondary structure arrangement restricts the accessibility of mPEG, a phenomenon that has also been previously observed (Pataki et al., 2018). According to the PEGylation results, op-UBXD8$_{53-153}$-mCherry adopts a monotopic topology in the ER bilayer membrane and has a longer membrane-embedded region than predicted by topology prediction algorithms.

In order to investigate the topology of op-UBXD8$_{53-153}$-mCherry membrane-embedded region in LD monolayer membranes, I expressed individual cysteine mutants in cells followed by the induction of LDs with oleate supplementation. LDs were then isolated from the cells by biochemical subcellular fractionation and subjected to PEGylation to probe the solvent accessibility of individual amino acid positions in op-UBXD8$_{53-153}$-mCherry in LD monolayer membranes. In both the LD monolayer and ER bilayer membranes, the N- and C-termini of the op-UBXD8$_{53-153}$-mCherry and partially solvent-exposed membrane interface regions, displayed a comparatively similar degree of labeling to mPEG after PEGylation. This indicates that op-UBXD8$_{53-153}$-mCherry adopts an overall similar topology in both the ER bilayer and LD monolayer membranes (Figure 17B and 17C). However, the major difference was observed in the membrane-embedded region (W_{94}-R_{122}) which was found to be more solvent-exposed in LD monolayer than in the ER bilayer, indicating that membrane environment can induce major changes in the positioning of amino acid residues. Interestingly, every third to fourth amino acid in the membrane-embedded region was partially solvent-exposed in a periodic pattern, which suggests an α-helical structure positioned close to the membrane-solvent interface on the LD monolayer (Figure 17B and 17C). Overall, the PEGylation assay results support a hairpin topology model for op-UBXD8$_{53-153}$-mCherry in the ER bilayer and LD monolayer membranes, while the membrane-embedded region was found to be more solvent-exposed in the LD monolayer membrane. Based on our PEGylation data, it could also be conceivable

that there is one single long helix which is slightly more deeply embedded within the ER compared to LDs.

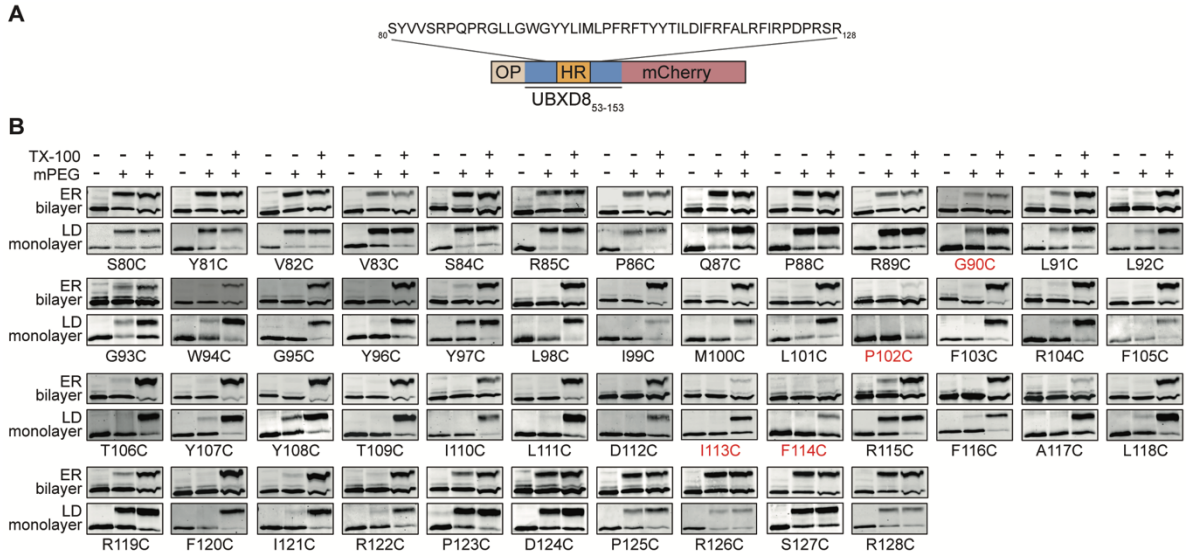
A
80SYVVSRPQPRGLLGWGYYLIMLPFRFTYYTILDIFRFALRFIRPDPRSR128
OP
HR
mCherry
UBXD8 53-153
B
TX-100
mPEG
ER bilayer
LD monolayer
S80C Y81C V82C V83C S84C R85C P86C Q87C P88C R89C G90C L91C L92C
G93C W94C G95C Y96C Y97C L98C I99C M100C L101C P102C F103C R104C F105C
T106C Y107C Y108C T109C I110C L111C D112C I113C F114C R115C F116C A117C L118C
R119C F120C I121C R122C P123C D124C P125C R126C S127C R128C

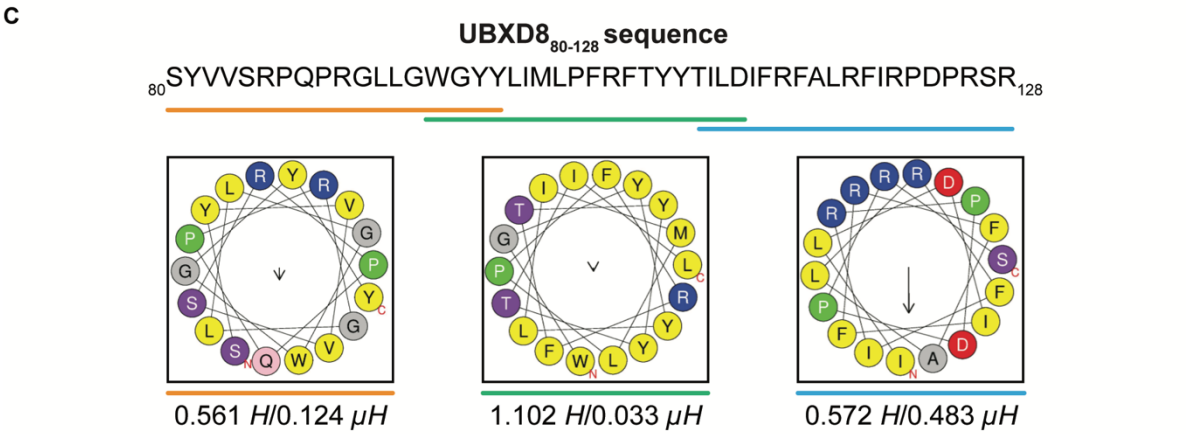
C
UBXD8 80-128 sequence
80SYVVSRPQPRGLLGWGYYLIMLPFRFTYYTILDIFRFALRFIRPDPRSR128
0.561 H/0.124 μH
1.102 H/0.033 μH
0.572 H/0.483 μH

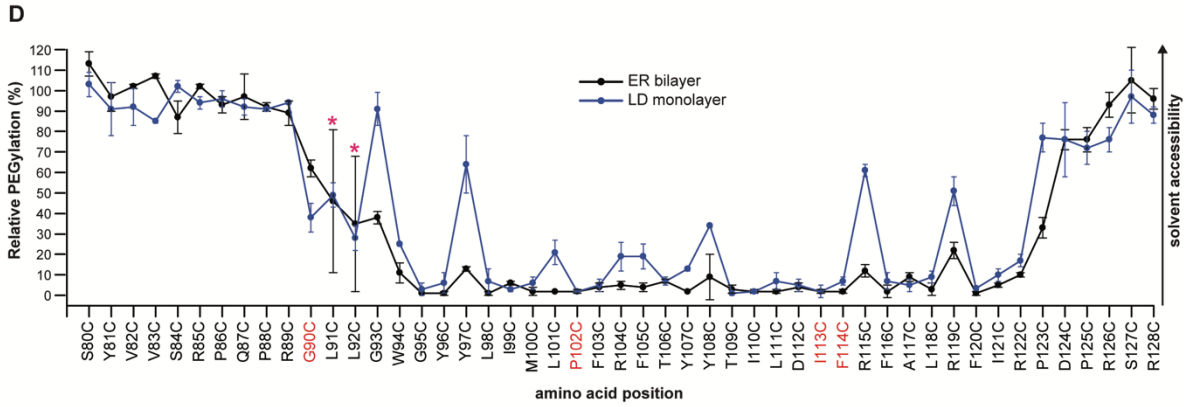
D
Relative PEGylation (%)
ER bilayer
LD monolayer
solvent accessibility
amino acid position
S80C Y81C V82C V83C S84C R85C P86C Q87C P88C R89C G90C L91C L92C G93C W94C G95C Y96C Y97C L98C I99C M100C L101C P102C F103C R104C F105C T106C Y107C Y108C T109C I110C L111C D112C I113C F114C R115C F116C A117C L118C R119C F120C I121C R122C P123C D124C P125C R126C S127C R128C

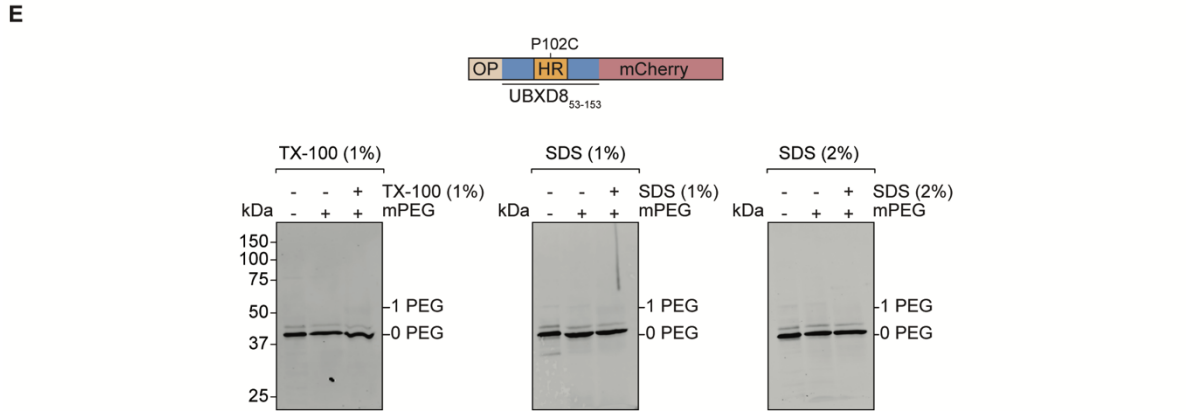
E
P102C
OP
HR
mCherry
UBXD8 53-153
TX-100 (1%)
SDS (1%)
SDS (2%)
kDa
mPEG
150
100
75
50
37
25
1 PEG
0 PEG

Figure 17: Topological mapping of op-UBXD8$_{53-153}$-mCherry membrane-embedded region in ER bilayer and LD monolayer membranes by PEGylation.

(A) Schematic outline of op-UBXD8$_{53-153}$-mCherry with opsin-tag on N-terminus and mCherry on C-terminus. Single cysteine mutations were introduced into the region covering the amino acid sequence (S_{80}-R_{128}), which also includes the hydrophobic region (shown in orange), and PEGylation was employed to test the solvent-accessibility of the mutant cysteines.

(B) Immunoblots showing the PEGylation data for the op-UBXD8$_{53-153}$-mCherry single cysteine mutants (S_{80C}-R_{128C}) probed with anti-mCherry antibody in the ER bilayer and LD monolayer membranes. The blots shown are a representative of two independent experiments. Lane 1: depicts a negative control without the addition of mPEG, lane 2: depicts samples treated with only mPEG, and lane 3: depicts a positive control where samples were solubilized with TX-100 before mPEG treatment.

(C) Line graph showing the relative PEGylation efficiency (%) of op-UBXD8$_{53-153}$-mCherry single cysteine mutants (S_{80C}-R_{128C}). Relative PEGylation (%) of the PEGylated op-UBXD8$_{53-153}$-mCherry (no TX-100 treatment) was calculated in relation to the densitometry intensity of the PEGylated band in the TX-100 treated condition, set to 100%. Error bar for each individual point represents mean +/- standard deviation from n=2 independent experiments. Error bar for L91C and L92C (indicated with asterisks) represents mean +/- standard deviation from n=4 independent experiments. The amino acid residues (G90C, P102C, I113C and F114C; indicated in red) showed minimal PEGylation after solubilization with TX-100 (1%) in comparison to other probed residues.

(D) Helical wheel projections of op-UBXD8$_{53-153}$-mCherry N-terminus (amino acids, 80-97), membrane-embedded region (amino acids, 94-111), and C-terminus (amino acids, 110-127) generated with HeliQuest (http://heliquest.ipmc.cnrs.fr). The calculated hydrophobicity (*H*) and hydrophobic moment (*μH)* for each helical wheel projection is indicated below.

(E) Immunoblots showing no PEGylation for P102C after solubilizing the ER-derived RMs with either TX-100 (1%) and SDS (1% and 2%), respectively.

4.7 Atomistic MD simulations suggest conformational changes in UBXD8$_{80-128}$ membrane-embedded region in bilayer and monolayer membranes

The solvent-accessibility assay revealed that op-UBXD8$_{53-153}$-mCherry is more solvent-exposed on the LD monolayer than in the ER bilayer. This assay, however, reveals rather binary results of whether an amino acid is accessible to PEGylation or not. It is unable to probe how deep a particular amino acid is embedded into the membrane, and it also fails to convey any information about the conformation of the membrane-embedded region within the membrane. In order to gain insight into the intramembrane positioning of the membrane-embedded amino acids, we collaborated with the laboratory of Prof. Jochen Hub (Theoretical Physics, UdS Saarbrücken, Germany), who employed MD simulations to obtain insight into the depth and orientation of the membrane-embedded region of UBXD8$_{80-128}$ within bilayer and

monolayer membranes. All MD simulation experiments were performed by Dr. Chetan Poojari in the Hub lab and the respective data were kindly provided to discuss them in the scope of this thesis work.

Currently, there is no crystal structure available for the UBXD8 membrane-embedded region. Therefore, the $UBXD8_{80\text{-}128}$ structure was predicted using the *ab initio* structure prediction tool QUARK (Xu & Zhang, 2012, 2013), specifically focusing on the membrane-embedded region. The predicted structure revealed a monotopic hairpin topology with two anti-parallel α-helices facing each other separated by a kink at position 102 (P102). Additionally, probing of amino acids (S_{80}-R_{128}) employing PEGylation assay revealed a monotopic topology with amino acids (W_{94}-R_{122}) buried inside the membrane. To understand the structure and dynamics of $UBXD_{80\text{-}128}$ in a bilayer membrane environment, it was inserted at different depths in a POPC bilayer simulation system. First, $UBXD8_{80\text{-}128}$ (starting structure) was deeply embedded into a 1-palmitoyl-2-oleyl-sn-glycero-phosphocholine (POPC) bilayer, and MD simulations revealed that the peptide remained deeply embedded while adopting a V-shaped monotopic topology (Figure 18A). Interesting characteristics were revealed by the peptide V-shaped monotopic topology, such as the basic amino acid arginine at position 104 (R104), which is positioned adjacent to the kink-inducing amino acid proline at position 102 (P102), snorkels toward the phosphate moieties on the bilayer's lumenal membrane-water interface. This interaction could be essential for maintaining the peptide deeply inserted into the hydrophobic core of the bilayer. The aromatic amino acid tyrosine at position (Y96, Y97, Y106, and Y107), in the opposing α-helices facing each other were positioned in the midplane of the membrane, which is usually considered to be an energetically unfavorable environment for aromatic amino acid residues (MacCallum et al., 2008; Ulmschneider & Sansom, 2001). In addition, the interaction of N- and C-termini located basic amino acid arginine at position (R85, R89, R115, and R119) with phosphate moieties at the cytosolic membrane-solvent interface of the bilayer might be essential for anchoring the peptide and maintenance of a monotopic topology (Figure 18A).

In comparison, when $UBXD8_{80\text{-}128}$ (starting structure) was only partially inserted into the bilayer simulation system, the peptide arrangement differed noticeably from that of its deeply embedded state. In this scenario, the $UBXD8_{80\text{-}128}$ peptide adopted an open and shallower V-shaped conformation along the membrane-solvent interface, resulting in a larger distance between the opposing α-helices (Figure 18B). This switch

in UBXD8$_{80\text{-}128}$ peptide conformation was accompanied by a change in the tilt angle of the peptide. The tilt angle changed from ~80° measured for the deeply embedded V-state to ~20° measured for the shallower V-shaped with respect to the membrane normal. Furthermore, the arginine at position 104 (R104) was flipped and snorkeled toward phospho-headgroups on the opposing bilayer leaflet, possibly anchoring the peptide there. Taken together, the atomistic MD simulations revealed that UBXD8$_{80\text{-}128}$ can in principle adopt two different conformations in a bilayer environment. However, the deep-V insertion would be most consistent with the solvent-accessibility assay (Figure 18B and 18C), which indicate that the amino acids (W_{94}-R_{122}) are completely membrane-embedded in the bilayer.

In order to investigate the UBXD8$_{80\text{-}128}$ structure and dynamics in an LD physicochemical environment, neutral lipids (triolein and cholesteryl oleate) were arranged between a flat bilayer to form a lipid trilayer arrangement to simulate the monolayer-surrounded LD. In these LD monolayer MD simulations, UBXD8$_{80\text{-}128}$ adopted an open and shallower conformation (Figure 18C), and within 1μs of simulation run the proline at position 102 (P102) orientated towards the monolayer membrane-solvent interface from its initial deeply inserted state (Figure 18C and 18E). The positioning of UBXD8$_{80\text{-}128}$ in LD monolayer was found to be very similar to the bilayer simulations in which the peptide was only partially inserted into the POPC bilayer (Figure 18B). As a result, it is possible that UBXD8$_{80\text{-}128}$ adopts an open and shallower conformation in both bilayer and monolayer membranes. However, the comparison of the calculated average insertion depth (which is the distance of the center of mass of individual amino acid residues (Cα atom) of a protein relative to the membrane plane) of UBXD8$_{80\text{-}128}$ individual amino acid residues in the bilayer (~2 nm) and monolayer (~1 nm) membranes from MD simulations (Figure 18D and 18E) with our PEGylation data (Figure 18C) supports a deeply inserted V-shaped conformation within the bilayer membranes, and an open and shallower conformation in monolayer membranes. If UBXD8$_{80\text{-}128}$ adopts a deeply embedded V-shaped conformation in the ER bilayer, the hairpin region must undergo structural rearrangement in order to transition from the deeply embedded V-shape to the shallowly inserted open conformation, which might be essential for its partitioning from the ER-to-LDs. Overall, the MD simulations and biochemical solvent-accessibility data suggests that the UBXD8$_{80\text{-}128}$ adopts two distinct conformations in the ER bilayer and LD monolayer membranes.

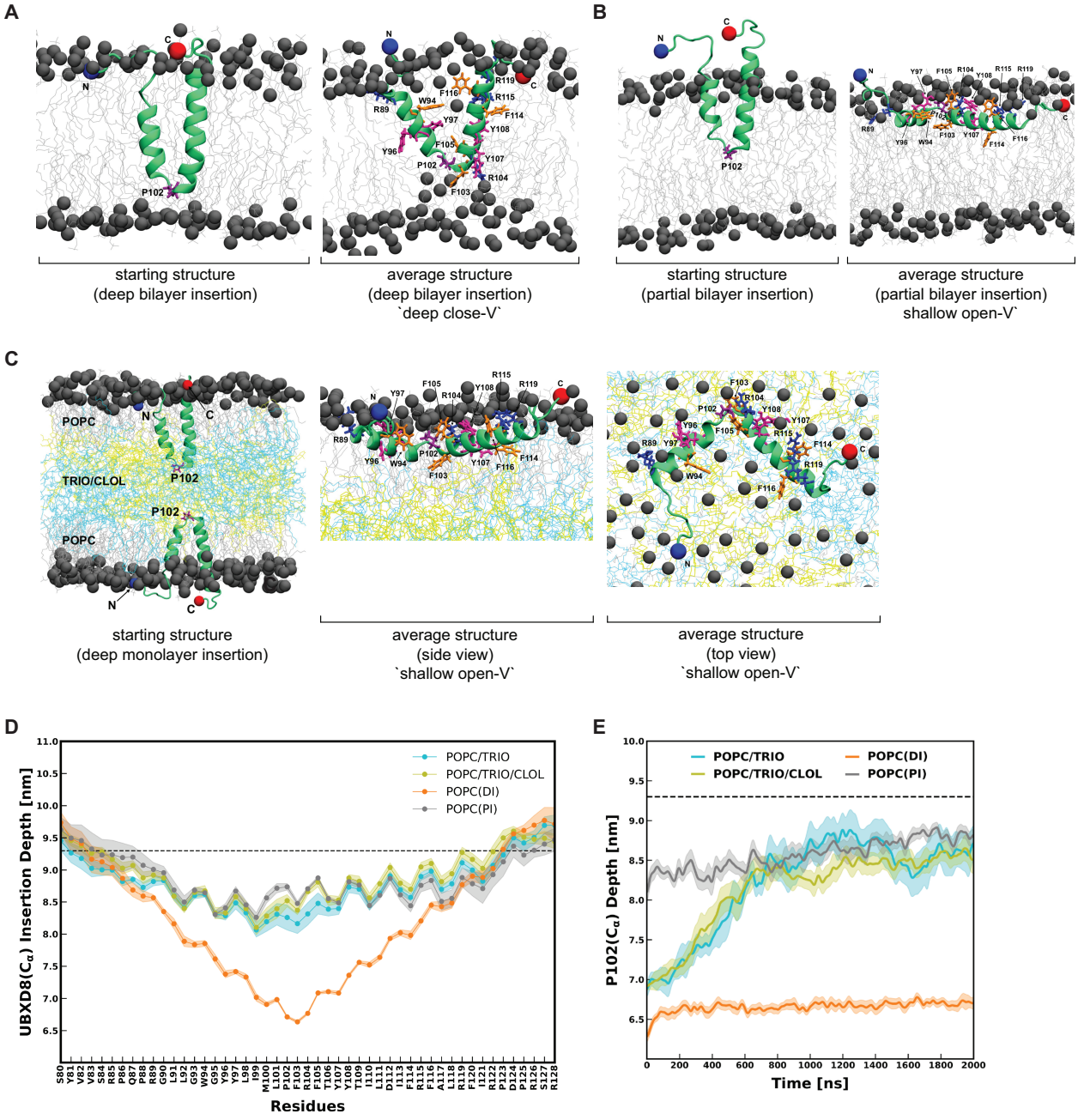

Figure 18: Atomistic MD simulations of UBXD8$_{80\text{-}128}$ membrane-embedded region in bilayer and monolayer membrane (data provided by Dr. Chetan Poojari from the laboratory of Prof. Jochen Hub, Theoretical Physics, Saarland University, Saarbrücken)

(A) UBXD8$_{80\text{-}128}$ atomistic MD simulations with a deeply inserted (DI) starting structure in a POPC bilayer. The average structure (right) was obtained from clustering analysis using last 300 ns of the 2 µs trajectory. Left: Starting structure, POPC: 1-palmitoyl-2-oleyl-sn-glycero-phosphocholine.

(B) UBXD8$_{80\text{-}128}$ atomistic MD simulations with a partially inserted (PI) starting structure in a POPC bilayer. The average structure (right) was obtained from clustering analysis using last 300 ns of the 2 µs trajectory. Left: Starting structure.

(C) Starting (left) and average structure of UBXD8$_{80-128}$ (side and top view; right) in a POPC monolayer for atomistic MD simulations run. The average structure was obtained from clustering analysis using last 300 ns of the 2 µs trajectory. The monolayer is composed of neutral lipids (triolein and cholesteryl oleate) sandwiched between POPC monolayers.
(D) Average membrane insertion depth (center of mass) of individual amino acid residues (Cα atom) of UBXD8$_{80-128}$ relative to the upper phosphate bilayer and monolayer plane (indicated with dotted black line). The insertion depth of UBXD8$_{80-128}$ was ~2 nm in bilayer and ~1 nm in monolayer. The solid lines indicate the average values for each individual amino acid insertion depth in POPC bilayer and monolayer. The shadows represent the standard deviation from n=5 independent MD simulations, each with a run time of 2 µs.
(E) Comparison of the average membrane insertion depth (center of mass) of P102 (Cα atom) relative to the upper phosphate bilayer and monolayer plane (indicated with dotted black line). The solid lines indicate the average values, and the shadows represent the standard deviation from n=5 independent MD simulations, each with a run time of 2 µs.

4.8 Intramolecular crosslinking supports structural rearrangement of membrane-embedded UBXD8$_{53-153}$ hairpin region during ER-to-LD partitioning

The MD simulations revealed that the membrane-embedded region of UBXD8$_{80-128}$ adopts a deeply inserted V-shaped conformation within the bilayer membrane, and an open and shallower conformation in a LD monolayer membrane. Using MD simulations, the average distance between the center of mass (Cα atom) of L91 and L118 located on the opposing α-helices of UBXD8 (Figure 19A) was found to be ~2 nm in the bilayer and ~3.5 nm in the monolayer (Figure 19B). To experimentally verify this change in the distance between the two anti-parallel α-helices of op-UBXD8$_{53-153}$-mCherry within the ER bilayer and LD monolayer membranes, an intramolecular crosslinking assay was implemented. If op-UBXD8$_{53-153}$-mCherry has a restricted V-shaped conformation within the ER bilayer, the amino acids at positions L91 and L118 should be available for intramolecular crosslinking. However, given the op-UBXD8$_{53-153}$-mCherry open and shallower conformation in the LD monolayer, they should be resistant to intramolecular crosslinking.

To perform intramolecular crosslinking, amino acid at positions L91 and L118 were substituted with cysteines *via* site-directed mutagenesis. Subsequently, the double-cysteine mutant (op-UBXD8$_{53-153_L91C_L118C}$-mCherry) was *in vitro* translated and inserted into ER-derived RMs. Additionally, the double-cysteine mutant was expressed in cells, followed by LDs induction and isolation. To assess intramolecular

crosslinking within ER bilayer and LD monolayer membranes the double-cysteine mutant was subjected to a homo-bifunctional, membrane-permeable maleimide crosslinker bismaleimidohexane (BMH) with a spacer-length of ~13Å (Figure 20C). The separation and detection of intramolecular crosslinked adducts on SDS-PAGE is difficult. To circumvent this, intramolecular crosslinking was combined with PEGylation approach. If there is no crosslinking, both cysteines will be free to react with mPEG upon solubilizing the membranes with a detergent, resulting in protein species that are PEGylated twice. However, if intramolecular crosslinking occurs, neither of the cysteines will be available for PEGylation later (Figure 19C). The ER-derived RMs containing *in vitro* translated op-UBXD8$_{53\text{-}153_L91C_L118C}$-mCherry reacted with mPEG, yielding a protein fraction that was PEGylated twice (Figure 19D, left blot, lane 1). This demonstrates that after solubilizing the membranes with Triton X-100, the cysteines are accessible to mPEG. When the crosslinker was added, there was significantly less PEGylation and an increase in the non-PEGylated (0PEG) protein fraction (Figure 19D, left blot, lane 2). This clearly shows that the cysteines at position L91C and L118C in the ER bilayer are in close proximity to each other and are therefore amenable to crosslinking with a ~13Å spacer-length crosslinker. Furthermore, this aligns with a V-shaped arrangement and excludes the presence of one single long helix buried deeply within the bilayer.

In the LD monolayer membranes, the cysteines at position L91C and L118C also underwent PEGylation in the absence of crosslinker (Figure 19D, right blot, lane 1). However, when the crosslinker was added, the doubly PEGylated protein fraction reduced while there was no increase in the non-PEGylated (0PEG) protein fraction (Figure 19D, right blot, lane 2). Instead, we detected high molecular weight crosslinked adducts that are mostly likely intermolecular crosslinked adducts of op-UBXD8$_{53\text{-}153_L91C_L118C}$-mCherry with other proteins on the isolated LDs (Figure 19D, right blot, lane 2). Densitometric analysis of the non-PEGylated (0PEG) protein fraction revealed that the relative intramolecular cysteine crosslinking on LD monolayer membranes was nearly 50% lower than on RMs (Figure 19E). When considered collectively, our results demonstrate that op-UBXD8$_{53\text{-}153_L91C_L118C}$-mCherry adopts an open conformation in LD monolayer membranes as opposed to a constricted V-shaped conformation in ER bilayer membranes.

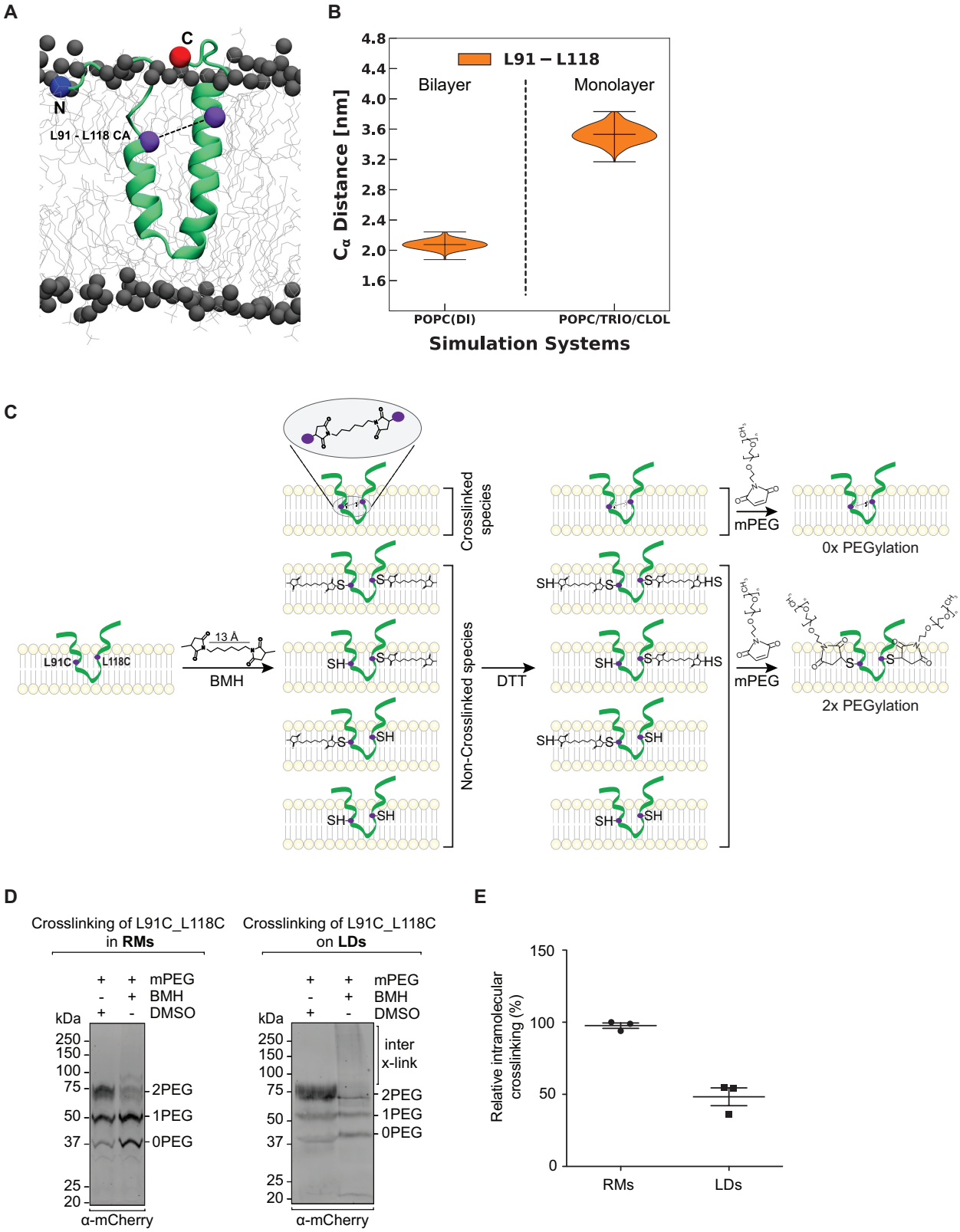

Figure 19: Intramolecular crosslinking suggests structural rearrangement of the membrane-embedded UBXD8$_{53-153}$ hairpin region during ER-to-LD partitioning.

(A) Atomistic starting structure of UBXD8$_{80-128}$, indicating that amino acids at positions L91 and L118 (linked by a black dotted line) were replaced with cysteine in op-UBXD8$_{53-153_L91C_L118C}$-mCherry. Image provided by Dr. Chetan Poojari.
(B) Violin-plots depicting the computed average distance between the Cα atom of L91 and L118 residues in POPC bilayer (DI: deeply inserted) and monolayer membrane (TRIO: triolein and CLOL: cholesteryl oleate) MD simulation systems, respectively.
(C) Schematic outline of the intramolecular cysteine crosslinking and PEGylation approach. A homo-bifunctional, membrane-permeable maleimide crosslinker (BMH, ~13Å spacer-length) was used to crosslink the (op-UBXD8$_{53-153_L91C_L118C}$-mCherry) in bilayer and monolayer membranes, resulting in a combination of crosslinked and non-crosslinked species. The DTT treatment will add a thiol group (-SH) to all the non-crosslinked species. The non-crosslinked species will be PEGylated (indicated with 1 PEG and 2 PEG) after treatment with mPEG (~5 kDa), leaving the BMH crosslinked op-UBXD8$_{53-153_L91C_L118C}$-mCherry fraction at 0 PEG.
(D) Representative immunoblots from three independent experiments showing BMH crosslinked and PEGylated op-UBXD8$_{53-153_L91C_L118C}$-mCherry in ER-derived RMs (left blot) and LDs isolated from cells (right blot), probed with anti-mCherry antibody. The non-PEGylated (0PEG), singly PEGylated (1PEG), and doubly PEGylated protein fractions are indicated on the right side of each blot. High molecular weight crosslinked adducts of op-UBXD8$_{53-153_L91C_L118C}$-mCherry are indicated with (inter x-link) on LD monolayer membranes (right blot).
(E) Scatter plot showing the intramolecular crosslinking (%) on LDs relative to the RMs as assessed by densitometry. From RMs and LDs immunoblots (Figure 19D), the non-PEGylated and crosslinked protein fraction (0PEG) of op-UBXD8$_{53-153_L91C_L118C}$-mCherry was quantified from lane 1 (negative DMSO control) and lane 2 (BMH-treated). The intramolecular crosslinking values on RMs and LDs (lane 2, BMH-treated) were calculated relative to the non-PEGylated band (0 PEG) in the DMSO control, set to 100%. To compare the efficiency of intramolecular crosslinking in RMs to LDs, the calculated crosslinking values on LDs were normalized to the highest crosslinking value in RMs, set to 100%. Data are presented as mean +/- standard deviation from n=3 independent experiments and data points represent individual replicates.

4.9 Systematic mutational screening to identify key amino acids required for UBXD8$_{53-153}$ ER-to-LD partitioning in living cells

The PEGylation and MD simulations data revealed key amino acids located in the hydrophobic and flanking regions of op-UBXD8$_{53-153}$-mCherry, which might play a crucial role in controlling the targeting of op-UBXD8$_{53-153}$-mCherry to the ER and later its partitioning to the LDs. For example, a central proline (P102) positioned within the kink region close to arginine (R104) between the two antiparallel α-helices of op-UBXD8$_{53-153}$-mCherry could be important for maintaining a monotopic hairpin topology. The twin tyrosine pair located in the mid-plane of the bilayer and stretch of

arginines on the N- and C-termini of op-UBXD8$_{53-153}$-mCherry might play a crucial in controlling both op-UBXD8$_{53-153}$-mCherry topology and its partitioning to the LDs.

To test the influence of these amino acids on the configuration of op-UBXD8$_{53-153}$-mCherry, which could either facilitate or impede its partitioning from the ER-to-LDs. The individual residues (indicated by different colors) were mutated either to a leucine or alanine (Figure 20A). Alanine, an aliphatic amino acid with a non-reactive methyl chain, aids in assessing the influence of a certain amino acid residue's side chain on protein structure and function without affecting the protein's secondary alpha-helical structure (Lefevre et al., 1997). Leucine, on the other hand, is a hydrophobic amino acid that is commonly present in the core of transmembrane-spanning proteins, and its side chain interaction within the bilayer membrane hydrophobic core stabilizes protein structure (Hikita & Mizushima, 1992). The mutant constructs with C-terminally tagged mCherry were transiently expressed in cells and LD biogenesis was induced by feeding the cells with oleate. The LDs loaded cells expressing mutant constructs were analyzed for their localization to the ER and LDs by live cell fluorescence microscopy (Figure 20B).

The UBXD8 membrane-embedded region also contain positively-charged and bulky aromatic amino acids. To assess the importance of two conserved tyrosine pairs that are positioned next to each other on two opposing op-UBXD8$_{53-153}$-mCherry helices in the mid-plane of the bilayer, each tyrosine was mutated to an alanine (4Y-4A) or leucine (4Y-4L), respectively. In cells, expression of these mutant constructs resulted in an overall increase in the numbers of LDs and an increased accumulation of the protein on LDs was observed compared to the wild type op-UBXD8$_{53-153}$-mCherry (Figure 20B, panel 1, panel 2, and 3). To determine whether charged residues (arginines) upstream (R85 and R89) and downstream (R115, R119, and R122) of the membrane-embedded region of op-UBXD8$_{53-153}$-mCherry are crucial for ER targeting and later for partitioning to the LDs, the 5R-5A and 5R-5L mutants were expressed in cells. Both these mutants formed punctate structures within the cytosol, which could be attributed to impaired ER targeting, resulting in reduced accumulation on LDs (Figure 20B, panel 4 and 5). However, in comparison to wild type op-UBXD8$_{53-153}$-mCherry, no difference was observed in LD accumulation of arginine mutants.

One of the characteristic features of monotopic hairpin proteins is the presence of the amino acid proline in the center of hydrophobic domain. Proline alone or in combination with other amino acids introduces a kink resulting in a monotopic hairpin

topology (Abell et al., 1997, Huang 1996). In MD simulations, we observed that UBXD8 membrane-embedded hydrophobic hairpin region adopted an open and shallower conformation when integrated into a monolayer compared to its deeply embedded V-shaped conformation in bilayer membrane (Figure 18). Therefore, it might be possible that the interactions between proline and surrounding amino acids within the kink region may dynamically modulate the opening angle, allowing membrane partitioning. Based on studies about AUP1, where it has been observed that mutating the PVG residues located within the kink region to a leucine switches AUP1 topology from monotopic to bitopic, which in turn influenced its accumulation on LDs (Stevanovic & Thiele, 2013), proline at position 102, together with phenylalanine (F103) and arginine (R104), in the kink region of op-UBXD8$_{53-153}$-mCherry was mutated to an alanine (PFR-AAA) and leucine (PFR-LLL), respectively. To investigate whether the PFR motif affects op-UBXD8$_{53-153}$-mCherry ER targeting and partitioning to the LDs, the localization of mCherry-tagged PFR-AAA and PFR-LLL mutants in cells were examined. The PFR mutants formed punctate structures within cells; a phenotype similar to the 5R-5L mutant (Figure 20B, panel 6 and 7). This similarity in phenotype may be due to their compromised ability to target the ER, leading to a reduced accumulation on LDs. Taken together, these preliminary results indicate that mutating amino acids such as proline, tyrosine, and arginine could switch op-UBXD8$_{53-153}$-mCherry configuration from a deep-V to an open and shallower state, which in turn control the accumulation of op-UBXD8$_{53-153}$-mCherry on LDs.

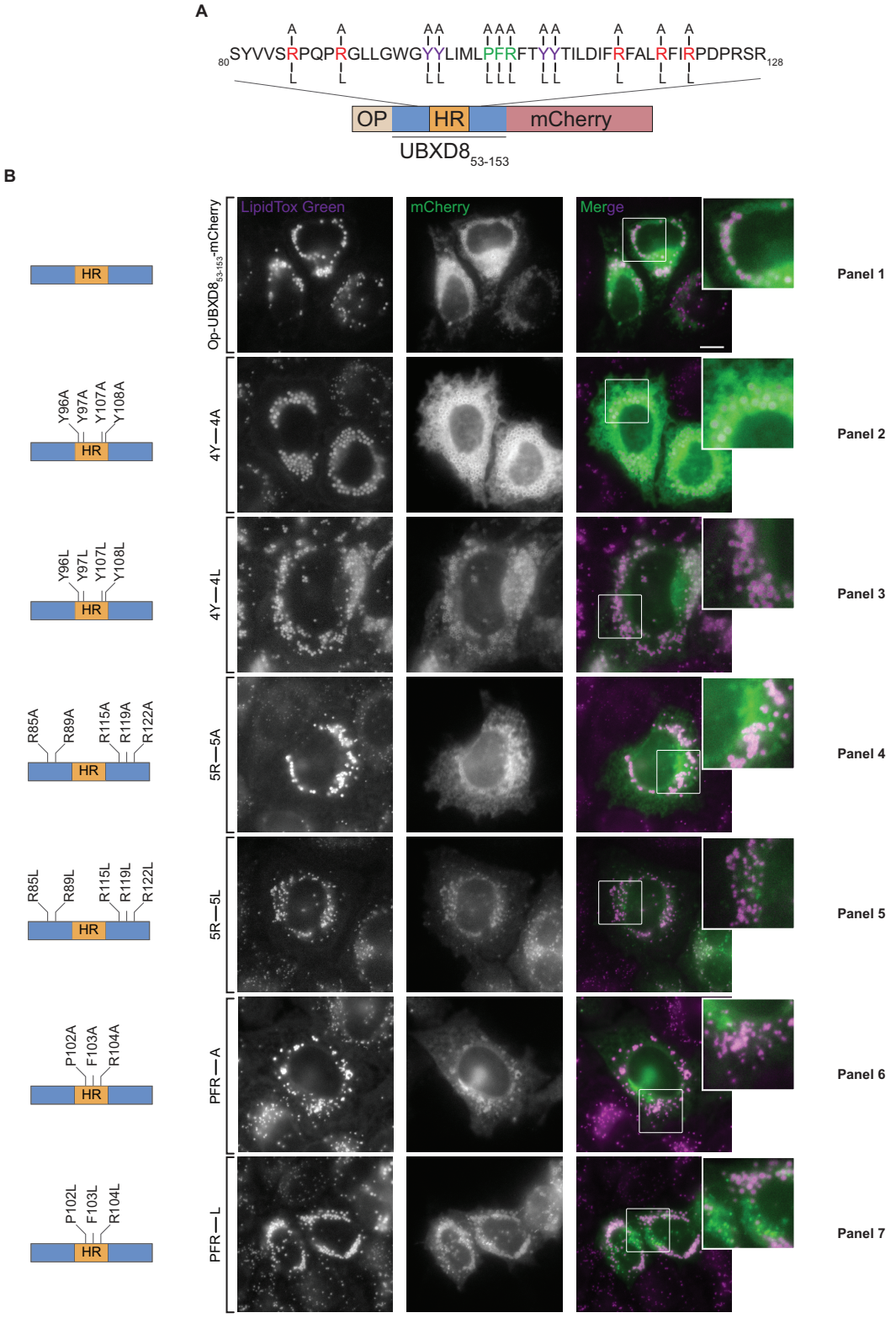

Figure 20: Identifying the key amino acids critical for UBXD8$_{53-153}$ ER-to-LD partitioning in living cells using systematic mutational screening.

(A) Schematic outline of op-UBXD8$_{53-153}$-mCherry with N-terminal opsin-tag and C-terminal mCherry. The region covering the amino acid sequence (S_{80}-R_{128}) including the hydrophobic region (indicated in

orange) showing the amino acids (indicated by different colors) mutated either to an arginine or leucine to generate multiple UBXD8$_{53-153}$ mutants (4Y-4A, 4Y-4L, 5R-5A, 5R-5L, PFR-AAA, and PFR-LLL). **(B)** Live cell imaging of HeLa Kyoto cells transiently expressing opsin and mCherry-tagged UBXD8$_{53-153}$ mutants (pseudocolored in green) after overnight oleate treatment to analyze their cellular localization. LDs were stained with HCS LipidTOX green (pseudocolored in magenta). The schematic of each mutant construct is shown next to the individual micrograph panel. Scale bar: 10 µm.

5. Discussion

LDs are dynamic cytoplasmic organelles consisting of a hydrophobic neutral lipid core surrounded by a phospholipid monolayer instead of a bilayer membrane (Lundquist, 2020; Walther & Farese, 2012). The phospholipid monolayer of LDs harbors a distinct set of proteins (class I and class II), which are acquired from both the ER and cytoplasm (Bersuker & Olzmann, 2017; Dhiman et al., 2020; Olarte et al., 2022). The diverse proteome of LDs enables them to play a central role in crucial cellular processes related to lipid metabolism and energy homeostasis (Ogasawara, 2020; Petan et al., 2018b; Welte, 2015). As a consequence, malfunctioning of LDs is associated with many diseases, such as obesity and its associated metabolic comorbidities (Krahmer et al., 2013; Onal et al., 2017; Zechner, 2015). In order to decipher the role of LDs in metabolic diseases, it is necessary to comprehend the molecular mechanisms and intrinsic structural features that govern the distribution of class I and class II LD proteins between the ER, LDs, and cytosol. While class II LD proteins have been extensively studied in terms of their structural features and targeting mechanisms (Prévost et al., 2018), the mechanisms and structural properties that regulate the targeting of class I LD proteins to the ER and later their partitioning to the LDs are not yet fully understood (Dhiman et al., 2020; Olarte et al., 2022). Currently, there is limited experimental data available on the intramembrane positioning of monotopic hairpin proteins (class I LD proteins) in both the ER bilayer and LD monolayer membranes. This is mainly due to the inability of current topology prediction algorithms, which are designed on the premise that a biological membrane is a phospholipid bilayer. As a consequence, topology prediction by such algorithms often contradicts the experimental findings on monotopic hairpin proteins which adopts distinct conformations in phospholipid bilayer and LD monolayer membranes. Additionally, there is a dearth of structural data on monotopic hairpin proteins for training the prediction algorithms and benchmarking them, which makes it difficult to develop accurate topology prediction algorithms (Ott & Lingappa, 2002; Pataki et al., 2018; von Heijne, 2006).

Currently, it is unclear how deep the membrane-embedded region of class I LD proteins penetrates the ER bilayer and LD monolayer membranes. To gain a comprehensive understanding into the structural arrangement of class I LD proteins membrane-embedded region at the molecular level, I employed UBXD8 as a model

monotopic hairpin protein. From a functional perspective, UBXD8 is one of the best characterized class I LD proteins and there is ample evidence of experimental data on how it is targeted and integrated into the ER bilayer (Schrul & Kopito, 2016). Hence, UBXD8 serves as a useful tool to understand how the membrane-embedded region of monotopic hairpin proteins is structurally defined within the bilayer versus monolayer membranes, and to address which intrinsic sequence elements are important for their partitioning from the ER-to-LDs.

In this study, the biochemical experiments in combination with MD simulations revealed that the membrane-embedded region of UBXD8 adopts distinct conformational states within the ER bilayer and LD monolayer membranes. In the ER bilayer membrane environment, UBXD8 was found to be deeply embedded adopting a V-shaped topology, whereby two opposing α-helices face each other with a kink in the center induced by a proline at position 102 (P102). The deeply embedded state within the bilayer was interpreted to be stabilized by the snorkeling of arginine (R104) towards the lower leaflet phosphate headgroups. In contrast, in the LD monolayer membrane environment, UBXD8 membrane-embedded region was found to be positioned close to the membrane-solvent interface, adopting an open and shallower conformation. Noticeably, the hydrophobic residues such as tyrosines were found to be reoriented from their energetically unfavorable state in the bilayer to a more favorable state in the LD monolayer (Ulmschneider & Sansom, 2001). Furthermore, the arginine at position 104 (R104) repositioned itself towards the LD monolayer-solvent interface. Overall, this study demonstrates that the membrane-embedded region of UBXD8 can adopt distinct topological states depending on the type of membrane environment. Specifically, the membrane-embedded region of UBXD8 adopted a deeply embedded V-shaped conformation within the ER bilayer compared to an open and shallower conformation compatible with the LD monolayer membrane environment.

Prior to this study, the prevailing model in the field was based on the assumption that monotopic hairpin proteins are exclusively embedded into the cytoplasmic leaflet of the ER bilayer membrane. It was believed that this specific intramembrane positioning allowed passive lateral diffusion of monotopic hairpin proteins during ER-to-LD partitioning. However, there was no experimental evidence available to support this model. Based on the findings on UBXD8 and other class I LD proteins (Olarte et al., 2020), the current model on how the monotopic hairpin proteins

are partitioned from the ER-to-LDs can be refined. It is now apparent that these proteins undergo major structural rearrangements during ER-to-LD partitioning, making the partitioning process much more intricate than previously anticipated.

5.1 Limitations of *in silico* topology prediction algorithms for ER/LD-localized membrane proteins

One approach for predicting the topology of monotopic hairpin proteins is to use bioinformatic tools such as TOPCONS (Tsirigos et al., 2015), which use multiple algorithms to identify TMDs within a protein sequence. These tools have been shown to be effective in predicting the topology of many different types of transmembrane proteins, however are limited in predicting the topology of monotopic hairpin proteins. These prediction algorithms use a combination of sequence and structural information to predict transmembrane helices. Additionally, some approaches use machine learning-based methods, such as neural networks, to predict the membrane-embedded regions of monotopic hairpin proteins (Ott & Lingappa, 2002; von Heijne, 2006). It is important to note that the prediction of monotopic hairpin proteins still remains a challenging task and experimental validation is crucial to confirm the predictions. In addition to the challenges mentioned earlier, another limitation of *in silico* tools in predicting the intramembrane positioning of monotopic hairpin proteins is their inability to account for the dynamic nature of these proteins (Allen et al., 2019; Entova et al., 2018). This can make it difficult for *in silico* tools to accurately predict their intramembrane positioning based on a single structure or conformation. These prediction algorithms are primarily based on the premise that a biological membrane is a phospholipid bilayer (Krogh et al., 2001; Tsirigos et al., 2015; Weill et al., 2019). As a consequence, topology prediction by such algorithms often contradicts the experimental findings on monotopic hairpin proteins that reside in both the phospholipid bilayer and LD monolayer membranes, and misclassifies the hydrophobic region of monotopic hairpin proteins as transmembrane helices. These discrepancies among the output of topology prediction algorithms intrigued us to precisely address the intramembrane positioning of the membrane-embedded region of UBXD8, which is often misclassified as transmembrane domain.

5.2 Topological positioning of UBXD8 in ER bilayer membrane: "deep-V" versus "shallow-open" conformation

In this study, we observed that the final topological state of $UBXD8_{80-128}$ was found to be impacted by its initial insertion depth within the POPC bilayer membrane during the commencement of MD simulations (MD simulations performed by Hub group). When $UBXD8_{80-128}$ was positioned in a deeply embedded state within the bilayer during simulations, it remained deeply-embedded adopting a V-shaped topology. On the contrary, $UBXD8_{80-128}$ adopted an open and shallower conformation along the membrane-solvent interface when it was partially inserted within the bilayer membrane at the beginning of the simulation. This change in conformation was reflected by a change in the tilt angle of the peptide from ~80° (measured for the deeply embedded V-state) to ~ 20° for the partially inserted state with respect to the membrane normal. Notably, the arginine at position 104 (R104) which stabilized the deeply embedded state by snorkeling towards the opposite bilayer leaflet, flipped and snorkeled towards the phospho-headgroups on the cytosolic membrane-solvent interface in the partially inserted state. Arginine being a basic amino acid with positively charged side chains form hydrogen bonds with the negatively charged headgroups of phospholipids. The snorkeling of arginine at position 104 (R104) towards phospho-headgroups observed during MD simulations indicates that basic amino acids positioned within the membrane-embedded region of UBXD8 and other monotopic hairpin proteins (Olarte et al., 2020), plays an important role in anchoring hairpin proteins within phospholipid membranes.

Among the two distinct topological arrangements observed for the membrane-embedded region of $UBXD8_{80-128}$ within the bilayer membrane during MD simulations, the biochemical cysteine solvent accessibility data provided support in favor of a deeply-embedded V-shaped conformation. This was evident from the fact that no sulfhydryl labeling for amino acid residues positioned within the membrane-embedded region of op-$UBXD8_{53-153}$-mCherry was detected after treatment with mPEG. Furthermore, a direct comparison of the biochemical solvent accessibility data with the calculated average insertion depth of each amino acid residue of $UBXD8_{80-128}$ within the ER bilayer, as determined by MD simulations, provided further evidence for a deeply-embedded V-shaped conformation in the bilayer environment. However, the cysteine solvent accessibility assay has a limitation that it cannot provide any insight into the insertion depth of a particular amino acid residue located within the

hydrophobic core of the membrane. To overcome this limitation, future experiments should employ biophysical techniques such as electron paramagnetic resonance (EPR) spectroscopy in combination with site-directed spin labeling (SDSL) to obtain quantitative information on the insertion depth of individual amino acid residues based on the EPR spectrum of the spin-labeled protein (Sahu & Lorigan, 2020). Nuclear magnetic resonance (NMR) spectroscopy is another approach used to determine the insertion depth of membrane proteins with high precision. However, both these methods require purification, specific labeling, and reconstitution of the protein into a suitable membrane-mimetic (Brady et al., 2015).

Recently, using atomistic MD simulations on two model peptides, Alg14 and LiveDrop, it was shown that the membrane-embedded region of these model peptides remained deeply embedded within the bilayer membrane (Olarte et al., 2020). The interaction of the arginines (R179 and R187) located in the kink region of LiveDrop with phospholipid headgroups on the opposing bilayer leaflet was shown to be responsible to keep the peptide deeply embedded within the bilayer membrane. In another study, the hydrophobic N-terminus region of class I LD protein, DHRS3, was shown to anchor the ER bilayer membrane adopting an interfacial amphipathic helix (Pataki et al., 2018). Furthermore, using coarse-grained MD simulations, the authors also examined six additional class I LD proteins with predicted N-terminus membrane-embedded hydrophobic regions, and suggested that these proteins also associate with the ER bilayer membrane *via* an interfacial amphipathic helix including the UBXD8 (Pataki et al., 2018). However, the helical wheel projection of the membrane-embedded region of UBXD8 revealed a hydrophobicity value of 1.102 *H* and a hydrophobic moment of 0.033 *μH*. These values were considerably lower than the hydrophobic moment of 0.26 *μH* observed for DHRS3 (Pataki et al., 2018). Hence, these differences strongly indicate that UBXD8 is unlikely to associate with the ER bilayer through an interfacial amphipathic helix. This notion is further supported by our findings from MD simulations and cysteine solvent accessibility assay, which clearly suggest that the membrane-embedded region of UBXD8 anchors the ER bilayer adopting a deeply embedded V-shaped conformation.

Furthermore, based on our findings of UBXD8, as well as previous research on class I LD proteins (Olarte et al., 2020; Pataki et al., 2018; Stevanovic & Thiele, 2013; Zehmer et al., 2008), it is intriguing to speculate that the location of the hydrophobic region might also be a critical determinant of whether a class I LD protein is partially

or deeply embedded within the ER bilayer. In future studies, switching the position of the hydrophobic region might help us to better understand to what extent a class I LD protein get inserted into the bilayer.

5.3 Topological positioning of UBXD8 in LD monolayer membranes

Our findings from MD simulations and cysteine solvent accessibility assay clearly indicate that UBXD8 is positioned differentially within the ER bilayer and LD monolayer membranes. As stated above, the findings from MD simulations and cysteine solvent accessibility assay support only a deep-V conformation in the ER bilayer. However, on LDs, UBXD8 was found to be oriented towards the membrane-solvent interface, adopting a shallowly inserted V-shaped conformation. This conformation was further supported by a change in the tilt angle of the peptide from ~80° for the deeply embedded V-state in the ER bilayer to ~ 20° in LD monolayer with respect to the membrane normal. As a consequence, the distance between the two anti-parallel α-helices of UBXD8 on LD monolayer is expected to be greater than on ER bilayer. When UBXD8 was subjected to intramolecular crosslinking on LD monolayer membranes, minimal crosslinking was observed, which further provided evidence in favor of an open and shallow V-shaped shaped conformation for UBXD8 on LDs. In this conformation, the arginine at position 104 (R104) located within the kink region of UBXD8 snorkel towards the membrane-solvent interface, effectively anchoring the peptide there.

However, in a recent study, the results of MD simulations performed on LiveDrop, a class I LD protein, indicated that the arginine residue at position 187 (R187) located within the kink region of the peptide, remained deeply embedded within the neutral lipids due to solvation by water molecules (Olarte et al., 2020). This is in contrast to what we have observed for UBXD8, and the disparity in results could be attributed to simulating the peptide at different stages of LD biogenesis. During the early stage of LD biogenesis (nucleation), the TAG lens between the ER bilayer leaflets is small, allowing the arginine to interact with water molecules. As the TAG lens grows by accumulating more neutral lipids, water molecules disperse, inducing structural rearrangements within the membrane-embedded region resulting in the snorkeling of arginine towards the phospholipid-solvent interface. However, when $UBXD8_{80\text{-}128}$ was simulated by varying the length of the neutral lipids patch between the phospholipid monolayers to mimic the initial and later stages of LD biogenesis (MD

simulations performed by Hub group), the MD simulations revealed no change in the positioning of the UBXD8$_{80\text{-}128}$ and it was always found to be oriented towards the monolayer-solvent interface (Figure S2). The different behavior of UBXD8$_{80\text{-}128}$ and LiveDrop (Olarte et al., 2020), during MD simulations could be due to differences in their physical and chemical properties. Additionally, the differential positioning of these proteins in bilayer and monolayer membrane environments might be quintessential for structural rearrangements during their partitioning from the ER-to-LDs.

To date, DHRS3 and UBXD8 are the only class I LD proteins whose membrane-embedded regions have been studied in detail on both the ER bilayer and LD monolayer membranes employing PEGylation assay (Pataki et al., 2018). DHRS3 is shown to anchor both the ER bilayer and LD monolayer by adopting a partially buried amphipathic helix, as revealed by the periodic distribution of amino acid residues (1-26) located within its N-terminus (Figure 21A). Additionally, when these amino acids were subjected to helical wheel projection, a distinct arrangement of hydrophobic and hydrophilic residues along the helix axis was observed, further supporting an amphipathic helix (Pataki et al., 2018) (Figure 21B). In contrast, the helical wheel projection of the membrane-embedded region of UBXD8 (amino acid residues, 91-114) displayed a hydrophobic moment value much lower than DHRS3 (Figure 21D). Therefore, no clear enrichment of polar and non-polar residues on either side of the helix was observed for UBXD8 similar to DHRS3. This suggests that UBXD8$_{80\text{-}128}$ might also adopt a deep-V hairpin-like conformation within LD monolayer membranes. However, in case of UBXD8$_{80\text{-}128}$, our PEGylation and MD simulations data have revealed that the peptide orient towards the monolayer-solvent interface to adopt an open and shallower conformation to attain an energetically favorable state well suited to the highly hydrophobic environment of LDs (Figure 21C). On average, the hydrophobic moment of class II LD proteins (for e.g., CCTα-0.48 *μH*, Cornell, 2016) amphipathic helices was found to be higher than class I proteins (for e.g., DHRS3-0.26 *μH*, Pataki et al., 2018). Therefore, the difference in hydrophobic moment i.e., the distribution of hydrophobic and hydrophilic amino acids along an amphipathic helix might be a crucial factor in deciding the conformation and how stably a protein associates with the LDs (Dhiman et al., 2020).

Additionally, there are discrete differences in the amino acid residues that made up the membrane-embedded region of DHRS3 and UBXD8$_{80\text{-}128}$. In comparison to DHRS3, the membrane-embedded region of UBXD8$_{80\text{-}128}$ contains a stretch of

positively-charged arginines positioned in the regions where the peptide enters and leaves the monolayer membrane. The periodic distribution of arginines as revealed by cysteine solvent accessibility assay indicated that UBXD8$_{80\text{-}128}$ associates with the monolayer membrane close to the C-terminus interface *via* an amphipathic helix. Additionally, there is a pair of aromatic hydrophobic residues (tyrosine) on each side of the helix which are positioned close to the LD monolayer membrane-solvent interface to attain a more energetically stable state (Ulmschneider & Sansom, 2001). This clearly indicates that not all class I LD proteins anchor the ER bilayer and LD monolayer membranes *via* amphipathic helix. Therefore, the type of topology a monotopic protein adopts in the bilayer or monolayer membranes might be highly dependent on the discrete amino acid residues that made up the hydrophobic region of these proteins. In the future, amino acid substitution studies could reveal the specific role these residues play in controlling the topology of monotopic hairpin proteins.

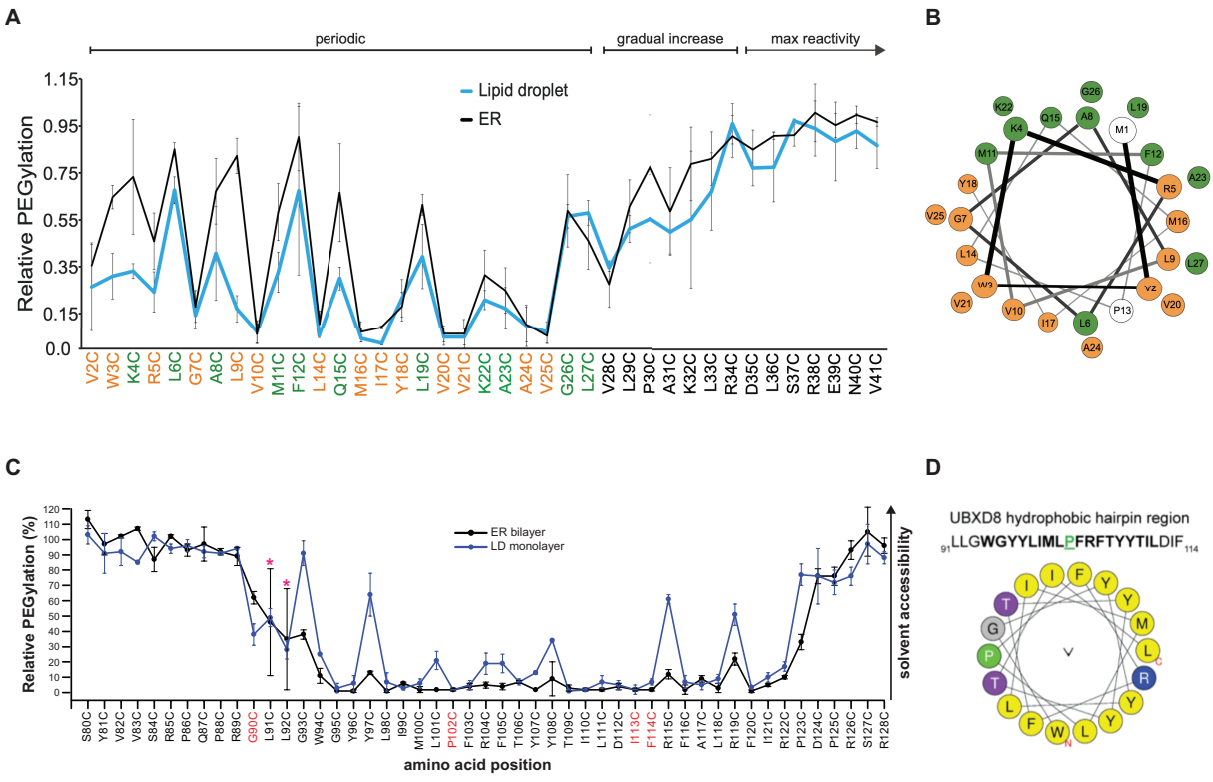

Figure 21: Comparison of solvent accessibility profile and helical wheel projections of the membrane-embedded region of class I LD proteins DHRS3 and UBXD8 revealed distinct conformations on LD monolayer.

(A) Solvent accessibility profile of DHRS3 exhibits an interfacial amphipathic topology indicated by periodic distribution of amino acid residues (1-26) positioned within its membrane-embedded

hydrophobic region (image taken from Pataki et al., 2018). **(B)** The helical wheel projection of DHRS3 depicting enrichment of hydrophobic (orange) and hydrophilic residues (green) along the helix (image taken from Pataki et al., 2018).
(C) Solvent accessibility profile of UBXD8 revealed periodic distribution of amino acid residues on LD monolayer indicating close proximity to membrane-solvent interface (this figure is a copy of the result figure 17C).
(D) The helical wheel projection of UBXD8 (generated using HeliQuest) depicting no clear enrichment of charged residues on either side of the helix suggests UBXD8 does not form an amphipathic helix, (this figure is a copy of the result figure 17D).

5.4 Potential determinants of hairpin topology and ER-to-LD partitioning

Typically, a bitopic protein transmembrane domain consists of a single α-helix that is around ~18 to 20 amino acid residues in length. The length of the transmembrane α-helix is crucial because it determines how the protein is positioned and interacts with other proteins and lipids within the bilayer membrane (Corradi et al., 2018; Enkavi et al., 2019). The PEGylation data revealed that the membrane-embedded region of op-UBXD8$_{53\text{-}153}$-mCherry was 29 amino acid residues long, consisting of a combination of charged, aromatic, and helix-breaking residues.

5.4.1 Role of helix-breaking residues

The presence of a proline residue at position 102 within the membrane-embedded region of op-UBXD8$_{53\text{-}153}$-mCherry may interfere with the formation of a regular α-helix due to its helix-breaking properties and can lead to the formation of kink or bend within the helix. The predicted structure of UBXD8$_{80\text{-}128}$ displayed a monotopic topology with a kink introduced by proline at position 102. The observed deep V-shaped conformation of UBXD8 within the ER bilayer adopted an open and shallower conformation in LD monolayer. This shift in conformation could be due to the dynamic nature of the kink region resulting in a change in angle opening between the two anti-parallel α-helices of UBXD8. Additionally, the electrostatic interactions between proline at position 102 (P102) with other amino acids such as phenylalanine (F103), and arginine (R104) within the kink might be crucial for inducing structural rearrangement within the membrane-embedded region of UBXD8. This structural rearrangement, in turn, could influence UBXD8 monotopic topology and its partitioning from ER-to-LDs.

For plant protein oleosin, it has been shown that substitution of the prolines to a leucine in the proline knot (triad of prolines) restricts the oleosin to the ER and hinders its localization to the plant LDs without any impact on its topology (Abell et al., 1997). Likewise, mutation of two prolines in the hydrophobic hairpin region of the HCV core protein restrict it to the ER and prevent its localization to the LDs (Hope et al., 2002). For AUP1, mutating proline in combination with valine and glycine (PVG motif) to leucine (Stevanovic & Thiele, 2013) and central proline to an alanine in caveolin-1 (Aoki et al., 2010) switches their topology from monotopic to bitopic. Mutation of the central conserved proline in the N-terminus hydrophobic domain of the AAM-B, ALDI, and CYB5R3 did not affect their targeting to the LDs (Zehmer et al., 2008). These findings further imply that proline mutation changes the topology of some class I proteins to bitopic, which in turn prevents their partitioning from the ER-to-LDs. Therefore, the importance of the proline might be dependent on the location of hydrophobic region within class I LD proteins.

For op-UBXD8$_{53\text{-}153}$-mCherry, I noticed that substitution of proline (P102) along with phenylalanine (F103), and arginine (R104) within the kink region to an alanine or leucine resulted in the formation of punctate structures within cells. Despite the introduced mutations, the altered protein was still detectable on LDs. This observed phenotype might be due to the compromised ability of the PFR mutant to effectively target the ER, resulting in decreased accumulation on LDs.

In the future, it is necessary to verify the expression levels of these mutants and the wild-type UBXD8 through immunoblotting to draw concrete conclusions. Additionally, atomistic MD simulations of the PFR mutant can reveal whether the UBXD8 is still deeply inserted within the bilayer or switches to an open and shallower conformation. This switch in UBXD8 conformation could, in turn, facilitate its partitioning from the ER-to-LDs. Overall, our microscopy data does not provide any concrete evidence regarding the influence of PFR mutant on the switch in UBXD8 conformation and its partitioning from the ER-to-LDs.

5.4.2 Positive-inside rule and role of charged and hydrophobic aromatic amino acid residues

In the past, numerous studies have demonstrated the importance of position-specific enrichment of charged residues in determining the final topology of membrane proteins (Baker et al., 2017; Bogdanov et al., 2009, 2014; Islam & Lam, 2013). According to the positive inside rule, the positively charged amino acids such as arginine and lysine have a tendency to enrich on the cytoplasmic side of the ER membrane and that positively charged residues can be used to manipulate the topology of membrane proteins (von Heijne, 1992). The PEGylation analysis of the op-UBXD8$_{53\text{-}153}$-mCherry in the ER bilayer and LD monolayer membranes revealed that positively charged arginine residues R85 and R89 located at the N-terminus, along with arginines R115, R119, and R122 positioned near the C-terminus, were partially solvent-exposed due to their snorkeling behavior. The presence of positively charged amino acids seems to be a conserved feature among class I LD proteins such as AUP1 (Stevanovic & Thiele, 2013), LiveDrop, and Alg14 (Olarte et al., 2020). It is important to mention that although the hydrophobic harpin region is essential for directing class I LD proteins to the LDs, the partitioning of certain monotopic hairpin proteins from the ER-to-LDs can be influenced by neighboring positively charged and bulky hydrophobic residues (Ingelmo-Torres et al., 2009). The substitution of positively charged residues (arginines) located upstream (R85 and R89) and downstream (R115, R119, and R122) of the hydrophobic region of op-UBXD8$_{53\text{-}153}$-mCherry resulted in formation of punctate structures within cells with op-UBXD8$_{53\text{-}153}$-mCherry still detectable on LDs, as evidenced by fluorescence microscopy images. It shows that mutating arginines seems to not affect partitioning of op-UBXD8$_{53\text{-}153}$-mCherry from the ER-to-LDs.

In cellular systems, positively charged residues located either upstream or downstream of the membrane-embedded region of LiveDrop, Alg14 (Olarte et al., 2020), AUP1 (Stevanovic & Thiele, 2013), ALDI, and caveolins (Ingelmo-Torres et al., 2009; Ostermeyer et al., 2004) have shown to be critical in controlling the partitioning of these proteins to the LDs. In these studies, biochemical fractionation followed by densiometric quantification of immunoblot signals from the membrane and LD fractions were employed to quantify the influence of mutations on the partitioning of proteins from the ER-to-LDs. However, the study from Olarte et al. measured the

signal of mCherry-tagged LiveDrop and Alg14 in both the entire cell and on LDs using fluorescence microscopy images. To calculate the LD enrichment factor, they divided the average intensity of the protein signal on LDs by the average intensity in the entire cell, excluding LDs (Olarte et al., 2020). In the future, biochemical fractionation experiments along with atomistic MD simulations could provide a detailed insight on the influence of amino acid substitutions on the partitioning of UBXD8 from the ER-to-LDs.

Additionally, it has been observed that the accumulation of LiveDrop and Alg14 on LDs is hindered by the mutation of bulky hydrophobic aromatic amino acids such as tryptophan, indicated by a change in their free energies (Olarte et al., 2020). On LDs, tryptophan amino acid residues positioned within the hydrophobic region of LiveDrop displayed lower free energies than in bulk water by forming H-bonds with glycerol moieties of TAG molecules. This suggests that aromatic residues prefer the highly hydrophobic environment of LDs (Olarte et al., 2020). Similar to LiveDrop, the $UBXD8_{80\text{-}128}$ membrane-embedded region contains two pairs of tyrosine that are positioned beside each other on opposing α-helices within the midplane of the ER membrane, which is an energetically unfavorable environment for hydrophobic residues (MacCallum et al., 2008; Ulmschneider & Sansom, 2001). However, the substitution of tyrosine residues located in the middle of opposing α-helices of op-$UBXD8_{53\text{-}153}$-mCherry resulted in an increased accumulation of op-$UBXD8_{53\text{-}153}$-mCherry on LDs, indicating that tyrosine residues hinder efficient partitioning of UBXD8 from the ER-to-LDs. This could be attributed to UBXD8 undergoing structural rearrangement within the ER bilayer when tyrosines are absent, leading to an open and shallower conformation that promotes its partitioning to LDs.

5.5 Free energy stabilization promotes ER-to-LD partitioning of class I LD proteins

Recent *in silico* studies have shown that class I LD proteins undergo conformational changes that drive their accumulation on LDs *via* repositioning of bulky hydrophobic residues and their interaction with the TAG molecules (Olarte et al., 2020). Additionally, using *in vitro* model membrane systems and MD simulations, the surface properties of LDs such as packing defects and surface tension have also been demonstrated to provide an energetically favorable environment that regulates the accumulation of class I and class II proteins on LDs (Caillon et al., 2020; Chorlay & Thiam, 2020; Kim

et al., 2021). Using MD simulations, it was shown that bulky aromatic amino acids such as tryptophan positioned within the membrane-embedded region of model peptide LiveDrop achieved the greatest degree of free energy stabilization when relocated to the monolayer of LDs. This change in free energy was suggested to act as a driving force in controlling the accumulation of monotopic hairpin proteins on LDs (Olarte et al., 2020). The authors pinpointed two specific tryptophan residues, W172 and W197, located on the opposite helices of the LiveDrop, which exhibited an enhanced degree of energy stabilization. This stabilization was achieved through either the interaction of the residues with the glycerol moieties of TAG molecules, in the case of W197, or through a reorientation towards the LD monolayer-solvent interface, as seen in the case of W172 (Olarte et al., 2020). In another study employing model membrane systems, it was demonstrated that monotopic hairpin proteins containing hydrophobic domains have higher preference to partition to LDs (Caillon et al., 2020). This behavior was attributed to a decrease in free energy that occurs as a result of higher affinity of hydrophobic domains of monotopic hairpin proteins for TAG molecules over membrane phospholipids (Caillon et al., 2020).

Based on the results of MD pulling experiments and the analysis of free energy profiles of UBXD8$_{80\text{-}128}$ in the planar bilayer and at the rim of the LD in continuity with the bilayer, it was concluded that the transition of UBXD8$_{80\text{-}128}$ from a deeply-embedded V-state to an open and shallower conformation is not an energetically favorable process (Figure S1). This suggests that UBXD8$_{80\text{-}128}$ deep-V state remains stable within the planar bilayer and is unlikely to spontaneously partition to the LD monolayer. Hence, the proposition of class I LD proteins attaining an energetically favorable state on LDs is not applicable to UBXD8. Therefore, in order for UBXD8$_{80\text{-}128}$ to partition from the ER bilayer to LD monolayer, a transition from deep-V to a shallower conformation is needed. This transition will require the R104 to flip towards the cytosolic side of the ER bilayer. Currently, the precise mechanism behind this transition is unknown, which raises the question of which parameters can enforce this transition. In future studies, MD simulations of UBXD8 in phospholipid membranes of varying thickness and composition mimicking *in vivo* environment could help us to better understand which factors influence the flipping of R104 from the lower leaflet towards the cytosolic side of the ER bilayer.

Additionally, it has been observed that certain class I LD proteins, such as GPAT4, partition efficiently to LDs (Wilfling et al., 2013), while endogenous UBXD8

shows more restricted partitioning to LDs, with a significant pool remaining within the ER (Olzmann et al., 2013; Schrul & Kopito, 2016). This regulated partitioning of UBXD8 to LDs could be considered as an evolutionary constraint, likely due to its essential functional role as an integral component of the ERAD machinery within the ER. Hence, it is possible that other accessory proteins, such as seipin, or TAG molecules could play an essential role in regulating the structural rearrangement and partitioning of the LD-destined pool of UBXD8 from the ER-to-LDs.

Recently, Song et al. proposed two distinct pathways for ER-to-LD targeting of class I LD proteins. These pathways include the early ERTOLD pathway, which mediates the targeting of proteins to the early LDs physically connected to the ER *via* accessory proteins such as seipin, and the late ERTOLD pathway, which drives the trafficking of proteins to mature LDs *via* physical connections between the ER and LDs (Song et al., 2022). Interestingly, this study categorized UBXD8, LiveDrop, and HPos (Kassan et al., 2013) as early ER-LD cargoes, and GPAT4 as a late ER-LD cargo (Figure 22). In seipin knockout cells, the late ER-LD cargo such as GPAT4 can still partition to early LDs, which suggests that homo-oligomeric seipin ring restricts late ER-LD cargoes such as GPAT4 from accessing early LDs formed within the ER.

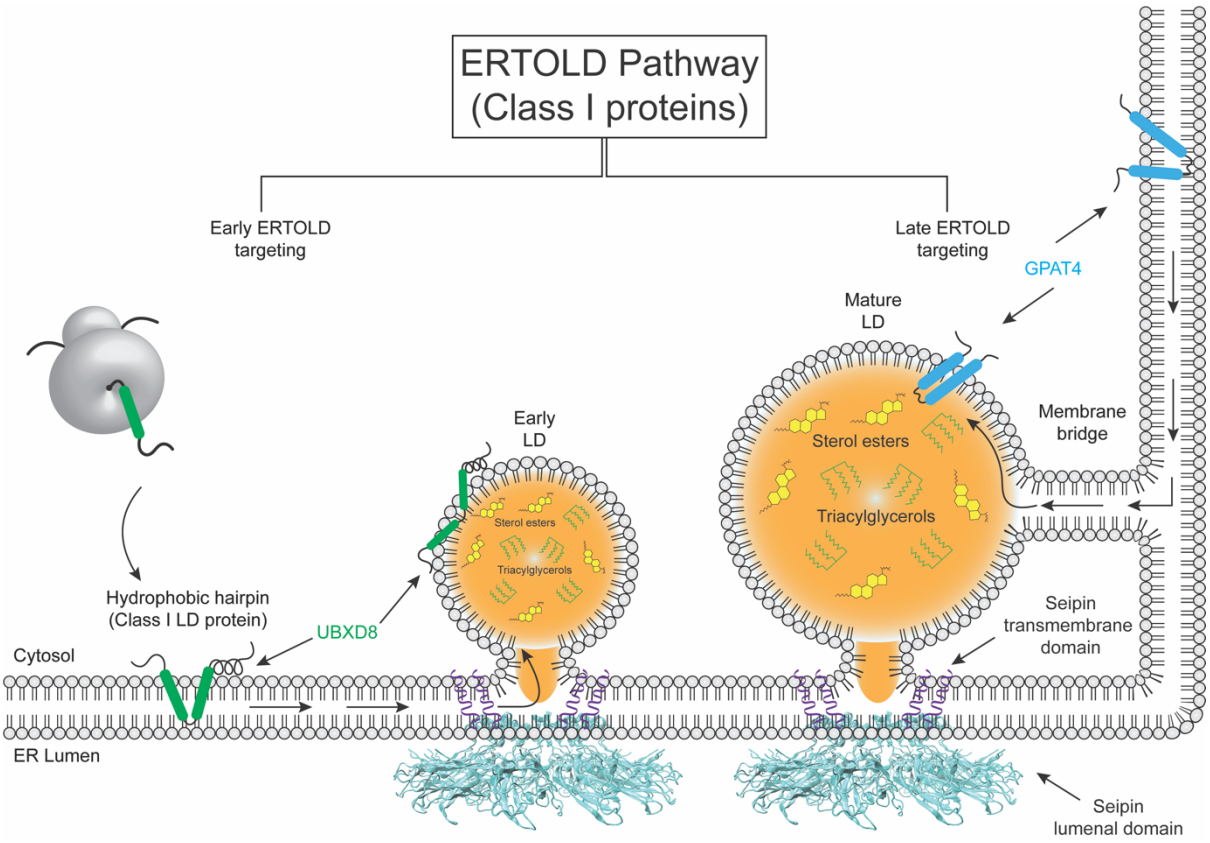

Figure 22: ERTOLD pathway for class I LD proteins targeting to LDs.
After translation in the cytosol, class I LD proteins are inserted into the ER membrane *via* hydrophobic hairpin domains. In the early ERTOLD pathway, proteins such as seipin form a barrel-shaped structure at the ER-LD contact sites, and proteins such as UBXD8 localize to the early LDs. On the other hand, in the late ERTOLD pathway, proteins like GPAT4 target the mature LDs supposedly through membrane bridges (adapted from Olarte et al., 2022).

The classification of UBXD8 as an early-LD cargo helped us to envisage a model (Figure 23), whereby UBXD8 undergoes a structural rearrangement from a deeply embedded V-shaped conformation to a shallowly inserted state within the bilayer, and this critical transition might allow UBXD8 to overcome the seipin barrier within the ER bilayer. I assume this transition to take place during the initial stages of LD biogenesis, when the neutral lipid lens is still small. This is because glycerol moieties of neutral lipids, as well as water molecules within the LD lens of nascent LDs, have the maximum likelihood to catalyze the permeation of R104 snorkeling to the lower ER leaflet and flip it towards the cytoplasmic ER leaflet. This switch in conformation might help UBXD8 in attaining a more energetically stable configuration,

which in turn might facilitate its partitioning from the ER-to-LDs. Furthermore, seipin and other hairpin-containing proteins residing within the ER bilayer may have a role in regulating the UBXD8 conformational transition and its subsequent partitioning from the ER-to-LDs. The recent cryo-EM studies have provided a detailed insight into structural features of seipin lumenal and transmembrane domains (Arlt et al., 2022; Klug et al., 2021). In the future, atomistic MD simulations of UBXD8 along with seipin within ER bilayer could enhance our understanding of how the interactions between seipin transmembrane domains and UBXD8 influence membrane thickness and curvature at the rim of the LD in continuity with the planar bilayer. Consequently, the change in membrane thickness and curvature may facilitate UBXD8 partitioning from the ER-to-LDs by mediating permeation of R104 snorkeling to the lower leaflet of ER bilayer.

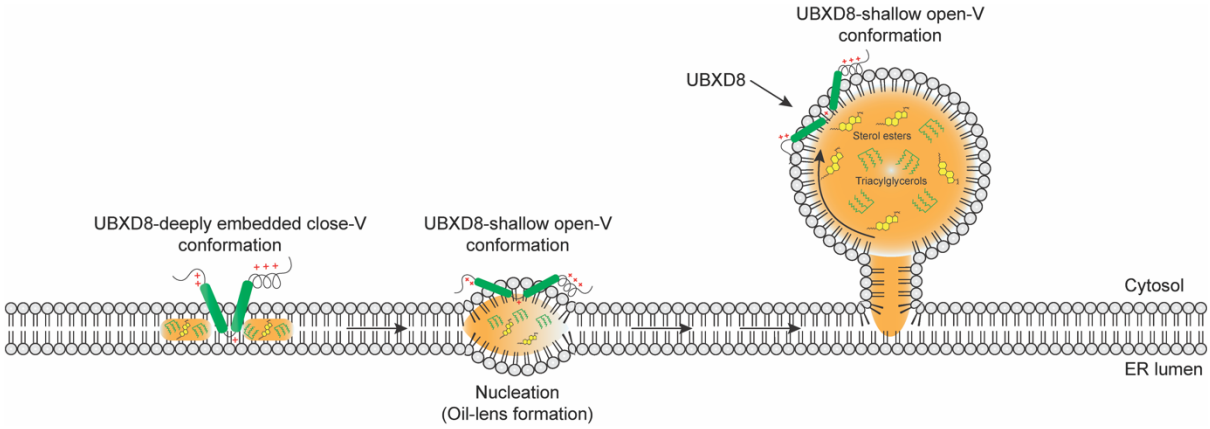

Figure 23: Model depicting the structural rearrangement in UBXD8 conformation from a deep-V to a shallower open-V state during its partitioning from the ER-to-LDs. Positively charged residues are indicated by "+". For details see text.

5.6 Comparison of ER-resident versus LD-destined monotopic proteins

Currently, a longstanding question in LD research is how class I LD proteins are selectively partitioned to LDs after their targeting and insertion into the ER. One hypothesis suggests that the hydrophobic hairpin region of these proteins is first inserted into the cytoplasmic leaflet of the ER bilayer membrane, and subsequently moves laterally to LD monolayer *via* the lipidic bridges connecting LDs to the ER (Jacquier et al., 2011; Song et al., 2022; Wilfling et al., 2013). However, not all proteins with a monotopic hairpin topology such as the class I LD proteins are partitioned to

LDs. For instance, reticulons and REEP (receptor expression enhancing proteins) often referred to as "ER-shaping" proteins play an important role in the maintenance and shaping of the ER. Reticulons facilitate the formation of ER tubules, while REEPs help to maintain and regulate the distribution of ER membranes. The ability of reticulons to induce and stabilize membrane curvature is believed to be influenced by their oligomerization property and specific topology (Shibata et al., 2010; Voeltz et al., 2006).

One distinctive characteristic of these proteins is the presence of a conserved ~200 amino acid residues long reticulon homology domain (RHD). Topology investigation of reticulons by employing protease protection and selective PEGylation experiments have provided evidence indicating that both N- and C-termini are oriented toward the cytosol (Voeltz et al., 2006; Zurek et al., 2011). The RHD is suggested to anchor the cytosolic ER leaflet adopting a double hairpin-like wedge-shaped (‘W’) topology and induces positive curvature possibly by oligomerization (Voeltz et al., 2006; Wang & Rapoport, 2019). The length of the membrane-embedded hydrophobic regions of reticulons are ~40 amino acid residues long (Yang & Strittmatter, 2007), which might be a critical factor in preventing the partitioning of these proteins from the ER-to-LDs.

In the future, hydrophobic domain swapping between reticulons and class I LD proteins, and domain extension experiments by manipulating discrete amino acids based on the recent partitioning data available on class I LD proteins (Caillon et al., 2020; Olarte et al., 2020, this study), could enable us to dissect whether length of the hydrophobic hairpin region or specific amino acid residues play an important role in controlling the partitioning of reticulons or similar proteins with hairpin topology from the ER-to-LDs. In conclusion, a monotopic topology cannot be the sole factor that drives the partitioning of class I LD proteins from the ER-to-LDs. Overall, a combination of monotopic hairpin topology along with the intrinsic protein features such as length of the membrane-embedded hairpin region, discrete amino acid residues located within the hydrophobic hairpin region, oligomerization, and their interaction with TAG molecules might be the crucial underlying factors controlling the partitioning of class I LD proteins from the ER-to-LDs. Currently, no data is available on UBXD8 homo-oligomerization within the ER bilayer and LD monolayer membranes. However, it is plausible that oligomerization of hairpin proteins could affect their partitioning from the ER-to-LDs. The oligomerization of UBXD8 within the ER bilayer

could impact its partitioning to LDs either positively or negatively, and conversely, the process can also influence its partitioning back from LDs to the ER.

5.7 Bridging biochemical experiments and MD simulations for membrane protein dynamics assessment in distinct physiochemical environments

Currently, biochemical techniques are employed to gain insight into the dynamic behavior of membrane proteins in distinct physiochemical environments. Although these techniques provide valuable insights into protein dynamics, they are limited in their ability to capture details at the atomistic scale. To overcome these challenges, in recent years MD simulations are being employed to gain information on protein dynamics at atomistic resolution and over microsecond timescales (Enkavi et al., 2019; Lindahl & Sansom, 2008; Loschwitz et al., 2020).

In this study, we bridge the power of biochemical experiments with MD simulations to gain insight into the intramembrane positioning of monotopic hairpin proteins. The integration of biochemical data and MD simulations provided a comprehensive and detailed understanding of the membrane-embedded region of UBXD8 in two distinct membrane environments at the atomistic level. Furthermore, this combined approach allowed for the identification of amino acids crucial for ER-to-LD partitioning and the characterization of different conformational states exhibited by UBXD8 in both the bilayer and monolayer membranes. In the past, most of the studies either derived their conclusions exclusively on the basis of MD simulations output or by employing artificial membrane-mimetics, which sometimes might result in misinterpretation of data due to lack of experimental evidence (Caillon et al., 2020; Olarte et al., 2020). This study is the first of its kind where the longstanding question on the positioning of the membrane-embedded region of monotopic hairpin proteins is addressed in both the ER bilayer and LD monolayer membranes by complementing biochemical experiments with MD simulations. Future studies should consider adopting this integrated approach as a standard for exploring membrane protein dynamics, particularly for proteins where structural information is limited or unavailable.

5.8 Future perspective

Overall, this study provided detailed insight into the positioning of the membrane-embedded region of UBXD8 at atomistic level in distinct physiochemical membrane

environments. The main findings of this study revealed that UBXD8 adopts a deeply embedded V-shaped conformation in the bilayer mediated by the interaction of arginine R104 located within the PFR kink region with the phospho-headgroups on the opposing bilayer leaflet. On the other hand, in the LD monolayer, UBXD8 adopts an open and shallower conformation positioned closer to the monolayer membrane-solvent interface. The synergistic use of experimental and MD simulations unraveled the positioning of discrete amino acid residues located within the membrane-embedded hairpin region of UBXD8. The key findings from this study establish a fundamental basis for future investigations aiming to enhance our current knowledge on the partitioning of class I LD proteins within a cellular environment. Furthermore, it paves the way for further exploration into the involvement of additional proteins such as seipin, and discrete sequence elements in regulating the partitioning of class I LD proteins from the ER-to-LDs.

In the future, the combination of experimental and computational methods can be applied to study the influence of the distinct lipid environment on the partitioning and conformation of class I LD proteins within the ER bilayer and LD monolayer membranes. The experimental data obtained from this study and previous research can be used to enhance the accuracy of current force fields and simulation models. This, in turn, would enable more precise predictions of the positioning of membrane-embedded region of monotopic hairpin proteins in both the ER bilayer and LD monolayer membranes. Exploring these fundamental questions is not only crucial for comprehending the LD biology but also for unraveling the molecular mechanisms that regulate the role of this organelle in various metabolic diseases. The monolayer of LDs is decorated with multiple proteins which have been shown to play a crucial role in regulating the function of this organelle and could serve as potential targets for therapeutic interventions (Jackson, 2019; Olzmann & Carvalho, 2019; Pol et al., 2014; Walther et al., 2017). For instance, studies have shown that UBXD8 interacts with other proteins and complexes involved in ERAD (Lee et al., 2008; Xia et al., 2014; Ye et al., 2017) and LD regulation (Olzmann et al., 2013; Yang & Mottillo, 2020). It has been suggested that UBXD8 together with p97/VCP on LDs inhibits the activity of the rate-limiting enzyme of triglycerides lipolysis, ATGL, which in turn leads to an increase in LDs size (Olzmann et al., 2013). While the precise mechanism of UBXD8 involvement in LD regulation is still being elucidated, its interaction with ATGL suggests a role in triglyceride metabolism and LD turnover. Further research is needed

to fully understand the molecular mechanisms and physiological significance of the ATGL/UBXD8 interaction in lipid metabolism and associated diseases (Imai et al., 2015; Olzmann et al., 2013; Stevenson et al., 2016). However, a detailed molecular understanding of how the recruitment of metabolically active proteins to LDs is regulated is key to developing novel therapeutic measures to combat metabolic disorders.

6. Supplementary Information

6.1 Free energy profiles of UBXD8$_{80\text{-}128}$ deep-V conformation in bilayer and at the rim of the LD in continuity with the planar bilayer membrane

Supplementary Figure S1

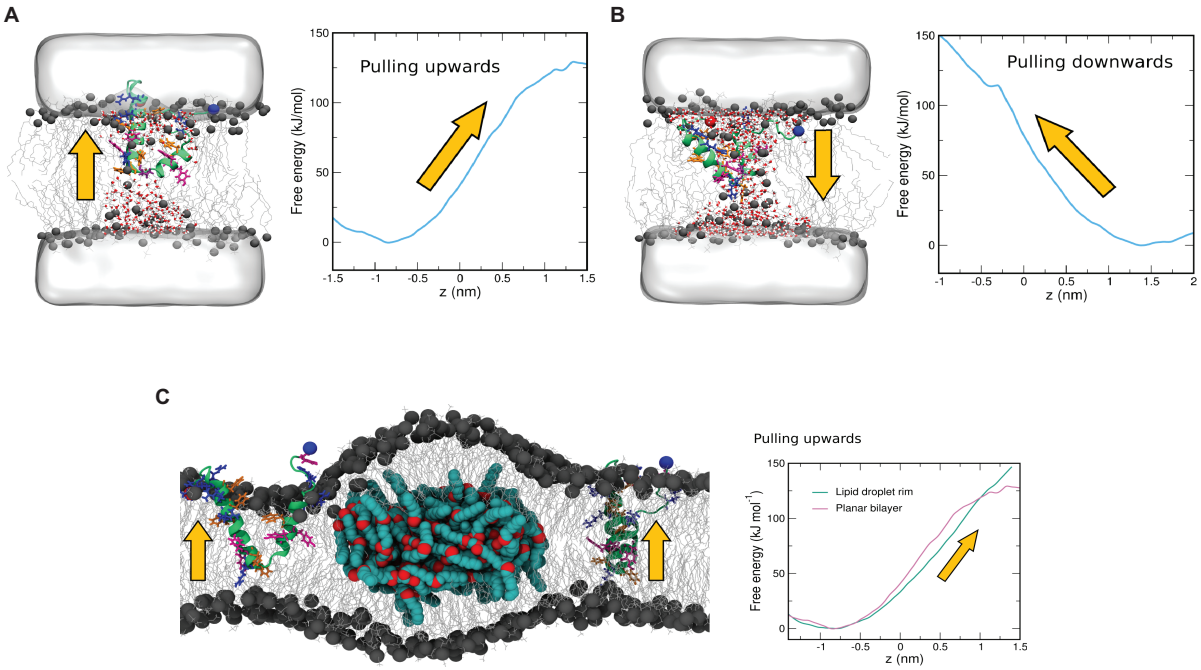

Figure S1: Free energy profiles of UBXD8$_{80\text{-}128}$ deep-V conformation in bilayer and at the rim of the LD in continuity with the planar bilayer membrane (data provided by Hub group).

(A-B) Pulling MD simulations revealed substantially high free energy barrier for the deep-V conformation of UBXD8$_{80\text{-}128}$, when pulled in both upward and downward directions within a planar POPC bilayer membrane.

(C) Pulling MD simulations performed on deep-V conformation of UBXD8$_{80\text{-}128}$ at the rim of the LD in continuity with the planar POPC bilayer.

6.2 Atomistic MD simulations of UBXD8$_{80\text{-}128}$ membrane-embedded region in a monolayer membrane with 2 nm neutral lipid patch

Supplementary Figure S2

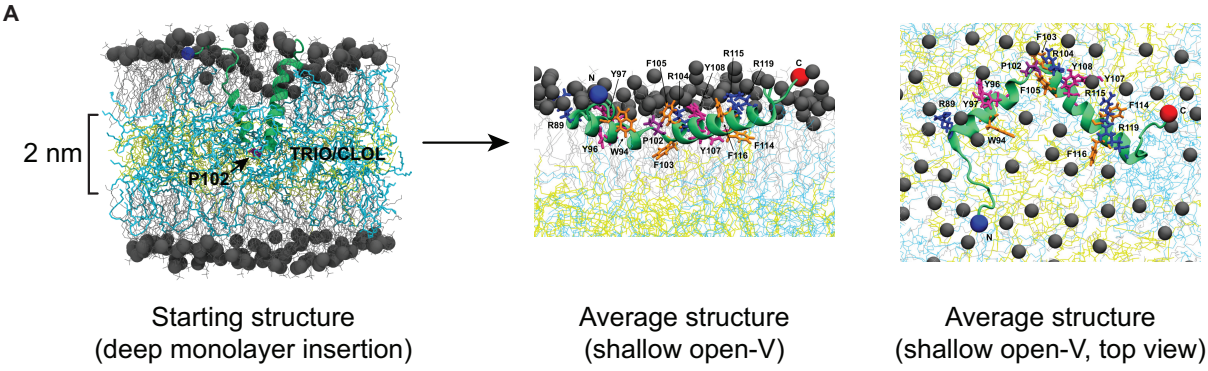

Figure S2: Atomistic MD simulations of UBXD8$_{80\text{-}128}$ membrane-embedded region in a monolayer membrane with 2 nm neutral lipid patch (data provided by Dr. Chetan Poojari, Hub group).
(A) Starting (left) and average structure of UBXD8$_{80\text{-}128}$ (side and top view; right) in a POPC monolayer for atomistic MD simulations run. The average structure was obtained from clustering analysis using last 300 ns of the 2 µs trajectory. The monolayer is composed of neutral lipids (triolein and cholesteryl oleate, 2 nm thick) sandwiched between POPC monolayers.

6.3 Plasmid maps and nucleotide sequence

Plasmid maps and nucleotide sequence of op_UBXD8$_{53_153}$_mCherry and UBXD8$_{53_153}$_mCherry_op used in this study are shown below:

ML_003_op_UBXD8$_{53_153}$_mCherry:

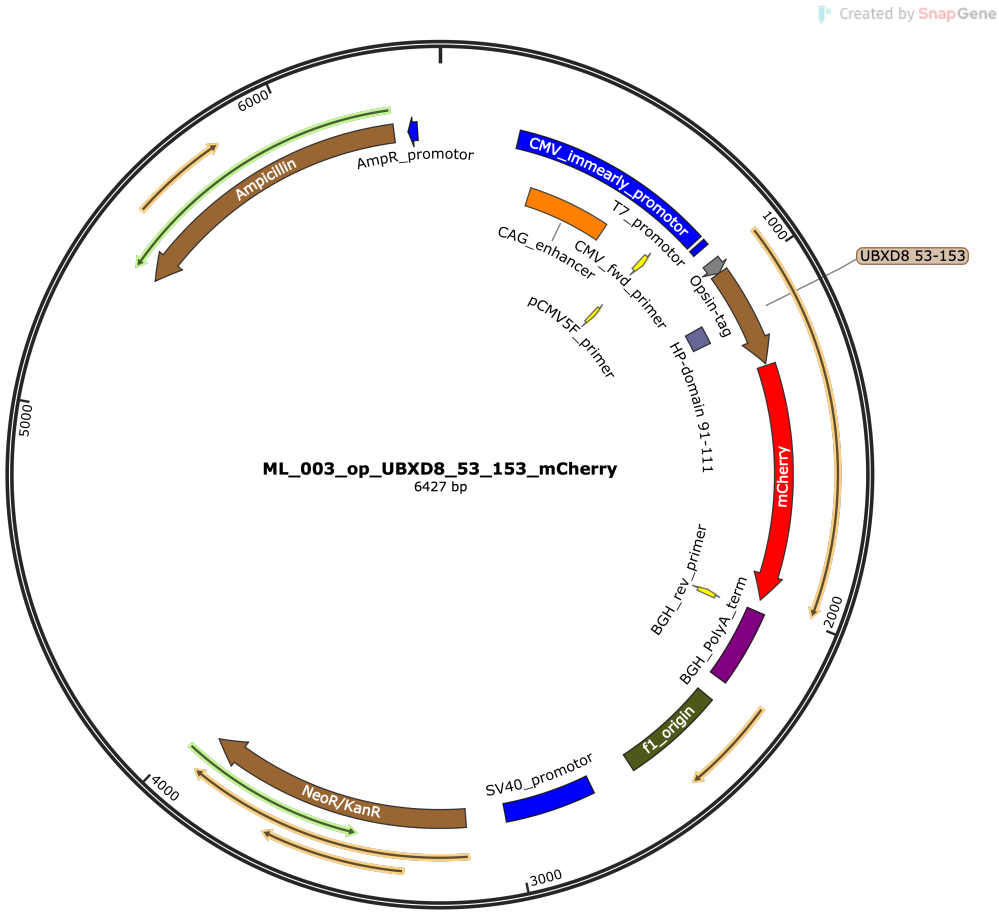

ATGGCCACCATGGGCCCAAACTTCTACGTGCCTTTCTCCAACAAGACGGGCGA
GCAAGAGGGCGTACCTAGTGTTTTCAACCCACCTCCATCACGACCCCTGCAGG
TTAATACAGCTGACCACAGGATCTACAGCTATGTTGTCTCAAGACCTCAACCAA
GGGGGCTGCTTGGATGGGGTTATTACTTGATAATGCTTCCATTCCGGTTTACCT
ATTACACGATACTTGATATATTTAGGTTTGCTCTTCGTTTTATACGGCCTGACCC
TCGCAGCCGGGTCACTGACCCCGTTGGGGACATTGTTTCATTTATGCACTCTTT
TGAAGAGAAATATGGGAGGGCACACCCTGTCGAATTCATGGTGAGCAAGGGCG
AGGAGGATAACATGGCCATCATCAAGGAGTTCATGCGCTTCAAGGTGCACATG
GAGGGCTCCGTGAACGGCCACGAGTTCGAGATCGAGGGCGAGGGCGAGGGC
CGCCCCTACGAGGGCACCCAGACCGCCAAGCTGAAGGTGACCAAGGGTGGCC
CCCTGCCCTTCGCCTGGGACATCCTGTCCCCTCAGTTCATGTACGGCTCCAAG

GCCTACGTGAAGCACCCCGCCGACATCCCCGACTACTTGAAGCTGTCCTTCCC
CGAGGGCTTCAAGTGGGAGCGCGTGATGAACTTCGAGGACGGCGGCGTGGTG
ACCGTGACCCAGGACTCCTCCCTGCAGGACGGCGAGTTCATCTACAAGGTGAA
GCTGCGCGGCACCAACTTCCCCTCCGACGGCCCCGTAATGCAGAAGAAGACC
ATGGGCTGGGAGGCCTCCTCCGAGCGGATGTACCCCGAGGACGGCGCCCTGA
AGGGCGAGATCAAGCAGAGGCTGAAGCTGAAGGACGGCGGCCACTACGACGC
TGAGGTCAAGACCACCTACAAGGCCAAGAAGCCCGTGCAGCTGCCCGGCGCC
TACAACGTCAACATCAAGTTGGACATCACCTCCCACAACGAGGACTACACCATC
GTGGAACAGTACGAACGCGCCGAGGGCCGCCACTCCACCGGCGGCATGGACG
AGCTGTACAAGTAA

ML_004_UBXD8_53_153_mCherry_op:

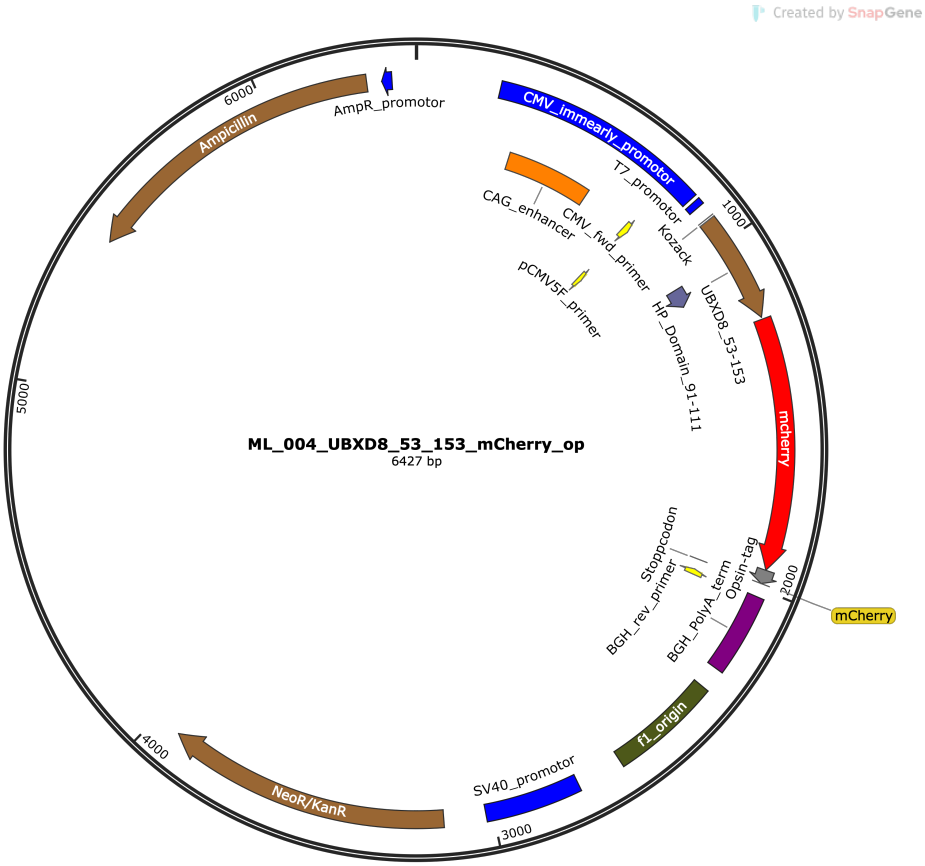

ATGGAGCAAGAGGGCGTACCTAGTGTTTTCAACCCACCTCCATCACGACCCCT
GCAGGTTAATACAGCTGACCACAGGATCTACAGCTATGTTGTCTCAAGACCTCA
ACCAAGGGGGCTGCTTGGATGGGGTTATTACTTGATAATGCTTCCATTCCGGTT
TACCTATTACACGATACTTGATATATTTAGGTTTGCTCTTCGTTTTATACGGCCT
GACCCTCGCAGCCGGGTCACTGACCCCGTTGGGGACATTGTTTCATTTATGCA

CTCTTTTGAAGAGAAATATGGGAGGGCACACCCTGTCGAATTCATGGTGAGCAA
GGGCGAGGAGGATAACATGGCCATCATCAAGGAGTTCATGCGCTTCAAGGTGC
ACATGGAGGGCTCCGTGAACGGCCACGAGTTCGAGATCGAGGGCGAGGGCGA
GGGCCGCCCCTACGAGGGCACCCAGACCGCCAAGCTGAAGGTGACCAAGGGT
GGCCCCCTGCCCTTCGCCTGGGACATCCTGTCCCCTCAGTTCATGTACGGCTC
CAAGGCCTACGTGAAGCACCCCGCCGACATCCCCGACTACTTGAAGCTGTCCT
TCCCCGAGGGCTTCAAGTGGGAGCGCGTGATGAACTTCGAGGACGGCGGCGT
GGTGACCGTGACCCAGGACTCCTCCCTGCAGGACGGCGAGTTCATCTACAAGG
TGAAGCTGCGCGGCACCAACTTCCCCTCCGACGGCCCCGTAATGCAGAAGAAG
ACCATGGGCTGGGAGGCCTCCTCCGAGCGGATGTACCCCGAGGACGGCGCCC
TGAAGGGCGAGATCAAGCAGAGGCTGAAGCTGAAGGACGGCGGCCACTACGA
CGCTGAGGTCAAGACCACCTACAAGGCCAAGAAGCCCGTGCAGCTGCCCGGC
GCCTACAACGTCAACATCAAGTTGGACATCACCTCCCACAACGAGGACTACACC
ATCGTGGAACAGTACGAACGCGCCGAGGGCCGCCACTCCACCGGCGGCATGG
ACGAGCTGTACAAGGCCACCATGGGCCCAAACTTCTACGTGCCTTTCTCCAACA
AGACGGGCTAA

7. References

Abell, B. M., Holbrook, L. A., Abenes, M., Murphy, D. J., Hills, M. J., & Moloney, M. M. (1997). Role of the proline knot motif in oleosin endoplasmic reticulum topology and oil body targeting. *The Plant Cell*, *9*(8), 1481–1493. https://doi.org/10.1105/tpc.9.8.1481

Abraham, M. J., Murtola, T., Schulz, R., Páll, S., Smith, J. C., Hess, B., & Lindahl, E. (2015). GROMACS: High performance molecular simulations through multi-level parallelism from laptops to supercomputers. *SoftwareX*, *1*, 19–25. https://doi.org/10.1016/j.softx.2015.06.001

Adam Kassan, Albert Herms, Andrea Fernández-Vidal, Marta Bosch, Nicole L. Schieber, Bjn Reddy, Alba Fajardo, Mariona Gelabert-Baldrich, Francesc Tebar, Carlos Enrich, Steven P. Gross, Robert G. Parton, Albert Pol, & A Pol. (2013). Acyl-CoA synthetase 3 promotes lipid droplet biogenesis in ER microdomains. *Journal of Cell Biology*. https://doi.org/10.1083/jcb.201305142

Ajjaji, D., Ben M'barek, K., Mimmack, M. L., England, C., Herscovitz, H., Dong, L., Kay, R. G., Patel, S., Saudek, V., Small, D. M., Savage, D. B., & Thiam, A. R. (2019). Dual binding motifs underpin the hierarchical association of perilipins1-3 with lipid droplets. *Molecular Biology of the Cell*, *30*(5), 703–716. https://doi.org/10.1091/mbc.E18-08-0534

Allen, K. N., Entova, S., Ray, L. C., & Imperiali, B. (2019). Monotopic Membrane Proteins Join the Fold. *Trends in Biochemical Sciences*, *44*(1), 7–20. https://doi.org/10.1016/j.tibs.2018.09.013

Altmann, Richard. (1894). *Die Elementarorganismen und ihre Beziehungen zu den Zellen*. https://doi.org/10.1515/9783112366967

Alvarez, H. M. (2016). Triacylglycerol and wax ester-accumulating machinery in prokaryotes. *Biochimie*, *120*, 28–39. https://doi.org/10.1016/j.biochi.2015.08.016

Amatya, B., Hewang Lee, Lee, H., Lee, H., Asico, L. D., Konkalmatt, P., Armando, I., Armando, I., Felder, R. A., Jose, P. A., & Jose, P. A. (2021). SNX-PXA-RGS-PXC Subfamily of SNXs in the Regulation of Receptor-Mediated Signaling and Membrane Trafficking. *International Journal of Molecular Sciences*, *22*(5), 2319. https://doi.org/10.3390/ijms22052319

Angel, A., & Angel, A. (1970). Studies on the compartmentation of lipid in adipose cells. I. Subcellular distribution, composition, and transport of newly synthesized lipid: Liposomes. *Journal of Lipid Research*, *11*(5), 420–432.

Aoki, S., Thomas, A., Thomas, A., Decaffmeyer, M., Brasseur, R., Richard M. Epand, & Epand, R. M. (2010). The role of proline in the membrane re-entrant helix of caveolin-1. *Journal of Biological Chemistry*, *285*(43), 33371–33380. https://doi.org/10.1074/jbc.m110.153569

Arinaminpathy, Y., Khurana, E., Engelman, D. M., & Gerstein, M. (2009). Computational analysis of membrane proteins: The largest class of drug targets. *Drug Discovery Today*, *14*(23), 1130–1135. https://doi.org/10.1016/j.drudis.2009.08.006

Arlt, H., Sui, X., Folger, B., Adams, C., Chen, X., Remme, R., Hamprecht, F. A., DiMaio, F., Liao, M., Goodman, J. M., Farese, R. V., & Walther, T. C. (2022). Seipin forms a flexible cage at lipid droplet formation sites. *Nature Structural & Molecular Biology*, *29*(3), 194–202. https://doi.org/10.1038/s41594-021-00718-y

Athenstaedt, K., & Daum, G. (2006). The life cycle of neutral lipids: Synthesis, storage and degradation. *Cellular and Molecular Life Sciences*, *63*(12), 1355–1369. https://doi.org/10.1007/s00018-006-6016-8

Athenstaedt, K., Zweytick, D., Jandrositz, A., Kohlwein, S. D., & Daum, G. (1999). Identification and Characterization of Major Lipid Particle Proteins of the Yeast Saccharomyces cerevisiae. *Journal of Bacteriology*, *181*(20), 6441–6448. https://doi.org/10.1128/jb.181.20.6441-6448.1999

Aviram, N., Ast, T., Costa, E. A., Arakel, E. C., Chuartzman, S. G., Jan, C. H., Haßdenteufel, S., Dudek, J., Jung, M., Schorr, S., Zimmermann, R., Schwappach, B., Weissman, J. S., & Schuldiner, M. (2016). The SND proteins constitute an alternative targeting route to the endoplasmic reticulum. *Nature*, *540*(7631), 134–138. https://doi.org/10.1038/nature20169

B. Hess, H. Bekker, H. Berendsen, & J. Fraaije. (1997). LINCS: A linear constraint solver for molecular simulations. *J. Comput. Chem.* https://doi.org/10.1002/(sici)1096-987x(199709)18:12%3c1463::aid-jcc4%3e3.0.co;2-h

Bacle, A., Gautier, R., Jackson, C. L., Fuchs, P. F. J., & Vanni, S. (2017). Interdigitation between Triglycerides and Lipids Modulates Surface Properties

of Lipid Droplets. *Biophysical Journal*, *112*(7), 1417–1430. https://doi.org/10.1016/j.bpj.2017.02.032

Baker, J. A., Wong, W.-C., Eisenhaber, B., Warwicker, J., & Eisenhaber, F. (2017). Charged residues next to transmembrane regions revisited: "Positive-inside rule" is complemented by the "negative inside depletion/outside enrichment rule." *BMC Biology*, *15*(1), 66. https://doi.org/10.1186/s12915-017-0404-4

Balali-Mood, Peter J. Bond, & Mark S.P. Sansom. (2009). Interaction of Monotopic Membrane Enzymes with a Lipid Bilayer: A Coarse-Grained MD Simulation Study†. *Biochemistry*. https://doi.org/10.1021/bi8017398

Bartz, R., Li, W. H., Venables, B. J., Zehmer, J. K., Roth, M. R., Welti, R., Anderson, R. G. W., Liu, P., & Chapman, K. D. (2007). Lipidomics reveals that adiposomes store ether lipids and mediate phospholipid traffic. *Journal of Lipid Research*, *48*(4), 837–847. https://doi.org/10.1194/jlr.m600413-jlr200

Becuwe, M., Bond, L. M., Pinto, A., Pinto, A. M., Antônio F.M. Pinto, Boland, S., Mejhert, N., Elliott, S. D., Cicconet, M., Graham, M., Liu, X., Ilkayeva, O., Saghatelian, A., Walther, T. C., & Farese, R. V. (2020). FIT2 is an acyl–coenzyme A diphosphatase crucial for endoplasmic reticulum homeostasis. *Journal of Cell Biology*, *219*(10). https://doi.org/10.1083/jcb.202006111

Beller, M., Riedel, D., Jänsch, L., Dieterich, G., Jürgen Wehland, Wehland, J., Jäckle, H., & Kühnlein, R. P. (2006). Characterization of the Drosophila Lipid Droplet Subproteome. *Molecular & Cellular Proteomics*, *5*(6), 1082–1094. https://doi.org/10.1074/mcp.m600011-mcp200

Berardinelli, W. (1954). An undiagnosed endocrinometabolic syndrome: Report of 2 cases. *The Journal of Clinical Endocrinology and Metabolism*, *14*(2), 193–204. https://doi.org/10.1210/jcem-14-2-193

Berendsen, H., Berendsen, H. J. C., Postma, J. P. M., van Gunsteren, W. F., DiNola, A., & Haak, J. R. (1984). Molecular dynamics with coupling to an external bath. *Journal of Chemical Physics*, *81*(8), 3684–3690. https://doi.org/10.1063/1.448118

Bersuker, K., Kirill Bersuker, Peterson, C. W. H., To, M., Sahl, S. J., Savikhin, V., Grossman, E. A., Nomura, D. K., & Olzmann, J. A. (2018). A Proximity Labeling Strategy Provides Insights into the Composition and Dynamics of Lipid Droplet Proteomes. *Developmental Cell*, *44*(1), 97–112. https://doi.org/10.1016/j.devcel.2017.11.020

Bersuker, K., & Olzmann, J. A. (2017). Establishing the lipid droplet proteome: Mechanisms of lipid droplet protein targeting and degradation. *Biochimica et Biophysica Acta (BBA) - Molecular and Cell Biology of Lipids*, *1862*(10), 1166–1177. https://doi.org/10.1016/j.bbalip.2017.06.006

Bersuker, K., & Olzmann, J. A. (2019). Identification of Lipid Droplet Proteomes by Proximity Labeling Proteomics Using APEX2. In M. Sunbul & A. Jäschke (Eds.), *Proximity Labeling* (Vol. 2008, pp. 57–72). Springer New York. https://doi.org/10.1007/978-1-4939-9537-0_5

Binns, D., Lee, S., Hilton, C. L., Jiang, Q.-X., & Goodman, J. M. (2010). Seipin is a discrete homooligomer. *Biochemistry*, *49*(50), 10747–10755. https://doi.org/10.1021/bi1013003

Blanchette-Mackie, E. J., Dwyer, N. K., Barber, T., Coxey, R. A., R A Coxey, Takeda, T., Rondinone, C. M., Theodorakis, J. L., Greenberg, A. S., & Londos, C. (1995). Perilipin is located on the surface layer of intracellular lipid droplets in adipocytes. *Journal of Lipid Research*, *36*(6), 1211–1226.

Blobel, Peter Walter, & Reid Gilmore. (1980). Intracellular protein topogenesis. *Proceedings of the National Academy of Sciences of the United States of America*. https://doi.org/10.1007/978-3-642-68211-7_22

Boeszoermenyi, A., Nagy, H. M., Arthanari, H., Pillip, C. J., Lindermuth, H., Luna, R. E., Wagner, G., Zechner, R., Zangger, K., & Oberer, M. (2015). Structure of a CGI-58 motif provides the molecular basis of lipid droplet anchoring. *Journal of Biological Chemistry*, *290*(44), 26361–26372. https://doi.org/10.1074/jbc.m115.682203

Bogdanov, M., Dowhan, W., & Vitrac, H. (2014). Lipids and topological rules governing membrane protein assembly. *Biochimica et Biophysica Acta (BBA) - Molecular Cell Research*, *1843*(8), 1475–1488. https://doi.org/10.1016/j.bbamcr.2013.12.007

Bogdanov, M., Heacock, P. N., & Dowhan, W. (2010). Study of polytopic membrane protein topological organization as a function of membrane lipid composition. *Methods in Molecular Biology (Clifton, N.J.)*, *619*, 79–101. https://doi.org/10.1007/978-1-60327-412-8_5

Bogdanov, M., Xie, J., & Dowhan, W. (2009). Lipid-Protein Interactions Drive Membrane Protein Topogenesis in Accordance with the Positive Inside Rule.

Journal of Biological Chemistry, *284*(15), 9637–9641. https://doi.org/10.1074/jbc.R800081200

Bogdanov, M., Zhang, W., Xie, J., & Dowhan, W. (2005). Transmembrane protein topology mapping by the substituted cysteine accessibility method (SCAMTM): Application to lipid-specific membrane protein topogenesis. *Methods*, *36*(2), 148–171. https://doi.org/10.1016/j.ymeth.2004.11.002

Bohnert, M. (2020a). New friends for seipin—Implications of seipin partner proteins in the life cycle of lipid droplets. *Seminars in Cell & Developmental Biology*, *108*, 24–32. https://doi.org/10.1016/j.semcdb.2020.04.012

Bohnert, M. (2020b). Tethering Fat: Tethers in Lipid Droplet Contact Sites. *Contact*, *3*, 251525642090814. https://doi.org/10.1177/2515256420908142

Borgese, N., & Fasana, E. (2011). Targeting pathways of C-tail-anchored proteins. *Biochimica et Biophysica Acta (BBA) - Biomembranes*, *1808*(3), 937–946. https://doi.org/10.1016/j.bbamem.2010.07.010

Bosch, M., & Pol, A. (2022). Eukaryotic lipid droplets: Metabolic hubs, and immune first responders. *Trends in Endocrinology & Metabolism*, *33*(3), 218–229. https://doi.org/10.1016/j.tem.2021.12.006

Bosch, M., Sánchez-Álvarez, M., Fajardo, A., Kapetanovic, R., Steiner, B., Dutra, F., Moreira, L., López, J. A., Campo, R., Marí, M., Morales-Paytuví, F., Tort, O., Gubern, A., Templin, R. M., Curson, J. E. B., Martel, N., Català, C., Lozano, F., Tebar, F., … Pol, A. (2020). Mammalian lipid droplets are innate immune hubs integrating cell metabolism and host defense. *Science*, *370*(6514), eaay8085. https://doi.org/10.1126/science.aay8085

Boström, P., Andersson, L., Rutberg, M., Perman, J., Lidberg, U., Johansson, B., Fernandez-Rodriguez, J., Ericson, J., Nilsson, T., Borén, J., & Olofsson, S.-O. (2007). SNARE proteins mediate fusion between cytosolic lipid droplets and are implicated in insulin sensitivity. *Nature Cell Biology*, *9*(11), 1286–1293. https://doi.org/10.1038/ncb1648

Brady, J. P., Claridge, J. K., Smith, P. G., & Schnell, J. R. (2015). A conserved amphipathic helix is required for membrane tubule formation by Yop1p. *Proceedings of the National Academy of Sciences*, *112*(7). https://doi.org/10.1073/pnas.1415882112

Brasaemle, D. L., Barber, T., Wolins, N. E., Serrero, G., Blanchette-Mackie, E. J., & Londos, C. (1997). Adipose differentiation-related protein is an ubiquitously

expressed lipid storage droplet-associated protein. *Journal of Lipid Research*, *38*(11), 2249–2263.

Brasaemle, D. L., Dolios, G., Shapiro, L., & Wang, R. (2004). Proteomic Analysis of Proteins Associated with Lipid Droplets of Basal and Lipolytically Stimulated 3T3-L1 Adipocytes *. *Journal of Biological Chemistry*, *279*(45), 46835–46842. https://doi.org/10.1074/jbc.m409340200

Buhman, K. K., Chen, H., & Farese, R. V. (2001). The enzymes of neutral lipid synthesis. *Journal of Biological Chemistry*, *276*(44), 40369–40372. https://doi.org/10.1074/jbc.r100050200

Caillon, L., Nieto, V., Gehan, P., Omrane, M., Rodriguez, N., Monticelli, L., & Thiam, A. R. (2020). Triacylglycerols sequester monotopic membrane proteins to lipid droplets. *Nature Communications*, *11*(1), 3944. https://doi.org/10.1038/s41467-020-17585-8

Caldas, H. (2003). NSDHL, an enzyme involved in cholesterol biosynthesis, traffics through the Golgi and accumulates on ER membranes and on the surface of lipid droplets. *Human Molecular Genetics*, *12*(22), 2981–2991. https://doi.org/10.1093/hmg/ddg321

Castro, I. G., Eisenberg-Bord, M., Persiani, E., Rochford, J. J., Schuldiner, M., & Bohnert, M. (2019). Promethin Is a Conserved Seipin Partner Protein. *Cells*, *8*(3), 268. https://doi.org/10.3390/cells8030268

Cerk, I. K., Salzburger, B., Boeszoermenyi, A., Heier, C., Pillip, C. J., Romauch, M., Schweiger, M., Cornaciu, I., Lass, A., Zimmermann, R., Zechner, R., & Oberer, M. (2014). A peptide derived from G0/G1 switch gene 2 acts as noncompetitive inhibitor of adipose triglyceride lipase. *Journal of Biological Chemistry*, *289*(47), 32559–32570. https://doi.org/10.1074/jbc.m114.602599

Chang, T.-Y., Li, B.-L., Chang, C. C. Y., & Urano, Y. (2009). ACYL-COENZYME A:CHOLESTEROL ACYLTRANSFERASE. *American Journal of Physiology-Endocrinology and Metabolism*, *66*(1), 613–638. https://doi.org/10.1152/ajpendo.90926.2008

Chen, F., Yan, B., Ren, J., Lyu, R., Yanfang Wu, Wu, Y., Guo, Y., Li, D., Zhang, H., & Hu, J. (2021). FIT2 organizes lipid droplet biogenesis with ER tubule-forming proteins and septins. *Journal of Cell Biology*, *220*(5). https://doi.org/10.1083/jcb.201907183

Chio, U. S., Cho, H., & Shan, S. (2017). Mechanisms of Tail-Anchored Membrane Protein Targeting and Insertion. *Annual Review of Cell and Developmental Biology*, *33*(1), 417–438. https://doi.org/10.1146/annurev-cellbio-100616-060839

Chorlay, A., Monticelli, L., Veríssimo Ferreira, J., Ben M'barek, K., Ajjaji, D., Wang, S., Johnson, E., Beck, R., Omrane, M., Beller, M., Carvalho, P., & Rachid Thiam, A. (2019). Membrane Asymmetry Imposes Directionality on Lipid Droplet Emergence from the ER. *Developmental Cell*, *50*(1), 25-42.e7. https://doi.org/10.1016/j.devcel.2019.05.003

Chorlay, A., & Thiam, A. R. (2018). An Asymmetry in Monolayer Tension Regulates Lipid Droplet Budding Direction. *Biophysical Journal*, *114*(3), 631–640. https://doi.org/10.1016/j.bpj.2017.12.014

Chorlay, A., & Thiam, A. R. (2020). Neutral lipids regulate amphipathic helix affinity for model lipid droplets. *Journal of Cell Biology*, *219*(4), e201907099. https://doi.org/10.1083/jcb.201907099

Choudhary, V., El Atab, O., Mizzon, G., Prinz, W. A., & Schneiter, R. (2020). Seipin and Nem1 establish discrete ER subdomains to initiate yeast lipid droplet biogenesis. *Journal of Cell Biology*, *219*(7), e201910177. https://doi.org/10.1083/jcb.201910177

Choudhary, V., Golani, G., Joshi, A. S., Cottier, S., Schneiter, R., Prinz, W. A., & Kozlov, M. M. (2018). Architecture of Lipid Droplets in Endoplasmic Reticulum Is Determined by Phospholipid Intrinsic Curvature. *Current Biology*, *28*(6), 915-926.e9. https://doi.org/10.1016/j.cub.2018.02.020

Choudhary, V., Golden, A., & Prinz, W. A. (2016). Keeping FIT, storing fat: Lipid droplet biogenesis. *Worm*, *5*(2). https://doi.org/10.1080/21624054.2016.1170276

Choudhary, V., Ojha, N., Golden, A., & Prinz, W. A. (2015). A conserved family of proteins facilitates nascent lipid droplet budding from the ER. *Journal of Cell Biology*, *211*(2), 261–271. https://doi.org/10.1083/jcb.201505067

Choudhary, V., & Schneiter, R. (2020). Lipid droplet biogenesis from specialized ER subdomains. *Microbial Cell*, *7*(8), 218–221. https://doi.org/10.15698/mic2020.08.727

Christianson, J. C., James A. Olzmann, Olzmann, J. A., Shaler, T. A., Sowa, M. E., Bennett, E. J., Richter, C. M., Caleb M. Richter, Tyler, R. E., Greenblatt, E. J.,

Harper, J. W., & Kopito, R. R. (2012). Defining human ERAD networks through an integrative mapping strategy. *Nature Cell Biology*, *14*(1), 93–105. https://doi.org/10.1038/ncb2383

Chung, Wu, X., Lambert, T. J., Lai, Z. W., Walther, T. C., & Farese, R. V. (2019). LDAF1 and Seipin Form a Lipid Droplet Assembly Complex. *Developmental Cell*, *51*(5), 551. https://doi.org/10.1016/j.devcel.2019.10.006

Coleman, R. A. (2020). The “discovery” of lipid droplets: A brief history of organelles hidden in plain sight. *Biochimica et Biophysica Acta (BBA) - Molecular and Cell Biology of Lipids*, *1865*(9), 158762. https://doi.org/10.1016/j.bbalip.2020.158762

Coleman, R. A., & Lee, D. P. (2004). Enzymes of triacylglycerol synthesis and their regulation. *Progress in Lipid Research*, *43*(2), 134–176. https://doi.org/10.1016/s0163-7827(03)00051-1

Čopič, A., Antoine-Bally, S., Giménez-Andrés, M., La Torre Garay, C., Antonny, B., Manni, M. M., Pagnotta, S., Guihot, J., & Jackson, C. L. (2018). A giant amphipathic helix from a perilipin that is adapted for coating lipid droplets. *Nature Communications*, *9*(1), 1332. https://doi.org/10.1038/s41467-018-03717-8

Cornell, R. B. (2016). Membrane lipid compositional sensing by the inducible amphipathic helix of CCT. *Biochimica et Biophysica Acta (BBA) - Molecular and Cell Biology of Lipids*, *1861*(8), 847–861. https://doi.org/10.1016/j.bbalip.2015.12.022

Corradi, V., Mendez-Villuendas, E., Ingólfsson, H. I., Gu, R.-X., Siuda, I., Melo, M. N., Moussatova, A., DeGagné, L. J., Sejdiu, B. I., Singh, G., Wassenaar, T. A., Delgado Magnero, K., Marrink, S. J., & Tieleman, D. P. (2018). Lipid–Protein Interactions Are Unique Fingerprints for Membrane Proteins. *ACS Central Science*, *4*(6), 709–717. https://doi.org/10.1021/acscentsci.8b00143

Currie, E., Guo, X., Christiano, R., Chitraju, C., Kory, N., Harrison, K. D., Haas, J. T., Walther, T. C., & Farese, R. V. (2014). High confidence proteomic analysis of yeast LDs identifies additional droplet proteins and reveals connections to dolichol synthesis and sterol acetylation. *Journal of Lipid Research*, *55*(7), 1465–1477. https://doi.org/10.1194/jlr.m050229

Czabany, T., Wagner, A., Zweytick, D., Lohner, K., Leitner, E., Ingolic, E., & Daum, G. (2008). Structural and Biochemical Properties of Lipid Particles from the

Yeast Saccharomyces cerevisiae. *Journal of Biological Chemistry*, *283*(25), 17065–17074. https://doi.org/10.1074/jbc.m800401200

Darden, T., York, D. M., & Pedersen, L. G. (1993). Particle mesh Ewald: An N·log(N) method for Ewald sums in large systems. *Journal of Chemical Physics*, *98*(12), 10089–10092. https://doi.org/10.1063/1.464397

Datta, S., Liu, Y., Hariri, H., Bowerman, J., & Henne, W. M. (2019). Cerebellar ataxia disease-associated Snx14 promotes lipid droplet growth at ER-droplet contacts. *Journal of Cell Biology*, *218*(4), 1335–1351. https://doi.org/10.1083/jcb.201808133

Dejgaard, S. Y., & Presley, J. F. (2019). Rab18: New insights into the function of an essential protein. *Cellular and Molecular Life Sciences*, *76*(10), 1935–1945. https://doi.org/10.1007/s00018-019-03050-3

Dhiman, R., Caesar, S., Thiam, A. R., & Schrul, B. (2020). Mechanisms of protein targeting to lipid droplets: A unified cell biological and biophysical perspective. *Seminars in Cell & Developmental Biology*, *108*, 4–13. https://doi.org/10.1016/j.semcdb.2020.03.004

Dias, Vinicius Cardoso Soares, Vinicius Cardoso Soares, André C. Ferreira, Carolina Q. Sacramento, Natalia Fintelman-Rodrigues, Jairo R. Temerozo, Lívia Teixeira, Ester A. Barreto, Mayara Mattos, Caroline S. de Freitas, Isaclaudia G. de Azevedo-Quintanilha, Pedro P. A. Manso, Eugenio D. Hottz, Camila R. R. Pão, Dumith Chequer Bou-Habib, Fernando A. Bozza, Thiago Moreno L. Souza, & Patrícia T. Bozza. (2020). Lipid droplets fuels SARS-CoV-2 replication and inflammatory response. *bioRxiv*. https://doi.org/10.1101/2020.08.22.262733

Doerr, A. (2009). Membrane protein structures. *Nature Methods*, *6*(1), 35–35. https://doi.org/10.1038/nmeth.f.240

Doll, S., Freitas, F. P., Shah, R., Aldrovandi, M., da Silva, M. C., Ingold, I., Goya Grocin, A., Xavier da Silva, T. N., Panzilius, E., Scheel, C. H., Mourão, A., Buday, K., Sato, M., Wanninger, J., Vignane, T., Mohana, V., Rehberg, M., Flatley, A., Schepers, A., … Conrad, M. (2019). FSP1 is a glutathione-independent ferroptosis suppressor. *Nature*, *575*(7784), 693–698. https://doi.org/10.1038/s41586-019-1707-0

Dollet, L., Magré, J., Cariou, B., & Prieur, X. (2014). Function of seipin: New insights from Bscl2/seipin knockout mouse models. *Biochimie*, *96*, 166–172. https://doi.org/10.1016/j.biochi.2013.06.022

Du, X., Zhou, L., Aw, Y. C., Mak, H. Y., Xu, Y., Rae, J., Wang, W., Zadoorian, A., Hancock, S. E., Osborne, B., Chen, X., Wu, J.-W., Jia-Wei Wu, Turner, N., Parton, R. G., Li, P., Li, P., & Yang, H. (2020). ORP5 localizes to ER-lipid droplet contacts and regulates the level of PI(4)P on lipid droplets. *Journal of Cell Biology*, *219*(1). https://doi.org/10.1083/jcb.201905162

Dubey, R., Craig, S., Nguyen, H. Q., Goo, Y.-H., Paul, A., Carette, J. E., Trost, B. M., & Rohatgi, R. (2020). Lipid droplets can promote drug accumulation and activation. *Nature Chemical Biology*, *16*(2), 206–213. https://doi.org/10.1038/s41589-019-0447-7

Eisenberg-Bord, M., Mari, M., Weill, U., Rosenfeld-Gur, E., Moldavski, O., Castro, I. G., Soni, K. G., Harpaz, N., Levine, T. P., Futerman, A. H., Reggiori, F., Bankaitis, V. A., Schuldiner, M., & Bohnert, M. (2018). Identification of seipin-linked factors that act as determinants of a lipid droplet subpopulation. *Journal of Cell Biology*, *217*(1), 269–282. https://doi.org/10.1083/jcb.201704122

Ellis, J. M., Frahm, J. L., Li, L. O., & Coleman, R. A. (2010). Acyl-coenzyme A synthetases in metabolic control. *Current Opinion in Lipidology*, *21*(3), 212–217. https://doi.org/10.1097/mol.0b013e32833884bb

Elofsson, A., & von Heijne, G. (2007). Membrane protein structure: Prediction versus reality. *Annual Review of Biochemistry*, *76*, 125–140. https://doi.org/10.1146/annurev.biochem.76.052705.163539

Engelman, D. M., Steitz, T. A., & Goldman, A. (1986). Identifying nonpolar transbilayer helices in amino acid sequences of membrane proteins. *Annual Review of Biophysics and Biophysical Chemistry*, *15*(1), 321–353. https://doi.org/10.1146/annurev.bb.15.060186.001541

Enkavi, G., Javanainen, M., Kulig, W., Róg, T., & Vattulainen, I. (2019). Multiscale Simulations of Biological Membranes: The Challenge To Understand Biological Phenomena in a Living Substance. *Chemical Reviews*, *119*(9), 5607–5774. https://doi.org/10.1021/acs.chemrev.8b00538

Entova, S., Billod, J.-M., Swiecicki, J.-M., Martín-Santamaría, S., & Imperiali, B. (2018). Insights into the key determinants of membrane protein topology

enable the identification of new monotopic folds. *eLife*, *7*, e40889. https://doi.org/10.7554/eLife.40889

Eriksson, H. M., Persson, K., Zhang, S., Shuguang Zhang, & Wieslander, Å. (2009). High-yield expression and purification of a monotopic membrane glycosyltransferase. *Protein Expression and Purification*, *66*(2), 143–148. https://doi.org/10.1016/j.pep.2009.03.008

Essmann, U., Perera, L., Berkowitz, M. L., Darden, T., Lee, H., & Pedersen, L. G. (1995). A smooth particle mesh Ewald method. *Journal of Chemical Physics*, *103*(19), 8577–8593. https://doi.org/10.1063/1.470117

Farese, R. V., & Walther, T. C. (2009). Lipid Droplets Finally Get a Little R-E-S-P-E-C-T. *Cell*, *139*(5), 855–860. https://doi.org/10.1016/j.cell.2009.11.005

Farré, J.-C., Mahalingam, S. S., Proietto, M., & Subramani, S. (2019). Peroxisome biogenesis, membrane contact sites, and quality control. *EMBO Reports*, *20*(1). https://doi.org/10.15252/embr.201846864

Fei, W., Shui, G., Gaeta, B., Du, X., Kuerschner, L., Li, P., Brown, A. J., Wenk, M. R., Parton, R. G., & Yang, H. (2008). Fld1p, a functional homologue of human seipin, regulates the size of lipid droplets in yeast. *Journal of Cell Biology*, *180*(3), 473–482. https://doi.org/10.1083/jcb.200711136

Fowler, P. W., Balali-Mood, K., Deol, S. S., Coveney, P. V., & Sansom, M. S. P. (2007). Monotopic enzymes and lipid bilayers: A comparative study. *Biochemistry*, *46*(11), 3108–3115. https://doi.org/10.1021/bi602455n

Fujimoto, T., & Parton, R. G. (2011). Not just fat: The structure and function of the lipid droplet. *Cold Spring Harbor Perspectives in Biology*, *3*(3). https://doi.org/10.1101/cshperspect.a004838

Giménez-Andrés, Manuel Giménez-Andrés, Manuel Gimenez-Andres, Tadej Emeršič, Sandra Antoine-Bally, Sandra Antoine-Bally, Sandra Antoine-Bally, Juan Martin D'Ambrosio, Juan Martin D'Ambrosio, Juan Martin D'Ambrosio, Bruno Antonny, Jure Derganc, Alenka Čopič, & Alenka Čopič. (2021). Exceptional stability of a perilipin on lipid droplets depends on its polar residues, suggesting multimeric assembly. *eLife*. https://doi.org/10.7554/elife.61401

Gimeno, R. E., & Cao, J. (2008). Thematic Review Series: Glycerolipids. Mammalian glycerol-3-phosphate acyltransferases: new genes for an old activity. *Journal*

of Lipid Research, *49*(10), 2079–2088. https://doi.org/10.1194/jlr.R800013-JLR200

Gong, J., Sun, Z., Wu, L., Xu, W., Nicole L. Schieber, Schieber, N. L., Xu, D., Shui, G., Yang, H., Parton, R. G., Li, P., & Li, P. (2011). Fsp27 promotes lipid droplet growth by lipid exchange and transfer at lipid droplet contact sites. *Journal of Cell Biology*, *195*(6), 953–963. https://doi.org/10.1083/jcb.201104142

Grabner, G. F., Xie, H., Schweiger, M., & Zechner, R. (2021). Lipolysis: Cellular mechanisms for lipid mobilization from fat stores. *Nature Metabolism*, *3*(11), 1445–1465. https://doi.org/10.1038/s42255-021-00493-6

Greenberg, A. S., Egan, J. J., Wek, S. A., Garty, N. B., E J Blanchette-Mackie, Blanchette-Mackie, E. J., & Londos, C. (1991). Perilipin, a major hormonally regulated adipocyte-specific phosphoprotein associated with the periphery of lipid storage droplets. *Journal of Biological Chemistry*, *266*(17), 11341–11346. https://doi.org/10.1016/s0021-9258(18)99168-4

Greenwood, D. J., Santos, M. S. dos, Huang, S., Russell, M. R. G., Collinson, L. M., Lucy M. Collinson, MacRae, J. I., James I. MacRae, West, A., Jiang, H., & Gutierrez, M. G. (2019). Subcellular antibiotic visualization reveals a dynamic drug reservoir in infected macrophages. *Science*, *364*(6447), 1279–1282. https://doi.org/10.1126/science.aat9689

Grippa, A., Buxó, L., Mora, G., Funaya, C., Idrissi, F.-Z., Mancuso, F., Gomez, R., Muntanyà, J., Sabidó, E., & Carvalho, P. (2015). The seipin complex Fld1/Ldb16 stabilizes ER–lipid droplet contact sites. *Journal of Cell Biology*, *211*(4), 829–844. https://doi.org/10.1083/jcb.201502070

Gross, D. A., Chenyang Zhan, Zhan, C., & Silver, D. L. (2011). Direct binding of triglyceride to fat storage-inducing transmembrane proteins 1 and 2 is important for lipid droplet formation. *Proceedings of the National Academy of Sciences of the United States of America*, *108*(49), 19581–19586. https://doi.org/10.1073/pnas.1110817108

Gross, D. A., Snapp, E. L., & Silver, D. L. (2010). Structural insights into triglyceride storage mediated by fat storage-inducing transmembrane (FIT) protein 2. *PLOS ONE*, *5*(5). https://doi.org/10.1371/journal.pone.0010796

Guan, X. L., Cestra, G., Gianluca Cestra, Shui, G., Kuhrs, A., Schittenhelm, R. B., Hafen, E., van der Goot, F. G., Robinett, C. C., Gatti, M., González-Gaitán,

M., & Wenk, M. R. (2013). Biochemical Membrane Lipidomics during Drosophila Development. *Developmental Cell*, *24*(1), 98–111. https://doi.org/10.1016/j.devcel.2012.11.012

Guo, Y., Walther, T. C., Rao, M., Stuurman, N., Goshima, G., Terayama, K., Wong, J. S., Vale, R. D., Walter, P., & Farese, R. V. (2008). Functional genomic screen reveals genes involved in lipid-droplet formation and utilization. *Nature*, *453*(7195), 657–661. https://doi.org/10.1038/nature06928

Hariri, H., Rogers, S., Ugrankar, R., Liu, Y. L., Feathers, J. R., & Henne, W. M. (2018). Lipid droplet biogenesis is spatially coordinated at ER–vacuole contacts under nutritional stress. *EMBO Reports*, *19*(1), 57–72. https://doi.org/10.15252/embr.201744815

Hariri, H., Speer, N. O., Bowerman, J., Rogers, S., Fu, G., E, R., Evan Reetz, Datta, S., Feathers, J. R., Ugrankar, R., Nicastro, D., & Henne, W. M. (2019). Mdm1 maintains endoplasmic reticulum homeostasis by spatially regulating lipid droplet biogenesis. *Journal of Cell Biology*, *218*(4), 1319–1334. https://doi.org/10.1083/jcb.201808119

Harris et al.,. (2011). DGAT enzymes are required for triacylglycerol synthesis and lipid droplets in adipocytes. *Journal of Lipid Research*. https://doi.org/10.1194/jlr.m013003

Hegde, R. S., & Keenan, R. J. (2022). The mechanisms of integral membrane protein biogenesis. *Nature Reviews Molecular Cell Biology*, *23*(2), 107–124. https://doi.org/10.1038/s41580-021-00413-2

Henne, W. M. (2020). *The Molecular Era of Lipid Droplets*. *3*, 251525642091209. https://doi.org/10.1177/2515256420912090

Henne, W. M., Zhu, L., Lu Zhu, Zsolt Balogi, Zsolt Balogi, Balogi, Z., Stefan, C. J., Pleiss, J. A., & Emr, S. D. (2015). Mdm1/Snx13 is a novel ER–endolysosomal interorganelle tethering protein. *Journal of Cell Biology*, *210*(4), 541–551. https://doi.org/10.1083/jcb.201503088

Herker, E., & Ott, M. (2011). Unique ties between hepatitis C virus replication and intracellular lipids. *Trends in Endocrinology and Metabolism*, *22*(6), 241–248. https://doi.org/10.1016/j.tem.2011.03.004

Hikita, C., & Mizushima, S. (1992). Effects of total hydrophobicity and length of the hydrophobic domain of a signal peptide on in vitro translocation efficiency.

Journal of Biological Chemistry, *267*(7), 4882–4888. https://doi.org/10.1016/S0021-9258(18)42913-4

Hoover, W. G. (1985). Canonical dynamics: Equilibrium phase-space distributions. *Physical Review A*, *31*(3), 1695–1697. https://doi.org/10.1103/physreva.31.1695

Hope, R. Graham Hope, Denis J. Murphy, John McLauchlan, & John McLauchlan. (2002). The domains required to direct core proteins of hepatitis C virus and GB virus-B to lipid droplets share common features with plant oleosin proteins. *Journal of Biological Chemistry*. https://doi.org/10.1074/jbc.m108798200

Huang. (1992). *Oil bodies and oleosins in seeds*. *43*(1), 177–200. https://doi.org/10.1146/annurev.pp.43.060192.001141

Huang. (1996). Oleosins and oil bodies in seeds and other organs. *Plant Physiology*. https://doi.org/10.1104/pp.110.4.1055

Huang, J., Rauscher, S., Nawrocki, G., Ran, T., Feig, M., de Groot, B. L., Grubmüller, H., & MacKerell, A. D. (2017). CHARMM36m: An improved force field for folded and intrinsically disordered proteins. *Nature Methods*, *14*(1), 71–73. https://doi.org/10.1038/nmeth.4067

Humphrey, W., Dalke, A., & Schulten, K. (1996). VMD: Visual molecular dynamics. *Journal of Molecular Graphics*, *14*(1), 33–38, 27–28. https://doi.org/10.1016/0263-7855(96)00018-5

Hunag. (1996). Oleosins and oil bodies in seeds and other organs. *Plant Physiology*, *110*(4), 1055–1061. https://doi.org/10.1104/pp.110.4.1055

Imai, N., Suzuki, M., Hayashi, K., Ishigami, M., Hirooka, Y., Abe, T., Shioi, G., Goto, H., & Fujimoto, T. (2015). Hepatocyte-Specific Depletion of UBXD8 Induces Periportal Steatosis in Mice Fed a High-Fat Diet. *PLOS ONE*, *10*(5), e0127114. https://doi.org/10.1371/journal.pone.0127114

Ingelmo-Torres, M., González-Moreno, E., Kassan, A., Hanzal-Bayer, M., Tebar, F., Herms, A., Grewal, T., Hancock, J. F., Enrich, C., Bosch, M., Gross, S. P., Parton, R. G., & Pol, A. (2009). Hydrophobic and basic domains target proteins to lipid droplets. *Traffic*, *10*(12), 1785–1801. https://doi.org/10.1111/j.1600-0854.2009.00994.x

Islam, S. T., & Lam, J. S. (2013). Topological mapping methods for α-helical bacterial membrane proteins – an update and a guide. *MicrobiologyOpen*, *2*(2), 350–364. https://doi.org/10.1002/mbo3.72

Itabe, H., Yamaguchi, T., Nimura, S., & Sasabe, N. (2017). Perilipins: A diversity of intracellular lipid droplet proteins. *Lipids in Health and Disease*, *16*(1), 83. https://doi.org/10.1186/s12944-017-0473-y

Jackson, C. L. (2019). Lipid droplet biogenesis. *Current Opinion in Cell Biology*, *59*, 88–96. https://doi.org/10.1016/j.ceb.2019.03.018

Jacquier, N., Choudhary, V., Mari, M., Toulmay, A., Reggiori, F., & Schneiter, R. (2011). Lipid droplets are functionally connected to the endoplasmic reticulum in Saccharomyces cerevisiae. *Journal of Cell Science*, *124*(14), 2424–2437. https://doi.org/10.1242/jcs.076836

Jansen, R. L. M., & Klei, I. J. (2019). The peroxisome biogenesis factors Pex3 and Pex19: Multitasking proteins with disputed functions. *FEBS Letters*, *593*(5), 457–474. https://doi.org/10.1002/1873-3468.13340

Javanainen, M., & Martinez-Seara, H. (2016). Efficient preparation and analysis of membrane and membrane protein systems. *Biochimica Et Biophysica Acta*, *1858*(10), 2468–2482. https://doi.org/10.1016/j.bbamem.2016.02.036

Jiang, W., & Napoli, J. L. (2013). The Retinol Dehydrogenase Rdh10 Localizes to Lipid Droplets during Acyl Ester Biosynthesis. *Journal of Biological Chemistry*, *288*(1), 589–597. https://doi.org/10.1074/jbc.M112.402883

Jones, H. E., Harwood, J. L., Bowen, I. D., & Griffiths, G. (1992). Lipid composition of subcellular membranes from larvae and prepupae of Drosophila melanogaster. *Lipids*, *27*(12), 984–987. https://doi.org/10.1007/bf02535576

Joshi, A. S., & Cohen, S. (2019). Lipid Droplet and Peroxisome Biogenesis: Do They Go Hand-in-Hand? *Frontiers in Cell and Developmental Biology*, *7*, 92. https://doi.org/10.3389/fcell.2019.00092

Joshi, A. S., Huang, X., Choudhary, V., Levine, T. P., Hu, J., & Prinz, W. A. (2016). A family of membrane-shaping proteins at ER subdomains regulates pre-peroxisomal vesicle biogenesis. *Journal of Cell Biology*, *215*(4), 515–529. https://doi.org/10.1083/jcb.201602064

Joshi, A. S., Nebenfuehr, B., Choudhary, V., Satpute-Krishnan, P., Levine, T. P., Golden, A., & Prinz, W. A. (2018). Lipid droplet and peroxisome biogenesis

occur at the same ER subdomains. *Nature Communications*, *9*(1), 2940. https://doi.org/10.1038/s41467-018-05277-3

Joshi, A. S., Ragusa, J. V., Prinz, W. A., & Cohen, S. (2021). Multiple C2 domain-containing transmembrane proteins promote lipid droplet biogenesis and growth at specialized endoplasmic reticulum subdomains. *Molecular Biology of the Cell*, *32*(12), 1147–1157. https://doi.org/10.1091/mbc.E20-09-0590

Kadereit, B., Kadereit, B., Kumar, P., Kumar, P., Pradeep Kumar, Pradeep Kumar, Kumar, P. K. P., Kumar, P. K. A., Kumar, P., Wang, W. J., Miranda, D. A., Snapp, E. L., Severina, N., Torregroza, I., Evans, T., & Silver, D. L. (2008). Evolutionarily conserved gene family important for fat storage. *Proceedings of the National Academy of Sciences of the United States of America*, *105*(1), 94–99. https://doi.org/10.1073/pnas.0708579105

Kassan, A., Herms, A., Fernández-Vidal, A., Bosch, M., Schieber, N. L., Reddy, B. J. N., Fajardo, A., Gelabert-Baldrich, M., Tebar, F., Enrich, C., Gross, S. P., Parton, R. G., & Pol, A. (2013). Acyl-CoA synthetase 3 promotes lipid droplet biogenesis in ER microdomains. *Journal of Cell Biology*, *203*(6), 985–1001. https://doi.org/10.1083/jcb.201305142

Kennedy, E. P. (1957). Metabolism of Lipides. *Annual Review of Biochemistry*, *26*(1), 119–148. https://doi.org/10.1146/annurev.bi.26.070157.001003

Khaddaj, R., Mari, M., Cottier, S., Reggiori, F., & Schneiter, R. (2021). The surface of lipid droplets constitutes a barrier for endoplasmic reticulum-resident integral membrane proteins. *Journal of Cell Science*, *135*(5), 1–47. https://doi.org/10.1242/jcs.256206

Khan, H. M., MacKerell, A. D., & Reuter, N. (2019). Cation-π Interactions between Methylated Ammonium Groups and Tryptophan in the CHARMM36 Additive Force Field. *Journal of Chemical Theory and Computation*, *15*(1), 7–12. https://doi.org/10.1021/acs.jctc.8b00839

Khandelia, H., Duelund, L., Pakkanen, K. I., & Ipsen, J. H. (2010). Triglyceride Blisters in Lipid Bilayers: Implications for Lipid Droplet Biogenesis and the Mobile Lipid Signal in Cancer Cell Membranes. *PLOS ONE*, *5*(9). https://doi.org/10.1371/journal.pone.0012811

Khelef, N., Buton, X., Beatini, N., Wang, H., Meiner, V. L., Ta-Yuan Chang, Chang, T.-Y., Farese, R. V., Maxfield, F. R., Ira Tabas, Ira Tabas, & Tabas, I. (1998). IMMUNOLOCALIZATION OF ACYL-COENZYME A:CHOLESTEROL O-

ACYLTRANSFERASE IN MACROPHAGES. *Journal of Biological Chemistry*, *273*(18), 11218–11224. https://doi.org/10.1074/jbc.273.18.11218

Kim, H., Zhang, H., Meng, D., Russell, G., Lee, J. N., & Ye, J. (2013). UAS domain of Ubxd8 and FAF1 polymerizes upon interaction with long-chain unsaturated fatty acids. *Journal of Lipid Research*, *54*(8), 2144–2152. https://doi.org/10.1194/jlr.m037218

Kim, S., Chung, J., Arlt, H., Pak, A. J., Farese, R. V., Walther, T. C., & Voth, G. A. (2022). Seipin transmembrane segments critically function in triglyceride nucleation and lipid droplet budding from the membrane. *eLife*, *11*, e75808. https://doi.org/10.7554/eLife.75808

Kim, S., Li, C., Farese, R. V., Walther, T. C., & Voth, G. A. (2022). Key Factors Governing Initial Stages of Lipid Droplet Formation. *The Journal of Physical Chemistry. B*, *126*(2), 453–462. https://doi.org/10.1021/acs.jpcb.1c09683

Kim, S., Oh, M. I., & Swanson, J. M. J. (2021a). Stressed Lipid Droplets: How Neutral Lipids Relieve Surface Tension and Membrane Expansion Drives Protein Association. *The Journal of Physical Chemistry B*, *125*(21), 5572–5586. https://doi.org/10.1021/acs.jpcb.1c01795

Kim, S., Oh, M. I., & Swanson, J. M. J. (2021b). Stressed Lipid Droplets: How Neutral Lipids Relieve Surface Tension and Membrane Expansion Drives Protein Association. *The Journal of Physical Chemistry B*, *125*(21), 5572–5586. https://doi.org/10.1021/acs.jpcb.1c01795

Kimmel, A. R., & Sztalryd, C. (2016). The Perilipins: Major Cytosolic Lipid Droplet–Associated Proteins and Their Roles in Cellular Lipid Storage, Mobilization, and Systemic Homeostasis*. *Annual Review of Nutrition*, *36*(1), 471–509. https://doi.org/10.1146/annurev-nutr-071813-105410

Kitamura, T., Takagi, S., Naganuma, T., & Kihara, A. (2015). Mouse aldehyde dehydrogenase ALDH3B2 is localized to lipid droplets via two C-terminal tryptophan residues and lipid modification. *Biochemical Journal*, *465*(1), 79–87. https://doi.org/10.1042/bj20140624

Klauda, J. B., Venable, R. M., Freites, J. A., Freites, J. A., O'Connor, J. W., Tobias, D. J., Mondragon-Ramirez, C., Vorobyov, I., MacKerell, A. D., & Pastor, R. W. (2010). Update of the CHARMM All-Atom Additive Force Field for Lipids: Validation on Six Lipid Types. *Journal of Physical Chemistry B*, *114*(23), 7830–7843. https://doi.org/10.1021/jp101759q

Klemm, E. J., Spooner, E., Spooner, E., & Ploegh, H. L. (2011). Dual Role of Ancient Ubiquitous Protein 1 (AUP1) in Lipid Droplet Accumulation and Endoplasmic Reticulum (ER) Protein Quality Control. *Journal of Biological Chemistry*, *286*(43), 37602–37614. https://doi.org/10.1074/jbc.m111.284794

Klug, Y. A., Deme, J. C., Corey, R. A., Renne, M. F., Stansfeld, P. J., Lea, S. M., & Carvalho, P. (2021). Mechanism of lipid droplet formation by the yeast Sei1/Ldb16 Seipin complex. *Nature Communications*, *12*(1), 5892. https://doi.org/10.1038/s41467-021-26162-6

Kory, N., Farese, R. V., & Walther, T. C. (2016). Targeting Fat: Mechanisms of Protein Localization to Lipid Droplets. *Trends in Cell Biology*, *26*(7), 535–546. https://doi.org/10.1016/j.tcb.2016.02.007

Kory, N., Grond, S., Kamat, S. S., Li, Z., Krahmer, N., Chitraju, C., Zhou, P., Fröhlich, F., Semova, I., Ejsing, C., Zechner, R., Cravatt, B. F., Farese, R. V., & Walther, T. C. (2017). Mice lacking lipid droplet-associated hydrolase, a gene linked to human prostate cancer, have normal cholesterol ester metabolism. *Journal of Lipid Research*, *58*(1), 226–235. https://doi.org/10.1194/jlr.M072538

Kory, N., Thiam, A.-R., Farese, R. V., & Walther, T. C. (2015). Protein Crowding Is a Determinant of Lipid Droplet Protein Composition. *Developmental Cell*, *34*(3), 351–363. https://doi.org/10.1016/j.devcel.2015.06.007

Krahmer et al. (2013a). Balancing the fat: Lipid droplets and human disease. *EMBO Molecular Medicine*, *5*(7), 973–983. https://doi.org/10.1002/emmm.201100671

Krahmer, N., Guo, Y., Wilfling, F., Hilger, M., Lingrell, S., Heger, K., Newman, H. W., Schmidt-Supprian, M., Vance, D. E., Mann, M., Farese, R. V., & Walther, T. C. (2011). Phosphatidylcholine Synthesis for Lipid Droplet Expansion Is Mediated by Localized Activation of CTP:Phosphocholine Cytidylyltransferase. *Cell Metabolism*, *14*(4), 504–515. https://doi.org/10.1016/j.cmet.2011.07.013

Krahmer, N., Hilger, M., Kory, N., Wilfling, F., Stoehr, G., Mann, M., Farese, R. V., & Walther, T. C. (2013b). Protein Correlation Profiles Identify Lipid Droplet Proteins with High Confidence. *Molecular & Cellular Proteomics*, *12*(5), 1115–1126. https://doi.org/10.1074/mcp.m112.020230

Krahmer, N., & Mann, M. (2019). Catching Lipid Droplet Contacts by Proteomics. *Contact*, *2*, 251525641985918. https://doi.org/10.1177/2515256419859186

Krogh, A., Larsson, B., von Heijne, G., von Heijne, G., & Sonnhammer, E. L. L. (2001). Predicting transmembrane protein topology with a hidden Markov model: Application to complete genomes. *Journal of Molecular Biology*, *305*(3), 567–580. https://doi.org/10.1006/jmbi.2000.4315

Kyte, J., & Doolittle, R. F. (1982). A simple method for displaying the hydropathic character of a protein. *Journal of Molecular Biology*, *157*(1), 105–132. https://doi.org/10.1016/0022-2836(82)90515-0

Landry, J. J. M., Pyl, P. T., Rausch, T., Zichner, T., Tekkedil, M. M., Stütz, A. M., Jauch, A., Aiyar, R. S., Pau, G., Delhomme, N., Gagneur, J., Korbel, J. O., Huber, W., & Steinmetz, L. M. (2013). The Genomic and Transcriptomic Landscape of a HeLa Cell Line. *G3: Genes, Genomes, Genetics*, *3*(8), 1213–1224. https://doi.org/10.1534/g3.113.005777

Lee, H., & Kim, H. (2014). Membrane topology of transmembrane proteins: Determinants and experimental tools. *Biochemical and Biophysical Research Communications*, *453*(2), 268–276. https://doi.org/10.1016/j.bbrc.2014.05.111

Lee, J., Cheng, X., Swails, J. M., Yeom, M. S., Eastman, P. K., Lemkul, J. A., Wei, S., Buckner, J., Jeong, J. C., Qi, Y., Jo, S., Pande, V. S., Case, D. A., Brooks, C. L., MacKerell, A. D., Klauda, J. B., & Im, W. (2016). CHARMM-GUI Input Generator for NAMD, GROMACS, AMBER, OpenMM, and CHARMM/OpenMM Simulations Using the CHARMM36 Additive Force Field. *Journal of Chemical Theory and Computation*, *12*(1), 405–413. https://doi.org/10.1021/acs.jctc.5b00935

Lee, J. N., Kim, H., Yao, H., Chen, Y., Weng, K., & Ye, J. (2010). Identification of Ubxd8 protein as a sensor for unsaturated fatty acids and regulator of triglyceride synthesis. *Proceedings of the National Academy of Sciences of the United States of America*, *107*(50), 21424–21429. https://doi.org/10.1073/pnas.1011859107

Lee, Zhang, X., Feramisco, J. D., Gong, Y., & Ye, J. (2008). Unsaturated fatty acids inhibit proteasomal degradation of Insig-1 at a postubiquitination step. *The Journal of Biological Chemistry*, *283*(48), 33772–33783. https://doi.org/10.1074/jbc.M806108200

Lefevre et al. (1997). Alanine-stretch scanning mutagenesis: A simple and efficient method to probe protein structure and function. *Nucleic Acids Research*, *25*(2), 447–448. https://doi.org/10.1093/nar/25.2.447

Leznicki, P., Schneider, H. O., Harvey, J. V., Shi, W. Q., & High, S. (2022). Co-translational biogenesis of lipid droplet integral membrane proteins. *Journal of Cell Science*, *135*(5), jcs259220. https://doi.org/10.1242/jcs.259220

Li, Z., Johnson, M. R., Zhonghe Ke, Ke, Z., Chen, L., & Welte, M. A. (2014). Drosophila Lipid Droplets Buffer the H2Av Supply to Protect Early Embryonic Development. *Current Biology*, *24*(13), 1485–1491. https://doi.org/10.1016/j.cub.2014.05.022

Li, Z., Thiel, K., Thul, P. J., Beller, M., Kühnlein, R. P., & Welte, M. A. (2012). Lipid droplets control the maternal histone supply of Drosophila embryos. *Current Biology*, *22*(22), 2104–2113. https://doi.org/10.1016/j.cub.2012.09.018

Lindahl, E., & Sansom, M. (2008). Membrane proteins: Molecular dynamics simulations. *Current Opinion in Structural Biology*, *18*(4), 425–431. https://doi.org/10.1016/j.sbi.2008.02.003

Liu, Y., Mi, Y., Mueller, T., Kreibich, S., Williams, E. G., van Drogen, A., Borel, C., Frank, M., Germain, P.-L., Bludau, I., Mehnert, M., Seifert, M., Emmenlauer, M., Sorg, I., Bezrukov, F., Béna, F., Hu Zhou, Zhou, H., Dehio, C., … Aebersold, R. (2019). Multi-omic measurements of heterogeneity in HeLa cells across laboratories. *Nature Biotechnology*, *37*(3), 314–322. https://doi.org/10.1038/s41587-019-0037-y

Loregger, A., Raaben, M., Tan, J. M. E., Josephine Tan, Scheij, S., Moeton, M., Martina Moeton, Marlene van den Berg, Marlene van den Berg, Marlene van den Berg, van den Berg, M., Gelberg-Etel, H., Stickel, E., Roitelman, J., Thijn R. Brummelkamp, Brummelkamp, T. R., & Zelcer, N. (2017). Haploid Mammalian Genetic Screen Identifies UBXD8 as a Key Determinant of HMGCR Degradation and Cholesterol Biosynthesis. *Arteriosclerosis, Thrombosis, and Vascular Biology*, *37*(11), 2064–2074. https://doi.org/10.1161/atvbaha.117.310002

Loschwitz, J., Olubiyi, O. O., Hub, J. S., Strodel, B., & Poojari, C. S. (2020). Computer simulations of protein–membrane systems. In *Progress in Molecular Biology and Translational Science* (Vol. 170, pp. 273–403). Elsevier. https://doi.org/10.1016/bs.pmbts.2020.01.001

Lundin, C., Nordström, R., Wagner, K., Windpassinger, C., Andersson, H., von Heijne, G., & Nilsson, I. (2006). Membrane topology of the human seipin

protein. *FEBS Letters*, *580*(9), 2281–2284. https://doi.org/10.1016/j.febslet.2006.03.040

Lundquist, P. K. (2020). Lipid droplets throughout the evolutionary tree. *Progress in Lipid Research*, 24.

Lutas, E. M., D Zucker-Franklin, & Zucker-Franklin, D. (1977). Formation of lipid inclusions in normal human leukocytes. *Blood*, *49*(2), 309–320. https://doi.org/10.1182/blood.v49.2.309.bloodjournal492309

Lyu, X., Wang, J., Jianqin Wang, Yin, Y., Zhu, Y., Lin-Lin Li, Li, L.-L., Huang, S., peng, shuang, Xue, B., Liao, R., Wang, S.-Q., Long, M., Wohland, T., Chua, B. T., Sun, Y., Li, P., Chen, X., Xu, L., … Li, P. (2021). A gel-like condensation of Cidec generates lipid-permeable plates for lipid droplet fusion. *Developmental Cell*, *56*(18). https://doi.org/10.1016/j.devcel.2021.08.015

MacCallum, J. L., Bennett, W. F. D., & Tieleman, D. P. (2008). Distribution of Amino Acids in a Lipid Bilayer from Computer Simulations. *Biophysical Journal*, *94*(9), 3393–3404. https://doi.org/10.1529/biophysj.107.112805

Magré, J., Magré, J., Delepine, M., Khallouf, E., Gedde-Dahl, T., Van Maldergem, L., Van Maldergem, L., Sobel, E. M., Papp, J. C., Meier, M., Mégarbané, A., Bachy, A., Alain Verloes, Verloes, A., D'abronzo, F. H., Seemanova, E., Assan, R., Baudic, N., C, B., … Capeau, J. (2001). Identification of the gene altered in Berardinelli-Seip congenital lipodystrophy on chromosome 11q13. *Nature Genetics*, *28*(4), 365–370. https://doi.org/10.1038/ng585

Martínez, L., Andrade, R., Birgin, E. G., & Martínez, J. M. (2009). PACKMOL: A package for building initial configurations for molecular dynamics simulations. *Journal of Computational Chemistry*, *30*(13), 2157–2164. https://doi.org/10.1002/jcc.21224

M'Barek, K. B., Ajjaji, D., Chorlay, A., Vanni, S., Foret, L., & Thiam, A. R. (2017). ER Membrane Phospholipids and Surface Tension Control Cellular Lipid Droplet Formation. *Developmental Cell*, *41*(6), 591–604. https://doi.org/10.1016/j.devcel.2017.05.012

Mejhert, N., Kuruvilla, L., Gabriel, K. R., Elliott, S. D., Guié, M.-A., Huajin Wang, Wang, H., Lai, Z. W., Lane, E. A., Christiano, R., Danial, N. N., Farese, R. V., & Walther, T. C. (2020). Partitioning of MLX-Family Transcription Factors to Lipid Droplets Regulates Metabolic Gene Expression. *Molecular Cell*, *77*(6), 1251. https://doi.org/10.1016/j.molcel.2020.01.014

Molenaar, M. R., Yadav, K. K., Toulmay, A., Wassenaar, T. A., Mari, M. C., Caillon, L., Chorlay, A., Lukmantara, I. E., Haaker, M. W., Wubbolts, R. W., Houweling, M., Vaandrager, A. B., Prieur, X., Reggiori, F., Choudhary, V., Yang, H., Schneiter, R., Thiam, A. R., Prinz, W. A., & Helms, J. B. (2021). Retinyl esters form lipid droplets independently of triacylglycerol and seipin. *Journal of Cell Biology*, *220*(10), e202011071. https://doi.org/10.1083/jcb.202011071

Nicolson, G. L., & Nicolson, G. L. (2014). The Fluid—Mosaic Model of Membrane Structure: Still relevant to understanding the structure, function and dynamics of biological membranes after more than 40 years. *Biochimica et Biophysica Acta*, *1838*(6), 1451–1466. https://doi.org/10.1016/j.bbamem.2013.10.019

Nolan, S. J., Romano, J. D., & Coppens, I. (2017). Host lipid droplets: An important source of lipids salvaged by the intracellular parasite Toxoplasma gondii. *PLOS Pathogens*, *13*(6). https://doi.org/10.1371/journal.ppat.1006362

Nørholm, M. H. H., Shulga, Y. V., Aoki, S., Epand, R. M., & von Heijne, G. (2011). Flanking Residues Help Determine Whether a Hydrophobic Segment Adopts a Monotopic or Bitopic Topology in the Endoplasmic Reticulum Membrane. *Journal of Biological Chemistry*, *286*(28), 25284–25290. https://doi.org/10.1074/jbc.m111.244616

Nosé, S. (2002). *A molecular dynamics method for simulations in the canonical ensemble*. *100*(1), 191–198. https://doi.org/10.1080/00268970110089108

Novikoff, Alex B. Novikoff, P M Novikoff, Phyllis M. Novikoff, O M Rosen, Ora M. Rosen, C S Rubin, & Charles S. Rubin. (1980). Organelle relationships in cultured 3T3-L1 preadipocytes. *Journal of Cell Biology*. https://doi.org/10.1083/jcb.87.1.180

Nugent, T., & Jones, D. T. (2012). Membrane protein structural bioinformatics. *Journal of Structural Biology*, *179*(3), 327–337. https://doi.org/10.1016/j.jsb.2011.10.008

Oelkers, P., & Sturley, S. L. (2004). *9 Mechanisms and mediators of neutral lipid biosynthesis in eukaryotic cells*. 289–311. https://doi.org/10.1007/978-3-540-40999-1_10

Ogasawara, Y. (2020). Multifarious roles of lipid droplets in autophagy – Target, product, and what else? *Seminars in Cell and Developmental Biology*, 8.

Ohashi, M., Mizushima, N., Kabeya, Y., & Yoshimori, T. (2003). Localization of Mammalian NAD(P)H Steroid Dehydrogenase-like Protein on Lipid Droplets. *Journal of Biological Chemistry*, *278*(38), 36819–36829. https://doi.org/10.1074/jbc.M301408200

Olarte, M.-J., Kim, S., Sharp, M. E., Swanson, J. M. J., Farese, R. V., & Walther, T. C. (2020). Determinants of Endoplasmic Reticulum-to-Lipid Droplet Protein Targeting. *Developmental Cell*, *54*(4), 471-487.e7. https://doi.org/10.1016/j.devcel.2020.07.001

Olarte, M.-J., Swanson, J. M. J., Walther, T. C., & Farese, R. V. (2022). The CYTOLD and ERTOLD pathways for lipid droplet–protein targeting. *Trends in Biochemical Sciences*, *47*(1), 39–51. https://doi.org/10.1016/j.tibs.2021.08.007

Olzmann, J. A., & Carvalho, P. (2019a). Dynamics and functions of lipid droplets. *Nature Reviews Molecular Cell Biology*, *20*(3), 137–155. https://doi.org/10.1038/s41580-018-0085-z

Olzmann, J. A., & Carvalho, P. (2019b). Dynamics and functions of lipid droplets. *Nature Reviews Molecular Cell Biology*, *20*(3), 137–155. https://doi.org/10.1038/s41580-018-0085-z

Olzmann, J. A., Richter, C. M., & Kopito, R. R. (2013). Spatial regulation of UBXD8 and p97/VCP controls ATGL-mediated lipid droplet turnover. *Proceedings of the National Academy of Sciences*, *110*(4), 1345–1350. https://doi.org/10.1073/pnas.1213738110

Onal, G., Kutlu, O., Gozuacik, D., & Dokmeci Emre, S. (2017). Lipid Droplets in Health and Disease. *Lipids in Health and Disease*, *16*(1), 128. https://doi.org/10.1186/s12944-017-0521-7

Ostermeyer, A. G., Ramcharan, L. T., Zeng, Y., Lublin, D. M., & Brown, D. A. (2004). Role of the hydrophobic domain in targeting caveolin-1 to lipid droplets. *Journal of Cell Biology*, *164*(1), 69–78. https://doi.org/10.1083/jcb.200303037

Ott, C. M., & Lingappa, V. R. (2002). Integral membrane protein biosynthesis: Why topology is hard to predict. *Journal of Cell Science*, *115*(Pt 10), 2003–2009. https://doi.org/10.1242/jcs.115.10.2003

Palade, G. E. (1956). THE ENDOPLASMIC RETICULUM. *Journal of Cell Biology*, *2*(4), 85–98. https://doi.org/10.1083/jcb.2.4.85

Parrinello, M., A. Rahman, & Rahman, A. (1981). Polymorphic transitions in single crystals: A new molecular dynamics method. *Journal of Applied Physics*, *52*(12), 7182–7190. https://doi.org/10.1063/1.328693

Parrinello, M., & Rahman, A. (1980). Crystal Structure and Pair Potentials: A Molecular-Dynamics Study. *Physical Review Letters*, *45*(14), 1196–1199. https://doi.org/10.1103/PhysRevLett.45.1196

Pataki, C. I., Rodrigues, J., Zhang, L., Qian, J., Efron, B., Hastie, T., Elias, J. E., Levitt, M., & Kopito, R. R. (2018). Proteomic analysis of monolayer-integrated proteins on lipid droplets identifies amphipathic interfacial α-helical membrane anchors. *Proceedings of the National Academy of Sciences*, *115*(35), E8172–E8180. https://doi.org/10.1073/pnas.1807981115

Paul, B., Weeratunga, S., Tillu, V. A., Hariri, H., Henne, W. M., & Collins, B. M. (2022). Structural Predictions of the SNX-RGS Proteins Suggest They Belong to a New Class of Lipid Transfer Proteins. *Frontiers in Cell and Developmental Biology*, *10*, 826688. https://doi.org/10.3389/fcell.2022.826688

Petan, T., Jarc, E., & Jusović, M. (2018a). Lipid Droplets in Cancer: Guardians of Fat in a Stressful World. *Molecules*, *23*(8), 1941. https://doi.org/10.3390/molecules23081941

Petan, T., Jarc, E., & Jusović, M. (2018b). Lipid Droplets in Cancer: Guardians of Fat in a Stressful World. *Molecules*, *23*(8), 1941. https://doi.org/10.3390/molecules23081941

Pfanner, N., Warscheid, B., & Wiedemann, N. (2019). Mitochondrial proteins: From biogenesis to functional networks. *Nature Reviews Molecular Cell Biology*, *20*(5), 267–284. https://doi.org/10.1038/s41580-018-0092-0

Pol, A., Gross, S. P., & Parton, R. G. (2014). Biogenesis of the multifunctional lipid droplet: Lipids, proteins, and sites. *Journal of Cell Biology*, *204*(5), 635–646. https://doi.org/10.1083/jcb.201311051

Porter, K. R., Claude, A., & Fullam, E. F. (1945). A STUDY OF TISSUE CULTURE CELLS BY ELECTRON MICROSCOPY : METHODS AND PRELIMINARY OBSERVATIONS. *Journal of Experimental Medicine*, *81*(3), 233–246. https://doi.org/10.1084/jem.81.3.233

Porter, K. R., & Palade, G. E. (1957). STUDIES ON THE ENDOPLASMIC RETICULUM : III. ITS FORM AND DISTRIBUTION IN STRIATED MUSCLE

CELLS. *Journal of Cell Biology*, *3*(2), 269–300. https://doi.org/10.1083/jcb.3.2.269

Prasanna, Veijo T. Salo, Shiqian Li, Katharina Ven, Helena Vihinen, Eija Jokitalo, Ilpo Vattulainen, & Elina Ikonen. (2021). Seipin traps triacylglycerols to facilitate their nanoscale clustering in the endoplasmic reticulum membrane. *PLOS Biology*. https://doi.org/10.1371/journal.pbio.3000998

Prévost, Morris E. Sharp, Nora Kory, Qingqing Lin, Gregory A. Voth, Robert V. Farese, & Tobias C. Walther. (2018). Mechanism and Determinants of Amphipathic Helix-Containing Protein Targeting to Lipid Droplets. *Developmental Cell*. https://doi.org/10.1016/j.devcel.2017.12.011

Prevost, Prévost, C., Sharp, M. E., Kory, N., Lin, Q., Voth, G. A., Farese, R. V., & Walther, T. C. (2018). Mechanism and Determinants of Amphipathic Helix-Containing Protein Targeting to Lipid Droplets. *Developmental Cell*, *44*(1), 73–86. https://doi.org/10.1016/j.devcel.2017.12.011

Radner, F. P. W., Streith, I. E., Schoiswohl, G., Schweiger, M., Kumari, M., Kumari, M., Eichmann, T. O., Rechberger, G. N., Koefeler, H., Eder, S., Schauer, S., Theussl, H. C., Preiss-Landl, K., Lass, A., Zimmermann, R., Hoefler, G., Zechner, R., & Haemmerle, G. (2010). Growth retardation, impaired triacylglycerol catabolism, hepatic steatosis, and lethal skin barrier defect in mice lacking comparative gene identification-58 (CGI-58). *Journal of Biological Chemistry*, *285*(10), 7300–7311. https://doi.org/10.1074/jbc.m109.081877

Ray, L. C., Das, D., Entova, S., Lukose, V., Lynch, A. J., Imperiali, B., & Allen, K. N. (2018). Membrane association of monotopic phosphoglycosyl transferase underpins function. *Nature Chemical Biology*, *14*(6), 538–541. https://doi.org/10.1038/s41589-018-0054-z

Robenek, H., Hofnagel, O., Buers, I., Robenek, M. J., Robenek, M. J., Troyer, D., & Severs, N. J. (2006). Adipophilin-enriched domains in the ER membrane are sites of lipid droplet biogenesis. *Journal of Cell Science*, *119*(20), 4215–4224. https://doi.org/10.1242/jcs.03191

Roberts, M. A., & Olzmann, J. A. (2020). Protein Quality Control and Lipid Droplet Metabolism. *Annual Review of Cell and Developmental Biology*, *36*(1), 115–139. https://doi.org/10.1146/annurev-cellbio-031320-101827

Rogers, S., Gui, L., Kovalenko, A., Reetz, E., Nicastro, D., & Henne, W. M. (2021). *Liquid-crystalline lipid phase transitions in lipid droplets selectively remodel the LD proteome* [Preprint]. Cell Biology. https://doi.org/10.1101/2021.08.30.458229

Rowe, E. R., Mimmack, M. L., Barbosa, A. D., Haider, A., Isaac, I., Ouberai, M. M., Thiam, A. R., Patel, S., Saudek, V., Siniossoglou, S., & Savage, D. B. (2016). Conserved Amphipathic Helices Mediate Lipid Droplet Targeting of Perilipins 1-3. *The Journal of Biological Chemistry*, *291*(13), 6664–6678. https://doi.org/10.1074/jbc.M115.691048

Ruan, X., Monjarás Feria, J., Hamad, M., & Valvano, M. A. (2018). *Escherichia coli* and *Pseudomonas aeruginosa* lipopolysaccharide O-antigen ligases share similar membrane topology and biochemical properties. *Molecular Microbiology*, *110*(1), 95–113. https://doi.org/10.1111/mmi.14085

Sahu, I. D., & Lorigan, G. A. (2020). Electron Paramagnetic Resonance as a Tool for Studying Membrane Proteins. *Biomolecules*, *10*(5), 763. https://doi.org/10.3390/biom10050763

Salo, V. T., Belevich, I., Li, S., Karhinen, L., Vihinen, H., Vigouroux, C., Magré, J., Thiele, C., Hölttä-Vuori, M., Jokitalo, E., & Ikonen, E. (2016). Seipin regulates ER –lipid droplet contacts and cargo delivery. *The EMBO Journal*, *35*(24), 2699–2716. https://doi.org/10.15252/embj.201695170

Salo, V. T., Hölttä-Vuori, M., & Ikonen, E. (2020). Seipin-Mediated Contacts as Gatekeepers of Lipid Flux at the Endoplasmic Reticulum–Lipid Droplet Nexus. *Contact*, *3*, 251525642094582. https://doi.org/10.1177/2515256420945820

Salo, V. T., & Ikonen, E. (2019). Moving out but keeping in touch: Contacts between endoplasmic reticulum and lipid droplets. *Current Opinion in Cell Biology*, *57*, 64–70. https://doi.org/10.1016/j.ceb.2018.11.002

Salo, V. T., Li, S., Vihinen, H., Hölttä-Vuori, M., Szkalisity, A., Horvath, P., Belevich, I., Peränen, J., Thiele, C., Somerharju, P., Zhao, H., Santinho, A., Thiam, A. R., Jokitalo, E., & Ikonen, E. (2019). Seipin Facilitates Triglyceride Flow to Lipid Droplet and Counteracts Droplet Ripening via Endoplasmic Reticulum Contact. *Developmental Cell*, *50*(4), 478-493.e9. https://doi.org/10.1016/j.devcel.2019.05.016

Santinho, A., Salo, V. T., Chorlay, A., Li, S., Xin Zhou, Zhou, X., Omrane, M., Ikonen, E., & Thiam, A. R. (2020). Membrane Curvature Catalyzes Lipid Droplet Assembly. *Current Biology*, *30*(13). https://doi.org/10.1016/j.cub.2020.04.066

Schrul, B., & Kopito, R. R. (2016). Peroxin-dependent targeting of a lipid-droplet-destined membrane protein to ER subdomains. *Nature Cell Biology*, *18*(7), 740–751. https://doi.org/10.1038/ncb3373

Schuberth, C., & Buchberger, A. (2008). UBX domain proteins: Major regulators of the AAA ATPase Cdc48/p97. *Cellular and Molecular Life Sciences*, *65*(15), 2360–2371. https://doi.org/10.1007/s00018-008-8072-8

Seip, M. (1959). Lipodystrophy and gigantism with associated endocrine manifestations. A new diencephalic syndrome. *Acta Paediatrica*, *48*, 555–574.

Shibata, Y., Hu, J., Kozlov, M. M., & Rapoport, T. A. (2009). Mechanisms Shaping the Membranes of Cellular Organelles. *Annual Review of Cell and Developmental Biology*, *25*(1), 329–354. https://doi.org/10.1146/annurev.cellbio.042308.113324

Shibata, Y., Shemesh, T., Prinz, W. A., Palazzo, A. F., Kozlov, M. M., & Rapoport, T. A. (2010). Mechanisms Determining the Morphology of the Peripheral ER. *Cell*, *143*(5), 774–788. https://doi.org/10.1016/j.cell.2010.11.007

Shin, O.-H., Han, W., Wang, Y., & Südhof, T. C. (2005). Evolutionarily Conserved Multiple C2 Domain Proteins with Two Transmembrane Regions (MCTPs) and Unusual Ca2+ Binding Properties. *Journal of Biological Chemistry*, *280*(2), 1641–1651. https://doi.org/10.1074/jbc.m407305200

Singer, S. J., Nicolson, G. L., & Nicolson, G. L. (1972). The fluid mosaic model of the structure of cell membranes. *Science*, *175*(4023), 720–731. https://doi.org/10.1126/science.175.4023.720

Smith, C. E., Tsai, Y. C., Liang, Y.-H., Khago, D., Mariano, J., Li, J., Tarasov, S. G., Gergel, E., Tsai, B., Villaneuva, M., Clapp, M. E., Magidson, V., Chari, R., Byrd, R. A., Ji, X., & Weissman, A. M. (2021). A structurally conserved site in AUP1 binds the E2 enzyme UBE2G2 and is essential for ER-associated degradation. *PLOS Biology*, *19*(12), e3001474. https://doi.org/10.1371/journal.pbio.3001474

Song, J., Mizrak, A., Lee, C.-W., Cicconet, M., Lai, Z. W., Tang, W.-C., Lu, C.-H., Mohr, S. E., Farese, R. V., & Walther, T. C. (2022). Identification of two

pathways mediating protein targeting from ER to lipid droplets. *Nature Cell Biology*, *24*(9), 1364–1377. https://doi.org/10.1038/s41556-022-00974-0

Spandl, J., Spandl, J., Lohmann, D., Kuerschner, L., Lars Kuerschner, Moessinger, C., Moessinger, C., & Thiele, C. (2011). Ancient Ubiquitous Protein 1 (AUP1) Localizes to Lipid Droplets and Binds the E2 Ubiquitin Conjugase G2 (Ube2g2) via Its G2 Binding Region. *Journal of Biological Chemistry*, *286*(7), 5599–5606. https://doi.org/10.1074/jbc.m110.190785

Stein, O., & Stein, Y. (1968). Iii electron microscopic radioautographic study of the rat heart perfused with tritiated oleic acid. *Journal of Cell Biology*. https://doi.org/10.1083/jcb.36.1.63

Stevanovic, A., & Thiele, C. (2013). Monotopic topology is required for lipid droplet targeting of ancient ubiquitous protein 1. *Journal of Lipid Research*, *54*(2), 503–513. https://doi.org/10.1194/jlr.m033852

Stevenson, J., Julian Stevenson, Huang, E. Y., Huang, E. Y., & Olzmann, J. A. (2016). Endoplasmic Reticulum–Associated Degradation and Lipid Homeostasis. *Annual Review of Nutrition*, *36*(1), 511–542. https://doi.org/10.1146/annurev-nutr-071715-051030

Sui, X., Arlt, H., Brock, K. P., Lai, Z. W., DiMaio, F., Marks, D. S., Liao, M., Farese, R. V., & Walther, T. C. (2018). Cryo–electron microscopy structure of the lipid droplet–formation protein seipin. *Journal of Cell Biology*, *217*(12), 4080–4091. https://doi.org/10.1083/jcb.201809067

Suzuki, M., Murakami, T., Cheng, J., Kano, H., Hiroyuki Kano, Fukata, M., & Fujimoto, T. (2015). ELMOD2 is anchored to lipid droplets by palmitoylation and regulates adipocyte triglyceride lipase recruitment. *Molecular Biology of the Cell*, *26*(12), 2333–2342. https://doi.org/10.1091/mbc.e14-11-1504

Suzuki, M., Otsuka, T., Ohsaki, Y., Cheng, J., Taniguchi, T., Hashimoto, H., Taniguchi, H., & Fujimoto, T. (2012). Derlin-1 and UBXD8 are engaged in dislocation and degradation of lipidated ApoB-100 at lipid droplets. *Molecular Biology of the Cell*, *23*(5), 800–810. https://doi.org/10.1091/mbc.e11-11-0950

Swanson, J. M. (2022). The influence of neutral lipid composition on the physical properties and protein recruitment of lipid droplets. *Biophysical Journal*, *121*(3), 172a. https://doi.org/10.1016/j.bpj.2021.11.1863

Szymanski, K. M., Binns, D., Bartz, R., Grishin, N. V., Li, W.-P., Agarwal, A. K., Garg, A., Anderson, R. G. W., & Goodman, J. M. (2007). The lipodystrophy

protein seipin is found at endoplasmic reticulum lipid droplet junctions and is important for droplet morphology. *Proceedings of the National Academy of Sciences*, *104*(52), 20890–20895. https://doi.org/10.1073/pnas.0704154104

Tauchi-Sato, K., Ozeki, S., Houjou, T., Houjou, T., Taguchi, R., & Fujimoto, T. (2002). The Surface of Lipid Droplets Is a Phospholipid Monolayer with a Unique Fatty Acid Composition. *Journal of Biological Chemistry*, *277*(46), 44507–44512. https://doi.org/10.1074/jbc.m207712200

Teixeira, V., Johnsen, L., Martínez-Montañés, F., Grippa, A., Buxó, L., Idrissi, F.-Z., Ejsing, C. S., & Carvalho, P. (2018). Regulation of lipid droplets by metabolically controlled Ldo isoforms. *Journal of Cell Biology*, *217*(1), 127–138. https://doi.org/10.1083/jcb.201704115

Thiam, A. R., Farese Jr, R. V., & Walther, T. C. (2013a). The biophysics and cell biology of lipid droplets. *Nature Reviews Molecular Cell Biology*, *14*(12), 775–786. https://doi.org/10.1038/nrm3699

Thiam, A. R., Farese Jr, R. V., & Walther, T. C. (2013). The biophysics and cell biology of lipid droplets. *Nature Reviews Molecular Cell Biology*, *14*(12), 775–786. https://doi.org/10.1038/nrm3699

Thiam, A. R., & Forêt, L. (2016). The physics of lipid droplet nucleation, growth and budding. *Biochimica et Biophysica Acta (BBA) - Molecular and Cell Biology of Lipids*, *1861*(8), 715–722. https://doi.org/10.1016/j.bbalip.2016.04.018

Thiam, A. R., & Ikonen, E. (2020). Lipid Droplet Nucleation. *Trends in Cell Biology*, S0962892420302312. https://doi.org/10.1016/j.tcb.2020.11.006

Tsirigos, K. D., Peters, C., Shu, N., Käll, L., & Elofsson, A. (2015). The TOPCONS web server for consensus prediction of membrane protein topology and signal peptides. *Nucleic Acids Research*, *43*. https://doi.org/10.1093/nar/gkv485

Tu, L., Khanna, P., & Deutsch, C. (2014). Transmembrane segments form tertiary hairpins in the folding vestibule of the ribosome. *Journal of Molecular Biology*, *426*(1), 185–198. https://doi.org/10.1016/j.jmb.2013.09.013

Turró, S., Ingelmo-Torres, M., Estanyol, J. M., Tebar, F., Fernández, M. A., Albor, C. V., Gaus, K., Grewal, T., Enrich, C., & Pol, A. (2006). Identification and Characterization of Associated with Lipid Droplet Protein 1: A Novel Membrane-Associated Protein That Resides on Hepatic Lipid Droplets. *Traffic*, *7*(9), 1254–1269. https://doi.org/10.1111/j.1600-0854.2006.00465.x

Ugrankar, R., Bowerman, J., Hariri, H., Chandra, M., Chen, K., Bossanyi, M.-F., Datta, S., Rogers, S., Eckert, K. M., Vale, G., Victoria, A., Fresquez, J., McDonald, J. G., Jean, S., Collins, B. M., & Henne, W. M. (2019). Drosophila Snazarus Regulates a Lipid Droplet Population at Plasma Membrane-Droplet Contacts in Adipocytes. *Developmental Cell*, *50*(5), 557-572.e5. https://doi.org/10.1016/j.devcel.2019.07.021

Ulmschneider, M. B., & Sansom, M. S. P. (2001). Amino acid distributions in integral membrane protein structures. *Biochimica et Biophysica Acta (BBA) - Biomembranes*, *1512*(1), 1–14. https://doi.org/10.1016/S0005-2736(01)00299-1

Utsumi, T., Hosokawa, T., Mayu Shichita, Misato Nishiue, Natsuko Iwamoto, Harada, H., Kiwado, A., Yano, M., Otsuka, M., & Moriya, K. (2021). ANKRD22 is an N-myristoylated hairpin-like monotopic membrane protein specifically localized to lipid droplets. *Scientific Reports*, *11*(1), 19233–19233. https://doi.org/10.1038/s41598-021-98486-8

Valm, A. M., Cohen, S., Cohen, S. S., Legant, W. R., Melunis, J., Hershberg, U., Wait, E., Cohen, A. R., Davidson, M. W., Betzig, E., & Lippincott-Schwartz, J. (2017). Applying systems-level spectral imaging and analysis to reveal the organelle interactome. *Nature*, *546*(7656), 162–167. https://doi.org/10.1038/nature22369

Vizeacoumar, F. J., Vreden, W. N., Aitchison, J. D., & Rachubinski, R. A. (2006). Pex19p Binds Pex30p and Pex32p at Regions Required for Their Peroxisomal Localization but Separate from Their Peroxisomal Targeting Signals. *Journal of Biological Chemistry*, *281*(21), 14805–14812. https://doi.org/10.1074/jbc.M601808200

Voeltz, G. K., Prinz, W. A., Shibata, Y., Rist, J. M., & Rapoport, T. A. (2006). A Class of Membrane Proteins Shaping the Tubular Endoplasmic Reticulum. *Cell*, *124*(3), 573–586. https://doi.org/10.1016/j.cell.2005.11.047

von Heijne, G. (1992). Membrane protein structure prediction: Hydrophobicity analysis and the positive-inside rule. *Journal of Molecular Biology*, *225*(2), 487–494. https://doi.org/10.1016/0022-2836(92)90934-c

von Heijne, G. (2006). Membrane-protein topology. *Nature Reviews Molecular Cell Biology*, *7*(12), 909–918. https://doi.org/10.1038/nrm2063

Wallin, E., von Heijne, G., & G. von Heijne. (1998). GENOME-WIDE ANALYSIS OF INTEGRAL MEMBRANE PROTEINS FROM EUBACTERIAL, ARCHAEAN, AND EUKARYOTIC ORGANISMS. *Protein Science*, *7*(4), 1029–1038. https://doi.org/10.1002/pro.5560070420

Walther et al. (2017a). *Lipid Droplet Biogenesis*. 20.

Walther, T. C., & Farese, R. V. (2009). The life of lipid droplets. *Biochimica et Biophysica Acta*, *1791*(6), 459–466. https://doi.org/10.1016/j.bbalip.2008.10.009

Walther, T. C., & Farese, R. V. (2012). Lipid Droplets and Cellular Lipid Metabolism. *Annual Review of Biochemistry*, *81*(1), 687–714. https://doi.org/10.1146/annurev-biochem-061009-102430

Walther, T. C., & Farese, R. V. (2019). Un-phased: Lipid Droplets Modulate the Bioavailability of Antibiotics. *Developmental Cell*, *50*(5), 530–532. https://doi.org/10.1016/j.devcel.2019.08.009

Walther, T. C., Jeeyun Chung, Chung, J., & Farese, R. V. (2017b). Lipid Droplet Biogenesis. *Annual Review of Cell and Developmental Biology*, *33*(1), 491–510. https://doi.org/10.1146/annurev-cellbio-100616-060608

Wang, H., Becuwe, M., Housden, B. E., Chitraju, C., Porras, A. J., Graham, M. M., Liu, X. N., Thiam, A. R., Savage, D. B., Agarwal, A. K., Garg, A., Olarte, M.-J., Lin, Q., Fröhlich, F., Hannibal-Bach, H. K., Upadhyayula, S., Perrimon, N., Kirchhausen, T., Ejsing, C. S., … Farese, R. V. (2016). Seipin is required for converting nascent to mature lipid droplets. *eLife*, *5*, e16582. https://doi.org/10.7554/eLife.16582

Wang, & Rapoport, T. A. (2019). Reconstituting the reticular ER network – mechanistic implications and open questions. *Journal of Cell Science*, *132*(4), jcs227611. https://doi.org/10.1242/jcs.227611

Wang, S., Idrissi, F.-Z., Hermansson, M., Grippa, A., Ejsing, C. S., & Carvalho, P. (2018). Seipin and the membrane-shaping protein Pex30 cooperate in organelle budding from the endoplasmic reticulum. *Nature Communications*, *9*(1), 2939–2939. https://doi.org/10.1038/s41467-018-05278-2

Wang, Yu-Hsuan Miao, & Yi-Shun Chang. (2014). Control of lipid droplet size in budding yeast requires the collaboration between Fld1 and Ldb16. *Journal of Cell Science*. https://doi.org/10.1242/jcs.137737

Weill, U., Cohen, N., Nir Cohen, Nir Cohen, Fadel, A., Ben-Dor, S., & Schuldiner, M. (2019). Protein Topology Prediction Algorithms Systematically Investigated in the Yeast Saccharomyces cerevisiae. *BioEssays*, *41*(8), 1800252. https://doi.org/10.1002/bies.201800252

Weiss, S. B., Weiss, S. B., Kennedy, E. P., John Y. Kiyasu, & Kiyasu, J. Y. (1956). The enzymatic synthesis of triglycerides. *Journal of Biological Chemistry*, *235*(1), 40–44. https://doi.org/10.1021/ja01595a088

Welte, M. A. (2015). Expanding Roles for Lipid Droplets. *Current Biology*, *25*(11), R470–R481. https://doi.org/10.1016/j.cub.2015.04.004

Wilfling, F., Haas, J. T., Walther, T. C., & Farese, R. V. (2014). Lipid Droplet Biogenesis. *Current Opinion in Cell Biology*, *29*, 39–45. https://doi.org/10.1016/j.ceb.2014.03.008

Wilfling, F., Huajin Wang, Wang, H., Haas, J. T., Krahmer, N., Gould, T. J., Uchida, A., Cheng, J.-X., Graham, M., Christiano, R., Fröhlich, F., Liu, X., Buhman, K. K., Coleman, R. A., Bewersdorf, J., Farese, R. V., & Walther, T. C. (2013). Triacylglycerol Synthesis Enzymes Mediate Lipid Droplet Growth by Relocalizing from the ER to Lipid Droplets. *Developmental Cell*, *24*(4), 384–399. https://doi.org/10.1016/j.devcel.2013.01.013

Wilson, E. B. (1896). *The cell in development and inheritance*. https://doi.org/10.5962/bhl.title.21641

Wingfield, P. (2001). Protein precipitation using ammonium sulfate. *Current Protocols in Protein Science*, *Appendix 3*, Appendix 3F. https://doi.org/10.1002/0471140864.psa03fs13

Xia, Y., Yan, L. H., Huang, B., Liu, M., Liu, X., & Huang, C. (2014). Pathogenic mutation of UBQLN2 impairs its interaction with UBXD8 and disrupts endoplasmic reticulum-associated protein degradation. *Journal of Neurochemistry*, *129*(1), 99–106. https://doi.org/10.1111/jnc.12606

Xu, D., & Zhang, Y. (2012). Ab initio protein structure assembly using continuous structure fragments and optimized knowledge-based force field. *Proteins*, *80*(7), 1715–1735. https://doi.org/10.1002/prot.24065

Xu, D., & Zhang, Y. (2013). Toward optimal fragment generations for ab initio protein structure assembly. *Proteins*, *81*(2), 229–239. https://doi.org/10.1002/prot.24179

Xu, Y., Liu, Y., Jin-gu Lee, Lee, J.-G., Yihong Ye, & Ye, Y. (2013). A Ubiquitin-like Domain Recruits an Oligomeric Chaperone to a Retrotranslocation Complex in Endoplasmic Reticulum-associated Degradation. *Journal of Biological Chemistry*, *288*(25), 18068–18076. https://doi.org/10.1074/jbc.m112.449199

Yan, M., Rachubinski, D. A., Joshi, S., Rachubinski, R. A., & Subramani, S. (2008). Dysferlin Domain-containing Proteins, Pex30p and Pex31p, Localized to Two Compartments, Control the Number and Size of Oleate-induced Peroxisomes in *Pichia pastoris*. *Molecular Biology of the Cell*, *19*(3), 885–898. https://doi.org/10.1091/mbc.e07-10-1042

Yan, R., Qian, H., Lukmantara, I., Gao, M., Du, X., Yan, N., & Yang, H. (2018). Human SEIPIN Binds Anionic Phospholipids. *Developmental Cell*, *47*(2), 248-256.e4. https://doi.org/10.1016/j.devcel.2018.09.010

Yang, Ding, Y., Chen, Y., Zhang, S., Huo, C., Wang, Y., Yu, J., Zhang, P., Na, H., Zhang, H., Ma, Y., & Liu, P. (2012). The proteomics of lipid droplets: Structure, dynamics, and functions of the organelle conserved from bacteria to humans. *Journal of Lipid Research*, *53*(7), 1245–1253. https://doi.org/10.1194/jlr.R024117

Yang, & Mottillo, E. P. (2020). Adipocyte lipolysis: From molecular mechanisms of regulation to disease and therapeutics. *Biochemical Journal*, *477*(5), 985–1008. https://doi.org/10.1042/bcj20190468

Yang, & Strittmatter, S. M. (2007). The reticulons: A family of proteins with diverse functions. *Genome Biology*, *8*(12), 234. https://doi.org/10.1186/gb-2007-8-12-234

Yang, X., Lu, X., Lombès, M., Rha, G. B., Chi, Y. I., Guerin, T., Smart, E. J., & Liu, J. (2010). The G0/G1 Switch Gene 2 Regulates Adipose Lipolysis through Association with Adipose Triglyceride Lipase. *Cell Metabolism*, *11*(3), 194–205. https://doi.org/10.1016/j.cmet.2010.02.003

Yap, W. S., Shyu, P., Gaspar, M. L., Jesch, S. A., Marvalim, C., Prinz, W. A., Henry, S. A., & Thibault, G. (2020). Yeast FIT2 homolog is necessary to maintain cellular proteostasis and membrane lipid homeostasis. *Journal of Cell Science*, *133*(21). https://doi.org/10.1242/jcs.248526

Ye, J. (2012). Cellular responses to unsaturated fatty acids mediated by their sensor Ubxd8. *Frontiers of Biology in China*, *7*(5), 397–403. https://doi.org/10.1007/s11515-012-1247-6

Ye, Y., Tang, W. K., Zhang, T., & Xia, D. (2017). A Mighty “Protein Extractor” of the Cell: Structure and Function of the p97/CDC48 ATPase. *Frontiers in Molecular Biosciences*, *4*, 39–39. https://doi.org/10.3389/fmolb.2017.00039

Yen, Scot J. Stone, Scot J. Stone, Scot J. Stone, Scot J. Stone, Scot J. Stone, Scot J. Stone, Sheldon Stone, Suneil K. Koliwad, Charles A. Harris, & Robert V. Farese. (2008). Thematic review series: Glycerolipids. DGAT enzymes and triacylglycerol biosynthesis. *Journal of Lipid Research*. https://doi.org/10.1194/jlr.r800018-jlr200

Zechner, R. (2015). FAT FLUX: Enzymes, regulators, and pathophysiology of intracellular lipolysis. *EMBO Molecular Medicine*, *7*(4), 359–362. https://doi.org/10.15252/emmm.201404846

Zehmer, J. K., Bartz, R., Bisel, B., Liu, P., Seemann, J., & Anderson, R. G. W. (2009). Targeting sequences of UBXD8 and AAM-B reveal that the ER has a direct role in the emergence and regression of lipid droplets. *Journal of Cell Science*, *122*(20), 3694–3702. https://doi.org/10.1242/jcs.054700

Zehmer, J. K., Bartz, R., Liu, P., & Anderson, R. G. W. (2008). Identification of a novel N-terminal hydrophobic sequence that targets proteins to lipid droplets. *Journal of Cell Science*, *121*(11), 1852–1860. https://doi.org/10.1242/jcs.012013

Zhang, C., & Liu, P. (2019). The New Face of the Lipid Droplet: Lipid Droplet Proteins. *PROTEOMICS*, *19*(10), 1700223. https://doi.org/10.1002/pmic.201700223

Zoni et al., (2019). To Bud or Not to Bud: A Perspective on Molecular Simulations of Lipid Droplet Budding. *Frontiers in Molecular Biosciences*. https://doi.org/10.3389/fmolb.2019.00124

Zoni, V., Khaddaj, R., Campomanes, P., Thiam, A. R., Schneiter, R., & Vanni, S. (2021). Pre-existing bilayer stresses modulate triglyceride accumulation in the ER versus lipid droplets. *eLife*, *10*, e62886. https://doi.org/10.7554/eLife.62886

Zoni, V., Khaddaj, R., Lukmantara, I. E., Shinoda, W., Yang, H., Schneiter, R., & Vanni, S. (2021). Seipin accumulates and traps diacylglycerols and triglycerides in its ring-like structure. *Proceedings of the National Academy of Sciences of the United States of America*, *118*(10). https://doi.org/10.1073/pnas.2017205118

Zurek, N., Sparks, L., & Voeltz, G. (2011). Reticulon Short Hairpin Transmembrane Domains Are Used to Shape ER Tubules. *Traffic*, *12*(1), 28–41. https://doi.org/10.1111/j.1600-0854.2010.01134.x

8. List of Figures

9. List of Tables

10. List of Abbreviations

Å	Angstrom
ACAT	Cholesterol acyltransferase
AGPAT	1-acyl glycerol-3-phosphate acyltransferase
ALDI	Associated with lipid droplets 1
ALG14	UDP-N-acetylglucosaminyltransferase subunit
APEX2	Enhanced ascorbate peroxidase
ApoB	Apolipoprotein B-100
ASCL	Acyl-CoA synthetase
ASCL3	Acyl-CoA synthetase long chain family member 3
ATGL	Adipose triglyceride lipase
AUP1	Ancient ubiquitous protein 1
BSCL2/CGL2	Berardinelli-Seip congenital lipodystrophy-2 or congenital generalized lipodystrophy
CoA	Coenzyme A
CCT	Phosphocholine cytidyltransferase
CG1-58	Comparative gene identification
CIDE	Cell death-inducing DNA fragmentation factor 45-like effector
CLOL	Cholesteryl oleate
CL	Cardiolipin
CN	C-terminal nexin
CYTOLD	Cytosol to lipid droplets
DAG	Diacylglycerol
DEVs	Droplet-embedded vesicles
DGAT	Diacylglycerol acyltransferase
DHRS3	Dehydrogenase/reductase 3
ER	Endoplasmic reticulum
ERAD	Endoplasmic reticulum associated protein degradation
EMC	Endoplasmic reticulum membrane complex
EPR	Electron paramagnetic resonance
ERTOLD	Endoplasmic reticulum to lipid droplets
FAs	Fatty acids

FAF2	Fas-associated factor family member 2
FIT	Fat storage-inducing transmembrane proteins
fld1Δ	Few lipid droplets
FRET	Fluorescence resonance energy transfer
FSP27	Fat-specific protein 27
G3P	Glycerol-3-phosphate
GET	Guided-entry of tail-anchored proteins
GPCRs	G protein-coupled receptors
GPAT	Glycerol-3-phosphate acyltransferase
GUVs	Giant unilamellar vesicles
HCV	Hepatitis C virus
HILPDA/HIG2	Hypoxia inducible lipid droplet associated
HMM	Hidden Markov models
HMGCR	Hydroxy-3-methylglutaryl coenzyme A reductase
HR	Hairpin region
HSD17B11	Hydroxysteroid 17-Beta Dehydrogenase 11
IMD	Integral membrane domain
Insig-1	Insulin induced gene 1
Las A	Lasonolide A
LCAT	Lecithin cholesterol acyltransferase
LDAH	Serine hydrolase
LDO	Lipid droplet organization
LDAH	Lipid droplet associated hydrolase
LDAF1	Lipid droplet assembly factor 1
Ldo16	Lipid droplet organization protein 16
Ldb16	Low dye binding
LD	Lipid droplet
LPA	Lysophosphatidic acid
LTPs	Lipid transfer proteins
MAG	Monoacylglycerol
MCTP	Multiple C2 domain containing transmembrane
MD	Molecular dynamics
Mdm1	Morphology 1
METTL7A/AAM-B	Methyltransferase-like protein 7A

MGAT	Monoacylglycerol acyltransferase
Nem1	Nuclear envelope morphology protein
nER	Nuclear ER
NPC2	Niemann-Pick type C2
NMR	Nuclear magnetic resonance
NSDHL	NAD(P)H steroid dehydrogenase-like
NT	Non-transfected cells
NVJ	Nucleus-vacuole junction
OP	Opsin
ORP5	Oxysterol binding protein
PA	Phosphatidic acid
PAP	Phosphatidic acid phosphohydrolase
PC	Phosphatidylcholine
PCP	Protein correlation profiling
PDB	Protein data bank
PE	Phosphatidylethanolamine
PG	Phosphatidylglycerol
PI	Phosphatidylinositol
pLDs	Peripheral LDs
PLIN1	Perilipin 1
PLIN2	Perilipin 2
PNS	Post-nuclear supernatant
POPC	Palmitoyl-2-oleyl-sn-glycero-phosphocholine.
PPVs	Preperoxisomal vesicles
PS	Phosphatidylserine
PX	Phox homology
PXA	Phox homology associated
p97/VCP	Valosin containing protein
RDH10	Retinol dehydrogenase 10
RGS	Regulator of G-protein signaling
RHD	Reticulon homology domain
RMs	Rough microsomes
RNAi	RNA interference
SARS-COV-2	Severe acute respiratory syndrome coronavirus 2

SDSL	Site-directed spin labeling
SDS-PAGE	Sodium dodecyl sulphate polyacrylamide gel electrophoresis
SEs	Sterol esters
SNXs	Sorting-nexins
Snz	Snazarus
SND	SRP-independent
SRP	Signal recognition particle
SREBP-1	Sterol-regulatory binding protein
SURF-TAG	Surface- triacylglycerol
TAGs	Triacylglycerols
TIM	Translocase of the inner membrane
TMDs	Transmembrane domains
TOM	Translocase of the outer membrane
TRIO	Triolein
UAS	Ubiquitin-associated domain
UBAC2	UBA domain containing 2
UBA	Ubiquitin-associated
UBX	Ubiquitin regulatory X
UBXD8	Ubiquitin regulatory X domain-containing protein 8

11. Acknowledgements

During my time at the Saarland University, I had the opportunity to meet and collaborate with excellent colleagues and friends. The work in this thesis would not have been possible without the excellent assistance from my lab mates and collaborators.

First and foremost, I would like to thank my supervisor Prof. Dr. Bianca Schrul for giving me an opportunity to carry my PhD under her supervision. I would also like to thank her for training me and her support during the writing of this thesis. Additionally, I would also like to thank Prof. Dr Robert Ernst and Prof. Dr. David Mick for their valuable suggestions and their constructive criticism during our joint lab meetings on the progress of my research project. I would also like to thank Prof. Dr. Jochen Hub and Dr. Chetan Poojari. Without their MD simulations data, it would be impossible to bring this story to fruition successfully. I would specifically like to thank Chetan for being a good friend and patiently answering my questions about MD simulations data and always going one step ahead to help me out.

I was lucky to have awesome lab mates from both the Schrul and Ernst group, who maintained a cordial environment within the lab and helped me in matters both inside and outside the lab. I would like to thank Lisa Friedmann and Louisa Krauß who provided excellent technical assistance with the PEGylation experiments, and whom I got the opportunity to supervise during my PhD. A big thank to Silke and Moni for managing the lab and their help with the experiments. I would also like to thank Rehani for taking over the project successfully and complementing the PEGylation and MD simulations data with the EPR experiments to put the publication together. I would also like to thank Stefanie, Luisa, Anne, and Moni for talk over coffee breaks and listening to me and sharing their lab experiences. I would like to thank all Ernst group members for their support and being good friends/neighbors during my time in the lab.

I would also like to express my gratitude to all excellent group leaders and Professors I had the opportunity to work with in Germany. At the end, I would like to thank my parents for their encouragement and support all the way from India.

12. Lebenslauf

Aus datenschutzrechtlichen Gründen wird der Lebenslauf in der elektronischen Fassung der Dissertation nicht veröffentlicht